Inaugural dissertation

for

obtaining the doctoral degree

of the

Combined Faculty of Mathematics, Engineering and Natural Sciences

of the

Ruprecht - Karls - University
Heidelberg

Presented by

M.Sc. Erik Župa

born in: Prešov, Slovak Republic

Oral examination: October 7th, 2022

Structural Analysis of gamma-Tubulin Complexes by Cryo-EM

Referees: Prof. Elmar Schiebel

Dr. Stefan Pfeffer

Contributions

The analyses and experiments presented in this PhD thesis were performed solely by me under supervision of Dr. Stefan Pfeffer if not stated otherwise. The cryo-EM analyses were performed on the samples purified from the research group of Prof. Scheibel, specifically Dr. Peng Liu, Anjun Zheng and Martin Wúrtz. Negative stain EM analyses were performed for some of the samples by Dr. Annett Neuner, Dr. Dirk Flemming and Martin Würtz. Biological and biochemical analyses mentioned in the thesis were conducted by my aforementioned collaborators who purified the samples for cryo-EM and others as Anna Böhler, Dr. Szymon Kmiecik, Lukas Rohland and Ariani Rahadian. Cryo-EM analysis of the 4-spoked assembly intermediate mentioned in this PhD thesis was performed by Giulia Tonon under my supervision.

Table of Contents

List of Figures

List of Tables

Abbreviations

IF, IFs- Intermediate filament/s

MT, MTs- Microtubule/s

TriC- T-complex protein ring complex

TBCA-TBCE- Tubulin specific chaperons A,B,C,D,E

FtsZ- Filamenting temperature-sensitive mutant Z

GTP- Guanosine-5'-triphsophate

K-fibers- Kinetochores fibers

ch-TOG- Colonic, hepatic tumor overexpressed gene

SAS-6- Spindle assembly abnormal protein 6 homolog

MT-A, MT-B, MT-C – Microtubule A, B, C

PCM- Pericentriolar material

MTOC- Microtubule organisational centre

CEP135- Centrosomal protein 135

Cryo-ET- Cryo-electron tomography

γ-TuC, γ-TuCs- γ-Tubulin Complex/es

PCM1- Pericentriolar Material 1

Cdk1- Cyclin-dependent kinase 1

Plk4- Polo-like kinase 4

CEP250- Centrosomal protein 250

CEP68- Centrosomal protein 68

LRRC45- Leucine Rich Repeat Containing 45

Nek2- NIMA-related kinase 2

PP1- Protein phosphatase 1

MAP, MAPs- Microtubule-associated protein/s

TIP, TIPs- Microtubule-tracking protein/s

EB1- Microtubule plus-end binding protein

GDP-Pi- Guanosine-5'-diphosphate with dihydrogen phosphate group

GDP- Guanosine-5'-diphosphate

TPX2- Targeting protein for Xklp2

DCX- Doublecortin

Ran-GTP- RAs-related Nuclear protein

CPC- Chromosomal passenger complex

INCENP- Inner centromere protein

NEDD1- Neural precursor cell expressed developmentally down-regulated protein 1

RHAMM- Receptor for Hyaluronan Mediated Motility

HAUS- HAUS augmin-like complex subunit

TIRF- Total Internal Reflection Fluorescence microscopy

GM130- Golgi matrix protein 130

AKAP450- The A-kinase anchor protein 450

Cdk5Rap2- CDK5 Regulatory Subunit Associated Protein 2

CAMSAP- Calmodulin-regulated spectrin-associated protein

CLASP- CLIP-associating protein

GM130- Golgi matrix protein 185

CEP350- Centrosomal protein 350

Nesprin-1- Nuclear envelope spectrin repeat protein 1

Sun1- SUN domain-containing protein 1

Sun2- SUN domain-containing protein 2

KASH- Klarsicht, ANC-1, Syne homology (membrane proteins)

MZT1- Mitotic Spindle Organizing Protein 1

MZT2- Mitotic Spindle Organizing Protein 2

GCP- Gamma-complex protein

γ-TuSC- γ-tubulin small complex

γ-TuRC- γ-tubulin ring complex

SPB- Spindle pole body

Spc110- Spindle pole body component 110

Spc29- Spindle pole body component 29

Cmd1-Calmodulin 1

Spc42- Spindle pole body component 42

Cnm67- Chaotic nuclear migration protein 67

Spc72- Spindle pole body component 72

CM1- Centrosomin motif 1

Ndc1- Nucleoporin NDC1

Mps2- Monopolar spindle protein 2

Bbp1- Bfr1 binding protein

Kar1- karyogamy protein 1

Mps3- Monopolar spindle protein 3

Cdc31- Cell division control protein 31

Sfi1- SFI1 centrin binding protein

Spc24- Spindle pole body component 24

Spc25- Spindle pole body component 25

Spc34- Spindle pole body component 34

EM- Electron microscopy

Spc97- Spindle pole body component 97

Spc98- Spindle pole body component 98

GRIP- γ-tubulin ring protein

Stu2- Suppressor of tubulin 2

TOG- Tumor overexpressed gene

Kar9- Karyogamy protein 9

iMTOC- Interphase microtubule organisation center

eMTOC- Equatorial microtubule organisation center

Mto1- Morphology defective microtubule organiser 1

Mto2- Morphology defective microtubule organiser 2

Gfh1- Gamma-complex protein gfh1

Mod21- Gamma-complex protein mod21

Alp16- Gamma-complex protein Alp16

FRET- Förster resonance energy transfer

NME7- Nucleotide diphosphate kinase 7

Plk1- Polo-like kinase 1

NME1- Nucleotide diphosphate kinase 1

NME2- Nucleotide diphosphate kinase 2

CEP152- Centrosomal protein 152

CEP192- Centrosomal protein 192

SPA- Single particle analysis

CTF- Contrast transfer function

CCD- Charge-couple device

DDD- Direct detector device

PDF- Probability distribution function

SDS-PAGE- sodium dodecyl sulphate- polyacrylamide gel electrophoresis

FSC- Fourier shell correlation

NTE- N-terminal extension

PDB- Protein database

R.M.S.D.- Root mean square deviation

IDo- Insertion domain

CD- Circular dichroism

Arp- Actin related protein

eGFP- Enhanced green fluorescent protein

2D- Two dimensional

3D- Three dimensional

LFQ- Label free quantification

MDFF- Molecular dynamics flexible fitting

Summary

The cytoskeleton is an essential component of cells composed of three types of polymer networks- actin filaments, intermediate filaments and microtubules. Together they ensure compartmentation, spatial and temporal regulation of cargo flow and regulate the cell shape. Microtubules, the largest polymers of the cytoskeleton, are hollow cylinders composed of α/β-tubulin dimers arranged in protofilaments. The orientation of α/β-tubulin dimers in protofilaments is giving rise to the polarity of microtubules with the β-tubulin-facing plus end and the α-tubulin-facing minus end. The microtubule plus end is dynamic while the minus end is the origin of microtubule nucleation.

In cells, microtubules are formed *de novo* in a process termed microtubule nucleation that is mediated by γ-TuCs composed of γ-tubulins and gamma-complex proteins (GCPs). These complexes serve as structural templates for microtubule nucleation, accelerating the process by decreasing an initial kinetic barrier. In fungi, the principal microtubule template is the γ-TuSC, which is assembled from Spc97 and Spc98 and two copies of γ-tubulin, and oligomerizes at the SPB into a ring-like structure templating microtubule nucleation. The vertebrate principal microtubule template, the γ-TuRC, is compositionally more complex. Besides containing homologs of fungal Spc97 and Spc98 termed GCP2 and GCP3, respectively, three additional GCP variants-GCP4, GCP5 and GCP6 - are present as well. Structural studies of the γ-TuRC have been not successful, preventing description of its molecular architecture and geometry and cryo-EM of the γ-TuSC reached only a medium resolution not allowing to elucidate details as an interface on a residue level or small conformational differences.

In this study, I present detailed structures of both types of γ-TuCs complemented with biological approaches performed by my collaborators. Using cryo-EM and negative stain EM analysis, I gained insights into the structure, conformation and geometry of these complexes.

Combining cryo-EM and negative stain EM analysis, I described the structure of the *Candida albicans* γ-TuSC heterotetramer as a representative of the fungal microtubule template. The high-resolution reconstruction allowed me to describe in detail the intermolecular interface of *Candida albicans* γ-TuSC subunits and to identify an extended interface specific for the fungal class of *Saccharomycetes, which* underlies conformational stability of the γ-TuSC. This interface is absent in the vertebrate γ-TuRC, where it is replaced by electrostatic interactions between neighbouring γ-tubulins. A comparison of representative genomes across evolution allowed me to dissect the evolutionary relationship of microtubule nucleators, revealing that the γ-TuSC evolved by simplification of the more complex γ-TuRC system.

Applying cryo-EM, I successfully resolved the vertebrate γ-TuRC at sufficient resolution to describe its shape and unambiguously assign after more than 20 years its molecular components in a specific order and position. Furthermore, I resolved an unexpected region in the lumen of the γ-TuRC composed of a helical scaffold binding one copy of actin. My model of the γ-TuRC allowed me to measure its helical parameters and compare it with microtubule parameters, identifying deviations that overall suggested a conformational activation mechanism for the γ-TuRC.

Cryo-EM of the γ-TuRC revealed its uniform structure assembled from more than 30 individual proteins, which I aimed to understand by addressing the γ-TuRC assembly mechanism. Reconstructing γ-TuRC assembly intermediates by cryo-EM, I proposed an assembly mechanism starting from a 6-spoked assembly intermediate containing GCP4,5,6, which is expanded by preformed γ-TuSC units. The expansion process is coupled to conformational rearrangements. Furthermore, preventing incorporation of actin into the γ-TuRC, I demonstrated that actin is a dispensable component for γ-TuRC structure and assembly.

In conclusion, this study represents a major breakthrough in the understanding of γ-TuC structures and their role in microtubule nucleation. It creates a basis for follow-up studies, e.g. structural studies of γ-TuC with their binding partners from the yeast SPB of yeasts or the vertebrate centrosome, aiming to elucidating their effect on microtubule nucleation.

Zussamenfassung

Ein wesentlicher Bestandteil von Zellen ist das Zytoskelett, welches aus drei Arten von Polymeren besteht - Aktinfilamente, Intermediärfilamente und Mikrotubuli. Zusammen sorgen sie für die Kompartmentalisierung der Zelle, deren äußeren Struktur, sowie für die räumliche und zeitliche Regulierung des intrazellulären Transports. Mikrotubuli, die größten Polymere des Zytoskeletts sind Hohlzylinder, die aus α/β-Tubulin-Dimeren bestehen, welche sich zu Protofilamenten anordnen. Die Orientierung von α/β-Tubulin-Dimeren in Protofilamenten macht Mikrotubuli zu polaren Strukturen, wobei die β-Tubulin zugewandte Seite als Plus-Ende und die α-Tubulin zugewandte Seite als Minus-Ende bezeichnet wird. Das Plus-Ende der Mikrotubuli ist dynamisch, wohingegen das Minus-Ende der Ursprung der Nukleation der Mikrotubuli ist.

In Zellen werden Mikrotubuli in einem als Mikrotubuli-Nukleation bezeichneten Prozess neu gebildet. Die Nukleation wir durch γ-TuCs vermittelt, die aus γ-Tubulin und Gamma-Komplex-Proteinen (GCPs) bestehen. Diese Komplexe dienen als strukturelle Vorlagen, die eine Schicht der Mikrotubuli-Helix nachahmen und damit als Startpunkt für die Assemblierung von Mikrotubuli dienen. Dadurch wird die initiale kinetische Barriere verringert und der Prozess beschleunigt sich. In Pilzen ist die Grundeinheit der Mikrotubuli-Nukleation der γ-TuSC, welcher aus Spc97 und Spc98 und zwei γ-Tubulin Proteinen zu einem Heterotetramer zusammengesetzt ist und am SPB zu einer ringartigen Struktur oligomerisiert. In Wirbeltieren dient der in seiner Zusammensetzung wesentlich komplexere γ-TuRC als strukturelle Vorlage für die Assemblierung von Mikrotubuli. Neben den in Pilzen vorkommenden Spc97 und Spc98 Proteinen, die als GCP2 bzw. GCP3 bezeichnet werden, sind noch drei weitere GCPs, GCP4, GCP5 und GCP6 vorhanden. Detaillierte strukturelle Informationen zur molekularen Architektur und Geometrie der beiden Komplexe fehlen, was das Verständnis ihrer Funktionsmechanismen stark einschränkt.

In dieser Studie präsentiere ich detaillierte Strukturen beider γ-TuCs, ergänzt durch biologische Experimente meiner Kollegen. Unter Verwendung von Kryo-EM und Negativkontrast EM-Analyse gewann ich Einblicke in die Struktur, Konformation und Geometrie dieser Komplexe.

Die hochaufgelöste Rekonstruktion des *Candida albicans* γ-TuSC, einem für Pilze repräsentativen γ-TuC Vertreter, ermöglichte es mir, die Interaktionsfläche der Untereinheiten detailliert zu beschreiben und dadurch ein erweitertes Interaktionsnetzwerk zu identifizieren, das spezifisch für die Klasse *Saccharomyceten* ist und der Konformationsstabilität des γ-TuSC zugrunde liegt. Dieses erweiterte Interaktionsnetzwerk fehlt im Wirbeltier γ-TuRC, wo elektrostatische Wechselwirkungen zwischen benachbarten γ-Tubulinen eine ähnliche Funktion besitzt. Eine vergleichende Genomanalyse klärte zudem das evolutionäre Verhältnis der Nukleationssysteme auf und zeigte, dass der γ-TuSC durch Vereinfachung des γ-TuRC entstanden sein muss.

Weiterhin gelang es mir mittels Kryo-EM die Struktur des γ-TuRC aus Wirbeltieren bei ausreichender Auflösung zu bestimmen, um seine teilweise asymmetrische Geometrie zu beschreiben und mehr als 20 Jahre nach seiner Entdeckung seine molekulare Architektur zu verstehen. Darüber hinaus habe ich eine neue Strukturkomponente im Lumen des γ-TuRC aufgelöst, die aus einem helikalen Gerüst und einem Molekül Aktin besteht. Das erhaltene atomare Modell des γ-TuRC ermöglichte es mir, die helikalen Parameter des γ-TuRC zu messen und sie mit den Parametern von Mikrotubuli zu vergleichen, wobei eine deutliche Abweichung festgestellt wurde, die auf eine mögliche konformationelle Regulation der γ-TuRC Aktivität hindeutete.

Meine Kryo-EM Experimente zeigten eine einheitliche räumliche Anordnung von mehr als 30 einzelnen Proteinen im γ-TuRC. Um besser zu verstehen wie diese einheitliche Anordnung zustande kommt, untersuchte ich den Assemblierungsmechanismus des γ-TuRC. Basierend auf Kryo-EM Rekonstruktionen von Zwischenstufen der γ-TuRC Assemblierung schlug ich einen Assemblierungsmechanismus vor, der mit einer 6-speichigen Zwischenstufe beginnt, welche GCP4,5,6 beinhaltet und anschließend um einzelne γ-TuSC-Einheiten erweitert wird. Diese Erweiterung ist verbunden mit Konformationsänderungen innerhalb der Zwischenstufen. Durch die strukturelle Analyse einer γ-TuRC Variante, bei der die Integration von Aktin gezielt verhindert wurde, konnte ich zudem zeigen, dass Aktin entbehrlich für die strukturelle Stabilität, sowie die Assemblierung des γ-TuRC ist.

Zusammenfassend stellt diese Studie einen großen Fortschritt im Verständnis der Struktur von γ-TuCs und ihrer Rolle bei der Nukleation von Mikrotubuli dar. Dabei wurde die Grundlage für weitere Studien geschaffen, die beispielsweise die Strukturbestimmung dieser Komplexe mit ihren Interaktionspartnern aus dem SPB in Hefen oder aus dem Zentrosom von Wirbeltieren verfolgen um die Regulation des Prozesses zu verstehen .

1 Introduction

1.1 The cytoskeleton of eukaryotic cells

Maintenance of intracellular composition, connection of cytosolic processes and ability to withstand and adapt to the environment are essential for survival of eukaryotic cells. In order to regulate these functions, cells have developed a network of polymers termed the cytoskeleton. The cytoskeleton is a dynamic component of the cell, temporally and spatially controlled to regulate biochemical processes, transport of cargo, cell motility, and to maintain and modify the shape of cell. The interplay of the cytoskeleton and cell organelles is essential for the intracellular environment. Provided network of cytoskeletal components allows for smooth transition between processes such as transcription and translation[1]. Additionally, the cytoskeleton controls local protein synthesis in the cell by transporting ribosomes and mRNA to specific cellular sites[2].

1.1.1 Composition of the cytoskeleton

The eukaryotic cytoskeleton is composed of three types of polymers- actin filaments, microtubules and intermediate filaments (Fig. 1a). Together, they generate forces inside of the cell to organise the cellular environment. All of them form compact networks between cell organelles and membranes and differ in composition, regulatory mechanisms and stiffness. Actin filaments are compositionally the simplest cytoskeletal polymers comprising only actin. Actin monomers assemble into helical filaments and form a highly branched network. A plethora of cytosolic proteins contain actin-binding sites and participate in regulation of actin filaments[3,4-6]. The network of actin filaments is polymerised in different cell sites upon signal responses and thus can react to specific needs. After fulfilling their role, actin filaments are depolymerised and monomeric components can be recycled for the actin polymerisation at different cellular sites. Intermediate filaments (IF) are cytoskeletal components that are compositionally simple but at the same time more versatile. Individual IF is always assembled of only one protein. However, several proteins were identified with ability to oligomerise and form IF, giving rise to different types of IF. Over the years, proteins of IF were grouped from type I to type V based on the protein identity and homology: type I-keratins, type II-vimentin, type III-desmin and glial fibrillary acidic protein, type IV- neurofilament proteins and type V-lamins[7]. Compared to actin and microtubules, IFs form networks not only in the cytosol but also in the nucleus[8]. The nuclear network of IFs is formed by lamin[9]. On the other hand, cytosolic IF composition varies depending on cell type, e.g. including desmin in muscle cells or keratin in epithelial cells[10,11]. Additionally, IFs are essential in tissue formation as they can connect cytoskeletal components of adjacent cells via cell-cell junctions[12].

1.1.2 Microtubule composition and specificity

The third component of the eukaryotic cytoskeleton are microtubules (MTs). Their width of 25 nm and the length that they can reach (up to 50 μm) make them the largest cytoskeletal structure. Basic components of MTs are α- and β-tubulins, folded upon action of TriC chaperonin[13], and later α- and β-tubulins assemble into stable heterodimeric by action of five tubulin-specific chaperones termed TBCA-TBCE[14]. Tubulins share distant homology with FtsZ proteins of the prokaryotic cytoskeleton, making FtsZ potential ancestors of tubulins[15]. Tubulins are globular proteins with one ligand binding site. In dimeric form, α-tubulin contains GTP that cannot be hydrolysed or displaced, while GTP in β-tubulin is exchangeable and is hydrolysed during MT growth. By oligomerisation, α/β-tubulin dimers assemble into linear structures termed protofilaments, which interact along their axes to form hollow cylinders, MTs[16]. The uniform orientation of α/β-tubulins in protofilaments creates polarity with α-tubulin facing towards the MT minus end and β-tubulin facing towards the MT plus end. *In vivo*, MTs are

structurally uniform and comprise of 13 protofilaments[17]. However, lower numbers of protofilaments were observed in nematodes[18]. *In vitro* spontaneous assembly of MTs results in protofilaments numbers ranging from 9-16, with 14-protofilament MTs being the most abundant form[19,20].

MTs can be distinguished into three groups- astral, interpolar and K-fibers (Fig. 1b) and all of them play a role in cell division. Astral microtubules are not essential for mitosis[21] but required for positioning of the mitotic spindle before chromosome segregation[22,23]. The position of the spindle and centrosomes is adjusted via forces applied by dynactin-dynein complexes on astral microtubules that are anchored to the cortex[24]. Together, these proteins determine the orientation and position of the daughter cell and the flux of cytosolic material to ensure proper cell division.

Interpolar MTs are the main component of the mitotic spindle growing from centrosomes towards chromosomes (Fig. 1b). They are characterised by highly dynamic growth and shrinkage with a half-life of less than one minute (Fig. 1b)[25]. During the early stages of mitosis, interpolar MTs interact dynamically with chromosomes and align them in the equatorial plane. Interaction of interpolar MTs with chromosomes is mediated by chromokinesins or by lateral interactions with kinetochores[26-28]. Despite their interaction with chromosomes, interpolar MTs do not directly participate in chromosome segregation and they are dispensable for meiosis in fission yeast[29].

Chromosome segregation is mediated by K-fibers in the mitotic spindle (Fig. 1b). They are more stable with a half-life of 4-8 minutes (Fig. 1b) and formed by 20-40 bundled microtubules aligned parallelly[30,31]. Bundling of MTs in K-fibers seems to be partially mediated by MT binding proteins, such as clathrin and ch-TOG[32]. Despite representing a smaller population of MTs during mitosis, they directly attach to chromosomes via the MT-kinetochore complex and segregate them to the poles of newly forming cells in anaphase (Fig. 1b)[33]. Chromosome segregation is happening via constant polymerisation and depolymerisation of K-fibers and dynamic changes on both the MT plus ends and minus ends[34,35].

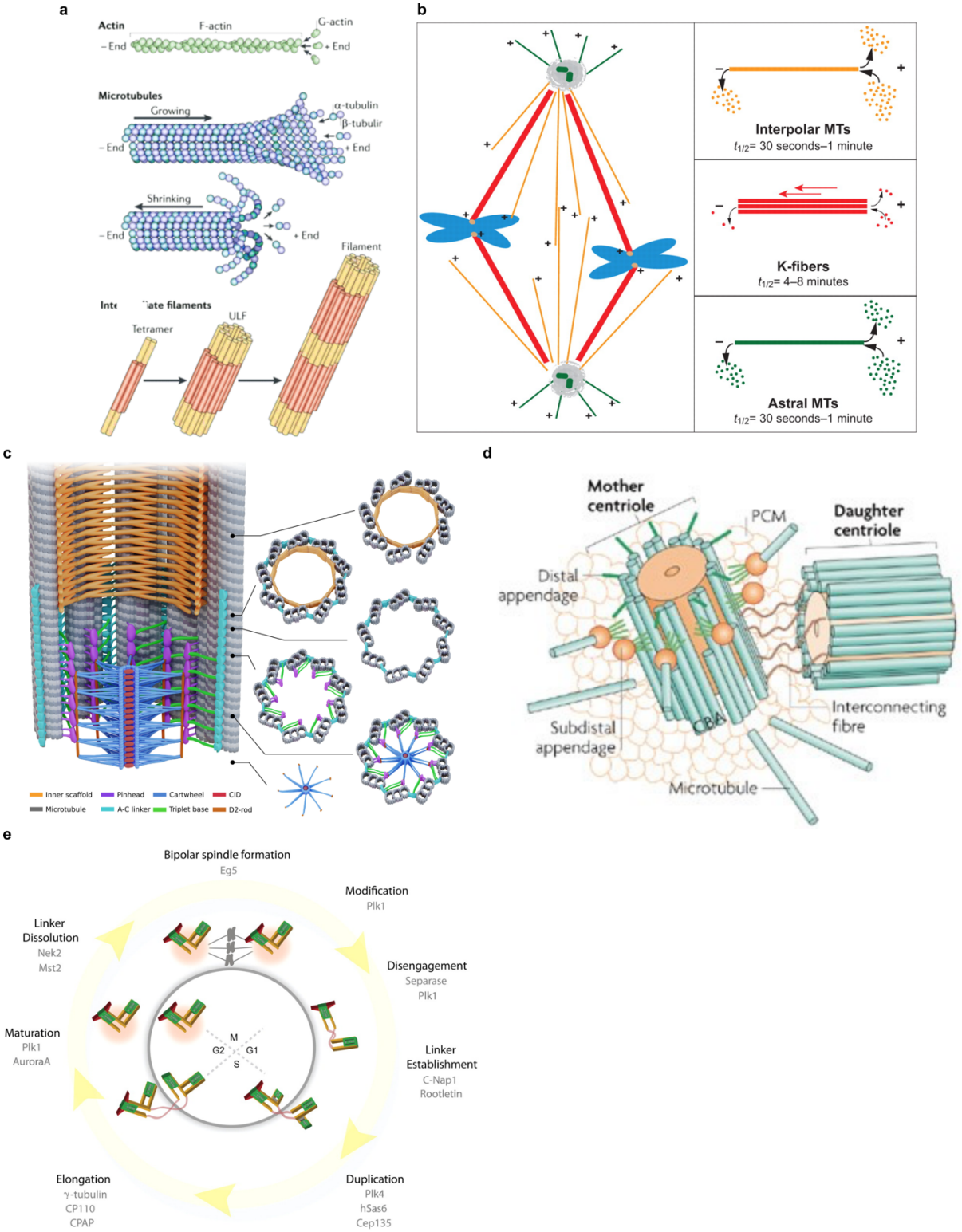

Figure 1: Components of the cytoskeleton and the centrosome architecture.
a) Components of the cytoskeleton-actin filaments, microtubules and intermediate filaments. Panel is from Hémonnot 2016[36].
b) Type of MTs nucleated in the cell with different half-time reflecting their stability. Panel is from Meunier *et al.*, 2012[21].
c) Schematic representation of the centriole architecture. MT triplets are connected with radial spokes via the pinhead and the cartwheel in the centre, which is formed by SAS-6. MT triplets are connected via linkers. Difference between the proximal end with the cartwheel and the distal end without the cartwheel is visible. Panel is from Klena *et al.*, 2020[37].
d) Schematic representation of the centrosome composed of two centrioles. MTs are nucleated from PCM and subdistal appendages. Panel is from Bettencourt-Dias *et al.*, 2007[38].

e) Schematic representation of the centrosome biogenesis during cell cycle with participating proteins indicated. Panel is from Mardin *et al*., 2012[39].

1.1.3 Centrosome structure

In addition to formation of the mitotic spindle, MTs are also components of the centrosome and other cellular structures, such as cilia and flagella. The centrosome is a cellular structure organising astral MTs, spindle MTs and K-fibers during mitosis and thus serves as the primary MTOC. As this name may indicate, the MTOC is a cell component/organelle that has capability to recruit all factors required for nucleation of MTs. The centrosome is composed of a centriole pair, which is formed by the mother and daughter centriole linked via their proximal ends (Fig. 1d). Each centriole is structurally composed of the cartwheel with the 9-fold radial symmetry (Fig. 1c). The asymmetric unit of this cartwheel contains the central hub at the proximal end (Fig. 1c), the radial spoke and the pinhead that connects centriolar MTs with radial spokes (Fig. 1c)[40]. The cartwheel is formed by 9 copies of the SAS-6 protein that extends with its C-terminus towards the radial part of the centriole[41]. The structure of the radial spoke is still under investigation, but interactions between SAS-6 and CEP135 have been reported, which together can form the base of the radial spoke, connecting MTs with the central hub[42]. In vertebrates, centriolar MTs are arranged in triplets with MT-A containing 13 protofilaments, MT-B containing 10 protofilaments and MT-C containing 10 protofilaments (Fig. 1c). In *Drosophila melanogaster,* the centriole contains only MT-doublets, lacking MT-C[43]. MT-A is directly connected to the radial spoke via the pinhead, which interacts with highly curved protofilaments 2-3 of MT-A[43]. Centriolar MTs grow from the proximal end to the distal end of the centriole (Fig. 1c). Recent studies using cryo-ET allowed to describe the structure of the MT triplet along length of the centriole in more details and provided insights into centriole biogenesis[40]. Biogenesis of the MT triplet starts with MT-A, the longest one, and continues with attachment of MT-B and MT-C along the proximal end of the centriole[40]. It is unclear how MT-B and MT-C assembly is specified and triggered during centriole biogenesis. Study identified 11 MIPs at the proximal end of centriole triplets, stabilising MTs and establishing junction between MTs in the triplet[40].

1.1.4 Centrosomes in cell cycle and centrosome duplication

The centrosome plays an essential role in cell division and binds a plethora of proteins that are implicated in regulatory processes. Entry of the centrosome into mitosis is controlled by activity of cyclins and kinases that are present on the centrosome. Cdk1 is recruited to the centrosome by AuroraA activity and triggers mitotic entry[44]. In addition to the action of centrosome-associated proteins, mitotic entry is probably coregulated via the PCM itself, but the mechanism is stillunknown. Mislocalisation of some centrosomal proteins that trigger mitotic exit, such as AKAP450[45] or Centriolin[46], has the same effect on cell cycle as centriole removal showing that protein composition of the centrosome matters in cell cycle progression.

After mitosis, daughter and mother centrioles need to be disconnected from each other to form new centrosomes and initiate the next cell cycle, which is achieved by separase (Fig. 1e)[47]. Before S phase, biogenesis of new procentrioles likely starts on existing centrioles in presence of centrin[48]. In the next steps, SAS-6 is recruited to mother and daughter centrioles to form the central hub of the procentriole and thereby inititates the 9-fold symmetry (Fig. 1e). Formation of the central hub requires activity of Plk4 kinase (Fig. 1e)[49], the *Drosophila melanogaster* homolog of which was shown to be implicated also in *de novo* centriole assembly[49]. Biogenesis of the procentriole continues with the growth of MT triplets, which seems to be regulated by ε-tubulin that affects the length of the centriole MTs and triplets assembly[50]. Progressing to G2 phase, centriole pairs with growing procentrioles need to be segregated

(Fig. 1e). Assembly of centriole pairs depends mainly on the coiled coil protein CEP250, the filamentous protein- rootletin and others, such as β-catenin, CEP68 and LRRC45, the precise role of which is still elusive. CEP250 is the main component of the centrosome junction, as it creates platform for binding of rootletin[51]. To keep the junction of centrioles assembled, CEP250 has to be kept in an unphosphorylated state. The combination of the kinase Nek2 and phosphatase PP1 regulates separation of the centriole pair (Fig. 1e)[52-54]. However, Nek2 is not essential for centriole separation due to pulling forces generated by antiparallel sliding of MTs, which contributes to the disjunction and if necessary, sliding can produce forces sufficient to split centrioles[55]. Maturation of the procentriole is completed in the next cell cycle and its transition into the mother centriole takes overall two cell cycles.

1.1.5 Microtubule shrinking and growing

MTs are highly dynamic structures that constantly grow and shrink – a process termed dynamic instability. This dynamic behaviour is essential for spindle pole MTs that have to position chromosomes in the equatorial plane, properly attach to chromosomes and later segregate chromatids into the cell poles during mitosis. Growing and shrinking of MTs is mostly propagated on the plus end where α/β-tubulin dimers elongate MTs. MT dynamic is dependent on the nucleotide state in β-tubulins at the plus end[56]. GTP presence results in the stable MT plus end[57] that recruits several MAPs and TIPs as EB1[58,59]. The MT plus end tip can assume a variety of shapes from the blunt to the curved end[60]. α/β-tubulin dimers always bind to the plus end tip in the GTP state, being in the curved conformation (Fig. 2a)[57,61]. Upon binding of new α/β-tubulin into a protofilament, the curved conformation of previous dimer changes into the straight conformation[56]. This conformational change is coupled to the hydrolysis of β-tubulin GTP, which results in the additional conformational change of α-tubulin (Fig. 2a). The conformational change of α-tubulin promotes catastrophe (switch to shrinkage) but shrinkage can be switched back to growth (rescue) after relaxation of α-tubulin (Fig. 2a)[60]. Besides the nucleotide state of tubulin, the dynamic behaviour of MTs is also modulated by other MT binding proteins[58]. MAP-triggered catastrophe and rescue are mediated by promoting a specific conformation of tubulin dimers in their vicinity. One of the proteins that influences stability of the plus end is EB1[62]. It binds to regions nearby the plus end but not directly at the tip of the MT plus (Fig. 2b)[59]. This is consistent with curved end of MTs at the tip, which does not provide two laterally bound protofilaments that would form the binding site for EB1 (Fig. 2b)[63,64]. Studies of the EB1 binding to MTs with GTPγS suggested that EB1 prefers tubulins in the GDP-Pi state where GTP is already hydrolysed but its phosphate is still present in the tubulin ligand pocket (Fig. 2b)[63]. However, it is likely that EB1 increases the hydrolysis of GTP, which could be caused by impacting tubulin dimers in the vicinity of its binding site.

EB1 is not the only MAP that modulates the conformation and dynamics of the MT plus end. Stathmin, MT depolymerases (e.g. Kinesin-13) and MT polymerase, ch-TOG, bind preferentially to the curved α/β-tubulin dimers and induce catastrophe or growth (Fig. 2d)[65-67]. This emphasises the role of α/β-tubulin conformation in MT dynamics. The effect of the ch-TOG binding to the MT plus end is highly dependent on the concentration of free α/β-tubulin units. At low concentration, ch-TOG stabilises the curved α/β-tubulin conformation and thereby increases depolymerisation (Fig. 2d)[68], while a high concentration of tubulin dimers leads to ch-TOG-mediated increase of the MT growth rate. Another MT plus end-binding protein, TPX2, has a stabilising effect and decreases the catastrophe rate, which is consistent with the described binding site of TPX2 on MT where TPX2 is contacting both longitudinal and lateral interfaces between tubulin dimers (Fig. 2c)[69]. A similar stabilisation effect on MTs is produced by DCX[70], a protein specific for neurons that binds to the interface of two tubulin dimers[71].

Nevertheless, none of the MT-growth promoting proteins was reported to promote rescue after MT catastrophe.

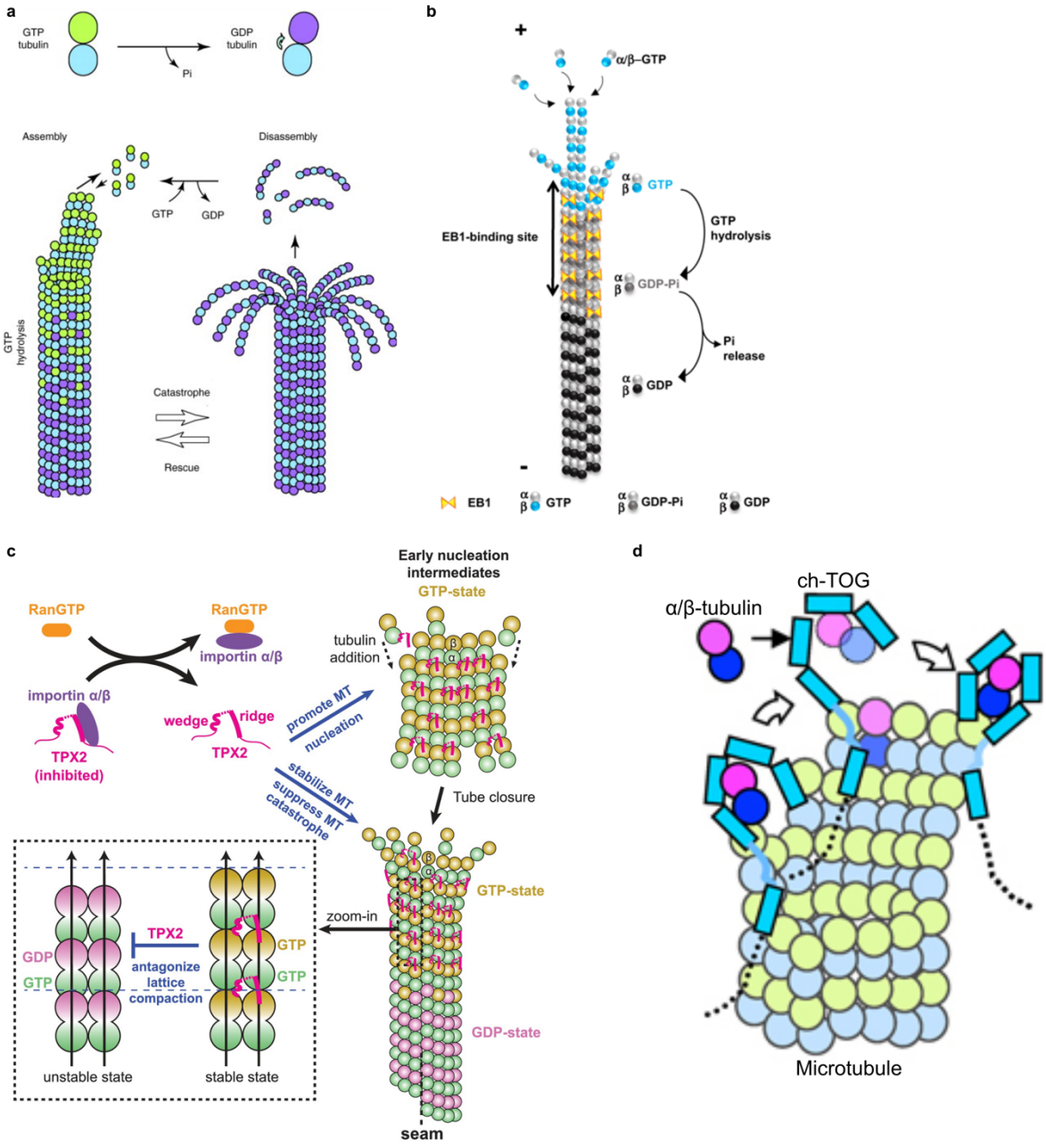

Figure 2: MT dynamics and the effect of MAPs on MT stabilisation.
a) Effect of GTP binding and hydrolysis on MT dynamics. The stable MT plus end with the GTP cap compared to the unstable MT plus end with the GDP cap promoting MT depolymerisation (catastrophe). Panel is from Al-Bassam *et al.*, 2011[72].
b) EB1 protein stabilising the MT plus end. EB1 binding to GDP-Pi tubulins below the tip of the plus end. Panel is from Nehlig *et al.*, 2017[73].
c) Schematic representation of the TPX2 role in MT nucleation and stabilisation. TPX2 released from importin-α/β is either promoting MT nucleation or stabilising the plus end, binding to GTP tubulins. Panel is from Zhang *et al.*, 2017[74].
d) The effect of ch-TOG on stabilisation of α/β-tubulin dimers in the curved conformation and in this way promoting MT depolymerisation. Panel is from Al-Bassam *et al.*, 2011[72].

1.1.6 Microtubule nucleation at chromatids and pre-existing MTs

Formation of the spindle during mitosis requires nucleation of many MTs in a short period of time. MT nucleation at centrosomes does not produce a sufficient number of MTs to position and segregate chromosomes. Therefore, the spindle is enriched for MTs nucleated from non-centrosomal MTOCs, namely pre-existing spindle MTs and chromatids. There are two known pathways of MT nucleation at chromatids- one driven by Ran-GTP-mediated activation of TPX2[75] and another based on Chromosomal Passenger Complex (CPC), which contains AuroraB, survivin, borealin and INCENP (Fig. 3a)[76]. The Ran-GTP pathway leads to a cascade of activation events important for chromatin-dependent MT nucleation. Activation of TPX2 results in activation of AuroraA, which in turn phosphorylates NEDD1 (Fig. 3b)[77]. Depletion of NEDD1 leads to loss of chromatin-MTs due to its role as the recruitment factor for γ-TuCs (Fig. 3b)[77].

The process of MT nucleation from pre-existing MTs is termed MT branching and is mediated by cooperation of the γ-TuC, Augmin and TPX2[78]. The best studied pathway of MT branching depends on the Ran-GTP activity releasing TPX2 from importin-α[79]. After its release, TPX2 binds directly to pre-existing MTs via its C-terminal half[74]. MTs decorated with TPX2 possess increased stability thereby allowing more efficient MT branching[74]. In addition to the functions of TPX2 in MT stabilisation and protein recruitment, the main role of TPX2 in MT nucleation comes from its ability to increase the local concentration of α/β-tubulins[80] by co-condensate formation. Another factor required for efficient MT branching is the octameric augmin complex. Composed of eight HAUS proteins (HAUS1-8) (Fig. 3c)[81], augmin serves as the recruitment and anchoring factor of γ-TuCs to the MT (Fig. 3c)[78,82-84]. As a component of the MT branching mechanism, augmin binds to pre-existing MTs via the HAUS8 N-terminus[85], while the γ-TuC binding is mediated separately by HAUS6, HAUS3 and HAUS5[86]. However, none of these proteins is able to bind γ-TuCs on their own, indicating a composite binding site formed by several HAUS proteins. Investigation of MT branching by TIRF microscopy provided complementary insights into kinetics of this process and the architecture of the branched MT network[87]. The vast majority of branched MTs is nucleated from mother MTs at shallow angles of ~10˚-30˚ (Fig. 3d) and branching events never occur in proximity of the MT plus end tip, indicating a mechanism for specific localisation of branching factors along the MT[87]. MT branching can be kinetically characterised as a two-step process. The first step is characterised by binding of branching factors, as for example TPX2, to mother MTs, defining a branching position. The second step is characterised by binding of additional factors as for example augmin, and MT nucleation itself[87]. It is likely that TPX2 and augmin affect kinetics of branching directly. Changes in their concentrations result in increase or decrease of branching kinetics for both reaction steps[87]. Augmin has been proven essential for MT branching, governing the second step of the process (together with the γ-TuCs)[87], while TPX2 governs the first step, marking a nucleation position on pre-existing MTs[87], in agreement with structural studies showing TPX2-decorated MTs[74]. Rather slow kinetics of the TPX2 binding to MTs would also explain why MT branching does not happen in the proximity of the growing MT plus end tip.

1.1.7 Microtubule nucleation at the Golgi apparatus

Uniform orientation of MTs is typical for MTs nucleated from the Golgi apparatus, which is the second most relevant MTOC in most mammalian cells[88]. Golgi MTs connect the Golgi membrane stacks and help to organise them after mitosis[89]. Uniformly oriented MTs at the Golgi enable directed transfer of cellular material[90]. Additionally, Golgi MTs participate in the organisation and positioning of the centrosomal MT network before mitosis[91]. Nucleation of MTs at the Golgi is γ-TuC-dependent but there is also an alternative pathway mediated by cis-Golgi protein GM130, which initiates TPX2-dependent MT nucleation[92]. The anchoring of γ-

TuCs to the Golgi is mediated by AKAP450 that binds to GM130[93] at the Golgi (Fig. 3e). Besides the γ-TuCs, AKAP450 recruits Cdk5Rap2[94] and myomegalin[95] that increase efficiency of γ-TuCs recruitment to the Golgi (Fig. 3e). AKAP450-anchored Cdk5Rap2 complex is sufficient for binding γ-TuC-capped MTs[91] but that does not hold true for the minus ends stabilised by CAMSAP2 that bind exclusively to the AKAP450-myomegalin complex (Fig. 3e)[91]. Non-capped MTs can be connected to the Golgi via CLASP proteins that bind to the CAMSAP2-stabilised minus ends (Fig. 3e)[91]. CLASP anchors MTs via interactions with the trans-Golgi protein GM185 (Fig. 3e)[96] but has also function in promoting the γ-TuC-mediated MT nucleation at the Golgi[97]. Interestingly, some isoforms of myomegalin are able to bind EB proteins[98], indicating their role in the regulation of MT polymerisation and nucleation from the Golgi. As mentioned above, MT nucleation requires pool of α/β-tubulins that is mainly provided by TPX2. Increased concentration of α/β-tubulins at the Golgi is provided by the tubulin chaperone TBCE that recycle tubulin in the Golgi surroundings[99]. The Golgi-nucleated MTs are more stable compare to the centrosomal one, which is caused by several proteins. Stabilisation of the minus end is provided by CAMSAP2 and CLASP as mentioned above (Fig. 3e). It was reported that even CEP350 participates in stabilisation of Golgi-MTs[100], likely indicating tied cooperation of the centrosome and the Golgi. The requirement for higher stability of the Golgi-nucleated MTs can be related to the fact that concentration of γ-TuCs directly present at the Golgi apparatus is not high[88] and stabilisation of MTs would prolong their lifespan without necessity to nucleate many MTs.

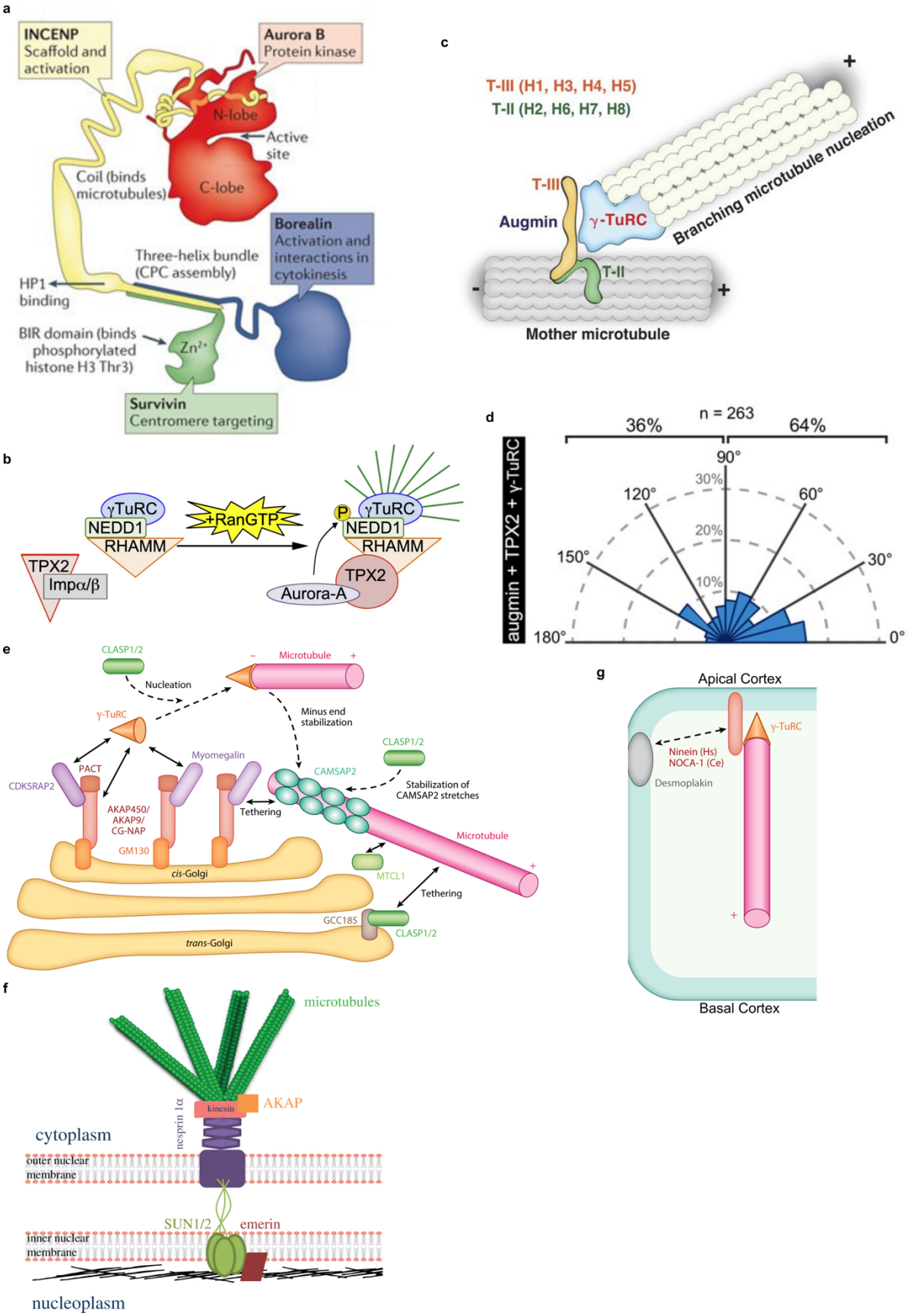

Figure 3: Protein complexes required for MT nucleation at different MTOCs.
a) Schematic representation of the CPC complex, which is responsible for MT nucleation at chromatids, with all components highlighted. Panel is from Carmena *et al.*, 2012[101].

b) Schematic representation of the RanGTP-induced complex responsible for MT nucleation at chromatids. All components are indicated. TPX2 recruits AuroraA to the RHAMM complex. Panel is from Scrofani *et al*., 2015[77].
c) Schematic representation of MT branching with all components except TPX2. Augmin is an essential factor (composed of HAUS proteins- H1-8) mediating connection between the γ-TuRC and the pre-existing MT. Panel is from Song *et al*., 2018[102].
d) Measurement of branching angles from *in vitro* MT nucleation assay. The majority of the angles is below 90º and most of the angles are between 0-30º. Panel is from Alfaro-Aco *et al*., 2020[103].
e) Schematic representation of MT nucleation from the Golgi with the involved proteins. Panel is from Wu *et al*., 2017[104].
f) Schematic representation of MT nucleation from the nuclear membrane. The Sun complex and nesprin-1 playing crucial role in the anchoring of MT nucleation base to the nuclear envelope. Panel is from Piccus *et al*., 2020[105].
g) Schematic representation of MT nucleation at the plasma membrane. Panel is from Wu *et al*., 2017[104].

1.1.8 Microtubule nucleation at the nuclear envelope

The nuclear envelope is one of the several non-centrosomal MTOCs typical for plant cells[106], as well as for muscle cells[107] where it serves as the main MTOC and *de novo* nucleated MTs contribute to positioning of nuclei within the syncytium (single cell with multiple nuclei). MT nucleation at the nuclear envelope requires nesprin-1 and AKAP450[108] (Fig. 3e). Recruitment of Akap450 to the outer nuclear membrane is mediated by Nesprin-1 (Fig. 3e), which associates also with other centrosomal proteins such as PCM1 and pericentrin[108]. The nuclear envelope is able to anchor Akap450 via the complex of several other inner nuclear membrane proteins as Sun1 and Sun2 (Fig. 3e) that interact with the outer membrane protein complex KASH, which in turn bound nesprin-1[108,109]. Formation of this membrane complex is crucial, as Sun1 and Sun2 depletion decreases amount of centrosomal proteins localised to the nuclear envelope, including the γ-TuCs[108,110]. However, it is not yet understood howγ-TuCs are recruited and localised to the nuclear envelope. Some evidence points to a role of nuclear pore proteins and possible involvement of MZT1 and MZT2 in the membrane deformation and the anchoring of γ-TuCs to complexes of the nuclear envelope[111].

1.1.9 Microtubule nucleation at the plasma membrane

The cellular cortex is a non-centrosomal MTOC where MTs are positioned close to the plasma membrane (Fig. 3f). This can be found in plant cells and animal epithelial cells[112,113]. Organisation of cortical MTs is often unipolar, with the MT minus ends located at the one side of cell and the plus ends on the other side of the cell[114], e.g. in epithelial cells where the minus end is located at the apical side and the plus end at the basal side (Fig. 3f)[115]. Such uniform MT orientation allows for directional transport of material. It was suggested that MT nucleation is mediated via γ-TuCs but their anchoring is not understood. The γ-TuC binding protein, NEDD1, was identified on the cortical nucleation sites, possibly having role in the anchoring or recruiting of γ-TuCs[116]. In epithelial cells, the anchoring of the γ-TuC is dependent on apical proteins, such as the actin-associated factor Shroom in *Xenopus laevis*[117]. Ninein was identified as another 'anchoring candidate', because it binds to the apical side of intestinal cells (Fig. 3f)[118]. Similarly, as for MT nucleation at the nuclear membrane, MZT1 and MZT2 are considered to participate in the anchoring of the γ-TuC to the plasma membrane[119]. Another mechanism of anchoring cortical MTs is mediated via the MT minus end-stabilising protein, CAMSAP3[115].

1.1.10 γ-tubulin as a part of a bigger complex

MT nucleation occurs at different MTOCs and in combination with different factors but almost all variants of the MTOC-based MT nucleation require the γ-TuCs. The discovery of γ-tubulin as a member of the tubulin superfamily[120] raised questions about its function. γ-tubulin identification as a part of MTOCs across eukaryotes revealed its role in MT nucleation. However, *in vivo*, γ-tubulin does not nucleate MTs on its own but only as a part of bigger

complexes. Purification of γ-TuCs from *Drosophila melanogaster*[121] and *Xenopus laevis*[122] revealed a ring-shaped complex with a diameter of ~28 nm. Despite high conservation of γ-tubulin across eukaryotes, the γ-TuC composition was observed to be different in fungi compared to other eukaryotes and mainly vertebrates. Studies in *Saccharomyces cerevisiae* revealed two components essential for MT nucleation apart from γ-tubulin, namely Spc97[123] and Spc98[124]. It was proposed that Spc97 and Spc98 bind γ-tubulin and form the fungi specific γ-TuC termed the γ-tubulin small complexes (γ-TuSC)[123]. Homologs of fungal Spc97 and Spc98 are present in other eukaryotes, where they are named GCP2 and GCP3[125], but analysis of the vertebrate γ-TuC revealed additional GCP proteins, for which no homologs were previously identified in *Saccharomyces cerevisiae*. Thus, GCP4,5,6 were identified as novel components of the eukaryotic γ-TuC termed the γ-tubulin ring complexes (γ-TuRC)[126,127].

1.2 Microtubule nucleation in fungi

1.2.1 The spindle pole body as the main MTOC in fungi

MT nucleation in fungi requires the interplay of several factors. Fungi in the class of *Saccharomycetes* contain instead of a MTOC multi protein complex, termed the Spindle pole body (SPB). The SPB is very well described in *Saccharomyces cerevisiae*. The SPB is a multiprotein component embedded in the nuclear envelope having a bipolar structure with the capability to nucleate MTs in the cytosol and the nucleus[128,129]. While nuclear MTs are general components of mechanical stabilisation in the fungal nucleus, other eukaryotes mostly rely on lamins for nuclear organisation [130] and nuclear microtubule filaments[131] are formed only in case of DNA damage. Cytosolic MTs in yeast are responsible for karyogamy and orient the spindle and nucleus[132]. Despite being a bipolar structure, the SPB is not symmetric and components of the cytosolic and nuclear face differ. The SPB is composed of three regions termed plaques (Fig. 4a). The nuclear side of the SPB contains the inner plaque, which consists of Spc110 that is able to bind and oligomerise the γ-TuSCs via its N-terminal part (Fig. 4a)[133]. The central plaque of the SPB is embedded in the nuclear envelope and is formed by Spc29 and Cmd1 that are connected to the nuclear plaque via interaction with the C-terminus of Spc110 (Fig. 4a)[134]. The central plaque of the SPB contains Spc42 that extends to the cytosol[129,135] via its C-terminus (Fig. 4a). The central plaque and the cytosolic plaque (the outer plaque) are connected via a bridge formed by Cnm67 (Fig. 4a)[135]. The outer plaque is composed of Nud1 and Spc72 that are anchored to Cnm67 (Fig. 4a)[136]. The domain composition of Spc72 is similar to the one of Spc110. The C-terminal part of Spc72 is anchored to Nud1[137] while the Spc72 N-terminus binds to the γ-TuSC (Fig. 4a)[138]. Specific binding of the γ-TuSC to the N-termini of Spc72 and Spc110 is mediated by the γ-TuSC-binding CM1 motif in Spc72 and Spc110 [139]. Additionally, both Spc72 and Spc110 are phosphorylated, but with different effects. While the Spc110 phosphorylation increases the γ-TuSC binding efficiency[139], the Spc72 phosphorylation results in relocation of Spc72 in the cytosolic plaque[140]. All above mentioned proteins have coiled coil regions that are essential for the SPB assembly[141] but none of them is involved in the anchoring of the SPB to the nuclear envelope, which requires two SPB membrane proteins, Ndc1[142] and Mps2 (Fig. 4a)[143]. The latter additionally binds to Bbp1[144], which mediates interaction with Kar1, component of the half-bridge (Fig. 4a)[144]. The half-bridge is a membrane-associated component of the SPB attached to the one side of the SPB and serves for duplication of the SPB (Fig. 4a). Together with Mps3, Cdc31 and Sfi1, Kar1 forms the half-bridge (Fig. 4a), which fulfills the role of the MT nucleation site as well via binding of Spc72 to Kar1 during karyogamy[48,145-147]. Half-bridge proteins occur on both sides of the nuclear envelope- Kar1, Cdc31 and Sfi1 on the cytosolic side and Mps3 on the nuclear side (Fig. 4a). SPB core proteins associate with many MT-associated proteins, such as Spc24, 25, 34 and mitotic exit proteins. The microtubule polymerase, Stu2, the yeast homolog of ch-TOG, binds specifically to Spc72 of the SPB[148,149]. During yeast cell duplication, chromosomes have to be segregated into newly formed daughter cells by two SPBs located on the opposite poles

of the cell. Duplication of the SPB happens in G1 phase and requires the half-bridge as the site for the assembly of new SPB[150]. Before SPB duplication, the half-bridge is expanded to double its length and forms the full bridge.

1.2.2 γ-TuSC as a template for microtubule nucleation

γ-tubulin is a member of the tubulin superfamily. Shortly after its gene was discovered, γ-tubulin was recognised to be enriched at the SPB in *Aspergillus nidulans* and it was observed that its depletion leads to severe impairment of MT nucleation[151]. γ-tubulin on its own is not sufficient for MT nucleation in yeasts but it is a component of the γ-TuSC[123]. The γ-TuSC is formed by one copy of Spc97 and Spc98 and two copies of γ-tubulins. In yeasts, the γ-TuSC is anchored to the SPB by interacting with Spc110 at the nuclear face and Spc72 at the cytosolic face[152]. The first negative stain EM data revealed the γ-TuSC shape resembling letter 'Y'[153] (Fig. 4b). The position of γ-tubulin was identified at the two tips of the Y-shaped complex, while Spc97 and Spc98 represent the arms of the complex contacting each other via their N-terminal regions, represented by the GRIP1 motif, and each binding one γ-tubulin molecule via their C-terminal region, represented by the GRIP2 motif (Fig. 4c)[153]. Recognition of the GRIP motifs in the Y-shaped complex, firstly identified in *Drosophila melanogaster*[154], was allowed by the X-ray structure of GCP4[155], a highly homologous protein[156]. However, the low-resolution negative stain EM reconstruction of the *S. cerevisiae* γ-TuSC did not allow for detailed insights into the heterotetramer. Based on the general shape of the complex, it was speculated whether several γ-TuSC units can assemble into higher order oligomers. Cryo-EM analysis showed that the γ-TuSCs can indeed assemble into a ring-like oligomer roughly reflecting geometry of MTs under suitable conditions (open conformation), indicating that γ-TuSC oligomers may serve as structural templates for MT nucleation[157]. The γ-TuSC spiral is established by lateral contacts between the γ-TuSC units and exposes in the 'open conformation' 14 γ-tubulins for longitudinal interactions of α/β-tubulin dimers[157]. Despite following a helical arrangement, the γ-TuSC spiral does not perfectly follow MT geometry, suggesting requirement of further factors to induce conformational changes in the γ-TuSC oligomer. The reconstruction of the γ-TuSC stabilised by crosslinking recapitulated the geometry of the MT almost precisely, having the same pitch of 120 Å as the MT and exposing only 13 γ-tubulins, reflecting the number of MT protofilaments (Fig. 4e)[156]. Surprisingly, the main difference between the open conformation of the γ-TuSC and the closed one that matches MT geometry was in the position of γ-tubulins of each γ-TuSC unit where one γ-tubulin of the γ-TuSC unit is spatially rearranged[156]. This rearrangment, likely mediated by a hinge region in the central parts of Spc97 and Spc98, aligns γ-tubulins with MT α-tubulins and brings them to same distance from the helical axis (Fig. 4b)[156] The γ-TuSC oligomer is assembled from seven repeating units of the γ-TuSC. The number of the γ-TuSCs in the oligomer is likely limited by Spc110 coiled coil dimer that binds to the N-termini part of γ-TuSC Spc proteins (Fig. 4d)[156].. It is not clear how this conformational change is triggered because Spc110 only impacts on oligomerisation of the γ-TuSC units but not their conformation.

1.2.3 Binding partners of the fungal γ-TuSC

Proteins of the SPB are not the only binding partners of the γ-TuSC. The small protein MZT1, originally identified in the purification of mitotic proteins from human cells[158], is an essential component for targeting of γ-TuCs to MTOCs. While the gene encoding MZT1 is missing in *S. cerevisiae,* other yeast species from the *Saccharomycetes* class, e.g. *C. albicans*, encode for MZT1. It was shown that MZT1 binds to the N-terminus of GCP3, the homolog of yeast Spc98[159]. The depletion of MZT1 in *C. albicans* confirmed its role localising γ-TuCs to the SPB[160]. Although the γ-TuSC architecture is very similar in *C. albicans* and *S. cerevisiae,* tendency of the γ-TuSC to form higher oligomers on its own differs between species, with the γ-TuSC of *S. cerevisiae* being more prone to oligomerisation. Negative stain EM analysis of

the *C. albicans* γ-TuSC revealed that MZT1 binds to a lower part of the Y-shaped complex (Fig. 4f)[159], which is in agreement with the expected position of the Spc98 N-terminal region shown to bind MZT1[153]. MZT1 as another binding partner of the γ-TuSC in *C .albicans* increase the complexity of interactions and could affect binding to Spc110 and Spc72. Combination of these proteins with the γ-TuSC-MZT1 system does not interfere with their binding to the γ-TuSC and presence of MZT1 actually increases their affinity[159]. Higher affinity of Spc110 and Spc72 can contribute to the higher oligomerisation rate of the γ-TuSC, thus indicating that MZT1 in *C. albicans* affects the assembly of the γ-TuSC ring-like oligomer (Fig. 4i).

Another γ-TuSC binding partner that contributes to MT nucleation and is present in all fungi is the MT polymerase Stu2[72]. Conserved across all eukaryotes[72], it increases efficiency and the rate of MT polymerisation and possibly also MT nucleation *in vivo*[72]. Stu2 is composed of two TOG domains (TOG1, TOG2) that each interact with one α/β-tubulin dimer[161], followed by a MT binding region, an α-helix that participates in Stu2 dimerisation via coiled coil formation[162] and by the Spc72 binding region[163]. TOG domains are formed by an array of coiled coils[164] and despite having same fold, TOG domain affinity for α/β-tubulin dimers differs. TOG1 exhibits higher affinity compared to TOG2, thus indicating different interfaces or residues for α/β-tubulin binding[164]. Detailed analysis of α/β-tubulin dimer binding to the TOG domains revealed decreased binding affinity under higher salt concentrations, suggesting a role of electrostatic interactions in the interface[164]. The X-ray crystallography structures of the TOG domains from fungal MT polymerases elucidated their architecture when bound to α/β-tubulin dimers[161]. Surprisingly, one X-ray crystallography study of Stu2 revealed that TOG domains dimerise even without the coiled coil α-helix in a square-like shape, where the N-terminus and the C-terminus of TOG1 and TOG2, respectively, contact each other and create an arrangement of the Stu2 dimer containing overall 4 TOG domains (Fig. 4g)[164]. Point mutations in the interfaces of the Stu2 dimer did not perturb α/β-tubulin binding but impacted on the conformation of the TOG domains[164]. Interruption of the dimer interface results in monomerisation and straightening of two TOG domains from their 90 degrees orientation in the Stu2 dimer (Fig. 4g)[164]. The square-like shape of the Stu2 dimer could be beneficial for α/β-tubulin dimer polymerisation during MT nucleation and growth. Structural studies showed that the TOG domains of Stu2 can generally arrange in a way that brings two α/β-tubulin dimers in contact[164]. Thus, dimerisation of Stu2 can potentially bring together four α/β-tubulin dimers to let them form longitudinal interactions assembling longer filaments. However, it is not clear what could trigger the reorganisation of the TOG domains from the square to the straight arrangement (Fig. 4g). Stu2 does not localise to the nuclear side of the SPB, but binds to Spc72 on the cytosolic side of the SPB where Stu2 promotes MT nucleation [163]. Moreover, Stu2, Spc72 and the γ-TuSC are likely to form a ternary complex, as suggested by a cooperative binding mode of all three components[163]. Thus, Stu2 could enhance Spc72 function for γ-TuSC oligomerisation, which is otherwise very poor. Stu2 interaction with another binding partner at the SPB, Kar9, plays a role in stabilisation of the minus-end capped MTs[163], which is in agreement with the impact of Stu2 on the Spc72-γ-TuSC interaction.

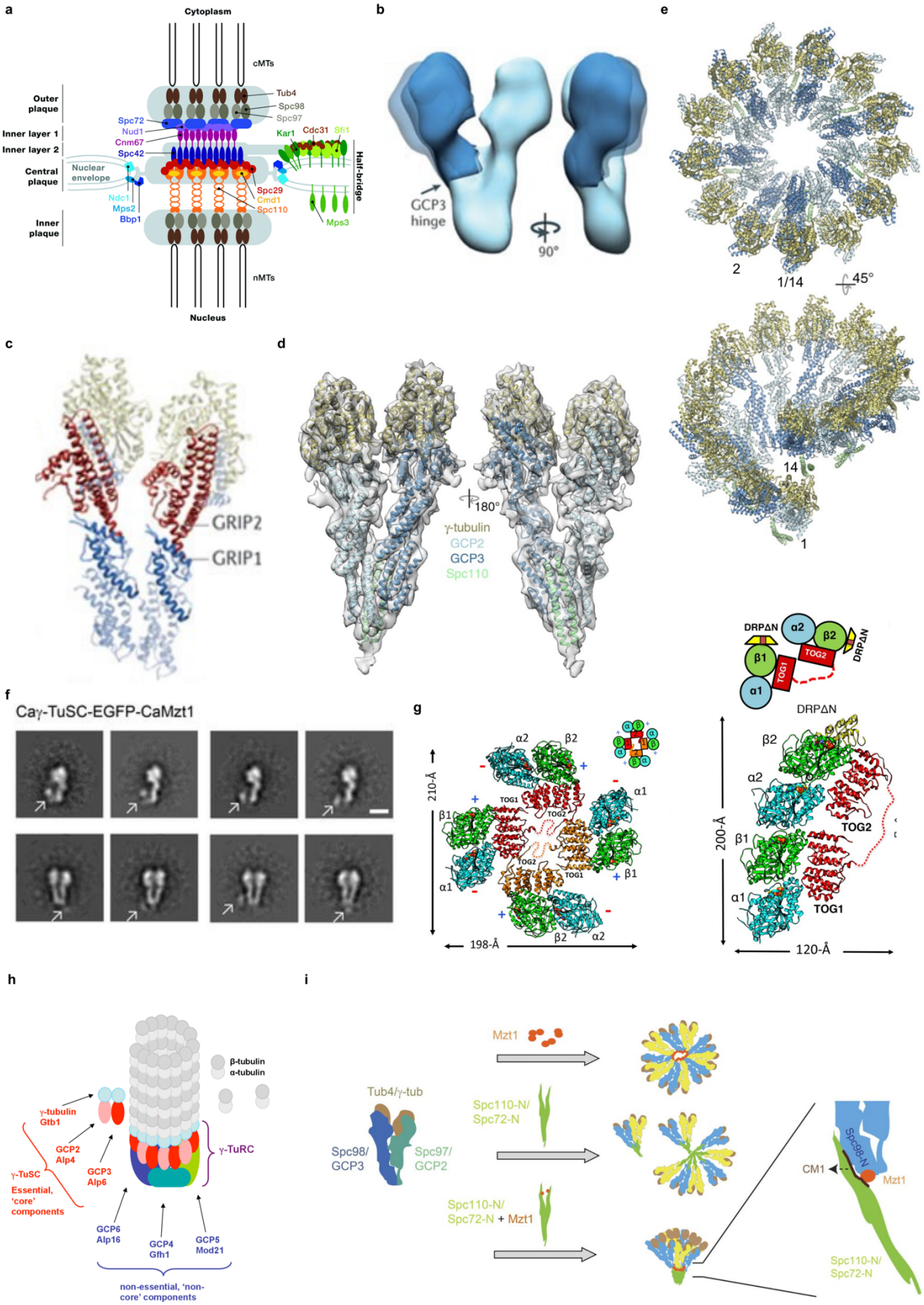

Figure 4: Fungal MT nucleation system.
a) Schematic representation of the SPB composition with all proteins indicated. The central, outer and inner plaque regions with the half-bridge expanded into the nuclear envelope. Panel is from Jaspersen *et al.*, 2004[165]

b) Negative stain EM reconstruction of the γ-TuSC resembling the shape of letter 'Y'. The hinge responsible for the conformational plasticity between the GRIP motifs is indicated. Panel is from Kollman *et al*., 2008[153].
c) Atomic model of the γ-TuSC with the labeled N-terminal GRIP1 motif and the C-terminal GRIP2 motif binding γ-tubulin. Panel is from Kollman *et al*., 2008[153].
d) Cryo-EM reconstruction of the γ-TuSC with bound dimer of Spc110. GCP2 and GCP3 interacting laterally and both of them binding γ-tubulin. Panel is from Kollman *et al*., 2015[156].
e) Atomic model of the γ-TuSC ring-like oligomer in the closed conformation with the first (1) and the last spoke (14) aligned, exposing only 13 γ-tubulins as shown from the top view. Panel is from Kollman *et al*., 2015[156].
f) Negative stain EM 2D class averages of the *C. albicans* γ-TuSC with bound MZT1. Density segment likely representing MZT1 is indicated by the arrow. Panel is from Lin *et al*., 2016[159].
g) Left, the atomic model of Stu2 in dimeric form, assembled in a square shape with each TOG domain binding one α/β-tubulin dimer. Right, straightened monomeric Stu2 with bound Darpin (DRPΔN) to prevent the assembly of Stu2 dimer. Panel is from Nithianantham *et al*., 2018[164].
h) Schematic representation of the proposed *S. pombe* γ-TuRC architecture with all components indicated. Panel is from Miller, 2010[166].
i) Proposed assembly of the *C. albicans* γ-TuSC ring-like oligomer triggered by the combination of MZT1 and Spc110 or Spc72. Panel is from Lin *et al*., 2016[159].

1.2.4 Diversity of fungal γ-TuCs and MT nucleation

The MT nucleation system in fungi is less complex than in higher eukaryotes. The number of MTOCs and nucleated MTs is strongly reduced. The simplest fungal MT nucleation system represented by *Saccharomyces cerevisiae* contains only the SPB, and solely relies on the γ-TuSC as MT nucleation template. However, not all fungi contain such simple nucleation system. *C. albicans*, a representative of the same class of fungi as *S. cerevisiae*, encodes for MZT1, an additional binding factor of the γ-TuSC, which plays a role in MT nucleation. *S. pombe*, a member of the class *Schizosaccharomycetes*, contains an even more complex MT nucleation system. In *S. pombe*, the SPB is not the only site of MT nucleation in cells, but there are two additional ones: the interphase MTOC (iMTOC) and the equatorial MTOC (eMTOC)[167]. While the SPB function is preserved in nucleating MTs for chromosome segregation[168], the iMTOC mediates MT array organisation during interphase and the eMTOC is a site of MT nucleation during late anaphase[169]. To nucleate MTs exclusively during late anaphase, the eMTOC is formed only in anaphase and later disassembled. The eMTOC function and disassembly impact on the formation of the iMTOC, indicating similarity in the protein composition[170]. Mto1 and Mto2 regulate the localisation and assembly of the eMTOC and iMTOC in *S. pombe*[171]. Both of these proteins control formation of the interphase MT array[171]. Mto1 self-localises to the γ-TuSC, while Mto2 binding to the γ-TuSC depends on Mto1[172]. Mto1 localise to these MTOCs as well via both its termini but their absence still leads to MT nucleation due to the Mto1 binding to the γ-TuSC via its CM1 motif[172]. The Mto1 CM1 motif is localised outside of the MTOC binding regions, which shows two functions of the Mto1, one in localisation to MTOCs and in other in binding of the γ-TuSC[172]. Thus, activation of the γ-TuSC and MT nucleation is independent from the Mto1 localisation to the MTOCs. Nucleation of MTs in *S. pombe* is templated by the γ-TuSC but besides components of the γ-TuSC, *S. pombe* encodes for additional proteins that are homologs to GCP4,5 and 6[173]. While GCP4,5,6 (Gfh1, Mod21, Alp16) are not strictly required for MT nucleation in *S. pombe* (Fig. 4h), the number of MTs nucleated in the cytosol from the iMTOC is reduced upon their depletion. However, it seems that GCP6 plays more important role than GCP5 and GCP4 in the fission yeast MT nucleation in concert with MZT1 by enhancing the recruitment of the γ-TuRC to the SPB[174]. Surprisingly, this recruitment is not dependent on GCP4 and GCP5 presence[174], which would suggest an interplay of the γ-TuSC ring-like oligomer with GCP6 and MZT1. It is unclear if GCP6 in fission yeast is a core component of such γ-TuSC ring-like oligomers or it just serves as a recruitment factor with MZT1.

1.3 MT nucleation in higher eukaryotes

1.3.1 γ-TuRC architecture

MT nucleation in higher eukaryotes is more complex as compared to yeasts and thus requires tighter regulation. A higher number of MTOCs and the requirement for spindle formation during mitotic chromosome segregation make MT nucleation system more complex, nucleating many MTs in a short period of time. All currently known MTOCs and MT nucleation pathways in higher eukaryotes rely on the γ-TuRC. The role of γ-tubulin in MT nucleation was recognised in *Xenopus laevis* where γ-tubulin was observed to cap the MT minus ends[122]. A closer look at the γ-TuRC in higher eukaryotes revealed several components. Besides GCP2 and GCP3, forming the γ-TuSC in yeasts, three additional GCP paralogs were identified as components in the human γ-TuRC, termed GCP4,5,6[126,127]. The presence of GCP5,6 in the γ-TuRC structure was confirmed by their cosedimentation with GCP2,3 and γ-tubulin[127]. The stoichiometry of GCP4,5,6 in the γ-TuRC was estimated at 1-2 copies per GCP compared to an estimated higher stoichiometry of 10 copies for GCP2,3 together[175]. All three proteins are similar on sequence level in the conserved GRIP1 and GRIP2 motifs, but overall sequence similarity is comparably low[176]. More detailed information on the γ-TuRC structure was obtained from EM tomography and negative stain EM of the *Drosophila melanogaster* γ-TuRC, demonstrating its ring-like shape with a diameter of ~28 nm[177]. However, none of these studies provided information on the positions of the γ-TuRC-specific components GCP4,5 and 6. Integrating structural data from the negative stain EM and cryo-EM of fungal γ-TuSC units[153,156] led to the hypothesis of the γ-TuRC spiral being formed by the repeated GCP2-3 units with GCP4,5,6 capping the γ-TuRC cone[178]. With the X-ray structure of GCP4, this idea had to be revised, because GCP4 adopted a very similar fold as GCP2 and GCP3 and sequence analysis showed that residues binding γ-tubulins in GCP2 and GCP3 were also conserved in GCP4[155]. Direct binding of γ-tubulin by GCP4 was further confirmed by immunoprecipitation[155] and indicated that GCP4,5,6 have a similar role in coordinating γ-tubulin molecules in the γ-TuRC as GCP2 and GCP3. Insights into contacts between GCP proteins were obtained by FRET experiments that indicated, similarly as for GCP2,3 in *S. cerevisiae*, interaction of GCP4 and GCP5 via their N-terminal GRIP1 domains and their possible arrangement in a lateral manner as for GCP2 and GCP3 in the γ-TuSC (Fig. 5b)[179]. However, in these experiments, GCP6 interactions were not detected, leaving the role of GCP6 elusive (Fig. 5b).

1.3.2 γ-TuRC binding partners

The γ-TuRC from *D. melanogaster* and *X. laevis* was copurified with many other proteins. Four proteins often copurified with the γ-TuRC were NEDD1[180], NME7[181], MZT1 and MZT2[158]. NEDD1 was originally identified in *Drosophila melanogaster* as a potential component of the γ-TuRC and the β-propeller domain in the NEDD1 N-terminal half was described (Fig. 5a)[154]. Initial interaction analysis of NEDD1 pointed to its ability to bind to several components of the γ-TuRC when coexpressed in pairs[182]. NEDD1 localises to the centrosome mainly at the onset of mitosis, as well as to spindle MTs in a smaller scale and additionally, NEDD1 colocalises with the γ-TuRC (Fig. 5a)[182]. Depletion of NEDD1 reduces the number of MTs nucleated during mitosis but NEDD1 is not required for γ-TuRC assembly, suggesting a role of NEDD1 in the γ-TuRC recruitment[182]. Furthermore, depletion of NEDD1 affects formation of daughter centrioles indicating a role in centriole duplication[182]. As the γ-TuRC recruitment factor, NEDD1 would be expected to bind both the PCM and the γ-TuRC. Indeed, splitting NEDD1 into the C- and N-terminal halves showed that the N-terminal half of NEDD1 containing the β–propeller domain binds to the PCM while the C-terminal half serves as the recruitment component for the γ-TuRC (Fig. 5a)[182]. Follow-up studies narrowed down the region associated with the γ-TuRC binding to 62 C-terminal residues of helical character[183]. Mutation of Leu642 and four other residues in this region resulted in a significant decrease of the γ-TuRC binding[183]. The

C-terminal region of NEDD1, as well as the full-length NEDD1, can form homooligomers, but stoichiometry of NEDD1 with the γ-TuRC suggests binding of the monomeric NEDD1[183]. NEDD1 plays a role in chromatin-dependent MT nucleation as well[77]. As is the case for most centrosome-related proteins, the NEDD1 activity is regulated by phosphorylations with context-specific effects. For instance, Ser411 phosphorylation impacts on the NEDD1 localisation to spindle MTs but not to centrosomes. NEDD1 is phosphorylated by three kinases, Cdk1, Plk1[184] and AuroraA[77] in case of chromatin-dependent MT nucleation. The first two kinases act on NEDD1 in a sequential manner and enhance the NEDD1 binding to the γ-TuRC[184]. Phosphorylation between residues Ser557-Ser574 is relevant for the NEDD1 recruitment to the γ-TuRC due to proximity to the C-terminal γ-TuRC-binding region on NEDD1. This region serves as a regulator for the γ-TuRC binding with some phosphorylation sites enhancing the γ-TuRC recruitment and others abolishing it[185].

Another protein identified to interact with the γ-TuRC is NME7 (Fig. 5c), a member of the NME family of proteins. The structure of NME7 is elusive but sequence analysis revealed two kinase domains- an active domain A, responsible for autophosphorylation of NME7, and an inactive domain B. NEDD1 and NME7 are localised at the PCM but NME7 does not have a role in γ-TuRC assembly or recruitment. Immunoprecipitation experiments against the γ-TuRC confirm localisation of NME7 on centrosomes, as cytosolic pools of the γ-TuRC contained only a small amount of this kinase. Mutation of Arg322 to alanine decreased binding efficiency of NME7 to the γ-TuRC, indicating the importance of the electrostatic interactions for NME7[186]. NME7 is a nucleotide diphosphate kinase and catalyses ATP-dependent production of GTP from GDP[186]. Tubulin family members are GTPases, so GTP production could have direct impact on efficiency of MT nucleation. The role of NME7 in the γ-TuRC-mediated MT nucleation is elusive but NME7 depletion decreases the rate of MT nucleation at centrosomes[181]. NME7 could serve to generate GTP ligand for tubulins during MT nucleation, however, its impact on the γ-TuRC-mediated MT nucleation could not be confirmed.

MZT1 and MZT2 were identified by mass spectrometry of the human γ-TuRC as additional core components of the γ-TuRC[158]. Originally termed GCP8A and GCP8B, these two proteins were detected in the γ-TuRC at all stages of cell cycle, which strengthens their role as direct components of the γ-TuRC[158]. Furthermore, MZT1 is highly conserved in animals[158], plants[187] and also in many fungi[159]. Initially, interactions of MZT1 with the GCP3 NTE of the GRIP1 domain were observed using NMR[188] and the same motifs of hydrophobic residues responsible for the MZT1 binding were also identified in GCP2,5 and GCP6[189]. Additional experiments revealed the role of MZT1 in binding of NEDD1 and in centrosomal localisation of the γ-TuRC, which supported the idea of MZT1 as a γ-TuRC component (Fig. 4c)[190]. Depletion of MZT1 led to cellular defects without disrupting the γ-TuRC composition indicating the MZT1-independent γ-TuRC assembly[190]. Besides the NEDD1 binding, MZT1 affects Cdk5Rap2 interactions with the γ-TuRC as well[190]. Cdk5Rap2 enhances MT nucleation activity of the γ-TuRC, thus MZT1 has a role in activation of the γ-TuRC. This was proved by knockdown of MZT1, which prevented Cdk5Rap2-mediated increase of MT nucleation by the γ-TuRC[190].

Besides binding partners identified in the purified endogenous γ-TuRC, there are other components that directly affect the γ-TuRC function by stimulating MT nucleation[191]. Cdk5Rap2 is one of several proteins containing a CM1 motif, similar to Spc72[139], Spc110[139] or Mto1[175]. Cdk5Rap2 is considered as an activator of the γ-TuRC, because binding to the γ-TuRC via its CM1 motif increases the MT nucleation rate (Fig. 5a). The CM1 motif in Cdk5Rap2 is located in its N-terminal part and N-terminal fragments including the first 50-200 residues bind to the γ-TuRC and enhance its nucleation activity[175]. Binding of the CM1 motif requires the fully assembled γ-TuRC because depletion of GCP4 prevented the CM1 binding to the remaining

γ-TuRC subcomplexes. Notably, the Cdk5Rap2 binding to the γ-TuRC is independent of NEDD1. The role of Cdk5Rap2 in MT nucleation is highlighted by the fact that deletion of its CM1 motif led to development of microcephaly in mice[192].

Another stimulator of MT nucleation that interacts with the γ-TuRC is ch-TOG (Fig. 5c)[193]. Being a MT polymerase as its homolog, Stu2, in fungi, ch-TOG binds to soluble α/β-tubulin dimers and increases the MT nucleation rate[193,194]. As the name of this protein indicates, ch-TOG is composed of TOG domains[195]. Compared to its fungal homolog, ch-TOG contains three additional TOG domains (five in total), but lacks the dimerisation helix preceding the C-terminal region in Stu2[196]. Analysis of the *Xenopus laevis* ch-TOG confirmed its role in MT nucleation, showing increased number of generated MTs upon addition of ch-TOG to the γ-TuRC in *in vitro* MT nucleation assay[193]. While the ch-TOG concentration correlates linearly with the number of nucleated MTs, there is a threshold of the MT nucleation rate that cannot be exceeded even at high ch-TOG concentrations[193]. ch-TOG enhances MT nucleation at centrosomes as well as on pre-existing MTs. Ch-TOG consists of five TOG domains and each of them contributes to MT nucleation in a different way. The first two TOG domains possess the ability to bind α/β-tubulin dimers on their own but do not enhance MT nucleation[193]. Deletion of all five TOG domains leads to abolishment of both α/β-tubulin binding and MT nucleation but when deleting the C-terminal domain and the last TOG5 domain, only a significant decrease of MT nucleation was observed without impairing α/β-tubulin binding[193]. Point mutations in the TOG5 domain aiming to prevent the α/β-tubulin binding showed no effect on MT nucleation compared to the TOG5 deletion thus indicating a role of TOG5 in anchoring ch-TOG to MT nucleation sites together with the ch-TOG C-terminal domain[193]. Indeed, size exclusion chromatography showed the capability of ch-TOG and specifically its C-terminal domain in combination with TOG5 domain to interact with isolated γ-tubulin molecules[193]. Whether such interactions can occur also on level of the fully assembled γ-TuRC remains to be investigated.

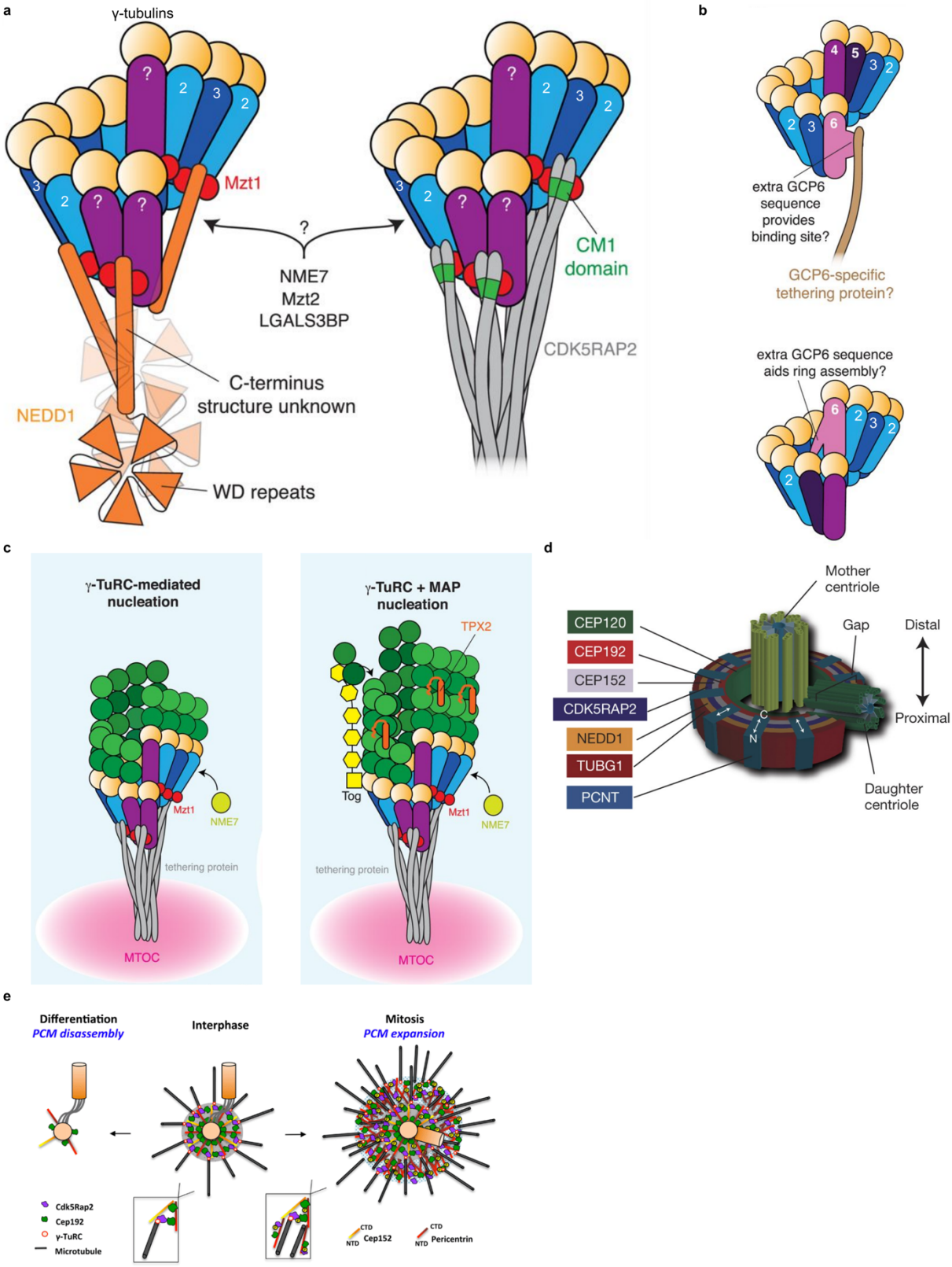

Figure 5: Characterisation of the vertebrate MT nucleation system.
a) Proposed architecture of the γ-TuRC with binding mechanism of other γ-TuRC effectors (NEDD1, Cdk5Rap2). Panel is from Tovey *et al.*, 2018[178]
b) Proposed position of the γ-TuRC-specific GCP4,5,6 based on FRET studies. GCP4 and GCP5 interacting together while GCP6 is closing or starting the γ-TuRC spiral. Panel is from Tovey *et al.*, 2018[178]
c) Schematic representation of the γ-TuRC-templated MT nucleation with MAPs. Panel is from Tovey *et al.*, 2018[178]

d) Schematic representation of the PCM architecture in interphase. Panel is from Lawo *et al*., 2012[197]. **e)** Schematic representation of the PCM during cell cycle-the PCM disassembly, the PCM assembly in interphase and expansion in mitosis. CEP152 and pericentrin expanding from the centriole to the periphery of the PCM and recruiting Cdk5Rap2 and CEP192 that anchor the γ-TuRC. Panel is from Fry *et al*., 2017[198].

1.3.3 MT nucleation at centrosomes and PCM

MT nucleation in higher eukaryotes is mediated by the γ-TuRC, which is targeted to the main MTOC of higher eukaryotes, the centrosome. The γ-TuRC nucleates MTs during the full cell cycle. In mitosis, specifically at the onset of metaphase, the centrosome volume increases, including the PCM where the γ-TuRC is recruited to and the most of spindle MTs are nucleated from[199]. During interphase, MT nucleation is mostly limited to subdistal appendages of the mother centriole[200]. Both the PCM and subdistal appendages as sites of MT nucleation must anchor the γ-TuRC. Thus, some proteins of these two sites must bind to the γ-TuRC or some of the γ-TuRC binding partners. Anchoring of the γ-TuRC to subdistal appendages is mediated by ninein. Its C-terminus binds to the mother centriole, while its N-terminus binds to the γ-TuRC. However, combining these two regions into a construct is not sufficient for anchoring the γ-TuRC to subdistal appendages, which indicates that other regions of ninein are also required[201]. Anchoring of the γ-TuRC to the PCM on the onset and during mitosis is mediated by CEP192[202] and Cdk5Rap2[175].

1.3.4 PCM architecture and assembly in interphase

The PCM is composed of several different proteins, many of them possessing coiled coil regions[203]. These proteins form a variable, but partially ordered organisation around the mother centriole. Especially during interphase, the PCM adopts defined shape and PCM proteins have a specific distribution, forming ring-like layers around the mother centriole (Fig. 5d)[197]. In contrast, in metaphase, when the PCM is expanded, its shape is amorphous and can reach a diameter of 1 µm (Fig. 5e)[199]. Major components of the PCM are Cdk5Rap2, CEP192, CEP152 and pericentrin[197]. Together, these proteins organise the PCM and participate in its remodellin during interphase[197]. Pericentrin fulfils a specific role in PCM organisation, defining the size of PCM during interphase[197]. It was shown that pericentrin assumes a distinct orientation in the interphase PCM with its C-terminus anchored on the mother centriole and its N-terminus in the PCM periphery (Fig. 5e)[197]. A similarly ordered arrangement was also observed for the CEP152 termini, indicating a specific role of this protein in organisation of the interphase PCM, as well (Fig. 5e)[197]. It is possible that pericentrin and CEP152 together start the assembly process of the PCM, recruiting further proteins. The other two major components of the PCM, CEP192 and Cdk5Rap2, are incorporated in a CEP152 and pericentrin-dependent manner[204]. Both of these proteins have been localised mostly in peripheral regions of the PCM (Fig. 5d).

1.3.5 PCM in mitosis

Expansion of the PCM at the onset of metaphase is caused by increased recruitment of aforementioned PCM proteins, as well as other proteins required for MT nucleation, such as NEDD1, the γ-TuRC, ch-TOG and TPX2. Furthermore, the mitotic PCM recruits kinases, such as Plk1[205] and AuroraA, which are essential for the PCM expansion and controlling activity of centrosomal proteins during MT nucleation[202]. Another layer of regulation for the PCM maturation are PCM-recruited phosphatases[206,207]. Plk1 phosphorylates Cdk5Rap2[208] and CEP192[202]. The phosphorylation-dependent expansion of the PCM by increased recruitment of PCM proteins was dissected in detail for Cdk5Rap2, which has the capability to form oligomers[209,210]. Phosphorylation has the ability to trigger oligomerisation of PCM proteins, increasing the protein mass of the PCM and at the same time transforming it into an amorphous, almost phase-separated condensate. The position of Cdk5Rap2 and CEP192 at the periphery of the expanded PCM allows them to directly act in recruitment of MT nucleation factors, such as the γ-TuRC (Fig. 5e). CEP192 has a similar tendency to oligomerise at the

PCM but only when in complex with AuroraA kinase[211], which is recruited to PCM in a CEP192-dependent manner[211]. Thus, AuroraA can trigger oligomerisation of CEP192. More copies of CEP192 present at the PCM due to oligomerisation increase recruitment of AuroraA. After its recruitment to the PCM, AuroraA activates its own kinase function by autophosphorylation. This activation allows for recruitment of Plk1. Active AuroraA, not only recruits Plk1 but also other MT nucleation factors. Recruited Plk1 is phosphorylated by AuroraA and both of them phosphorylate CEP192[202]. Depletion of Plk1 abolishes recruitment of ch-TOG and the γ-TuRC to the PCM, indicating the involvement of CEP192 phosphorylation by Plk1[202]. The Plk1 phosphorylation of CEP192 is required to form binding sites for these MT nucleation factors. Additionally, the CEP192 recruitment and binding of AuroraA and Plk1 affect interaction with NEDD1 and its phosphorylation, which is dramatically reduced in absence of CEP192 [202].

1.4 Cryo-EM as a method for structural analysis of macromolecular complexes

1.4.1 Physics behind EM imaging

Electron microscopy is an imaging method applying high magnification for capturing 2D images of cell organelles, protein complexes and individual proteins. The structures of proteins or protein complexes are reconstructed in 3D using an image processing workflow, termed single particle analysis (SPA), which was the main method applied in this work. An electron microscope consists of an electron source and a series of lenses to focus, align and magnify an image (Fig. 6a). Finally, the image is recorded on a camera, optionally including an energy filter to remove noise. As the name of the method indicates, this imaging technique uses electrons instead of photons as in light microscopy or X-ray crystallography. The wavelength of electrons determines the attainable resolution. The smaller the wavelength, the higher the resolution achievable under ideal conditions. The wavelength of electrons depends on their speed. Electrons accelerated in high-end EM reach a wavelength range of 3.7 to 2 pm, which would in an ideal case allow to reach far sub-ångstrom resolution (100 pm = 1 Å = 0.1 nm), but the imperfect lens systems of EMs currently limit resolution to ~1 Å. Electrons provide two kinds of contrast, coming from the wave-particle duality of electrons- amplitude contrast and phase contrast. Amplitude contrast is produced by loss of electron energy when electrons are scattered at specimen. Phase contrast originates solely from a change in the phase of the electron wave, not from loss of energy- elastically scattered electrons (Fig. 6b). Phase contrast is weak due to small phase shift resulting in small interference with none scattered electrons (wave without phase shift) (Fig. 6c). As phase shift is always far away from 90º, final interference of waves is destructive. In an ideal case, we would like to obtain a 90º phase shift to reach high interference and high phase contrast (Fig. 6c). Furthermore, similar atomic composition of proteins and the surrounding ice in cryo-EM give rise to low signal-to-noise ratio.

1.4.2 Characterisation of negative stain EM and cryo-EM grid preparation and imaging

Cryo-EM SPA requires purified proteins or protein complexes of interest in sufficient homogeneity and concentration. However, these parameters are not so strict as for X-ray crystallography where very high homogeneity and concentrations of 10 mg/ml and higher are required. Electron microscopy, depending on the specific imaging and grid preparation method, requires protein concentrations from 0.01 mg/ml for negative stain EM to 1-3 mg/ml for cryo-EM of small proteins or small protein complexes. Homogeneity of the sample should be sufficient for the protein of interest to represent the majority of imaged particles. Negative stain EM is a method in which the purified sample is applied on an EM grid (metal mesh with circular shape of approx. 3 mm diameter) that is covered by a layer of continuous carbon with different thickness, ranging from 5 to 10 nm depending on a preparation of this layer and protein size (Fig. 6d). This layer of continuous carbon allows particles to attach themselves,

which leads to decreased requirements of protein concentration. Sample is incubated on a grid for a short period of time and afterwards washed by a water and stained by a heavy metal-based stain solution (Fig. 6d). The most common stains are ammonium molybdate, uranyl acetate and uranyl formate and all differ in grain size. The stain covers proteins on a grid (Fig. 6d) and produces strong contrast during imaging. All stain solutions contain heavy metal components, which are the source of strong amplitude contrast from elastically and inelastically scattered electrons during imaging. However, the gain of high contrast originating from the heavy metal stain comes with the cost of achievable resolution. Because electrons scatter at the heavy metal stain and not at the protein itself, structural analysis is mostly limited to the general shape and outline of a complex and achieving details on molecular architecture, such as secondary structure elements or protein side chains is not possible.

This level of details is achievable using cryo-EM SPA. In this method, the 3D structure of a protein is obtained by imaging protein in a close-to-native state. This is achieved by vitrification of the sample where the purified sample is applied on a grid before the excess of sample is blotted away and the grid is plunge-frozen in liquid ethane (Fig. 6d). Vitrification provides fixation of the sample on a grid avoiding sublimation in the high vacuum of the microscope that is required to prevent scattering of electrons on air molecules. Preservation of vitreous ice in the microscope is achieved by cooling down specific microscope components to temperatures of liquid nitrogen. Additionally, vitrification protects the sample against radiation damage[212]. Freezing of grids is performed in liquid ethane, propane or in an ethane/propane mixture due to their high cooling-rates, which produces vitreous/amorphous ice that does not have crystal properties (water molecules assembled into crystals via hydrogen bonds). Crystal ice is less penetrable for electrons (depends on the thickness) and the regular arrangement of water molecule often leads to the formation of Bragg patterns on an image caused by diffraction of electrons on crystalline ice. Furthermore, crystal ice damages biological structures leading to their disassembly.

EM grids used nowadays in cryo-EM SPA either have regularly spaced holes in the carbon support foil (holey carbon grids), a spiderweb-like irregular pattern (lacey grids), or a continuous support film to improve distribution of particles. This continuous film can be formed by carbon or graphene oxide. Affinity of the support film for particles can be increased by decorating film layers with antibodies or PEG bound to affinity ligands. Such affinity-based grids decrease requirements on sample concentration, because typically more than 95% of particles in solution applied on a common holey carbon grids are blotted away, which is the reason for the more than ten times higher required of protein concentration compared to negative stain EM.

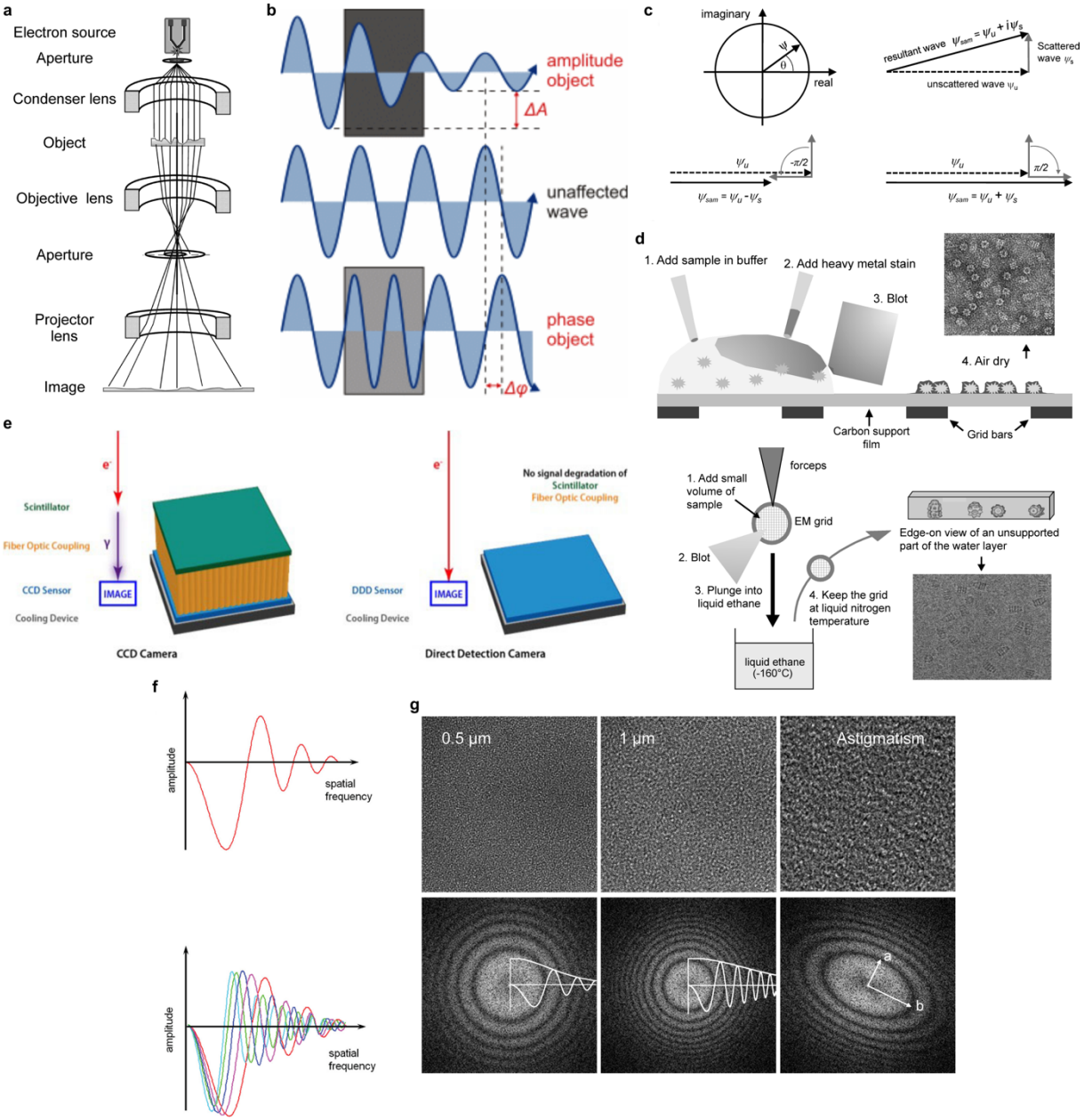

Figure 6: Basic characteristics of EM method.
a) Schematic representation of electron microscope with electron source and series of lenses focusing electron beam. Panel is from Orlova *et al*., 2011[213].
b) Difference between amplitude change and phase change of wave. Amplitude change is source of contrast in negative stain EM while phase change is source of phase contrast in cryo-EM. More details on phase contrast in (**c**). Panel is from diploma thesis of Steve Pawlizak, 2009.
c) Phase contrast formation by interference between scattered and unscattered wave. Interference leads to small contrast (comparison of real component between resulting and unscattered wave). Phase change of -90º leads to interference with unscattered wave producing negative contrast compared to phase change of 90º that produces positive phase contrast. Panel is from Orlova *et al*., 2011[213].
d) Comparison of grid preparation for negative stain EM and cryo-EM. Panel is from Orlova *et al*., 2011[213].
e) Composition of CCD and DDD sensors. CCD with energy transfer between electron and photon mediate via scintillator while DDD sensor detects electrons without any preceding energy transfer. Panel from Panel is from Direct Electron website- https://www.directelectron.com/de.series/.
f) Representation of 1D CTF. Signal is decreasing along spatial frequency and contain several 0 points (no signal points). To cover all spatial frequencies images are acquired at different defoci to shift signal propagation. Panel is from Orlova *et al*., 2011[213].
g) Representation of 2D CTF also called Thon Rings (Fourier transform of 2D image). Difference between 2D CTFs of images acquired at defocus 0.5 and 1 µm. Thon rings oscillate more at defocus 1

µm better covering low resolutions/low spatial frequencies while at defocus 0.5 µm slower oscillation better cover high spatial frequencies. The third image represent astigmatism where Thon rings do not propagate in the same way in all directions. Thus, 1D CTF differs in different directions (a, b). Panel is from Orlova *et al*., 2011[213].

1.4.3 Detection of electrons in EM

Imaging of grids at high magnification in a transmission electron microscope produces thousands of images ideally capturing the proteins of interest from all possible orientations. The contrast of images in cryo-EM is much weaker as compared to negative stain EM for two reasons: 1) the exposure dose for each single image is ultimately limited by the radiation sensitivity of biological material; 2) the majority of contrast formation originates solely from the change in phase of the electron wave, not from loss of energy. Phase contrast is weak but contains high and low-spatial frequency information corresponding to high and low resolution, respectively. The signal-to-noise ratio of recorded EM images improved over the years by the introduction of direct detector devices (DDD) that replace previously used CCD chips (Fig. 6e). The main difference and advantage of DDD over CCD cameras comes from the way they detect electrons. CCD chips do not directly detect the imaging electrons, but the electrons are converted to photons in a scintillator layer, before the photons travel through optic fibres to the sensor where they are converted into electrons again and detected by the accumulation of charge (Fig. 6e). Electrons hitting the scintillator in this process tend to produce many photons that scatter in fibre optics to produce even more photons and eventually create signal on many pixels at different regions of the sensor. DDDs on the other hand directly detect electrons hitting the sensor per pixel and produce signal in binary mode – pixels with signal (hit by electron) and pixels without signal (not it by electrons) (Fig. 6e). The very fast readout speed of DDDs furthermore allows to acquire images in so-called dose fractionation mode, in which the cumulative signal is distributed over many frames per image. This allows for computational correction of beam-induced particle motion in the ice.

1.4.4 Processing of images in SPA

At the beginning of a typical SPA processing workflow, particle motion over the individual frames of one image is corrected and the frames are averaged into one final image with higher contrast. The aligned and summed images are used in the next step for estimation of the contrast transfer function (CTF), which provides information content of the image and thus the theoretically achievable resolution. The CTF corresponds to the Fourier transform of point spread function of the imaging system (microscope). Thus, to determine the CTF, the image is Fourier-transformed and a mathematical model for the CTF is fitted (Fig. 6f, g). Knowledge of the CTF allows to restore the original information, i.e. the signal of the object not convoluted by the PSF, during image processing. The CTF contains information on how much signal is preserved/transferred at different spatial frequencies (Fig. 6f). Ideally, the signal would be constant across all spatial frequencies, allowing to obtain structures at a resolution limited only by the Nyquist theorem, i.e. by the signal sampled across two digital pixels (signal, no signal) and thus by the object pixel size on the detector. However, in reality, the signal is modulated by an envelope function, depending among other factors on the defocus and the spherical aberration of the imaging system (Fig. 6f). Retention of high-spatial frequencies (high-resolution information) is ideal at focus or close to focus, but at the cost of low-spatial frequencies (low-resolution information), which decreases visibility of particles on 2D image (Fig. 6g). Thus, images are acquired in a range of defoci from low defocus (close to focus) to higher defocus to obtain signal at all spatial frequencies and with reasonable signal/contrast (Fig. 6f).

1.4.5 Processing steps of SPA to obtain 3D reconstruction of proteins or protein complexes

The aim of all following processing steps in SPA is to obtain a structurally homogeneous set of particles from 2D images at different orientations that allows to reconstruct their 3D

representation with high level of details (high resolution). The first step after motion correction and CTF estimation is the localisation of particles on images, either manually or automatically using 2D reference/s or 3D reference/s that are used for cross-correlation based search on the images. Picked particles are extracted from the 2D images and subjected either to 2D classification or 3D classification.

2D,3D classification and 3D refinement apply in the process an algorithm called Expectation maximisation that is used in averaging of aligned particles (making a class average or new reconstruction). Aligned images are compared on a pixel level. Each of the aligned images has pixels with different signals at same spot that are plotted as PDF (Fig. 7b). To create new reference, the probability is averaged, leading to increase of signal per pixel (expectation maximisation). This process is done for each pixel of aligned images to produce 2D or 3D class averages or 3D reconstruction that will be used as a new reference in the next iteration. (Fig. 7b).

2D classification is aligning particles and calculating cross-correlation function between the particle images, without using any reference, to decide, which particles to group and average (Fig. 7a). Disadvantage of 2D classification is the loss of protein orientations represented by low population of particles that are not well clustered to class averages over iterations and many times lost in noisy class averages.

3D classification starts with reference filtering to remove high-resolution information and thus reduce reference bias. The reference is decomposed to 2D. images in initiation phase according to the chosen angular sampling, which defines how fine this decomposition will be (Fig. 7c). Then, particles are aligned as for 2D classification and compared with the reference images to assign angular parameters. Particles assigned to the same class are then back-projected to generate a set of updated 3D reconstructions at the end of each iteration (Fig. 7c).

However, this approach can lead to artificial accumulation of noise in various areas of the reconstructions that may lead to 3D class averages following the general shape of the initial reference, but reconstructed almost exclusively from noisy images/particles. Distinguishing such biased and artificial 3D class averages from true 3D class averages is easily done via the level of details (high-resolution 3D class average) or by removing small components of the initial 3D reference to test if they can be recovered during the averaging process.

After selecting a homogeneous set of particles representing the protein of interest, one can obtain 3D reconstructions at high resolution by subjecting particles to 3D refinement with an input 3D reference but in this case (ideally) using 3D class average of the selected particles. At the beginning of 3D refinement, selected particles are split into two random half-sets that are treated independently throughout the whole process. The 3D reference is again angularly sampled to produced 2D images of 3D representation and particle images are assigned to 2D images produced from the reference and later projected to form the new 3D reconstruction (Fig. 7b) (same expectation maximisation as in 3D classification) (Fig. 7c), In the next iteration, the updated 3D reconstruction is used as a reference and again sampled but using finer angles to improve angular assignment of particle images and thereby improve 3D reconstruction. Refinement is repeated iteratively; this way trying to improve the resolution of the reconstruction and converge the angular and translational assignment for all particles untill it is unable to obtain any improvement and it converges on a 3D reconstruction with a certain level of details. The level of detail, resolution, is calculated at each iteration using gold standard Fourier Shell Correlation by comparing Fourier transforms of 3D reconstructions from random particle half-sets. Fourier transforms are compared band-wise from the centre (low spatial frequencies) to the periphery (high spatial frequencies) Resolution is estimated as the spatial frequency with a correlation of 0.143 between Fourier transforms of two 3D reconstructions.

The final 3D reconstruction of protein/protein complex in many cases suffers from the loss of information due to CTF-induced signal damping or structural inhomogeneity. The signal loss is most severe for high-resolution information. This can be partially compensated for by application of b-factor sharpening. This approach modulates the signal amplitude structure factors contributing to the reconstruction in a frequency-dependent manner and in this way improves interpretability at high resolution. However, application of high b-factor value may lead to ‘over-sharpening’ and a very noisy representation of the reconstruction.

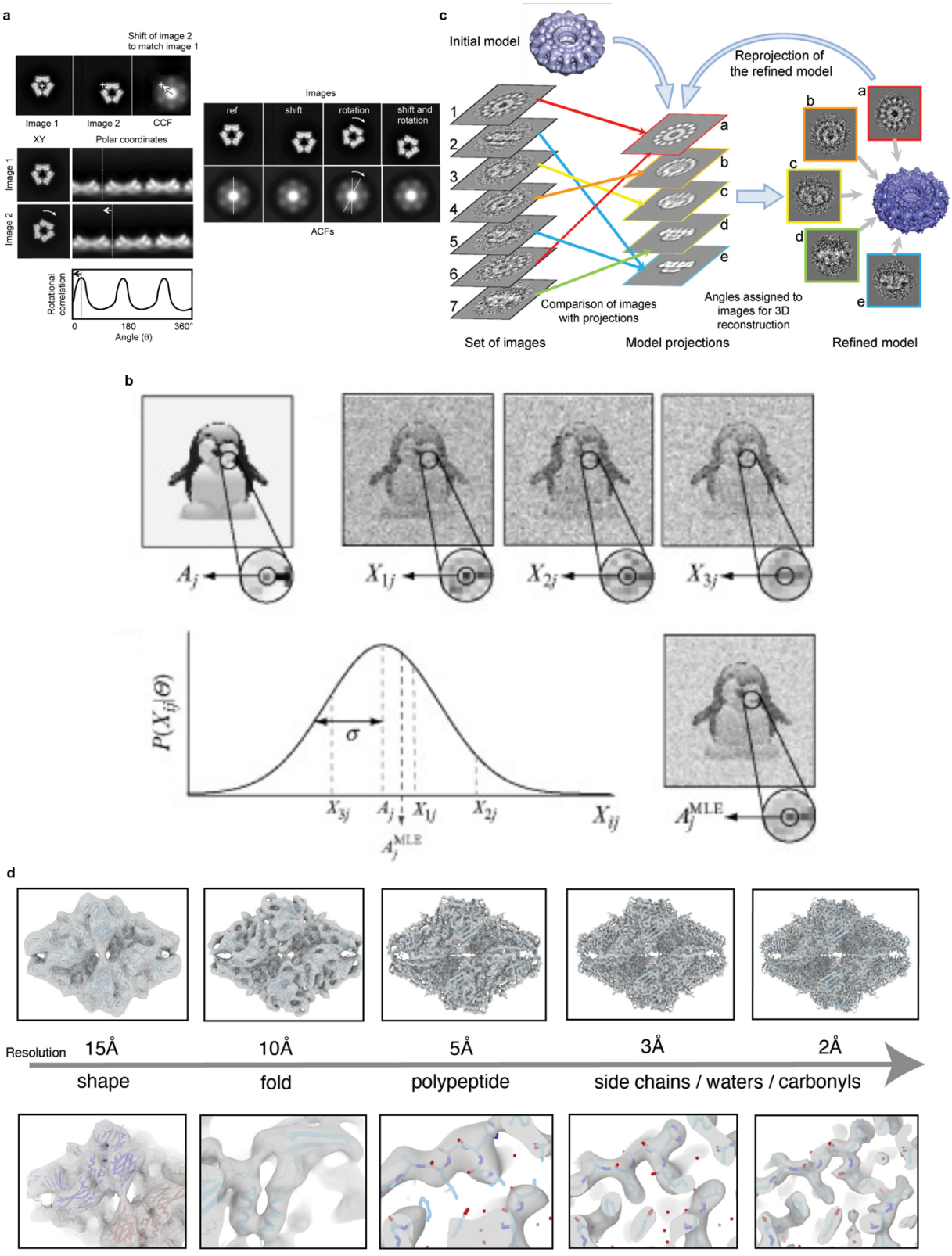

Figure 7: Alignment, reconstruction and interpretation of EM data.
a) Particle image alignment in 2D classification. Combination of shift (translation) and rotation followed by calculation of cross-correlation function is used to classify particles. Panel is from Orlova *et al.*, 2011[213]
b) Simplified representation of 3D reconstruction and angular assignment used in 3D classification and refinement. Reconstruction of 3D model at each representation is preceded by expectation maximisation explained in panel (**c**). Panel is from Orlova *et al.*, 2011[213]
c) Expectation maximisation explained on three images with different noise. For each pixel of aligned images, PDF is plotted representing probability of pixel with signal. Expectation maximisation algorithm

average probability of signal to be present in the image giving new pixel signal as you can see on average of three images next to the plot. Panel is from Sigworth *et al*., 2010[214].
d) Comparison of details visible in cryo-EM reconstructions at different resolutions. Panel is from Beckers *et al*., 2021[215].

1.4.6 Interpretation of cryo-EM 3D reconstruction

A sharpened high-resolution reconstruction is ideal for interpretation of protein or protein complex structure by model building. Today, achievable resolution ranges are pushed towards 2 Å but any reconstruction within a resolution range of 2-3.5 Å can be used for *de novo* building of atomic model without using any prior structural information (Fig. 7d). In this resolution range, amino acid side chains are clearly resolved (Fig. 7d). Reconstructions with lower resolutions of 3.5-5 Å are not readily usable for *de novo* modelling as most of the residue side chains are not resolved with the exception of bulky aromatic amino acid residues that can appear as bigger protrusions (blobs) from the protein backbone (Fig. 7d). This resolution range is sufficient to recognise secondary structure elements, mainly α-helices, allowing fitting of protein domains with previously solved structures or refinement of models form homology modelling (Fig. 7d). α-helices are well resolved to a resolution of up to 9-10 Å (Fig. 7d). Resolution in a range of 10-30 Å do not provide details about secondary structure anymore and only individual domains of proteins are visible (Fig. 7d).

2 Aims of this study

The overall objective of this PhD thesis was to structurally describe diverged γ-TuCs from different biological systems (the vertebrate γ-TuRC and the fungal γ-TuSC) and to get detailed insights into their molecular architecture and compare their structural characteristics.
The vertebrate γ-TuRC was identified in eukaryotes in 1996 and since then the molecular architecture of this complex remained unknown Thus, the first aim of my PhD studies was to describe the structure of the γ-TuRC in collaboration with Dr. Peng Liu (RG Schiebel, ZMBH). Using cryo-EM SPA, I aimed to obtain a γ-TuRC cryo-EM reconstruction at sufficient resolution and quality that would allow me to assign all components that were identified and described before. Because the γ-TuRC function is considered a structural template for MT nucleation, I planned to measure the helical parameters of the γ-TuRC and the ideal MT spiral in order to compare their geometries.

While the vertebrate γ-TuRC was for more than 20 years structurally black hole, the fungal γ-TuSC was described structurally at least at low resolution. Initial cryo-EM studies elucidated the shape and the composition of the γ-TuSC but low resolution impeded the understanding of the γ-TuSC architecture and stability as a heterotetramer. Thus, the second aim of my PhD studies in collaboration with Anjun Zheng (RG Schiebel, ZMBH) was to obtain a high-resolution cryo-EM reconstruction of the *C. albicans* γ-TuSC, which would allow me to analyse the molecular interface between the γ-TuSC components in order to get insights into the γ-TuSC stabilisation and conformation, and additionally to compare the structures and interfaces of the γ-TuSC and the γ-TuRC.

The third aim of my PhD studies has been raised from the results of the first aim. In collaboration with Martin Würtz (RG Schiebel, ZMBH), I planned to mechanistically understand how more than 30 components of the γ-TuRC assembly into uniform complexes and understand the role of actin in the assembly process. Design and application of the recombinant system for the γ-TuRC by Martin Würtz in combination with cryo-EM SPA allowed me to obtain reconstructions of different γ-TuRC assembly intermediates and propose an assembly pathway for this complex. Taking advantage of the recombinant expression system to perturb the actin binding site in the γ-TuRC, I planned to get insights into the actin-deficient γ-TuRC to understand the impact of actin on γ-TuRC assembly.

3 Results

All experiments and analyses in the result section were performed by me if there is no other person stated or specified.

3.1 The γ-TuSC as a basic unit of the fungal MT nucleation template

Results presented in this chapter were published in Nature Communications with me as a co-first author[216].

3.1.1 Purification and cryo-EM reconstruction of the *Candida albicans* γ-TuSC

In the fungi, MT nucleation system in comparison to vertebrate one produces much less *de novo* nucleated MTs because mitosis in fungi does not require formation of the complex spindle for a cell division. MT nucleation template is composed in fungi of Spc97, Spc98 and γ-tubulin, which assemble into the γ-TuSC heterotetramer that oligomerise at the SPB into a ring-like oligomer. In order to obtain insights into the composition of the γ-TuSC and understand its stability in form of a heterotetrameric complex, Anjun Zheng coexpressed the *Candida albicans* γ-TuSC components- Spc97, Spc98 and γ-tubulin - in insect cells and purified the γ-TuSC via his-tag-based affinity purification followed by anion exchange chromatography (Fig. 8a). The C. *albicans* γ-TuSC was purified in high homogeneity and concentration (Fig. 8b), suitable for cryo-EM SPA and obtaining a 3D reconstruction at near-atomic resolution. After the purification, I applied the sample on grids and acquired several thousand images (Fig. 9a). The images were subjected to automated particle picking and several tiers of computational particle-sorting that led to the final set of particles refined to 4.1 Å global resolution (Fig. 9b, c). Local resolution filtering revealed that the γ-TuSC reached the highest resolution at the interface between Spc GRIP2 domains and γ-tubulins, while the lowest resolution was attained at the N-terminal half of the Spc proteins (Fig. 9c). Additionally, 3D classification revealed flexibility between the two spokes in the γ-TuSC. In order to address this flexibility and improve resolution of the complex, both spokes were refined separately, resulting in a overall 3D reconstruction of the γ-TuSC at 3.6 Å global resolution (Fig. 9d, e). To create an atomic model of the *C. albicans* γ-TuSC, composed of two γ-tubulins, Spc97 and Spc98 as described for the *S. cerevisiae* γ-TuSC[153], I prepared a homology model of γ-tubulin based on the human γ-tubulin[217] and models of Spc97, Spc98 based on the X-ray structure of GCP4[155]. All homology models were firstly rigid body fitted, refined and extended according to the cryo-EM reconstruction to achieve satisfactory refinement statistics and provide high cross-correlation with the cryo-EM reconstruction.

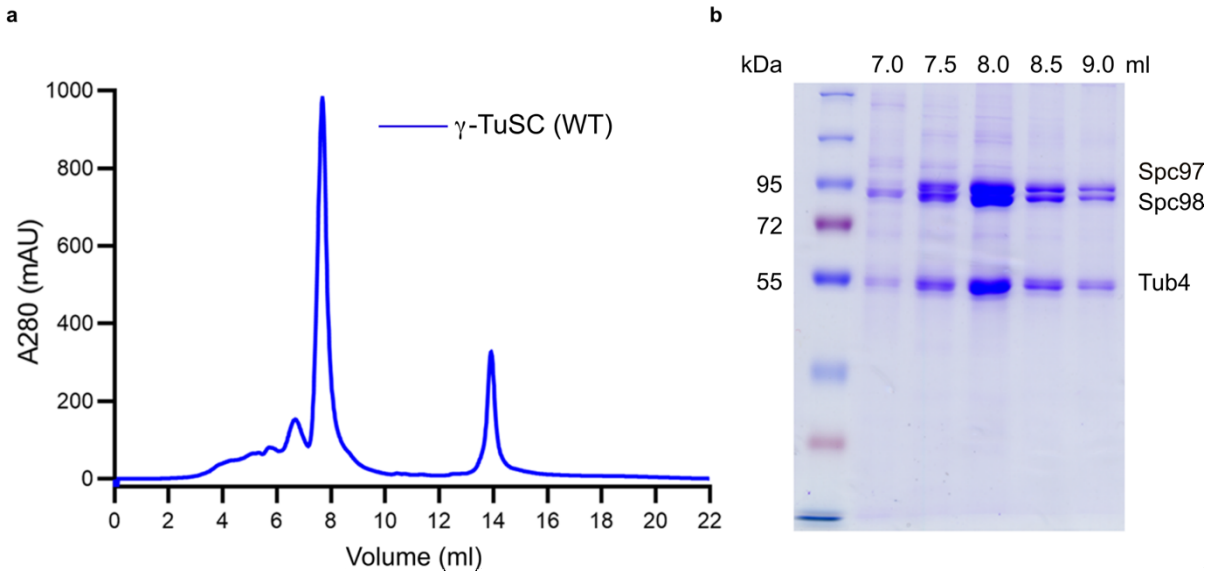

Figure 8: Purification of the *C. albicans* γ-TuSC.
a) Elution profile from anion exchange chromatography of the γ-TuSC.
b) SDS-PAGE of eluted fractions from anion exchange chromatography. Fractions are given according to the elution volume. Important molecular weights of a marker are given. Bands representing the γ-TuSC components are given.
All experiments and analyses in this figure were performed by Anjun Zheng.
Figure was modified from Zupa *et al.*, 2020[216].

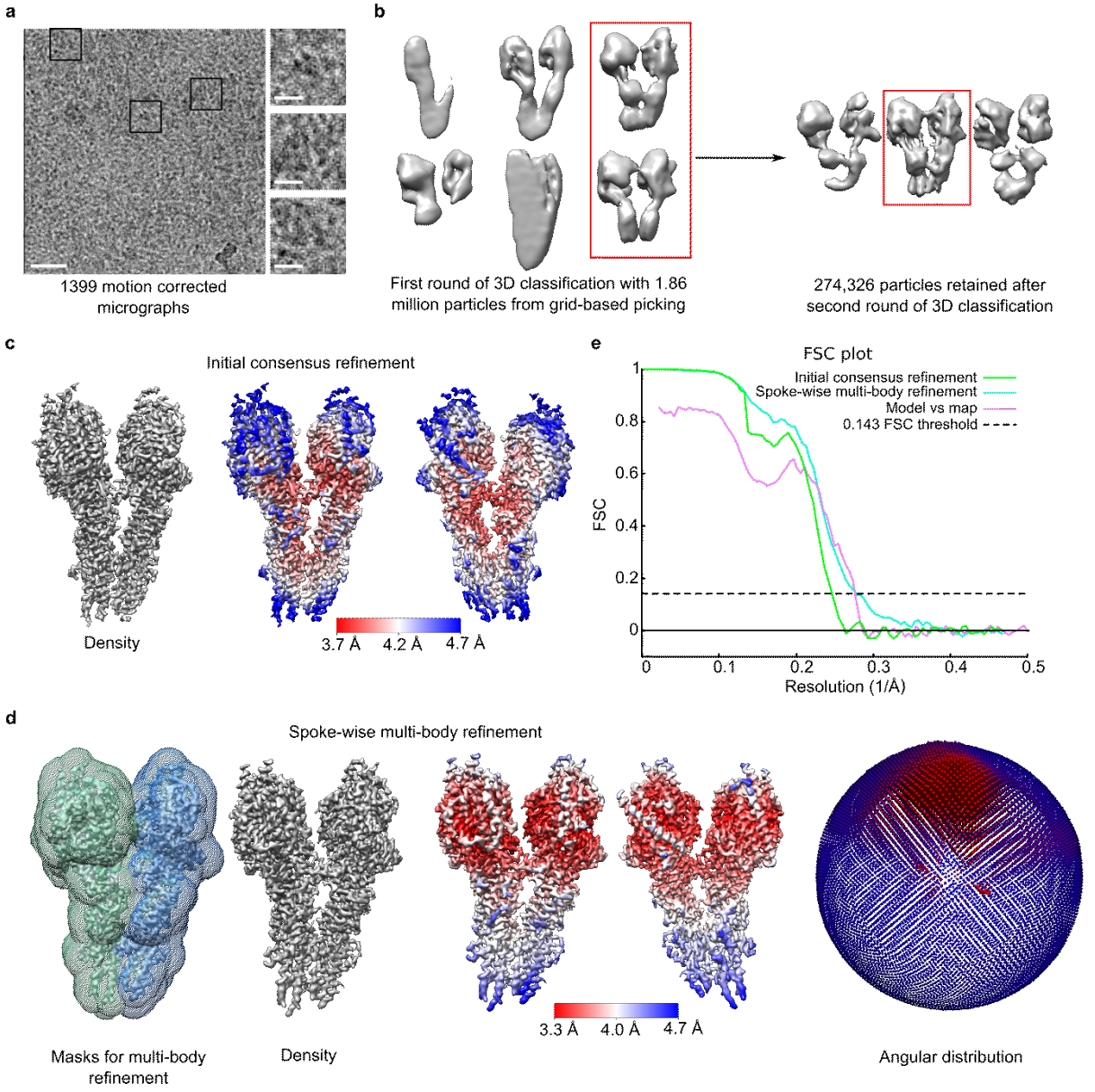

Figure 9: Schematic flowchart of the γ-TuSC cryo-EM data processing.
a) Zoom on a representative image from the γ-TuSC cryo-EM data acquisition. Three representative particles from the image are shown in zoom. Particles are indicated on the image by black rectangles. The number of acquired images is given. Scale bars, 30 nm (image) and 10 nm (particles).
b) Left, results of the first round of 3D classification. Right, results of the second round of 3D classification. Output class averages are shown in both cases. Selected class averages are indicated by red rectangles. The number of input particles is given.
c) Left, the cryo-EM reconstruction of the γ-TuSC from initial consensus refinement (grey). Right, the cryo-EM reconstruction of the γ-TuSC from initial consensus refinement filtered according to a local resolution. Resolution scale and colour scheme are depicted.
d) Multi-body refinement of the γ-TuSC reconstruction. Left, Masks applied for multi-body refinement and resulting composite cryo-EM reconstruction of the γ-TuSC in grey. Right, Composite cryo-EM reconstruction of the γ-TuSC filtered according to a local resolution. Resolution scale and colour scheme are depicted. Angular distribution of the γ-TuSC particles applied in 3D auto-refinement and multi-body refinement.
e) FSC plot of the γ-TuSC reconstruction after initial 3D auto-refinement, after multi-body refinement and model vs map validation. Gold standard FSC threshold is depicted as dashed line.
Figure was modified from Zupa *et al.*, 2020[216].

The shape of the *C. albicans* γ-TuSC was similar to the *S. cerevisiae* γ-TuSC (Fig. 10a)[153,156]. The quaternary structure resembled the letter 'Y' with a height of 180 Å, a width of 60 Å in the N-terminal part and 100 Å in the C-terminal part (Fig. 10b). The 'Y' shape is comprised of two spokes, one represented by Spc97 with associated γ-tubulin and the other represented by Spc98 with associated γ-tubulin (Fig. 10a). Both Spc proteins possesses an α-helical fold as GCP4 and contain two domains- the N-terminal GRIP1 domain and the C-terminal GRIP2 domain (Fig. 10c). Each GRIP domain is formed by an α-helical bundle that interacts in the hinge region of the Spc proteins (Fig. 11a). Stability of the GRIP domain fold is ensured by hydrophobic interactions that form the interface between the GRIP domains as well (Fig. 11b). The GRIP1 domains in both Spc proteins are not located at the complete N-terminus as in the case of GCP4 but they are preceded by longer extensions that were not resolved in the cryo-EM reconstruction indicating conformational flexibility (Fig. 10c). A rigid body fit of the homology models of the γ-TuSC components into the cryo-EM reconstruction revealed a density segment on the periphery of the GRIP1 domains not covered by any of the models (Fig. 10a). This low-resolution density segment is in contact with the GRIP1 domains of both Spc proteins. Due to high purity of the sample and precise stoichiometry of the γ-TuSC components (Fig. 8a, b), I could exclude that the density segment is represented by any γ-TuSC binding partner. Thus, the density segment is likely represented by an unmodeled part of the γ-TuSC components. Good candidates for the density segment were NTEs of the Spc proteins due to the position of the density segment at the periphery of the GRIP1 domains. However, low resolution and lack of connectivity did not allow me to trace the density segment unambiguously to the GRIP1 domain of a specific Spc protein.

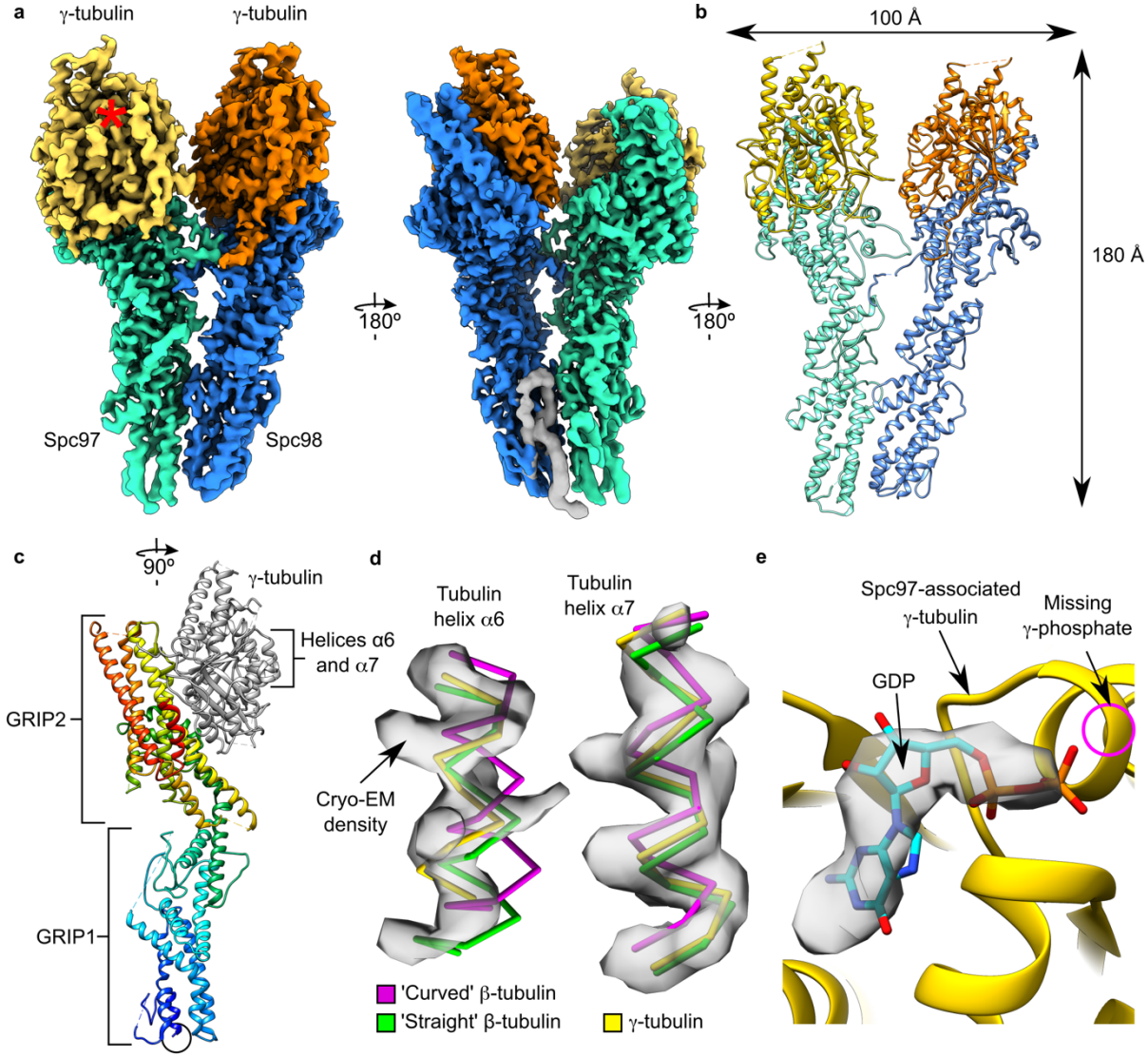

Figure 10: The structure of the *C. albicans* γ-TuSC.
a) Segmented cryo-EM reconstruction of the *C. albicans* γ-TuSC. Density segments for γ-tubulins in yellow and orange, Spc97 in aquamarine and Spc98 in blue. The unassigned density segment is visualised in grey. Position of a ligand in γ-tubulin is indicated by red asterisk.
b) Size of the γ-TuSC. Dimensions are given. Model coloured same as in (**a**).
c) Representation of the γ-TuSC spoke. γ-tubulin in grey. Spc97 coloured in rainbow from the N- to C-terminus. The GRIP domains are indicated. Helices α6 and α7 used for assignment of the γ-tubulin conformation are indicated. The unresolved NTE region preceding the GRIP1 domain is indicated by black circle.
d) γ-tubulin helices α6 and α7 from the γ-TuSC reconstruction (yellow), from β-tubulin in the straight conformation (green) and curved conformation (magenta) superposed to the Spc97-associated γ-tubulin cryo-EM reconstruction (grey).
e) GDP ligand (cyan) superposed to the cryo-EM reconstruction in the ligand pocket of the Spc97-associated γ-tubulin (yellow). Position of the third phosphate group that is present in GTP is indicated by pink circle.
Figure was modified from Zupa *et al.*, 2020[216].

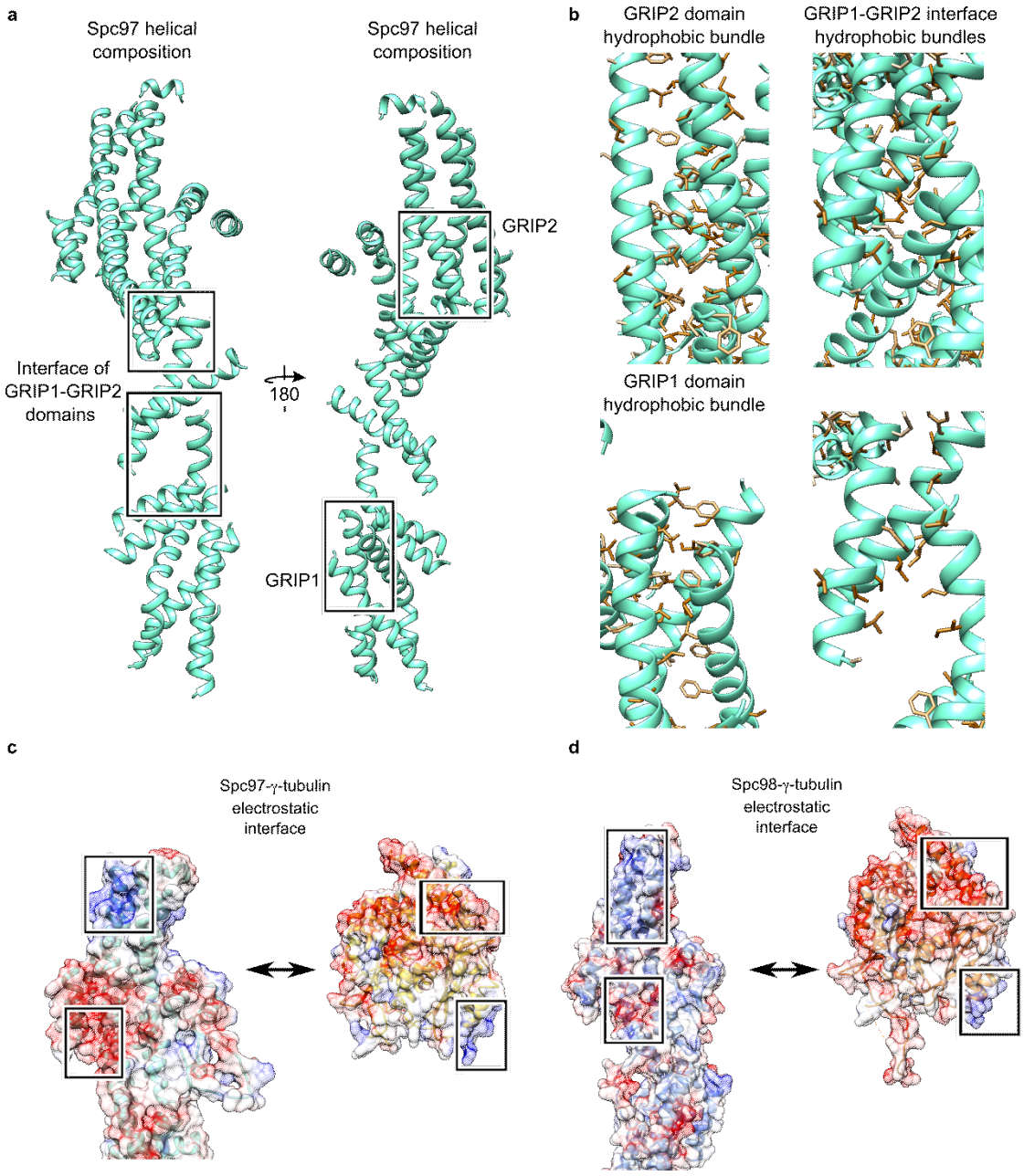

Figure 11: Interfaces responsible for folding of the GRIP1 and GRIP2 domains and binding of γ-tubulin.
a) A helical fold of the Spc proteins. Regions of the intra-molecular interface are indicated by black rectangles. **b)** Zoom on the intra-molecular interfaces of the Spc proteins. Left, the GRIP2 and GRIP1 domain hydrophobic residues (brown) mediating folding of the Spc proteins. Right, Hydrophobic residues (brown) responsible for interactions between the GRIP1 and GRIP2 domains.
c, d) Electrostatic interface between Spc97 and γ-tubulin, and between Spc98 and γ-tubulin. Charged residue patches mediating interactions are indicated by black rectangles.
Figure was modified from Zupa *et al.*, 2020[216].

3.1.2 Conformation of γ-tubulin in the γ-TuSC complex

One of the characteristics of MT dynamics is a GTP-hydrolysis-driven conformational change from a curved to a straight conformation of α/β-tubulin dimers upon extension of protofilament by newly bound tubulin dimers. A question of a conformational state was raised as well for γ-tubulins bound to the Spc proteins. Both conformational states were described for α/β-tubulin dimers using X-ray crystallography (PDB 4FFB[67], PDB 5W3F[218]). The difference between these two conformational states of α/β-tubulin dimers is most pronounced for α-helices 6,7 and

the connecting loop. Thus, I focused on these secondary structure elements in γ-tubulin as well in order to identify the γ-tubulin conformation. Due to flexibility, the loop between the α-helices was not resolved, leaving the two α-helices as the only structural elements to distinguish between the two conformations. I generated simulated density segments for the two α-helices based on β-tubulin atomic model to measure cross-correlation between the two α-helices of β-tubulin and γ-tubulin, and R.M.S.D. of their protein backbones (Fig. 10d, Table 1). Both measurements clearly identified the straight conformation of γ-tubulins in the γ-TuSC (Table 1). Another factor affecting conformational state of tubulin dimers is the ligand status (GDP vs. GTP). Investigating the ligand pocket of γ-tubulin and fitting both GTP and GDP to the corresponding density segment, I concluded presence of GDP ligand in γ-tubulin considering missing density segment for the third phosphate group of GTP (Fig. 10e).

Table 1: Elucidation of the γ-tubulin conformation in the context of the γ-TuSC.

	R.M.S.D. of Cα atoms		Cross-correlation between density segments	
	β-tubulin curved	β-tubulin straight	β-tubulin curved	β-tubulin straight
γ-tubulin (Spc97)	2.128	1.302	0.7876	0.8309
γ-tubulin (Spc98)	1.635	1.167	0.7950	0.8349

3.1.3 The γ-TuSC spokes are interacting via an extended interface

Fungal γ-TuSC exists as a stable heterotetramer that oligomerise into a ring-like structure. At the time, such unit has not been observed in higher eukaryotes suggesting some stabilisation of the fungal γ-TuSC. The achieved resolution allowed me to investigate interfaces between the components of the γ-TuSC that are responsible for the γ-TuSC assembly. Two separate spokes are formed by interactions between the Spc proteins and γ-tubulins. Binding of γ-tubulins is mediated by charged patches on the Spc proteins (Fig. 11c, d), which was in agreement with observation in the GCP4 X-ray structure[155], suggesting conserved properties of these residues across organisms. The interface between the Spc proteins that defines the Y-shape of the complex and brings the two spokes together is consisting of two regions (Fig. 12). The GRIP1 domains of the Spc proteins form an interface that was observed also in the structure of the vertebrate γ-TuRC between individual spokes at the same position[219-221] (Fig. 12a, b). In-depth investigation of that interface characteristics revealed a hydrophobic interface between *C. albicans* Spc97 and Spc98 (Fig. 12a) and an electrostatic interface between GCP2 and GCP3, the vertebrate homologs of Spc97 and Spc98, respectively (Fig. 12b). Overall, this showed that while the position of the interface is same, residue properties differ between fungi and vertebrates. The second interface between fungal Spc proteins, located between their GRIP2 domains, in the γ-TuSC is absent between vertebrate GCP2 and GCP3 of the γ-TuRC. This extended interface of the Spc proteins is formed by the insertions of Spc97 and Spc98 in the GRIP2 domains and Spc98-associated γ-tubulin (Fig. 12c). All three insertions are missing in the vertebrate homologs of these proteins explaining the absence of such extended interface in the vertebrate γ-TuRC. Compared to their vertebrate homologs, Spc97 contains insertions between Thr232-Asp272, Glu495-Pro502, Asn539-Ser566, Ala686-Ile737 and Spc98 contains insertion between Asn626-Leu656 (Fig. 13a, b and Fig. 14). The insertion of Spc98 forms the main part of the extended interface that is completed by the insertion Glu495-Pro502 from Spc97 and the insertion Thr38-Tyr72 from γ-tubulin of Spc98 (Fig. 12c, Fig. 13c and Fig. 14). The Spc98 insertion reaches to the GRIP2 domain of Spc97 via its N-terminal part and creates an interface with hydrophobic residues- Leu630, Leu631, Leu632, Phe636, Met637, Leu639

that bind to a hydrophobic groove of the Spc97 GRIP2 domain (Fig. 12d). The Spc97 insertion contacts the Spc98 insertion and likely locks it in a specific position (Fig. 12c). Stabilisation of the Spc98 insertion is enhanced by the γ-tubulin insertion that reaches towards the C-terminal part of the Spc98 insertion and binds via hydrophobic residues to a hydrophobic groove formed by the Spc98 GRIP2 domain and C-terminal part of the Spc98 insertion (Fig. 12e). The γ-tubulin insertion is not resolved in Spc97-associated γ-tubulin, which can be explained by a missing hydrophobic groove on Spc97 for stabilisation and anchoring. In conclusion, the insertions in all three γ-TuSC components create an extended interface that is absent in the γ-TuRC of vertebrates.

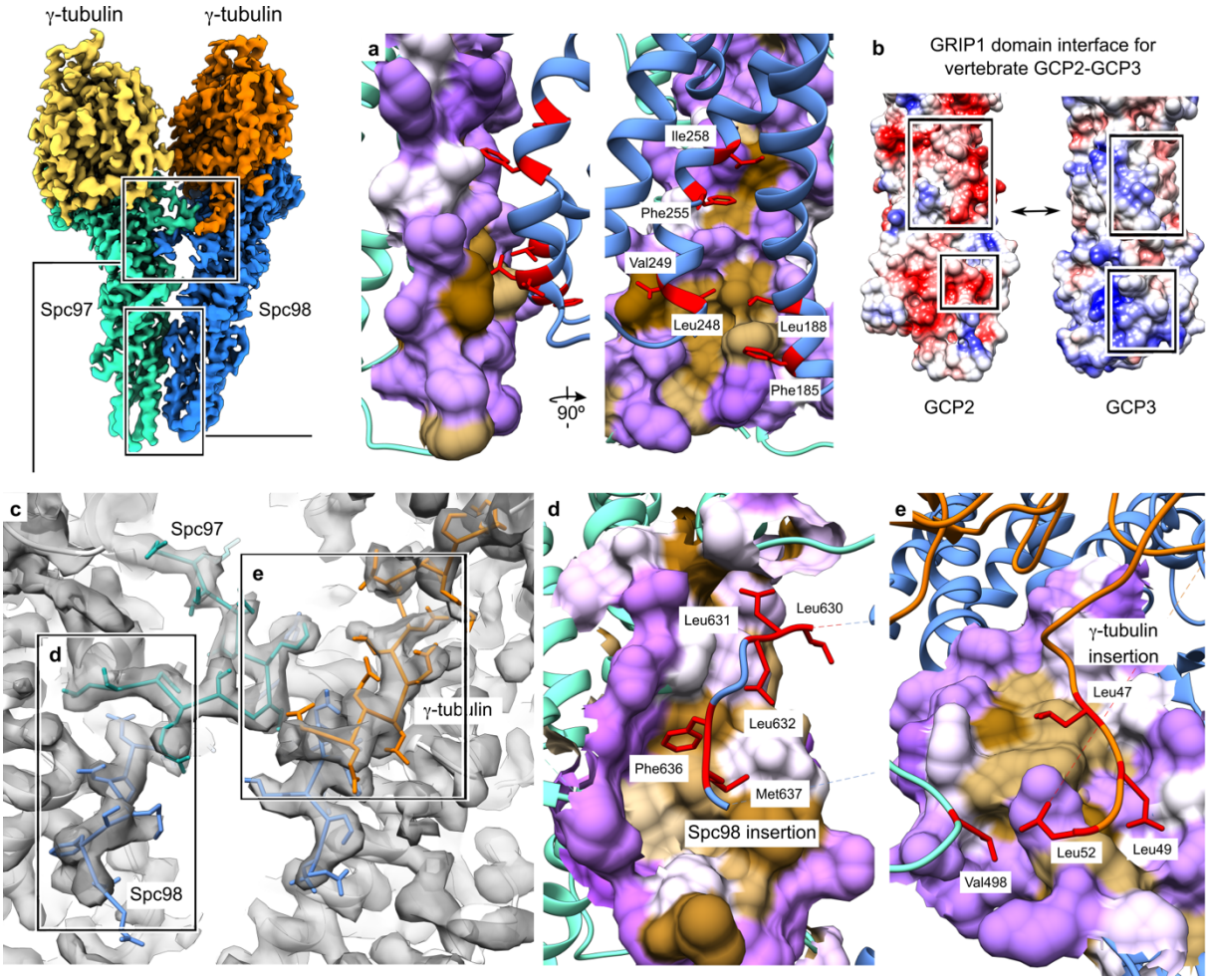

Figure 12: Characterisation of the *C. albicans* γ-TuSC inter-spoke interface.
a) Zoom on the interface between the GRIP1 domains of the *C. albicans* γ-TuSC. Surface representation of the Spc97 GRIP1 domain interface coloured according to a hydrophobicity from purple (hydrophilic) to brown (hydrophobic). Hydrophobic residues of Spc98 bound in the hydrophobic pocket of Spc97 are depicted in red. Spc98 hydrophobic residues are indicated.
b) Interface of the GRIP1 domains of GCP2 and GCP3 integrated in the γ-TuRC coloured according to a coulombic potential (red-negative, blue-positive, white-neutral). Patches of oppositely charged residues are indicated.
c) Zoom on the extended interface between the *C. albicans* γ-TuSC spokes. Components participating in the extended interface are indicated and regions forming the extended interface are coloured as in Figure 10. Rest of atomic models is coloured in white. The γ-TuSC atomic model is fitted to the γ-TuSC reconstruction in grey.
d) Zoom on the extended interface between the Spc98 insertion and the Spc97 hydrophobic pocket. Representation and colouring are same as in (**a**). The Spc98 interacting residues are indicated.
e) Zoom on the extended interface between the Spc98 and γ-tubulin insertions. Representation and colouring are same as in (**a**). γ-tubulin and Spc97 interacting residues are indicated.

Figure was modified from Zupa *et al.*, 2020[216].

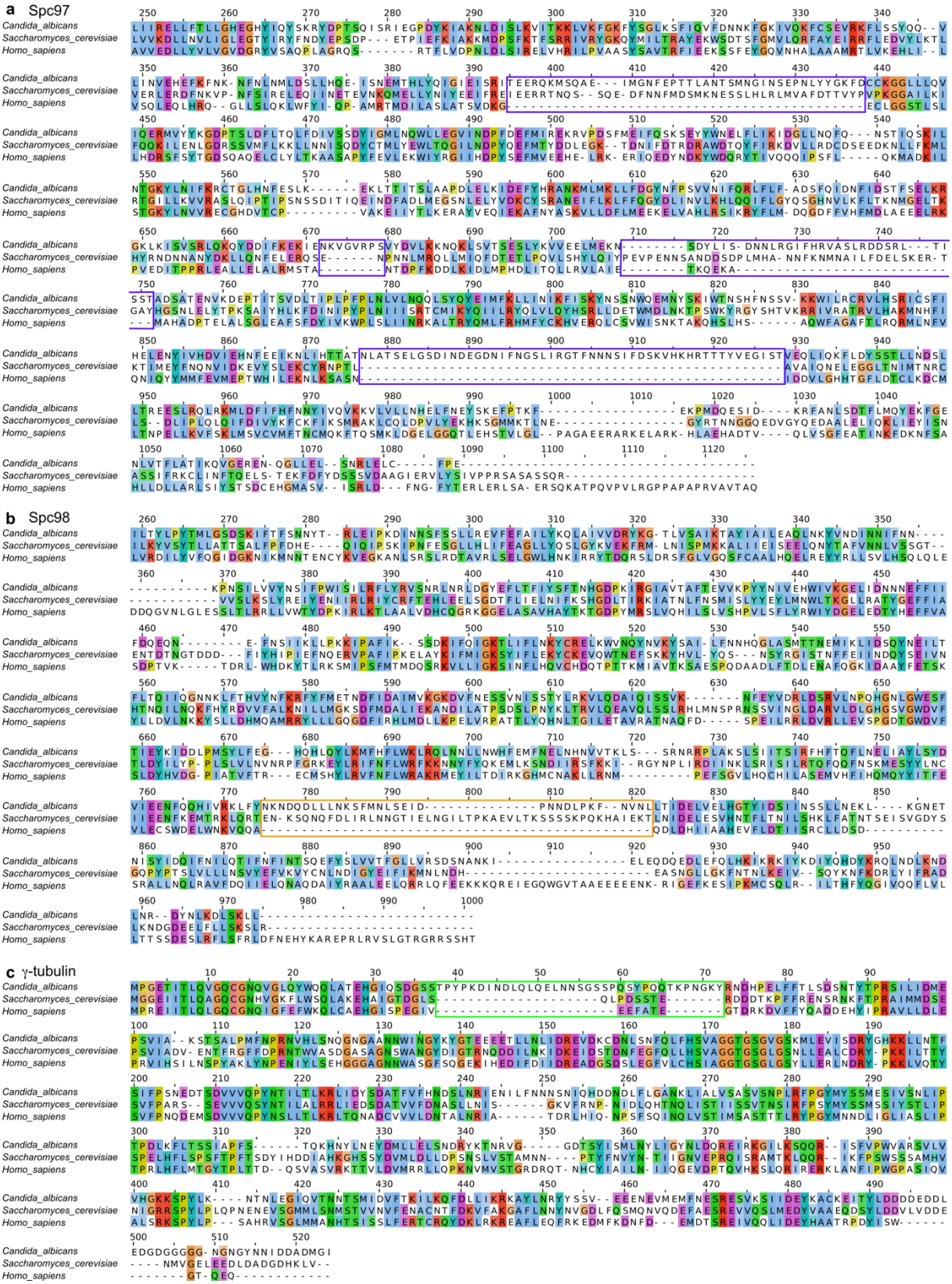

Figure 13: Sequence alignment of the γ-TuSC components from *C. albicans*, *S. cerevisiae* and *H. sapiens*.
a) Sequence alignment of Spc97 (GCP2). The Spc97-specific insertions are indicated by purple rectangles.
b) Sequence alignment of Spc98 (GCP3). The Spc98-specific insertion is indicated by orange rectangle.
c) Sequence alignment of γ-tubulin. The γ-tubulin-specific insertion is indicated by green rectangle.

All insertions are shown on the γ-TuSC model in Figure 14.
Figure was modified from Zupa *et al.*, 2020[216].

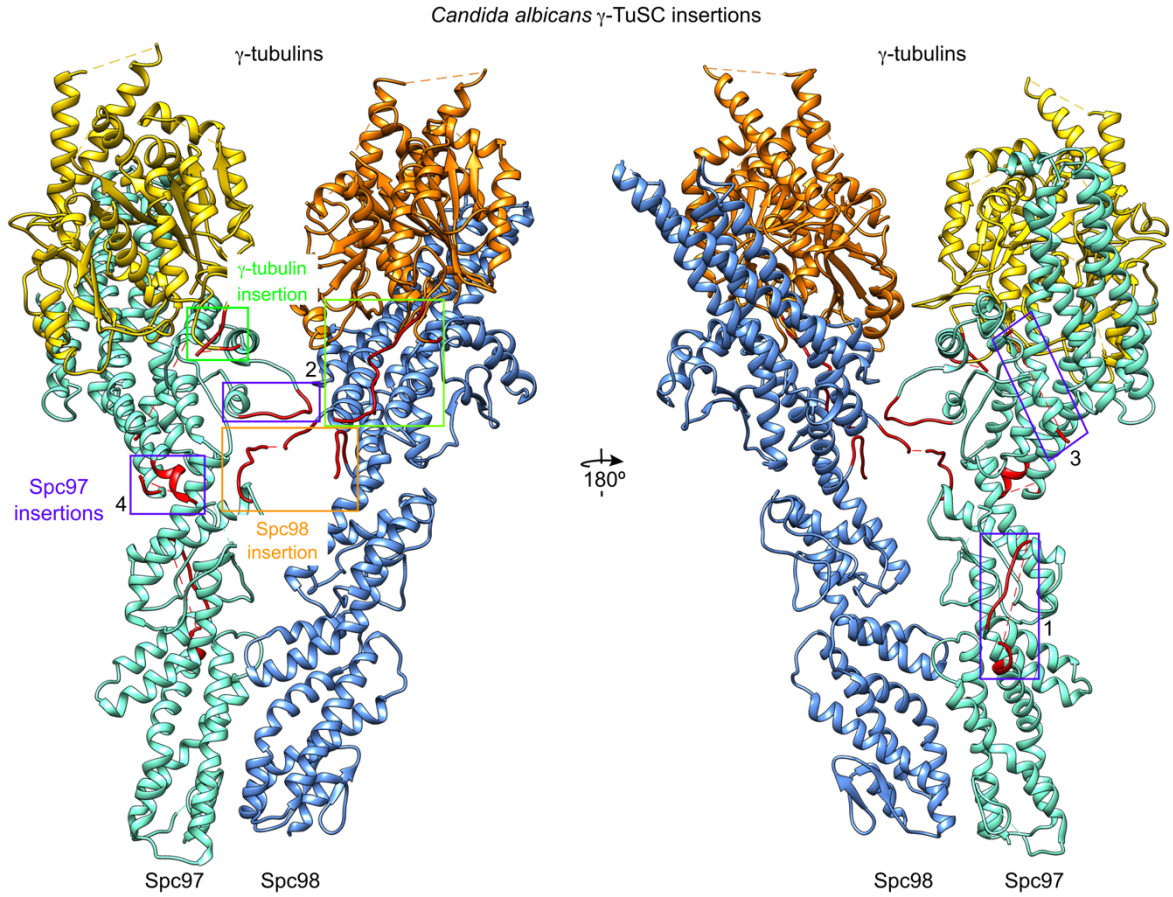

Figure 14: Mapping the insertions into the *C. albicans* γ-TuSC model.
Insertions of Spc97 are indicated by purple rectangles. The Spc98 insertion is indicated by orange rectangle and the γ-tubulin insertion is indicated by green rectangle. Insertions of Spc97 are numbered according to their occurrence in the sequence from N-terminus. Modelled residues of the insertions are depicted in red.
Figure was modified from Zupa *et al.*, 2020[216].

3.1.4 The extended interface defines relative orientation of spokes

The extended interface in the *C. albicans* γ-TuSC and its absence in the interface between GCP2 and GCP3 of the vertebrate γ-TuRC[219-221], raised questions about its role. Considering that GCP2 and GCP3 in the γ-TuRC, and Spc97 and Spc98 in the γ-TuSC have similar positions and assemble into similar Y-shaped complexes, Anjun Zheng and I wanted to test if the GRIP1 domain interface would be sufficient to define the γ-TuSC shape. Thus, Anjun Zheng and I decided to remove the insertion of Spc98, the biggest contributor to the extended interface providing strong hydrophobic interactions. Additionally, Anjun Zheng and I decided to test contribution of the γ-tubulin insertion to the extended interface. In order to analyse the role of these two insertions, two constructs of the γ-TuSC were prepared by Anjun Zheng- a mutant construct of the γ-TuSC lacking the Spc98 insertion (Spc98$^{\Delta D627\text{-}K650}$) (Fig. 15a, b) and a mutant construct of the γ-TuSC lacking the γ-tubulin insertion (Tub4$^{\Delta T38\text{-}K71}$) (Fig. 15c, d). Anjun Zheng coexpressed all the γ-TuSC components including either Spc98 lacking its insertion or γ-tubulin lacking its insertion and purified them the same way as for the wild-type γ-TuSC (Fig. 15a, c). Purified mutant γ-TuSC versions were subjected to negative stain EM together with the wild-type γ-TuSC as a positive control to explore the shape of the complex

and arrangement of spokes (Fig. 16a-c and Fig. 17a, b, c).. SDS-PAGE performed by Anjun Zheng revealed that concentrations of the γ-TuSC components is much lower after their overexpression (Fig. 15b, d), which suggested problems with an assembly of spokes and lower stability of the mutant versions (Fig. 15b, d). Analysis of the negative stain EM data for the γ-TuSC wild-type that were collected by Dr. Annett Neuner (RG Schiebel, ZMBH) led to 2D class averages recapitulating the typical Y-shape of the complex (Fig. 17a). Similarly, analysis of the γ-TuSC with the Spc98 insertion deletion showed that spokes were still assembled into the γ-TuSC, preserving its quaternary structure (Fig. 17b). Thus, the GRIP1 domain interface was sufficient to bring spokes together. However, the Y-shape of the γ-TuSC was in many cases perturbed, resulting in 51% particles having a wider angle between the GRIP2 domains of the Spc proteins while the interface of the GRIP1 domains was preserved (Fig. 17b). The rest of the γ-TuSC particles assembled into a Y-shaped complex comparable to the wild-type γ-TuSC. Analysis of the γ-TuSC without the γ-tubulin insertion led to similar results as in the case of aforementioned γ-TuSC construct (Fig. 17c). Two types of 2D class averages were observed again- one with a wider angle between the GRIP2 domains of spokes and another one resembling the Y-shape of the wild-type but the ratio of the particles in the two distinct classes changed significantly towards the wild-type shape with a ratio of 28% to 72%, respectively (Fig. 17c). Higher relative number of the wild-type-shaped γ-TuSC particles indicates that the insertion of the Spc98-associated γ-tubulin is not playing a major role in stabilisation of the γ-TuSC conformation but likely contributes by stabilising position of the Spc98 insertion while the Spc98 insertion itself defines the conformation of the γ-TuSC.

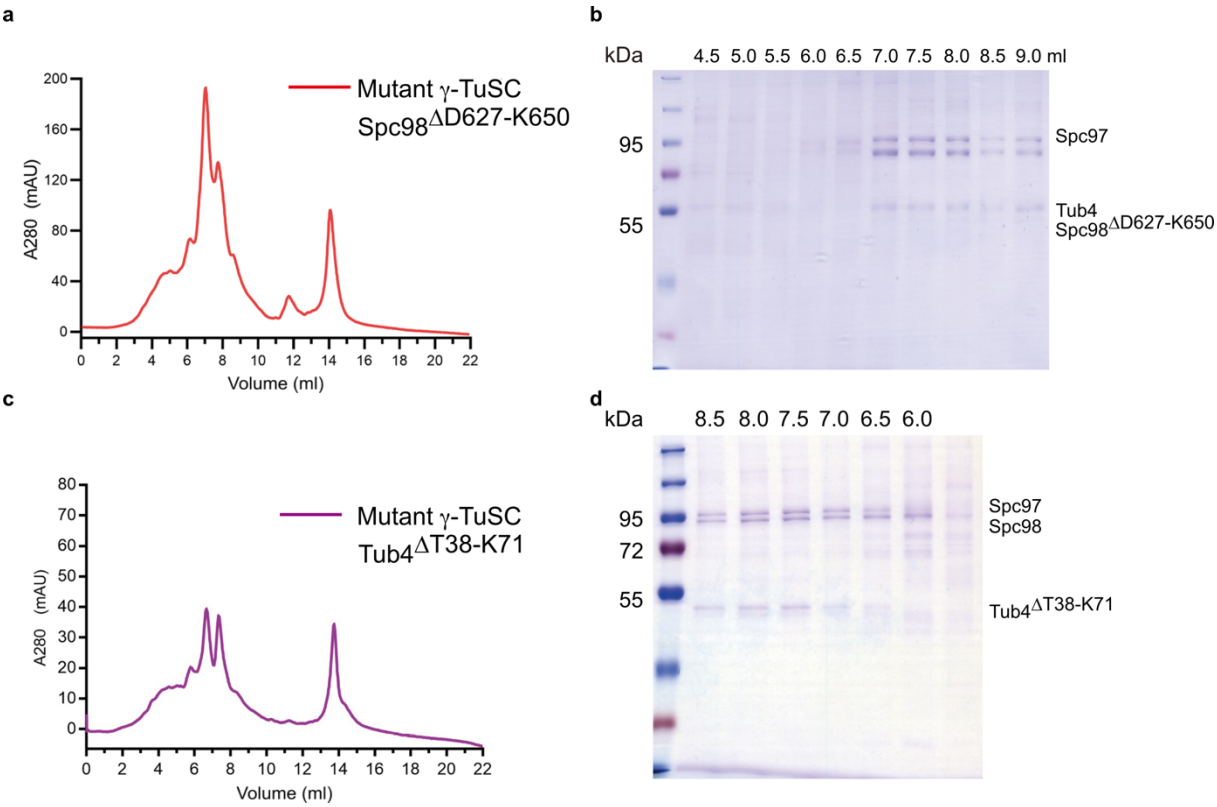

Figure 15: Purification of the γ-TuSC mutant versions.
a) Elution profile from anion exchange chromatography of the γ-TuSC mutant version with Spc98 lacking its insertion.
b) SDS-PAGE of the eluted fractions from the anion exchange chromatography of (**a**). Fractions are given according to the elution volume. Important molecular weights of a marker are given. Bands representing the γ-TuSC components are indicated.

c) Elution profile from anion exchange chromatography of the γ-TuSC mutant version with γ-tubulin lacking its insertion.
d) SDS-PAGE of the eluted fractions from anion exchange chromatography of panel (**c**). Labeling same as in (**b**).
All experiments and analyses in this figure were performed by Anjun Zheng.
Figure was modified from Zupa *et al*., 2020[216].

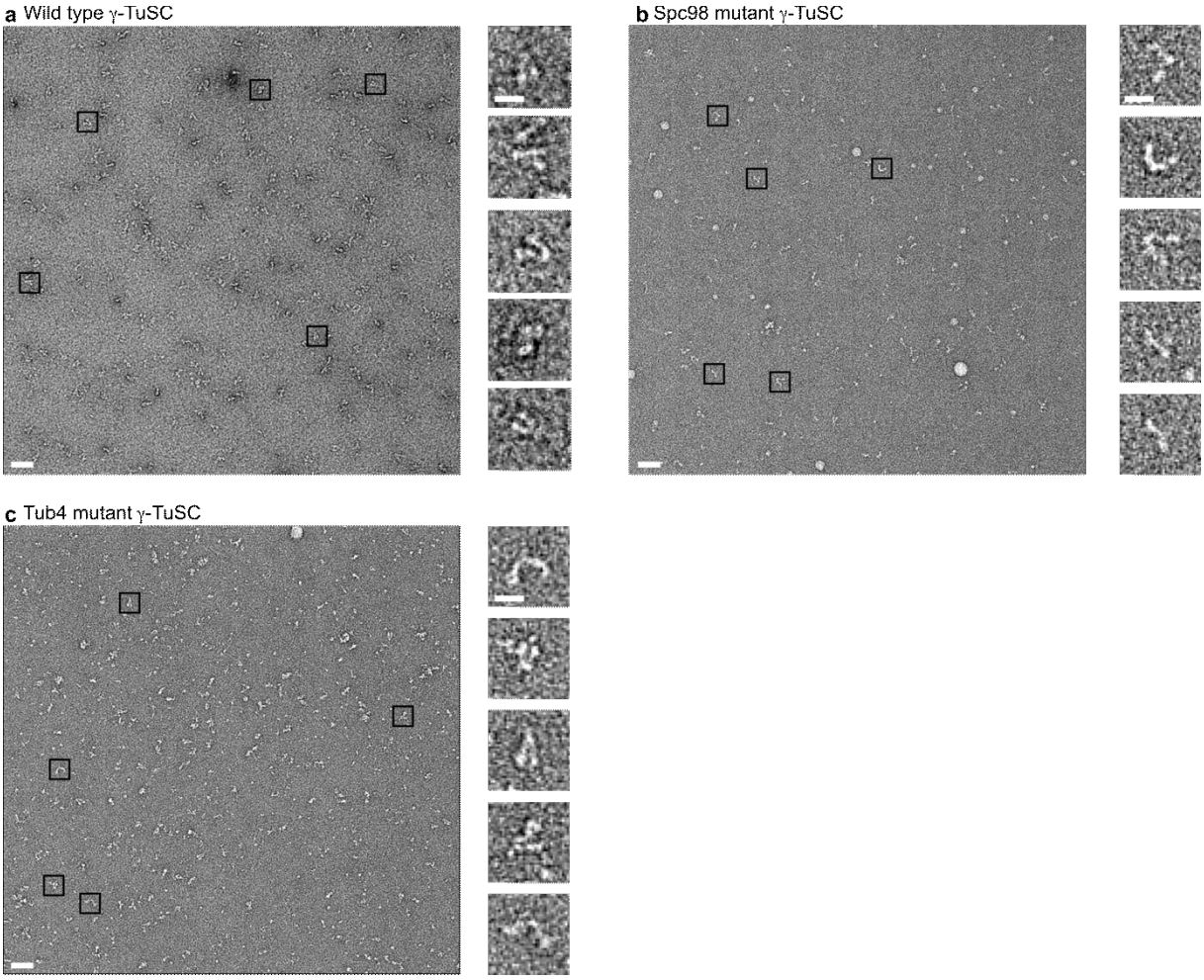

Figure 16: Negative stain EM data of the *C. albicans* γ-TuSC wild-type and the mutant versions.
a) Representative image from the negative stain EM of the *C. albicans* γ-TuSC wild-type.
b) Representative image from the negative stain EM of the *C. albicans* γ-TuSC with Spc98 lacking its insertion.
c) Representative image from the negative stain EM of the *C. albicans* γ-TuSC with γ-tubulin lacking its insertion. Five representative particles are shown in zoom and depicted by black rectangles per each panel. Scale bars, 50 nm (images) and 20 nm (particles).
Data in this figure were produced in a joint effort with Dr. Annett Neuner.
Figure was modified from Zupa *et al*., 2020[216].

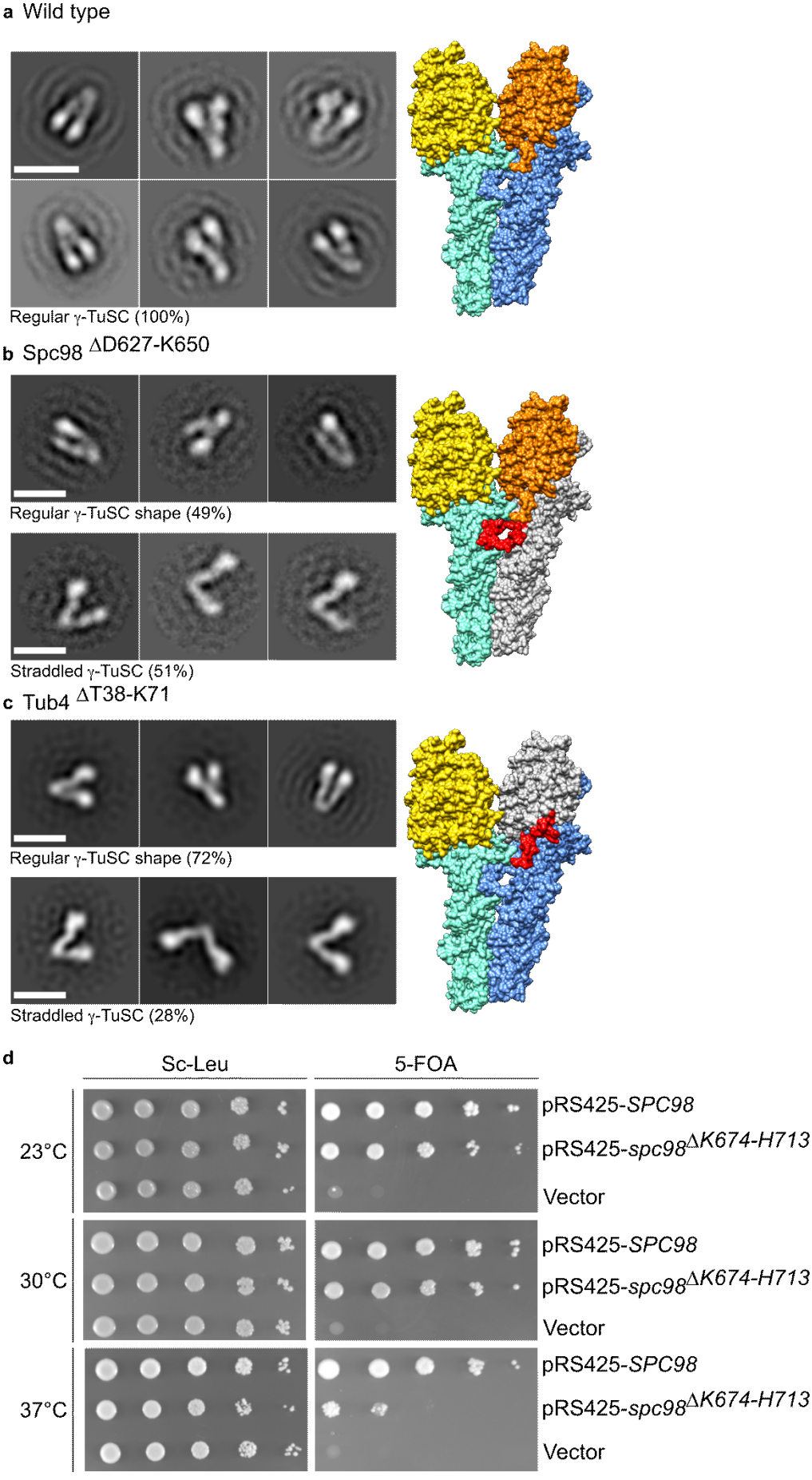

Figure 17: The Role of the extended interface in the structure and function of the γ-TuSC.

a-c) Negative stain EM analysis of the wild-type γ-TuSC, the Spc98$^{\Delta D627\text{-}K650}$ γ-TuSC mutant version and the Tub4$^{\Delta T38\text{-}K71}$ γ-TuSC mutant version. Representative classes are shown. Scale bars, 20 nm.
a) The wild-type γ-TuSC represented by a regular Y-shape of the γ-TuSC in all selected particles. Model of the γ-TuSC in surface representation shown on the right. γ-tubulins coloured in gold and orange, Spc97 coloured in aquamarine and Spc98 coloured in blue.
b) The Spc98$^{\Delta D627\text{-}K650}$ γ-TuSC mutant version represented by a regular Y-shape and a straddled shape with the ratio of the particles 49% to 51%, respectively. Model of the γ-TuSC in surface representation shown on the right. Deleted region is coloured in red and mutated protein in grey.
c) The Tub4$^{\Delta T38\text{-}K71}$ γ-TuSC mutant version represented by a regular Y-shape and a straddled shape with the ratio of the particles 72% to 28%, respectively. Model of the γ-TuSC in surface representation shown on the right. Deleted region is coloured in red and mutated protein in grey.
d Viability assay of the *S. cerevisiae* cells transformed with plasmid containing Spc98$^{\Delta K674\text{-}H713}$. Different dilutions at 3 different temperatures on Sc-Leu and 5-FOA plates. Data in panel (**d**) were produced by Anjun Zheng.
Figure was modified from Zupa *et al*., 2020[216].

The extended interface thus defines the conformation of the γ-TuSC spokes but it was not clear if such increased conformational plasticity would reflect in perturbed MT nucleation function of the γ-TuSC. To measure MT nucleation activity of the mutant complexes, Anjun Zheng used *S. cerevisiae* as a highly similar model organism and as an alternative to *C. albicans*, which is a pathogenic organism and laboratory work with such organism is allowed only under S2 conditions. The *S. cerevisiae* γ-TuSC contains a similar Spc98 insertion as *C. albicans*, which is the main contributor in defining the γ-TuSC shape, but it is missing the Spc97 and the γ-tubulin insertions (Fig. 17a-c). Based on the sequence alignment with *C. albicans* Spc98, I identified the *S. cerevisiae* Spc98 insertion to be represented by the residue range K674-H713. This assignment was later supported by the cryo-EM analysis of the *S. cerevisiae* γ-TuSC[222]. To test the importance of the Spc98 insertion *in vivo*, the *S. cerevisiae* cells missing the SPC98 gene were recombinantly supplied with LEU-2 based plasmids, performed by Anjun Zheng, either encoding for the Spc98 wild-type or for the Spc98$^{(\Delta K674\text{-}H713)}$. Anjun Zheng selected cells missing the SPC98 gene on 5-FOA plates (Fig. 17d). Negative control cells with plasmid missing the SPC98 gene did not grow at any temperature confirming efficient selection of cells on 5-FOA plates (Fig. 17d). Cells expressing the Spc98 wild-type grew at all temperatures while cells expressing the Spc98$^{(\Delta K674\text{-}H713)}$ grew at 23℃ and 30℃ but the growth rate was significantly perturbed at 37℃, suggesting impaired MT nucleation at higher temperatures (Fig. 17d). Inefficient MT nucleation is likely a result of the spoke flexibility in the γ-TuSC due to the missing Spc98 insertion creating the extended interface, hampering functionality of the γ-TuSC as a MT nucleation template. Additionally, MT nucleation ability and the formation of spindles were tested by Anjun Zheng for the γ-TuSC mutant variants in *S. cerevisiae* using expression of GFP labelled tubulin and mCherry labelled Spc42, a component of the SPB. Cells expressing the Spc98$^{(\Delta K674\text{-}H713)}$ at 37℃ formed defective monopolar or multipolar spindles while cells expressing the wild-type Spc98 at 37℃ formed bipolar spindles (Fig. 18a, b), which indicated defective spindle organisation when Spc98 is missing the insertion and the extended interface is perturbed.

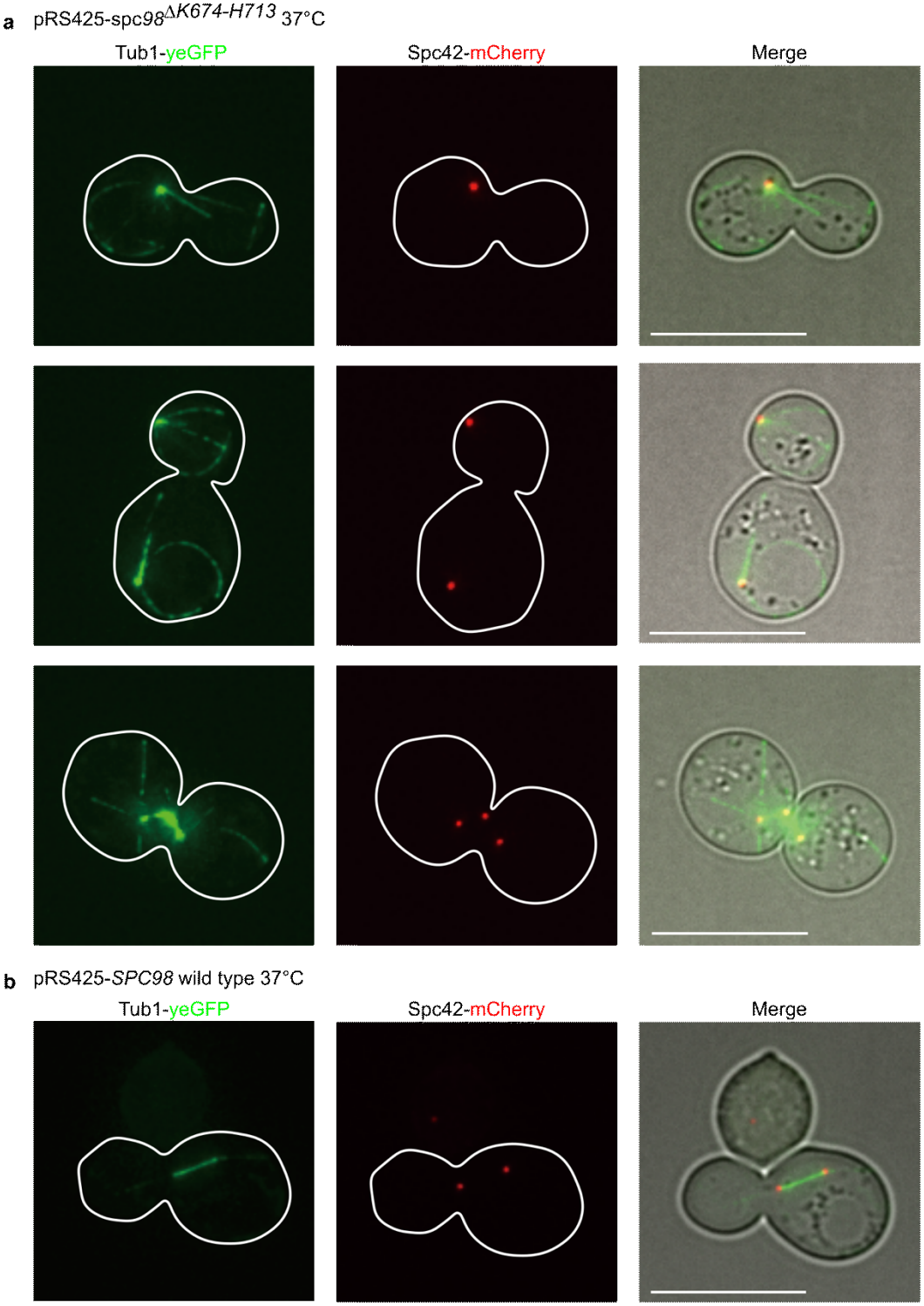

Figure 18: Impact of the Spc98 insertion on the cell viability and mitosis.
a) Fluorescence microscopy of the *S. cerevisiae* cells transformed with a vector containing SPC98 with the deleted insertion. α-tubulin was labeled with eGFP and Spc42 was labeled with mCherry. Merged images showed defective MTs and multiple SPBs during mitosis.
b) Fluorescence microscopy of the *S. cerevisiae* cells transformed with a vector containing SPC98 wild-type. No defects during mitosis were observed.
All experiments and analyses in this figure were performed by Anjun Zheng.
Figure was modified from Zupa *et al.*, 2020[216].

3.1.5 The *C. albicans* extended interface is replaced by the electrostatic γ-tubulin interface in other eukaryotes

The strong impact of the extended interface on the conformation and MT nucleation activity of the fungal γ-TuSC let me wonder if an alternative interface would play a similar role in other eukaryotes. Thus, I decided to analyse the exposed surface area of the human γ-TuSC units integrated in the γ-TuRC, aiming to identify an additional interface besides the interaction of the GRIP1 domains. Surfaces of GCP2 and GCP3 did not indicate any additional interface but surface analysis of γ-tubulins revealed oppositely charged patches on the neighbouring γ-tubulins (Fig. 19a) that are not conserved in fungal γ-tubulins. Furthermore, I noticed that γ-tubulins in the vertebrate γ-TuRC are in the proximity of each other compared to fungal γ-tubulins in the γ-TuSC, which are further away (Fig. 19a). Next, I aimed to analyse whether charged residues of γ-tubulins are a general feature of other eukaryotes or specific only for vertebrates. Systematic comparison of protein sequences for organisms across evolution revealed that the charged residues forming the interface between γ-tubulins in vertebrates are present in all eukaryotes, except for one specific class of fungi (*Saccharomycetes)*, which conversely all encoded for the Spc98 insertion (Fig. 19b, c). This indicated that the γ-tubulin interface has a similar stabilising role as the Spc98 insertion. Furthermore, when I blasted sequences of the γ-TuRC specific GCP proteins (GCP4,5,6) in different organisms, all organisms possessed these proteins except for fungi from class of *Saccharomycetes* (Fig. 20). This means that organisms with the extended interface between γ-tubulins possess a more complex MT nucleation system, the γ-TuRC. Evolutionary relationship of the analysed organisms indicates that the γ-TuSC system in *Saccharomycetes* likely evolved from the γ-TuRC by simplification of their genome (rather than the other way around), accompanied by replacement of the inter-γ-tubulin interface by the insertion-based extended interface of the GRIP2 domains.

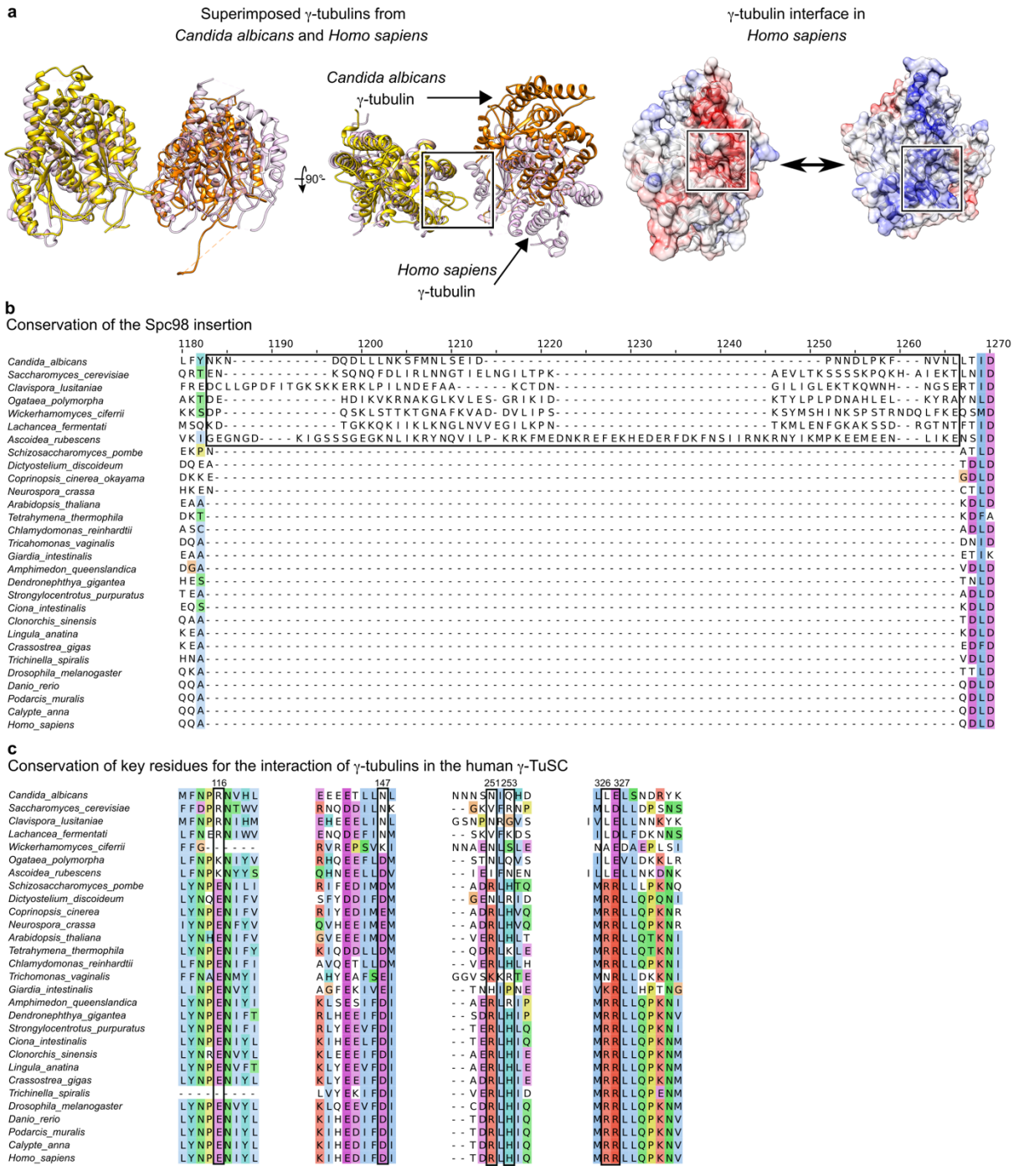

Figure 19: The γ-tubulin interface present in the human γ-TuRC may replace the role of the Spc98 insertion in the γ-TuSC of other eukaryotes.
a) Superposition of γ-tubulins of the *C. albicans* γ-TuSC (yellow, orange) and the human γ-TuSC (pink). The interface area is indicated by black rectangle. The Interface is formed by oppositely charged residue patches that are indicated by black rectangles.
b) Sequence alignment of the region for the Spc98 (GCP3) insertion between different organisms showing that this insertion is present only in some fungi and missing in other eukaryotes.
c) Cutouts of the regions from the γ-tubulin sequence alignment between different organisms with indicated charged residues forming the γ-tubulin interface.
Figure was modified from Zupa *et al.*, 2020[216].

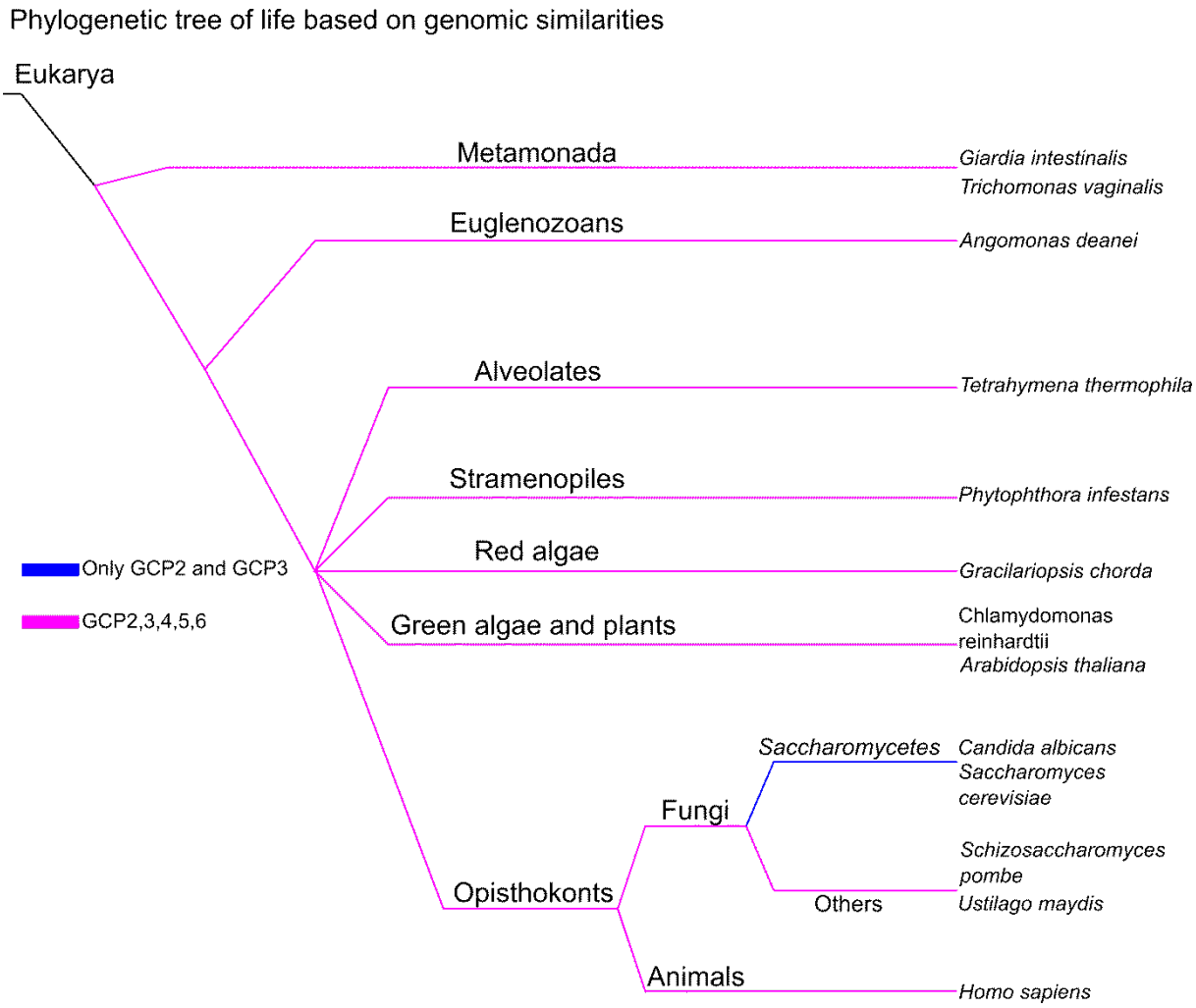

Figure 20: Presence of the γ-TuRC components across eukaryotic organisms at different evolutionary state.
Colour coding for the presence of the γ-TuRC components is given. Fungi encoding only for Spc97 (GCP2) and Spc98 (GCP3) are from class *Saccharomycetes*.
Figure was modified from Zupa *et al.*, 2020[216].

3.1.6 The isolated fungal γ-TuSC in a heterotetrameric form assumes a conformation incompatible with an ideal MT lattice.

Comparison of γ-tubulins between the *C. albicans* γ-TuSC and the vertebrate γ-TuSC unit integrated in the γ-TuRC showed that their relative positions differ in these complexes. As MT nucleation templates, γ-TuCs are thought to reflect or at least be very similar to the MT helical geometry in the positioning of γ-tubulins by the GRIP2 domains. The *S. cerevisiae* γ-TuSC assembles into a higher oligomer of a ring-like shape with seven γ-TuSC units, mimicking the MT shape[157]. I therefore decided to investigate whether the 'isolated' γ-TuSC unit requires conformational rearrangements to reach the MT helical geometry. Using available models of the vertebrate γ-TuRC[220], the *C. albicans* γ-TuSC and the cryo-EM reconstructions of the *S. cerevisiae* ring-like γ-TuSC oligomer in the open conformation[223] , and *S. cerevisiae* ring-like γ-TuSC oligomer in the closed conformation[223], I compared the arrangement of Spc (GCP) proteins and associated γ-tubulins. The γ-TuSC units were firstly superposed according to Spc97 (GCP2) and then R.M.S.D. of the protein backbone was calculated (Table 2) for components of the γ-TuSC. The displacement of residues between structures was also visualised in a vector representation for relevant conformational changes.

First, I compared the model of the *C. albicans* γ-TuSC with the structure of the *S. cerevisiae* γ-TuSC in open conformation, which is not matching the MT helical geometry. These two atomic models revealed high similarity in their protein backbone resulting in low R.M.S.D. values for all components of the γ-TuSC (Table 2). In contrast, comparison of the *C. albicans* γ-TuSC with the *S. cerevisiae* γ-TuSC in closed MT-like conformation showed bigger differences. While the GRIP1 domains were only minimally displaced (Fig. 21a), high R.M.S.D. values were measured for the Spc98 GRIP2 domain and both γ-tubulins (Table 2). Considering that the *S. cerevisiae* γ-TuSC in the closed conformation perfectly mimics the helical MT geometry[156,223], a strong displacement indicated extensive conformational changes required for the *C. albicans* γ-TuSC to reach a MT-compatible geometry and to become an ideal structural template for MT nucleation. The required conformational change can be described as a displacement of the Spc98-associated γ-tubulin towards the helical axis defined by the γ-TuSC ring-like oligomer and this rearrangement at the same time brings both γ-tubulins closer to each other (Fig. 21a). Moreover, the corresponding conformational change would require rearrangements in the extended interface to avoid clashing of protein backbones. When comparing the *S. cerevisiae* γ-TuSC in the closed conformation with the human γ-TuSC unit in the γ-TuRC, measured R.M.S.D. values revealed higher similarity (Table 2). Nevertheless, γ-tubulins of the human γ-TuSC unit require a small conformational change, which surprisingly would bring them further apart in order to mimic MT geometry (Fig. 21b). This indicated that the human γ-TuSC requires an opposite movement of γ-tubulins compared to γ-tubulins of the *C. albicans* γ-TuSC where both γ-tubulins are brought closer to each other. Thus, while the γ-TuRC-specific GCP4,5,6 subunits are main contributors to an asymmetry in the γ-TuRC (see chapter 3.2.4.), GCP2 and GCP3 of the γ-TuSC units also require small conformational rearrangements.

Table 2: R.M.S.D. between the γ-TuSC components in different conformations.

	Homo Sapiens: *S. cerevisiae* in 'closed' conformation	*Candida albicans*: *S. cerevisiae* in 'closed' conformation	*Candida albicans*: *S. cerevisiae* in 'open' conformation
Spc97 GRIP1	4.088	3.262	2.661
Spc98 GRIP1	2.447	1.483	2.716
Spc97 GRIP2	7.310	5.579	5.872
Spc98 GRIP2	7.784	13.692	7.234
Spc97 γ-tubulin	2.934	1.432	3.728
Spc97 γ-tubulin	7.199	18.591	4.490

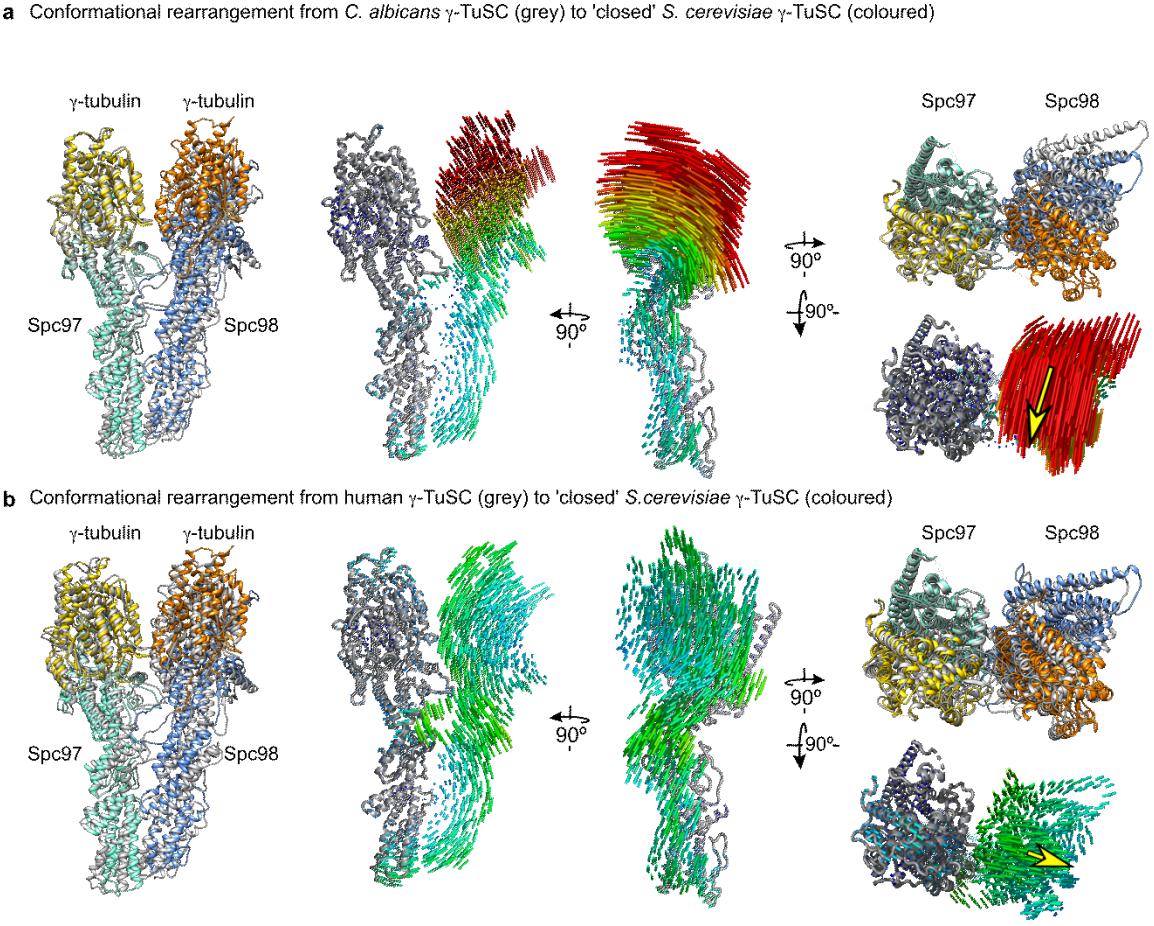

Figure 21: The *C. albicans* γ-TuSC requires a conformational rearrangement to mimic the position of tubulins in the MT lattice.
a) The conformational rearrangement of the *C. albicans* γ-TuSC. Superposition of the *C. albicans* γ-TuSC (grey) with the *S. cerevisiae* γ-TuSC (coloured). Vector representation coloured according to R.M.S.D. in three different views. Yellow arrow is indicating the conformational rearrangement of γ-tubulin to mimic the position of tubulins in the MT lattice.
b) Conformational rearrangement of the human γ-TuSC unit. Superposition of the human γ-TuSC (grey) with the *S. cerevisiae* γ-TuSC (coloured). Vector representation coloured according to R.M.S.D. in three different views. Yellow arrow is indicating the conformational rearrangement of γ-tubulin to mimic the position of tubulins in the MT lattice.
Figure was modified from Zupa *et al.*, 2020[216].

In conclusion, cryo-EM analysis of the *C. albicans* γ-TuSC allowed me comprehensively compare the structures and conformational states of the fungal γ-TuSC and vertebrate γ-TuRC. I identified a common interface for both complexes between the GRIP1 domains. Besides that, I identified the extended interface specific to the fungal γ-TuSC but missing in the vertebrate γ-TuRC where it is replaced by an extended interface between γ-tubulins. Analysing the presence of the γ-TuRC-specific GCPs in different organisms, I demonstrated that γ-TuSC in *Saccharomycetes* evolved by simplification of the γ-TuRC, likely losing genes encoding for GCP4,5,6. Investigating the precise position of γ-tubulins in the fungal γ-TuSC, I showed extensive conformational rearrangements required for the *C. albicans* γ-TuSC to reach a MT-compatible geometry.

3.2 Elucidating the structure and function of the γ-TuRC

Results presented in this chapter were published in Nature with me as a co-first author[219].

3.2.1 Elucidating the molecular architecture of the γ-TuRC

Components of the γ-TuRC including γ-tubulin and GCP2,3,4,5 and GCP6 have been identified for years but their arrangement in the complex remained for a long time a mystery. Low-resolution electron tomography data combined with negative stain EM data over the years at least revealed a helical shape of the complex[177]. Biochemical data suggested the presence of 4-5 copies of the γ-TuRC specific GCP4,5,6 subunits [175]. However, the molecular architecture, the order of GCPs in the γ-TuRC and geometry of the complex remained unknown for almost 20 years. Therefore, I aimed to characterise the architecture and composition of the vertebrate γ-TuRC using cryo-EM SPA. Sample of the γ-TuRC for cryo-EM was purified by Dr. Peng Liu from *Xenopus laevis* meiotic egg extract supplied by Dr. Oliver Gruss. A one-step purification was performed via an affinity chromatography using γ-tubulin antibody beads (Fig. 22a). The purified sample of the γ-TuRC was analysed by several methods performed by Dr. Peng Liu. Activity of the purified γ-TuRC was measured by an *in vitro* MT nucleation assay where MTs were visualised using fluorescence microscopy and the number of MTs per image counted (Fig. 22b). The composition of the complex was analysed by SDS-PAGE and immunoblotting (Fig. 22c, d), demonstrating that all GCPs identified in previous studies are present in the eluted sample but also revealing the presence of the γ-TuRC binding partner, NEDD1 (Fig. 22c). The molecular weight of the γ-TuRC was verified by a sucrose gradient centrifugation, which resulted in γ-tubulin bands in the same fractions as observed in previous studies of the γ-TuRC[127,175] (Fig. 22e). Initial structural insights into the shape of the purified γ-TuRC were provided from a negative stain EM analysis by Dr. Annett Neuner and Dr. Dirk Flemming. 2D class averages showed a ring-like shape of the γ-TuRC with fourteen visible spokes (Fig. 22f-h), which was in agreement with previous negative stain EM analysis of the γ-TuRC[193]. Next, Dr. Peng Liu and I decided to assess the stoichiometry of GCPs in the γ-TuRC by the label-free quantification mass spectrometry performed by Dr. Thomas Ruppert. The γ-TuRC was previously shown to be assembled from five different GCP paralogs, which indicates that one or more of the GCPs must be present in several copies. Stoichiometry of all components was normalised to 14 γ-tubulins that were expected to be present in the γ-TuRC. The mass spectrometry LFQ analysis revealed 5 copies of GCP2 and GCP3, 2-3 copies of GCP4 and 1 copy of GCP5 and GCP6 with an overall stoichiometry of GCPs 5:5:2/3:1:1, respectively (Fig. 23a). Moreover, the mass spectrometry analysis indicated the presence of the γ-TuRC binding partners, such as NEDD1 and NME7 in one or two copies per the γ-TuRC (Fig. 23a).

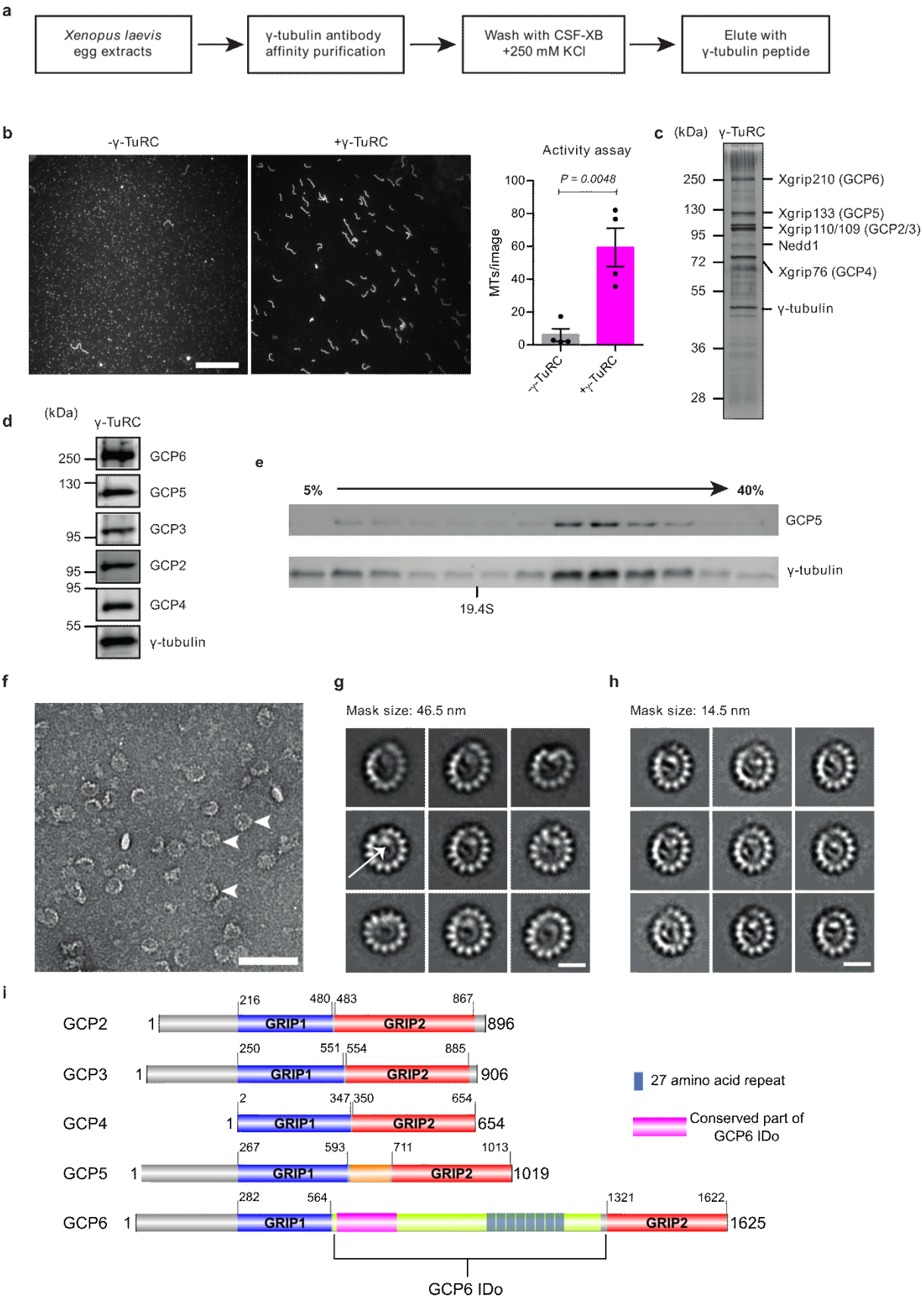

Figure 22: Biochemical characterisation of the *Xenopus laevis* γ-TuRC.
a) Purification scheme for the γ-TuRC. All steps are given.
b) Microtubule nucleation activity assay. Two representative images from a light microscopy at two conditions- with and without the γ-TuRC. Scale bar, 10 µm. Right, quantification of MTs from all acquired images at both conditions represented as mean + s.d. *P* value is given.

c) Silver stained SDS-PAGE of the eluted γ-TuRC from an affinity-based purification. Molecular weights and protein names are given.
d) Immunoblotting of the eluted γ-TuRC from an affinity-based purification. Molecular weights and protein names are given.
e) Immunoblotting of sucrose gradient centrifugation of the γ-TuRC. Gradient is given. The γ-TuRC presence was verified by GCP5 and γ-tubulin antibodies.
f) Zoom on a representative image from negative stain EM data of the purified γ-TuRC. Scale bar, 100 nm. Picked particles are indicated by white arrowheads.
g, h) Representative class averages of the γ-TuRC from negative stain EM data. The number of particles and mask diameter are given. Contrast in the γ-TuRC lumen is indicated by white arrow. Scale bars, 20 nm.
i) Domain representation of GCPs. The GRIP1 and GRIP2 domains with residue ranges are labeled in blue and red, respectively. The GCP6 insertion domain (IDo) is labeled including its specific components-29 amino acid repeats and its conserved part. N and C-terminal residues are given for each GCP.
Data in panels (**a-e**) were produced by Dr. Peng Liu.
Data in panels (**f-h**) were produced by Dr. Annett Neuner and Dr. Dirk Flemming.
Figure was modified from Liu *et al.*, 2020[219].

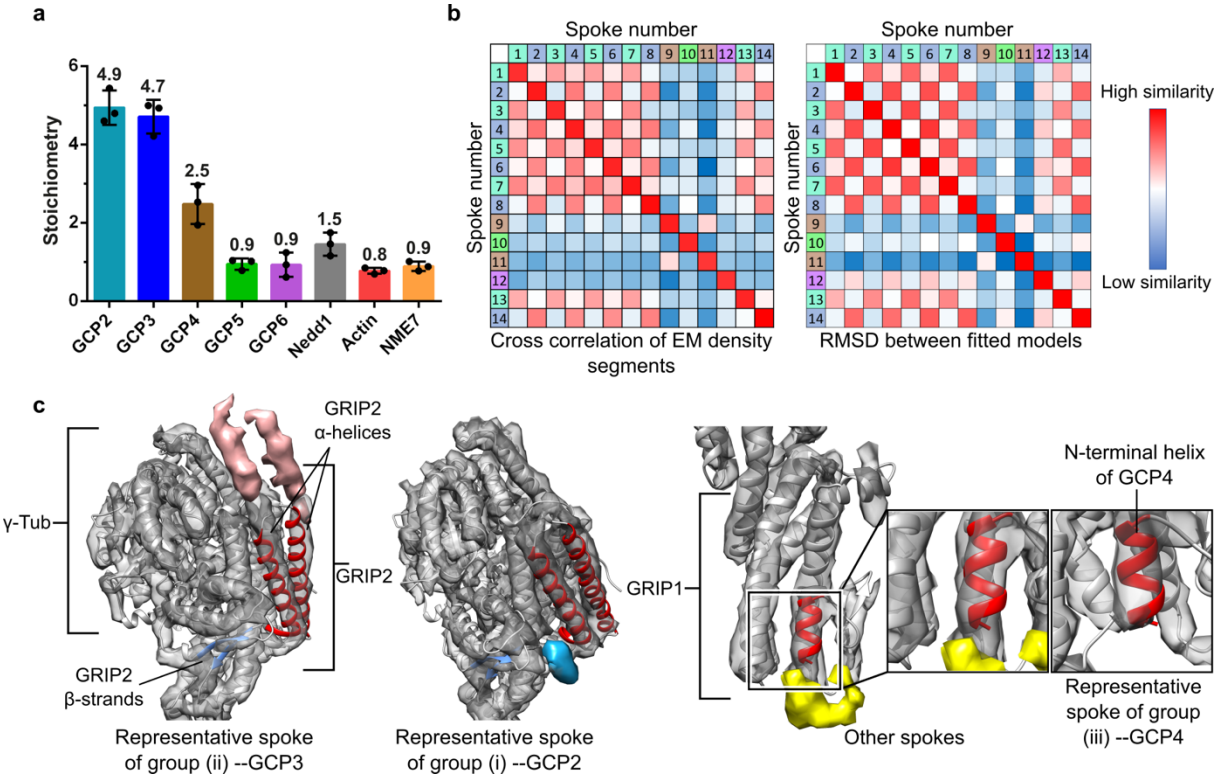

Figure 23: Stoichiometry and structural clustering of the γ-TuRC spokes.
a) Stoichiometry of the γ-TuRC components determined by the LFQ mass spectrometry. Abundance of the γ-TuRC components is normalised to 14 γ-tubulins.
b) Results of two approaches for a structural clustering of the γ-TuRC spokes. Left, results of the cross-correlation measurement between pairs of the spokes. Right, results of the R.M.S.D. measurement between Cα atoms of domain-wise docked atomic models.
c) Left, assignment of GCP3 to cluster (ii) based on the longer C-terminal α-helices of the GRIP2 domains. Specific feature is highlighted by red colour (model and density segment). Assignment of GCP2 to cluster (i) based on a continuous density segment representing a longer loop between two β-strands. Specific feature is highlighted by blue colour (model and density segment). Right, assignment of GCP4 to cluster (iii) based on a missing continuous density segment (yellow density segment) at the N-terminal α-helix (red) of the GRIP1 domains.
Data in panel (**a**) were produced by Dr. Thomas Ruppert and plot prepared by Dr. Peng Liu.
Figure was modified from Liu *et al.*, 2020[219].

Next, the purified γ-TuRC was applied on grids and subjected to cryo-EM analysis. Data were acquired in four individual sessions and using an extended SPA workflow, I reconstructed the vertebrate γ-TuRC (Fig. 24a-d, f). To improve resolution of the initial cryo-EM reconstruction, I segmented the γ-TuRC into smaller components that were aligned and reconstructed individually using multi-body refinement[224], which yielded a global resolution of 4.8 Å and a local resolution ranging from 4.6-6 Å (Fig. 24e, g, h). The cryo-EM reconstruction of the vertebrate γ-TuRC resembled a shape of a left-handed spiral with a height of 25 nm and a diameter of 32 nm, which was very similar to the shape of the *S. cerevisiae* γ-TuSC ring-like oligomer[156]. The γ-TuRC was comprised of fourteen spokes as was indicated already by the negative stain EM data (Fig. 25a). The shape of each spoke was almost identical to the yeast GCP homolog with an associated γ-tubulin from cryo-EM reconstruction of the *S. cerevisiae* γ-TuSC[156] (Fig. 25b). Based on these data, I could conclude that each spoke of the γ-TuRC consists of GCP with an associated γ-tubulin via the GCP GRIP2 domain while the GRIP1 domain is in the lower part of the γ-TuRC forming an interface between the spokes. The domain organisation of GCPs showed an NTE preceding the GRIP1 domain for all GCPs except of GCP4 (Fig. 22i). However, none of the spokes contained larger defined density segments preceding the GRIP1 domains, indicating flexibility of these NTEs (Fig. 25b).

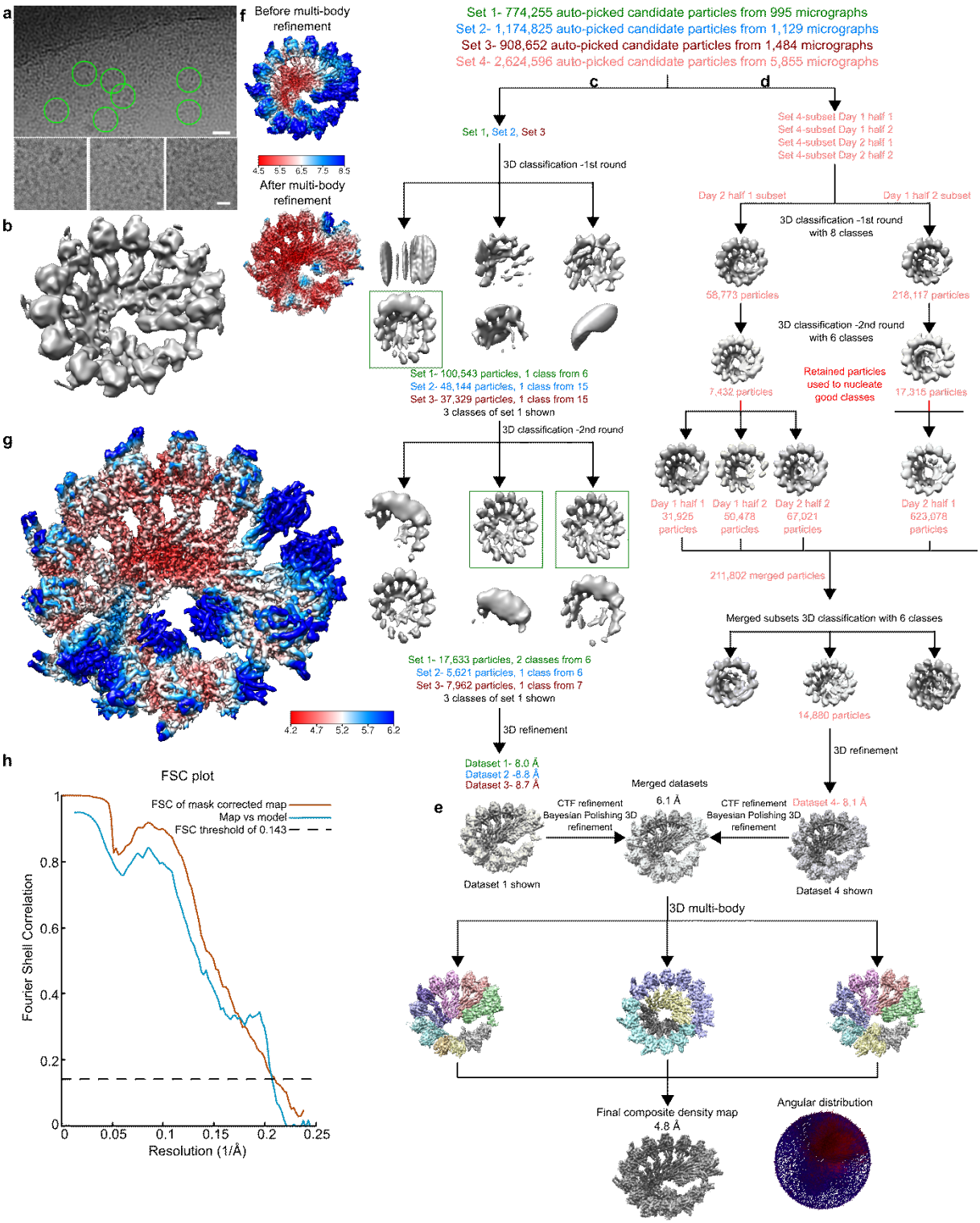

Figure 24: Schematic flowchart of the cryo-EM data processing for the γ-TuRC.
a) Zoom on a representative image from the cryo-EM data of the γ-TuRC with picked particles indicated by green circles. Three representative particles are shown below. Scale bars, 50 nm (image) and 10 nm (particles).
b) *Ab-initio* reconstruction of the γ-TuRC from 3,000 manually selected particles.
c) Four acquired datasets with the indicated number of particles and images. First three datasets were submitted into two rounds of 3D classification. Class averages from dataset 1 are shown and selected averages are indicated by rectangles. Selected particles from the second round of 3D classification were subjected into 3D refinement.
d) Dataset number four was split into 4 subsets. Two subsets with better quality were subjected to two rounds of 3D classification and selected particles from class averages were combined with all four

subsets to yield as high number of particles as possible. Selected particles from all four subsets were combined and subjected into a final round of 3D classification. The best set of particles was afterwards submitted into 3D refinement. Class averages selected for the processing in each step are shown. The number of particles in class averages is given.
e) Particles from all four datasets were subjected to CTF refinement and Bayesian polishing, subsequently combined and subjected into 3D refinement. Obtained reconstruction was split in three different ways to create segments for multi-body refinement. Reconstructed bodies were combined into a final cryo-EM reconstruction. Segments per each multi-body refinement are indicated by different colours. The resolution is given and the angular distribution of the final cryo-EM reconstruction is shown.
f) Cryo-EM reconstruction filtered and coloured according to a local resolution before and after multi-body refinement. Resolution scale is given.
g) Final reconstruction filtered and coloured according to a local resolution. Resolution scale is given.
h) Fourier Shell Correlation plot. FSC of mask corrected map (purple) and model vs map (green) are shown. FSC gold standard threshold of 0.143 plot as dashed line.
Figure was modified from Liu *et al*., 2020[219].

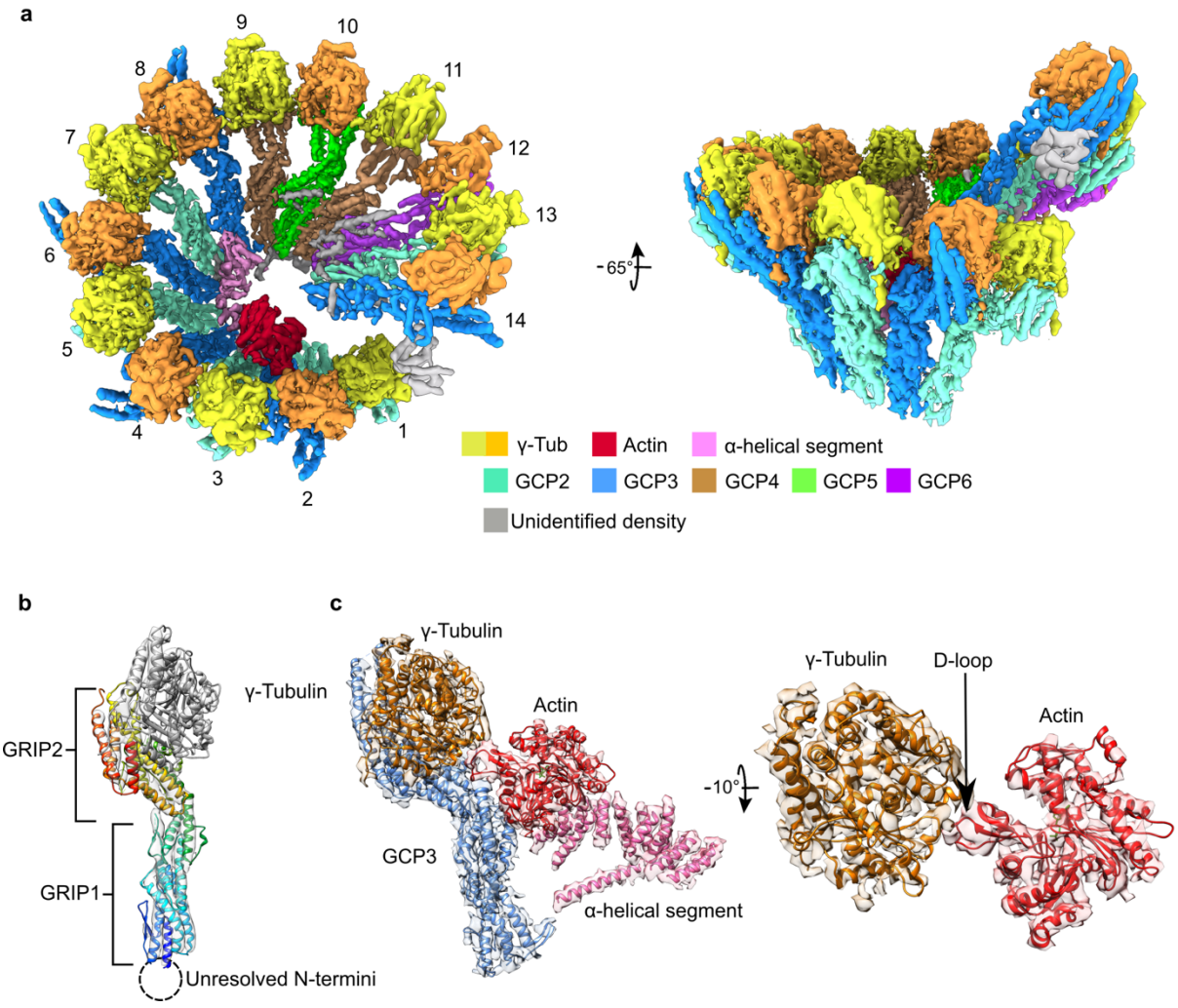

Figure 25: Cryo-EM reconstruction of the γ-TuRC from *Xenopus laevis*.
a) Segmented cryo-EM reconstruction of the *X. laevis* γ-TuRC filtered according to a local resolution. Spoke numbering is given.
b) Organisation of the γ-TuRC spoke- γ-tubulin (grey), GCP2 (rainbow colouring from blue N-terminus to red C-terminus). The GRIP1 and GRIP2 domain are indicated. The unresolved NTE is indicated by dashed circle.
c) Detailed view on the γ-TuRC-incorporated actin binding via two components: γ-tubulin and α-helical segment in the γ-TuRC lumen. Right, detailed view on the D-loop-mediated binding of actin to γ-tubulin.
Figure was modified from Liu *et al*., 2020[219].

In the next step, I started to analyse the γ-TuRC cryo-EM reconstruction in more detail. Mass spectrometry revealed that most GCPs were present in more than one copy, which meant that some of the spokes had to be represented by same GCP, thus to be identical or more similar than others. Thereby, I decided to cluster the spokes based on their similarities. To address similarities between the spokes, I measured two parameters- cross-correlation between the density segments of the spokes (Fig. 26a) and R.M.S.D. between protein backbones of the atomic models representing the spokes (Fig. 26b). I created such atomic models, by combination of the X-ray structure of human GCP4[155] (PDB 3RIP) with γ-tubulin[217] (PDB 1Z5W) and docked them into each spoke as one rigid body. Afterwards, in order to address conformational variabilities specific for each spoke, I docked γ-tubulin, the GRIP2 domain and the GRIP1 domain as separate rigid bodies. Both approaches, cross-correlation and R.M.S.D. measurements clustered the fourteen spokes into five clusters (Fig. 23b, Fig. 26a, b). The first cluster (i) was formed by spokes 1,3,5,7 and 13, the second cluster (iI) was formed by spokes 2,4,6,8 and 14, the third cluster (iii) was formed by spokes 9 and 11, the fourth (iv) and fifth (v) clusters were formed by one unique spoke 10 and 12, respectively (Fig. 23b, Fig. 26a, b). Overall, these clusters recapitulated the stoichiometry determined by mass spectrometry with the ratio of GCPs 5:5:2:1:1 (Fig. 23a). Comparison of the mass spectrometry results with the identified structural clusters of these spokes already indicated that cluster (i) and (ii) could be represented by GCP2 and GCP3, cluster (iii) could be represented by GCP4 and clusters (iv), (v) could be represented by GCP5 and GCP6. To unambiguously assign all GCPs to a specific cluster, I aimed to use structural features, such as the secondary structure elements and bulky amino acid side chains specific to GCPs. Firstly, I focused on distinguishing GCP2 and GCP3 and their assignment to cluster (i) or (ii). I used the secondary structure predictions to identify significant differences on the level of α-helices or β-strands (Fig. 27a, b). One of the most significant differences were two α-helices in the GRIP2 domain being predicted longer for GCP3 compared to the same α-helices in any other GCP (Fig. 27a). I could trace this feature in the density segments of spokes 2,4,6,8 and 14 that formed cluster (ii) when docking the GCP4 atomic model (Fig. 23c and Fig. 26c). This allowed me to assign GCP3 to cluster (ii) and suggested that cluster (i) with five spokes represents GCP2. Investigating the secondary structure predictions, I identified a feature specific for GCP2, which is formed by an extended loop between two β-strands of the GRIP2 domain (Fig. 27b). I indeed could observe this feature in the density segments of cluster (ii), thus assigning GCP2 to this cluster (Fig. 23c and Fig. 26c). Cluster (iii), represented by two spokes was the only one matching with the determined stoichiometry of GCP4. To confirm GCP4 at spoke 9 and 11, I focused on the NTEs missing in GCP4 and present in other GCPs (Fig. 22i). I inspected the cryo-EM reconstruction at the N-terminus of GCP GRIP1 domains and noticed continuous density segments in all spokes except spokes 9 and 11 (Fig. 23c and Fig. 26d), thus assigning GCP4 to cluster (iii) (Fig. 22i).

a Cross correlation of EM density segments

	Spoke 1	Spoke 2	Spoke 3	Spoke 4	Spoke 5	Spoke 6	Spoke 7	Spoke 8	Spoke 9	Spoke 10	Spoke 11	Spoke 12	Spoke 13	Spoke 14
Spoke 1	0.96	0.90	0.92	0.90	0.92	0.90	0.92	0.89	0.87	0.87	0.85	0.87	0.92	0.89
Spoke 2	0.89	0.97	0.88	0.93	0.88	0.93	0.88	0.93	0.83	0.87	0.82	0.88	0.88	0.93
Spoke 3	0.93	0.89	0.96	0.89	0.93	0.89	0.93	0.87	0.87	0.86	0.84	0.87	0.92	0.88
Spoke 4	0.90	0.94	0.89	0.97	0.90	0.94	0.90	0.93	0.85	0.89	0.82	0.88	0.89	0.93
Spoke 5	0.93	0.89	0.93	0.90	0.96	0.90	0.93	0.89	0.88	0.87	0.86	0.88	0.92	0.89
Spoke 6	0.89	0.93	0.89	0.93	0.89	0.96	0.90	0.93	0.84	0.88	0.81	0.88	0.89	0.92
Spoke 7	0.93	0.90	0.93	0.91	0.94	0.91	0.97	0.90	0.88	0.88	0.86	0.88	0.93	0.90
Spoke 8	0.89	0.93	0.88	0.93	0.89	0.93	0.89	0.97	0.85	0.89	0.83	0.88	0.89	0.93
Spoke 9	0.88	0.86	0.89	0.86	0.89	0.87	0.88	0.86	0.96	0.86	0.90	0.86	0.88	0.85
Spoke 10	0.86	0.87	0.86	0.87	0.86	0.88	0.87	0.88	0.84	0.96	0.84	0.87	0.86	0.87
Spoke 11	0.85	0.84	0.86	0.85	0.86	0.85	0.85	0.84	0.90	0.85	0.96	0.86	0.85	0.85
Spoke 12	0.85	0.86	0.86	0.86	0.85	0.86	0.85	0.86	0.82	0.86	0.84	0.96	0.86	0.85
Spoke 13	0.92	0.89	0.92	0.89	0.92	0.90	0.92	0.89	0.87	0.87	0.85	0.88	0.96	0.89
Spoke 14	0.88	0.93	0.88	0.93	0.88	0.93	0.88	0.93	0.83	0.88	0.83	0.88	0.89	0.97

b RMSD between fitted atomic models

	Spoke 1	Spoke 2	Spoke 3	Spoke 4	Spoke 5	Spoke 6	Spoke 7	Spoke 8	Spoke 9	Spoke 10	Spoke 11	Spoke 12	Spoke 13	Spoke 14
Spoke 1	0	1.736	0.756	1.572	0.688	1.551	0.638	1.87	2.588	2.477	3.634	2.138	1.2	1.932
Spoke 2	1.736	0	2.188	0.51	1.899	0.536	1.838	0.626	3.765	1.909	4.729	1.462	1.935	0.712
Spoke 3	0.756	2.188	0	2.008	0.471	1.922	0.591	2.259	2.383	2.639	3.457	2.333	0.946	2.269
Spoke 4	1.572	0.51	2.008	0	1.72	0.366	1.632	0.688	3.656	1.952	4.614	1.378	1.767	0.746
Spoke 5	0.688	1.899	0.471	1.72	0	1.633	0.53	1.953	2.494	2.361	3.6	2.073	0.75	1.951
Spoke 6	1.551	0.536	1.922	0.366	1.633	0	1.565	0.567	3.557	1.727	4.548	1.35	1.602	0.612
Spoke 7	0.638	1.838	0.591	1.632	0.53	1.565	0	1.903	2.715	2.376	3.815	2.046	0.91	1.864
Spoke 8	1.87	0.626	2.259	0.688	1.953	0.567	1.903	0	3.868	1.709	4.879	1.531	1.932	0.622
Spoke 9	2.588	3.765	2.383	3.656	2.494	3.557	2.715	3.868	0	3.928	1.61	3.689	2.781	3.94
Spoke 10	2.477	1.909	2.639	1.952	2.361	1.727	2.376	1.709	3.928	0	5.08	1.892	2.136	1.625
Spoke 11	3.634	4.729	3.457	4.614	3.6	4.548	3.815	4.879	1.61	5.08	0	4.695	3.89	5.007
Spoke 12	2.138	1.462	2.333	1.378	2.073	1.35	2.046	1.531	3.689	1.892	4.695	0	2.06	1.423
Spoke 13	1.2	1.935	0.946	1.767	0.75	1.602	0.91	1.932	2.781	2.136	3.89	2.06	0	1.819
Spoke 14	1.932	0.712	2.269	0.746	1.951	0.612	1.864	0.622	3.94	1.625	5.007	1.423	1.819	0

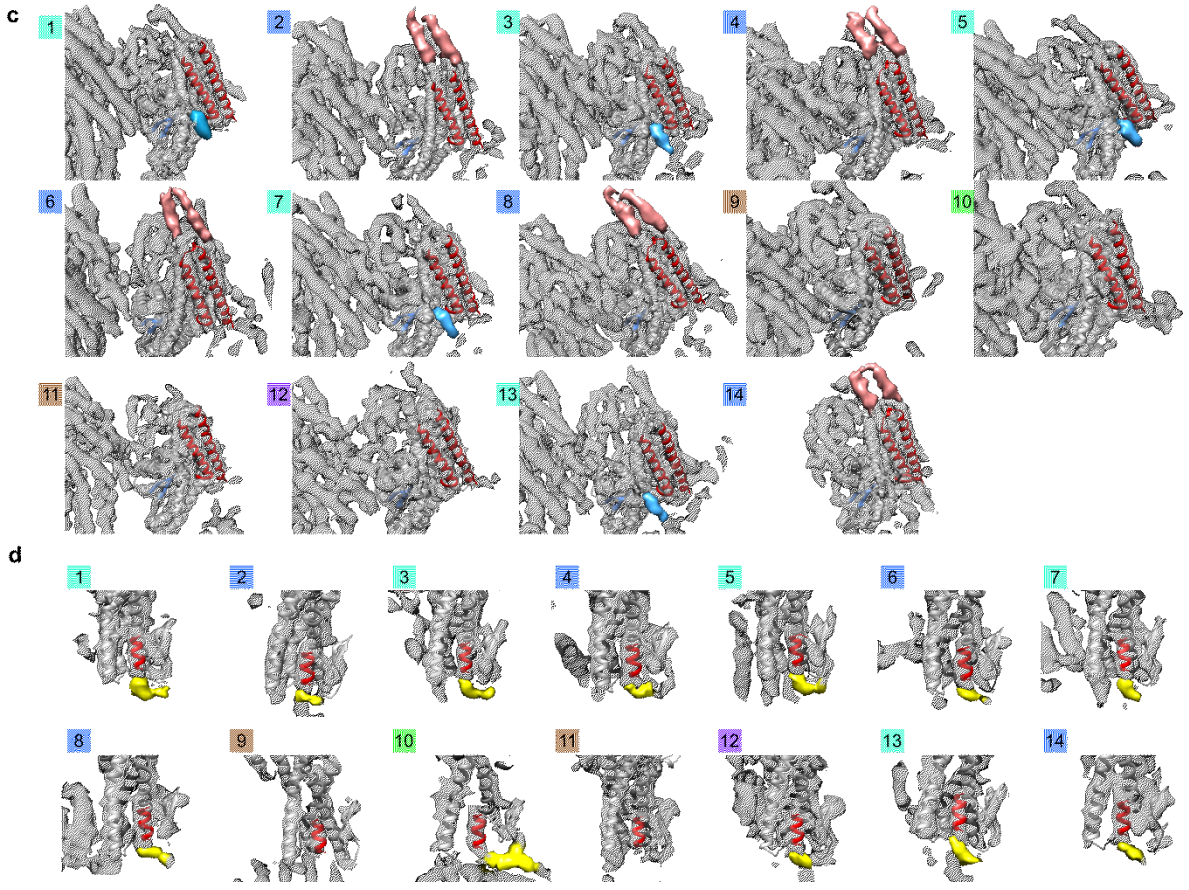

Figure 26: Clustering of the γ-TuRC spokes based on structural features in order to assign GCPs to the specific spokes.
a) Clustering of the spokes according to a pairwise cross-correlation using the density segments of each spoke. Colour scheme from low cross-correlation (blue) to high cross-correlation (red) and cross-correlation values are given.

b) Clustering of the spokes according to R.M.S.D of protein backbones between the atomic models representing one spoke (GCP4 with γ-tubulin). R.M.S.D. values are given and colour scheme is same as in (**a**). Clusters of the spokes are indicated by colour scheme.
c, d) Gallery of the spokes showing specific features for GCP2, GCP3 and GCP4.
c) Gallery of the spokes showing specific features for GCP2 and GCP3. GCP3 spokes feature the longer GRIP2 C-terminal α-helices (red density segment and red α-helices) while GCP2 spokes feature the density extension (blue density segment) between two β-strands (blue) of the GRIP2 domains.
d) Gallery of the spokes showing a specific feature missing in GCP4. All spokes feature the NTE of the GRIP1 domain (yellow density segment) except spokes of GCP4, which does not possess NTEs on the sequence level. The N-terminal helix of GCP4 is coloured in red. Colouring of spoke clusters is indicated. Figure was modified from Liu *et al*., 2020[219].

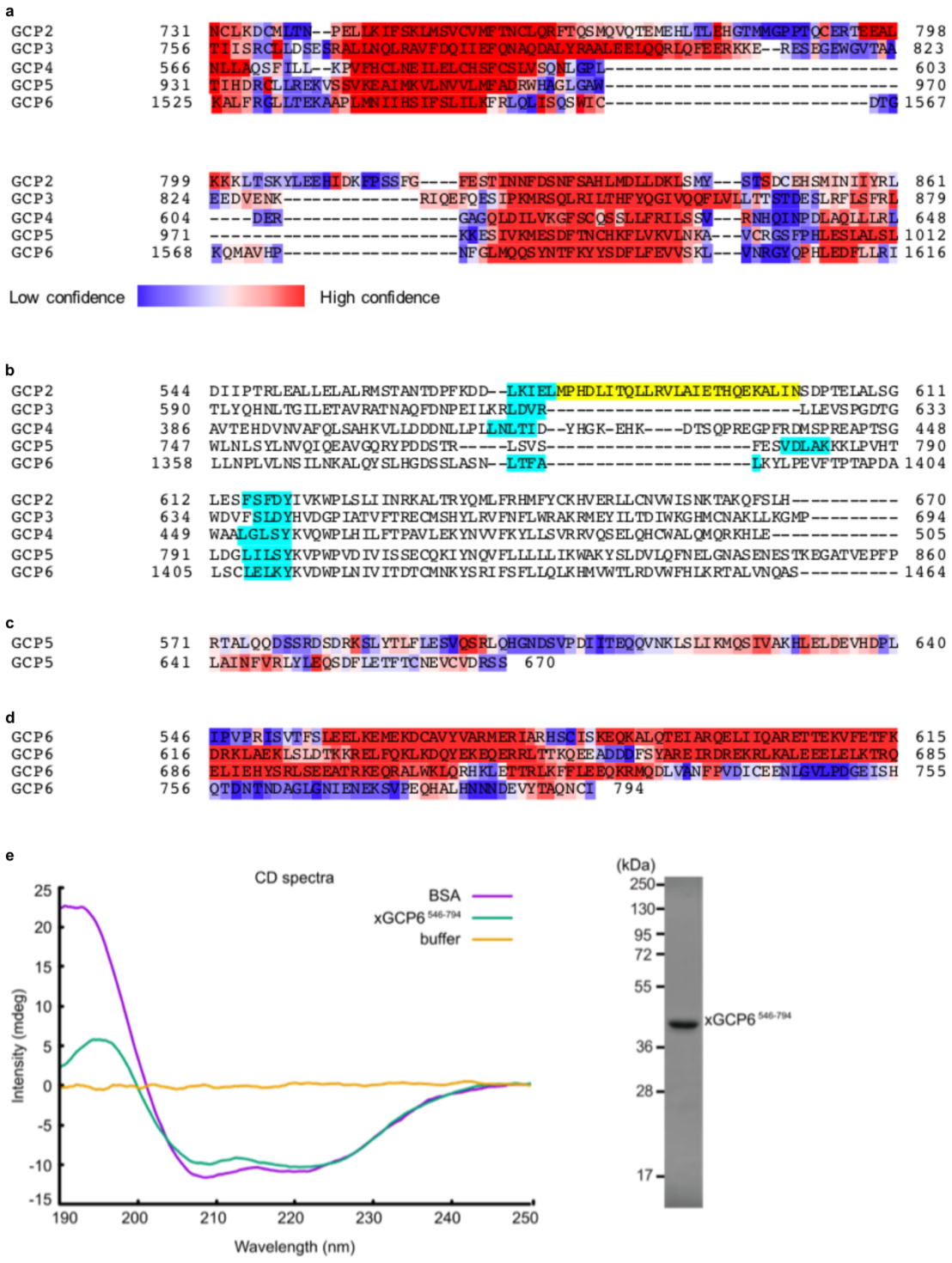

Figure 27: The secondary structure predictions of the GCP-specific features and characterisation of the GCP6 N-terminal segment of the GCP6 IDo.
a) The Secondary structure prediction of a region representing the GCP3-specific feature. Sequence is coloured according to a confidence for α-helical features. Confidence range is given.
b) The secondary structure prediction of a region representing the GCP2-specific feature. Residues of β-strands are labeled in cyan and a linker between two β-strands is coloured in yellow.
c) The secondary structure prediction of a region representing the GCP5 insertion between the GRIP1 and GRIP2 domains. Sequence is coloured same way as in (**a**) and confidence range is as in (**a**) as well.
d) The secondary structure prediction of a region representing the N-terminal part of the GCP6 IDo. Sequence is coloured same way as in (**a**) and confidence range is as in (**a**) as well.
e) Characterisation of secondary structure features for the N-terminal region of the GCP6 IDo by circular dichroism (CD). Left, plot of CD spectra for a buffer, bovine serum albumin (BAS) as a control and the

N-terminal region of the GCP6 IDo. Colour coding for samples is given. Right, SDS PAGE of the GCP6 IDo N-terminal segment showing purity of the sample.
Data in panel (**e**) were produced in a joint effort with Anna Böhler and Dr. Szymon Kmiecik.
Figure was published in Liu *et al*., 2020[219].

Assignment of GCP2,3 and 4 to the specific positions left only spokes 10 and 12 for GCP5 and GCP6. Both GCPs contain longer insertions between the GRIP1 and GRIP2 domain compared to other GCPs (Fig. 22i) but investigation of the GCP5 and GCP6 density segments revealed that these insertions are not resolved, indicating their flexibility or disordered nature. Furthermore, the GRIP1 and GRIP2 domains of GCP5 and GCP6 did not contain any obvious difference in their fold or the secondary structure elements that would allow me assignment of these proteins either to spoke 10 or spoke 12. Therefore, I decided to inspect bulky amino acid side chains of GCP5 and GCP6 resolved in some areas of the spoke 10 and 12 and use them for unambiguous assignment of these two GCPs. I prepared homology models of γ-tubulin and GCPs based on the X-ray structure of human γ-tubulin[217] and GCP4[155]. All models except GCP5 and GCP6 were firstly rigid body docked into the cryo-EM reconstruction based on the previous assignment and afterwards refined accordingly. Next, I validated assignment of GCP2, GCP3 and GCP4 by inspecting their bulky amino acid side chains. Variations in local resolution per spoke allowed me to recognise and fit several bulky amino acid side chains specific for each of these GCPs confirming their previous assignment (Fig. 28). Then, I docked GCP5 and GCP6 homology models to spokes 10 and 12 and located bulky amino acid side chains that matched their density segments in the cryo-EM reconstruction (Fig. 28), which allowed me to unambiguously assign GCP5 to spoke 10 and GCP6 to spoke 12, resulting in the following sequence of GCPs: GCP(2-3)$_4$-GCP4-GCP5-GCP4-GCP6-GCP(2-3) (Fig. 25a). The position of GCP4,5,6 in the centre of the γ-TuRC was surprising, since most of the previous studies suggested the γ-TuRC specific GCPs to be located at the end of the γ-TuRC left-handed spiral[178].

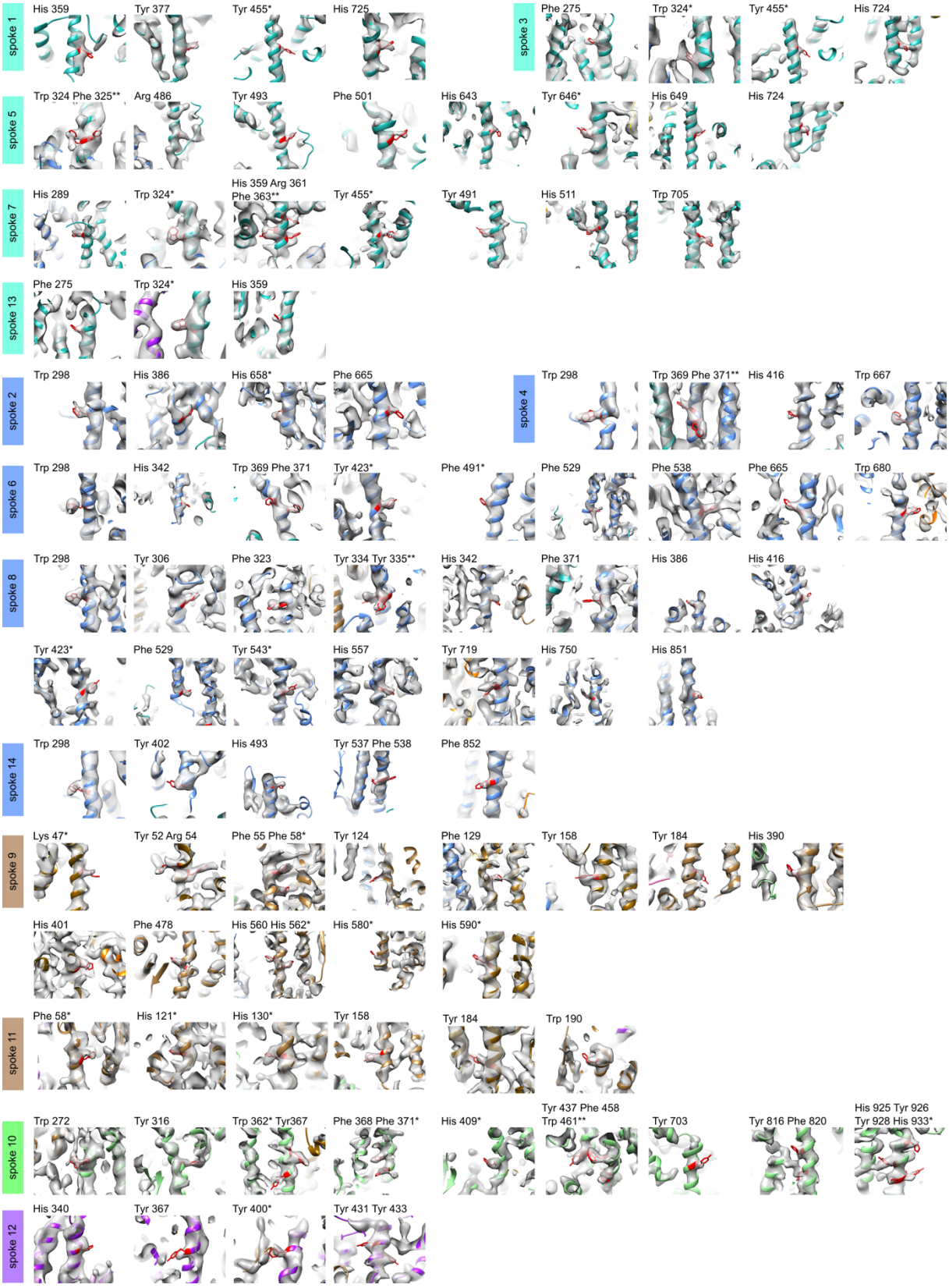

Figure 28: Bulky amino acid side chains used for the assignment of GCPs to individual spokes. Spoke numbers are given and coloured according to clusters. Residue number and name of amino acid are given as well. Bulky amino acid residues used for the assignment are coloured in red while the rest of atomic models is coloured according to clusters.

3.2.2 Actin is an integral component of the γ-TuRC

Fitting GCPs and γ-tubulins into the γ-TuRC reconstruction left some of the density segments unassigned mainly in the lumen of the γ-TuRC. The luminal density segment was represented by two specific parts- one formed by a bundle of α-helices and the other one represented by a globular protein at the tip of the luminal density segment. In order to assign components representing the luminal density segment, I used the list of proteins identified in the γ-TuRC sample by mass spectrometry and performed a structure-guided search that would have allowed me to assign proteins to the luminal density segment. To verify the structure-guided approach, I applied it firstly on γ-tubulin and GCP4 as positive controls and ovalbumin as a negative control (Fig. 29a, b). Afterwards, I focused on components that are direct binding partners of the γ-TuRC, such as NEDD1, NME7 and MZT1. Even though NEDD1 and NME7 were identified by mass spectrometry in the sample, my search did not localise them in the cryo-EM reconstruction (Fig. 29c). Similarly, MZT1 was not localised as well (Fig. 29c). This likely indicates that these γ-TuRC binding partners are not covered by the cryo-EM reconstruction. However, their absence in the cryo-EM reconstruction did not exclude possibility of their binding to some flexible components of GCPs. Tries to localise other proteins from the mass spectrometry list (Table 3) using the structure-guided search resulted in an unexpected assignment of actin to the globular density segment at the tip of the luminal part (Fig. 25a, c and Fig. 29d). At this position, actin connects the rest of the luminal density segment with the GCP3-associated γ-tubulin at spoke 2 ($GCP3_{(2)}$-associated γ-tubulin) of the γ-TuRC (Fig. 25a, c). Interaction of actin with $GCP3_{(2)}$-associated γ-tubulin is mediated via the actin D-loop that represents a canonical interaction site in actin filaments[225] and in the complex of actin with DNaseI[226]. To verify the presence of actin in the γ-TuRC, actin was confirmed by immunoblotting performed by Dr. Peng Liu (Fig. 29e). Moreover, immunofluorescence microscopy performed by Dr. Peng Liu revealed colocalisation of actin with GCP6 (Fig. 29f, g), suggesting a possibility that actin interacts with GCP6. The presence of actin in the lumen of the γ-TuRC raised questions about the role of this γ-TuRC-integrated actin in nucleation of actin filaments. Nucleation of actin filaments was proposed before for centrosomes[227], thus Anna Böhler (RG Schiebel, ZMBH) with Lukas Rohland (RG Mayer, ZMBH) tested nucleation of actin filaments using the purified γ-TuRC sample but they did not observe any nucleation activity indicating that actin inside of the γ-TuRC is inactive or in an incompatible position for a nucleation (Fig. 29h). The role of actin in nucleation of actin filament was excluded but as an integral component of the γ-TuRC, actin can still affect MT nucleation. To test whether actin as a component of the γ-TuRC has an effect on MT nucleation, Dr. Peng Liu performed an actin-inhibition experiment using DNaseI to disturb actin positioning in the γ-TuRC or to even completely remove actin. Incubation of the γ-TuRC with DNaseI led to a significant decrease in the γ-TuRC-mediated MT nucleation activity compared to a positive control of the γ-TuRC (Fig. 29i, j). The effect of the γ-TuRC-integrated actin on MT nucleation was not observed when pre-incubating DNaseI with actin to saturate DNaseI. These results overall confirm that actin is a *bona fide* component of the γ-TuRC, with a role in MT nucleation.

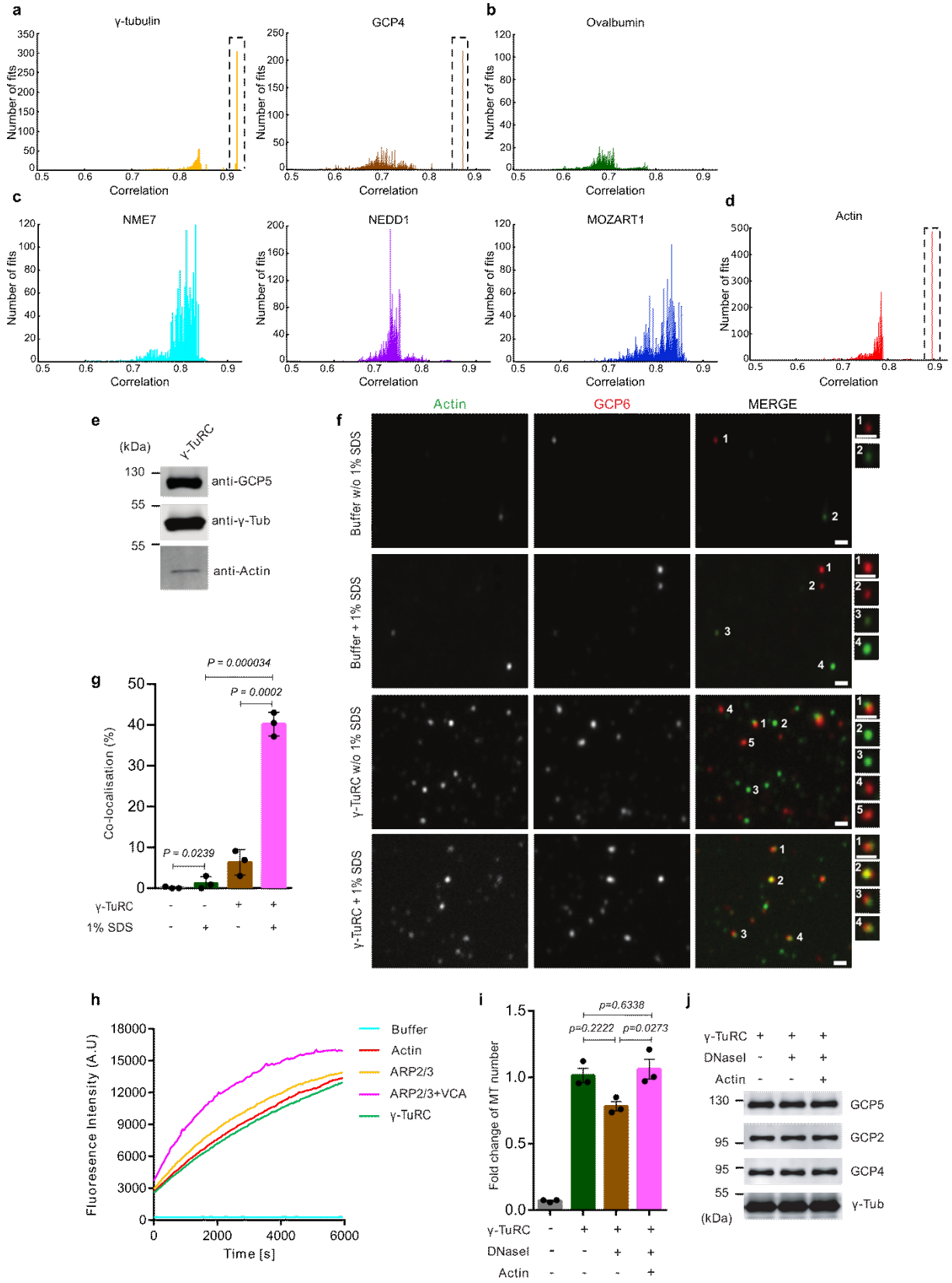

Figure 29: Analysis of the γ-TuRC-incorporated actin.
a-d) The structure-guided approach for the assignment of proteins into the γ-TuRC reconstruction.
a) Positive control of the structure-guided approach using GCP4 and γ-tubulin. Peak represented by high number of fits at high cross-correlation is indicated by dashed line.
b) Negative control of the structure-guided approach using ovalbumin. None of fits reached high cross-correlation.

c) Results of the structure-guided approach for fitting of the γ-TuRC binding partners: NME7, NEDD1, MOZART1. None of these proteins yielded high number of fits at high cross-correlation as in the case of the positive control.
d) Results of the structure-guided approach for fitting of actin. Actin yielded high number of fits at high cross-correlation, which is indicated by dashed line.
e) Immunoblot of the purified γ-TuRC using GCP5, γ-tubulin and actin antibodies confirms the presence of actin. Molecular weights are given.
f, g) Colocalisation assay of GCP6 and actin.
f) Representative images from a fluorescence microscopy with several magnified images. Magnified images are indicated by numbers. Conditions are given.
g) Quantification of colocalisation events normalised to the GCP6 signal. *P* values are given. Addition of 1% SDS increased accessibility of actin.
h) Actin polymerisation assay measuring change of fluorescence over time. Buffer control without a signal. Positive control of Arp2/3-VCA complex essential for binding of monomeric actin resulted in a robust nucleation. The γ-TuRC as the rest of the conditions without VCA showed no nucleation activity.
i) MT nucleation assay testing effect of the γ-TuRC-incorporated actin on MT nucleation. Sample with and without the γ-TuRC as a positive control and a negative control, respectively. Test of actin impact on MT nucleation by incubating the γ-TuRC with DNaseI and with a preformed complex of actin-DNaseI. *P* values are given.
j) Immunoblot of the γ-TuRC sample used for the MT nucleation assay to confirm same amount of the γ-TuRC in each sample.
Data in panels (**e-g**) and (**i, j**) were produced by Dr. Peng Liu.
Data in panel (**h**) were produced by Anna Böhler and Lukas Rohland.
Figure was modified from Liu *et al*., 2020[219].

Table 3: Proteins used for fitting in the structure-guided approach.

UniProt code	Protein name	Template probability	LFQ intensity
A0A1L8H345	dynamin-1	100	8.72E+09
Q8AVE2	Hsc70 protein	100	5.89E+09
A0A1L8FKY3	Hsp70	100	5.5E+09
A0A1L8HW84	tight junction protein ZO-3	100	5.47E+09
Q7ZTN1	tight junction protein ZO-3	100	5.42E+09
A0A1L8GWY3	protein transport protein Sec24a	100	5.26E+09
A0A1L8FW10	insulin-like growth factor 2 mRNA-binding protein 3	99.95	4.34E+09
A0A1L8EKZ2	polyadenylate-binding protein	100	4.32E+09
A0A1L8G1U5	protein transport protein SEC23	100	3.92E+09
A0A1L8ES55	polyadenylate-binding protein	100	3.72E+09
A0A1L8H4P1	CSD_1 domain-containing protein	99.35	3.36E+09
A0A1L8G7U0	protein transport protein SEC23	100	2.75E+09

A0A1L8GRB6	uncharacterized protein	100	2.47E+09
A0A1L8GY92	WD_REPEATS_REGION domain-containing protein	99.96	1.77E+09
A0A1L8HEX9	uncharacterized protein	100	1.67E+09
A0A1L8FA78	heat shock-related 70 kDa protein; signalling protein	100	1.62E+09
A0A1L8F1H5	dynamin-1	100	1.47E+09
A0A1L8HWC1	uncharacterized protein	100	1.45E+09
A0A1L8GMZ9	dynamin-1	100	1.39E+09
Q8AVK9	NSEP1 protein	99.33	1.15E+09
A0A1L8F457	protein transport protein SEC23	100	1.07E+09
A0A1L8FAZ8	protein transport protein SEC23	100	1.01E+09
A0A1L8GWQ5	WD repeats region domain-containing protein	100	8.22E+08
A0A1L8HF79	nucleoside diphosphate kinase 7	99.92	7.27E+08
A0A1L8G3Y8	fragile X mental retardation syndrome-related protein 1	100	7.13E+08
A3KMH8	fragile X mental retardation syndrome-related protein 1	100	7.11E+08
A0A1L8EWC9	interferon-inducible double-stranded RNA-dependent protein kinase activator A	100	6.98E+08
A0A1L8FKW5	serine/threonine-protein kinase TOR	100	6.7E+08
A0A1L8F6I3	HSPA5 protein	100	6.64E+08
A0A1L8GQQ7	uncharacterized protein	100	5.84E+08
A0A1L8HM56	protein transport protein Sec24B	100	5.23E+08
A0A1L8FTJ1	polyadenylate-binding protein	100	4.81E+08
A0A1L8FZR3	polyadenylate-binding protein	100	4.81E+08
A0A1L8EM44	γ-actin	100	4.77E+08

A0A1L8ETE5	uncharacterized protein	100	4.77E+08
A0A1L8HRT0	DZF domain-containing protein	100	4.46E+08
A0A1L8GT63	tight junction protein ZO-1	100	4.42E+08
Q6GMC1	ubiquitin-40S ribosomal protein S27a	100	4.27E+08
A0A1L8G5V1	ubiquitin-like domain-containing protein	100	4.27E+08
A0A1L8HQK4	polyubiquitin-C	100	4.26E+08
Q7SY79	Ubc-prov protein	100	4.26E+08
Q6GQF3	ubiquitin-60S ribosomal protein L40	100	4.26E+08
A0A1L8HX68	ubiquitin-like domain-containing protein	99.94	4.26E+08
A0A1L8HCZ9	uncharacterized protein	100	4.26E+08
A0A1L8H6E1	nucleoside diphosphate kinase 7	99.92	4.13E+08

3.2.3 GCP6 has a role in the assembly of the γ-TuRC

After identification of actin as a component of the γ-TuRC, the highly α-helical segment of the luminal density segment was the only unassigned part (Fig. 25a). Because none of the proteins from the mass spectrometry list produced robust fits to this density segment, I decided to revisit the domain organisation and secondary structure predictions of GCPs. In particular, I explored the secondary structure predictions of previously unassigned parts of GCPs, such as the NTEs and the insertions in GCP5 and GCP6 (Fig. 27c, d). The secondary structure predictions identified a long α-helical segment in the N-terminal part of the 750 amino acid residues-long insertion of GCP6 (Fig. 27d). The length of this N-terminal part of the GCP6 insertion was in good agreement with the length of α-helices built in the luminal density segment. To confirm the α-helical character of the N-terminal part of the GCP6 insertion experimentally, Anna Böhler expressed and purified segment of GCP6- 'GCP6$^{546-794}$' and with help of Dr. Szymon Kmiecik (AG Mayer, ZMBH) analysed the secondary structure of this segment by circular dichroism. Results of circular dichroism confirmed an α-helical character and made it a probable candidate to represent the α-helical density segment in the lumen of the γ-TuRC (Fig. 27e). However, a follow-up research of the γ-TuRC eventually refute this hypothesis, assigning two copies of MZT1 and the NTEs of GCP3 and GCP6 into the the α-helical luminal density segment[228].

Besides interacting directly with actin, the α-helical luminal density segment is in contact with the GRIP1 domains of several GCPs. Based on our assumption that the α-helical luminal density represents the GCP6 insertion domain, Dr. Peng Liu decided to test ability of the GCP6 insertion to interact with the N-terminal domains of GCPs (Fig. 30a). Co-immunoprecipitation performed by Dr. Peng Liu showed stronger binding of the GCP6 insertion (GCP$^{606-1499}$) with the GCP2 and GCP5 N-terminal segments and only weak binding to the GCP3 N-terminal segment. Because the GCP6 insertion is represented by almost 800 amino acid residues (Fig. 30a), Dr. Peng Liu aimed to specify part of the insertion directly responsible for the binding of

the GCP5 and GCP2 N-termini. The GCP6 insertion was divided into three parts-the first one representing the segment preceding a region with the nine repeats, the second one containing the nine repeats and the last one representing the segment after the nine repeats (Fig. 30a). Dr. Peng Liu observed that the only segment interacting with the GCP5 and GCP2 N-termini is the first part of the GCP6 insertion represented by residues 606-1007 (Fig. 30b), including also the α-helical segment. This opens the possibility the N-terminal part of the GCP6 insertion plays a role in the recruitment of GCP5 and GCP2 into the γ-TuRC.

To get better insights into the stability and the assembly mechanism of the γ-TuRC, Dr. Peng Liu performed a salt treatment of the γ-TuRC by washing the sample bound to beads with a high salt buffer. Elution of the residual γ-TuRC from the beads after a harsh salt wash showed that residual components bound to beads were GCP4,5,6 suggesting a stable γ-TuRC core formed by these three GCPs (Fig. 30c). Structural insights into the disassembly of the γ-TuRC were obtained from the eluted sample treated by a mild salt wash (Fig. 30d). Negative stain 2D class averages obtained by Dr. Annett Neuner and Dr. Dirk Flemming (Cryo-EM facility, BZH) revealed that the γ-TuRC started to disassemble from the peripheral spokes of a left-handed spiral always shedding one γ-TuSC unit (GCP2-GCP3 with associated γ-tubulins) (Fig. 30d). Combined with previous data on the GCP6 insertion, Dr. Peng Liu and I came up with a hypothetical assembly mechanism of the γ-TuRC starting from the GCP6 spoke or the GCP6-GCP4 dimer that would recruit the GCP5-GCP4 dimer. In next steps, the stable core would recruit the γ-TuSC units (Fig.30e). The assembly of the γ-TuRC from the individual GCP dimers would be supported by a distance measurement of γ-tubulins between spokes showing a shorter distance between the aforementioned dimers compared to inter-dimer distances in the γ-TuRC (Fig. 30f, g). Additionally, the existence of γ-TuSC unit would be in agreement with the heterotetrameric γ-TuSC of *S. cerevisiae*[153].

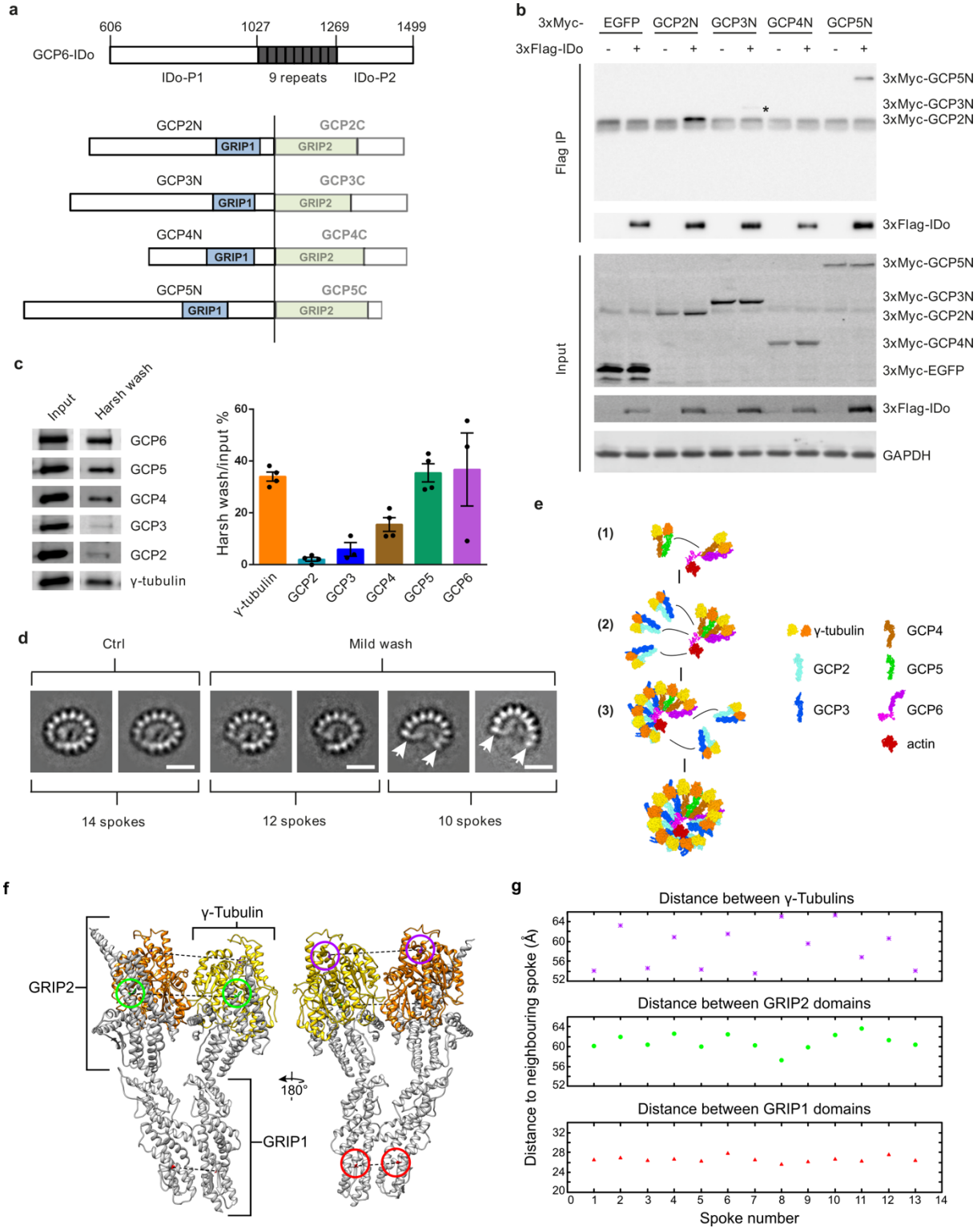

Figure 30: The role of the GCP6 insertion domain in an recruitment of other GCPs.
a) Trimmed GCPs used for immunoprecipitation. Insertion domain (IDo).
b) Co-IP of the N-terminally Flag-tagged GCP6 IDo with the Myc-tagged N-terminal segments of other GCPs. Negative control was performed using the Myc-tagged eGFP. Band of the Myc-tagged GCP3 N-terminal segment is marked by asterisk. Positions of different proteins used in Co-IP are indicated on the right side next to the gel.
c) Analysis of the high-salt treated γ-TuRCs that were eluted after harsh wash and subsequently immunoblotted. Right, plot of quantified signals from immunoblots.
d) Negative stain EM of the mild-salt treated γ-TuRCs. 2D class averages from negative stain EM analysis are shown. Positions of missing spokes are indicated by white arrows. Scale bars, 20 nm.

e) Hypothetical stepwise assembly mechanism of the γ-TuRC. (1) Assembly of the GCP4-GCP5 dimer and the GCP4-GCP6 dimer into the 4-spoked intermediate of GCP4-5-4-6. (2) Extension of the 4-spoked intermediate by three dimers of γ-TuSC units that would be recruited via the GCP6 IDo binding to the GCP2 N-terminal part. The 10-spoked intermediate would be in the last step extended on both peripheral spokes by γ-TuSC units.
f) Indication of residues used to measure distances between neighbouring spokes. Defined points are represented by Cα atoms of conserved amino acid residues. One point is present in γ-tubulin and represented by Asn187 (magenta), the second point is present in the GRIP1 domain and represented by Ala266-Gly297 (red) and the third point is present in the GRIP2 domain represented by Phe757-Phe784 (green).
g) Plots of distances between selected residues of neighbouring spokes in the γ-TuRC. Same colouring as in (**f**).
Data in panels (**a-c**) were produced by Dr. Peng Liu.
Data in panel (**d**) were produced by Dr. Peng Liu, Dr. Annett Neuner and Dr. Dirk Flemming.
Figure was modified from Liu *et al*., 2020[219].

3.2.4 The isolated γ-TuRC does not assume helical symmetry

The vertebrate γ-TuRC is a part of a complex machinery *in vivo* where it is anchored to the PCM during mitosis and interacting with other factors, such as Cdk5Rap2, TPX2 and ch-TOG that increase MT nucleation activity in a regulated manner[79,175,193]. It was shown that the γ-TuSC ring-like oligomer in *S. cerevisiae* in its active form mimics the geometry of MT, thus likely acting as a structural template for MT nucleation[156]. However, it was not clear if the assembled γ-TuRC reflects MT geometry or needs its binding partners that, besides having a functional role, may have a structural role in altering the γ-TuRC geometry. Thus, I aimed to investigate the geometry of the γ-TuRC, in particular positioning of the 14 γ-tubulin subunits. Because the γ-TuRC is a left-handed spiral, I first approximated the helical axis to determine local helical parameters as the pitch increment and radius (Fig. 31a). Measuring the distance of γ-tubulins from the helical axis and the pitch increment, I observed that both parameters deviated from MT geometry (Fig. 31b, c). The biggest deviations were observed for the last four spokes of the γ-TuRC (Fig. 31b c). The positions of γ-tubulins are dependent on relative arrangement of the GRIP1 and GRIP2 domains in each GCP. Therefore, I measured and compared the arrangement of these two domains in each spoke (Fig. 31d) and Dr. Peng Liu calculated average of angles in case of GCP2,3 and GCP4 that are represented in more copies. Of notice, the only difference in a domain inclination compared to other GCPs was found for GCP4 and GCP6 where the GRIP domains were more kinked relative to each other (Fig. 31d), which could cause distortions from a helical symmetry.

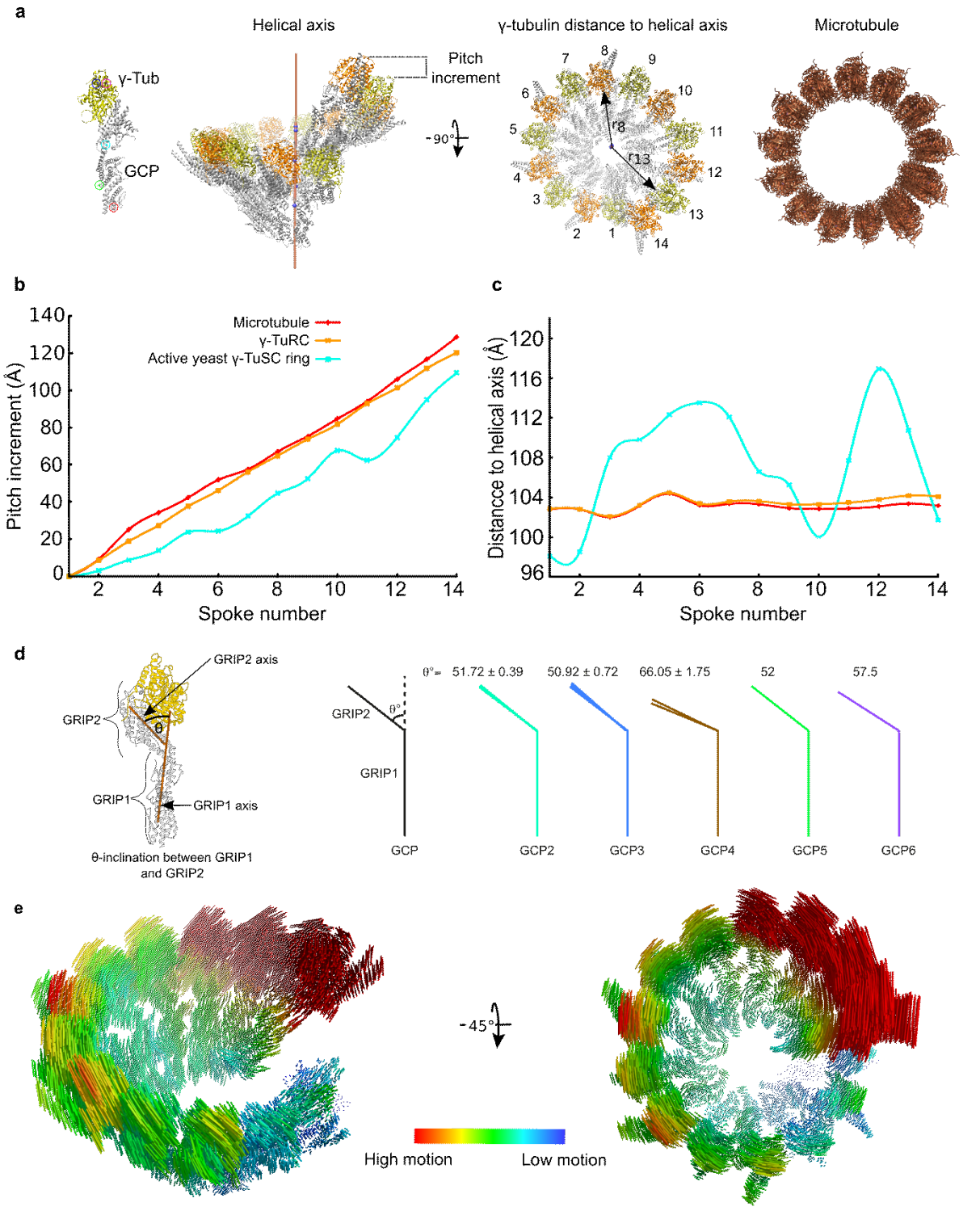

Figure 31: Analysis of the γ-TuRC helical parameters.
a) Left, representation of the spoke with labeled residues (coloured circles) used to define centroids in order to create the approximate helical axis (brown). Left, top view of the γ-TuRC and the MT. Spoke numbers are given together with the representation of the γ-tubulin distance from the helical axis.
b) Plot of the measured pitch increment for the spokes along the helical axis of the γ-TuRC, along the closed γ-TuSC spiral (PDB 5FLZ) and along the 13-spoked MT (PDB 6EW0).
c) Plot of the measured distances of γ-tubulins from the helical axis. for the same complexes as in (**b**).
d) Left, defined axes for the measurement of an inclination between the GRIP1 and GRIP2 domains of GCPs. Right, The measured inclination for GCP variants in the γ-TuRC. Inclinations of GCP2,3 and 4 given as mean with s.e.m.

e) Vector representation of a motion required to bring the γ-TuRC into a MT-compatible geometry. Vector lengths represent motion range (red-high motion, blue-low motion).
Data in panel (**d**) were produced in joint effort with Dr. Peng Liu who performed averaging of the measured angles.
Figure was modified from Liu *et al*., 2020[219].

To understand the conformational rearrangements that would be required to bring the γ-TuRC into helical symmetry of MTs, I simulated the γ-TuRC atomic model in a MT-compatible geometry using the cryo-EM reconstruction of the *S. cerevisiae* γ-TuSC ring-like oligomer in the closed conformation and visualised residue displacement (Fig. 31e). As expected from the aforementioned measurements of the pitch increment and radius, the γ-TuRC spokes must undergo a contraction to decrease the γ-TuRC diameter and γ-tubulins are moved inwards to create a regular spacing matching the arrangement protofilaments in the MT. The biggest rearrangement was observed for the last four spokes, which move along the spiral to close the ring by aligning spoke 14 with spoke 1 and exposing only 13 γ-tubulins (Fig. 31e). This conformational rearrangement could occur passively during MT nucleation by binding of α/β-tubulin dimers or could be actively induced by binding of other factors, such as Cdk5Rap2. The effect of Cdk5Rap2 on the γ-TuRC geometry was examined by adding excess of the Cdk5Rap2 N-terminal segment, which includes the CM1 motif to the γ-TuRC. Using negative stain EM data acquired by Dr. Annett Neuner, I observed no structural changes induced by the Cdk5Rap2 N-terminal segment (Fig. 32a). This is consistent with *in vitro* MT nucleation assays performed by Dr. Peng Liu who did not observe increased MT nucleation activity by Cdk5Rap2 N-terminal segment (Fig. 32b, c), which indicates that combination of more factors is required to activate the γ-TuRC. The effect of the Cdk5Rap2 N-terminal segment on MT nucleation was tested also on level of egg extract by Dr. Peng Liu. Increase of MT nucleation activity was observed only in combination with Ran(Q69L)GTP that is defective in GTP hydrolysis (Fig. 32d). However, mutation of F75A in the CM1 motif of the Cdk5Rap2-N segment resulted in weaker binding to the γ-TuRC and abolished MT nucleation activity even in combination with Ran(Q69L)GTP (Fig. 32d).

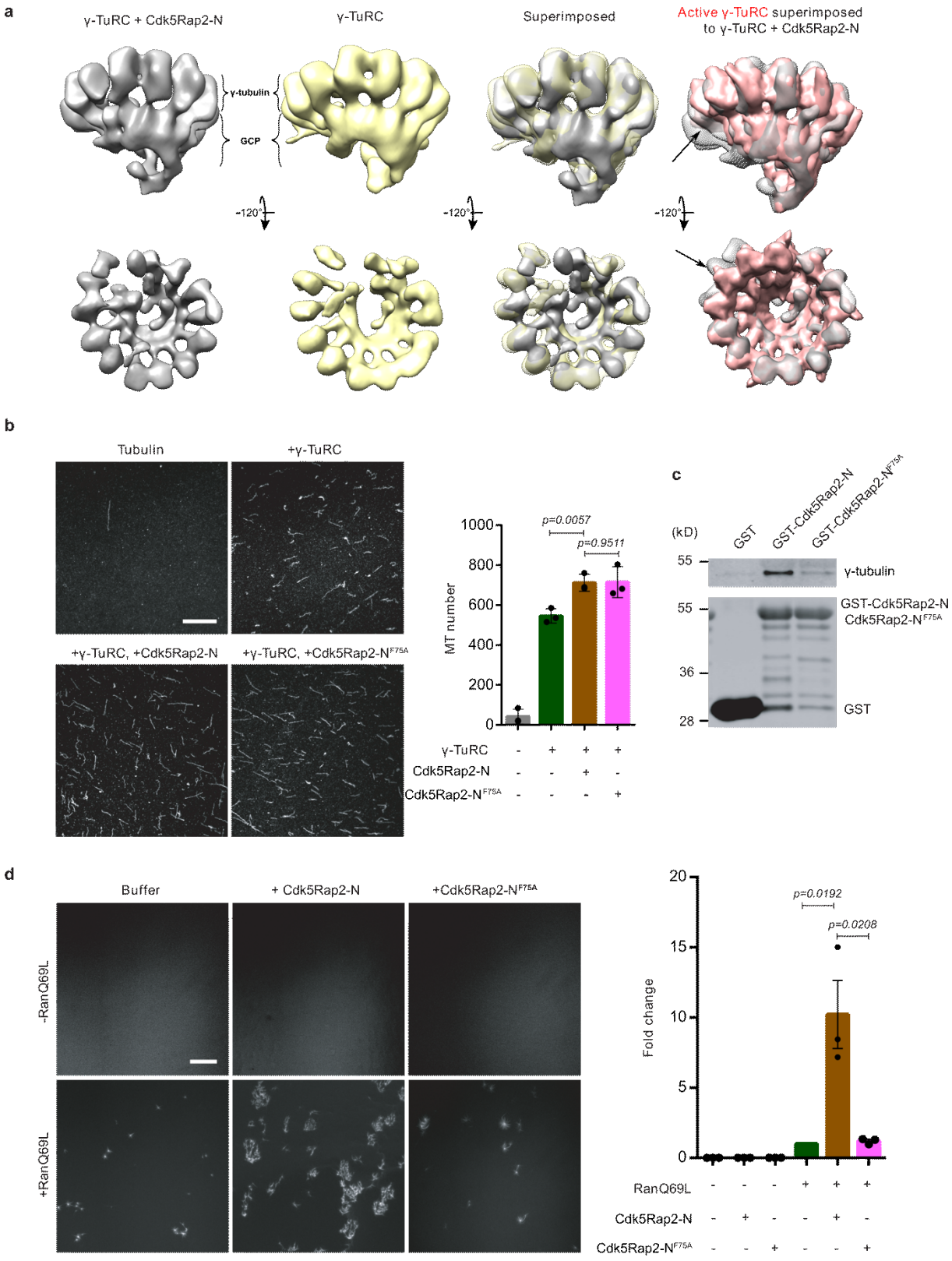

Figure 32: The effect of the CM1 motif on the conformation and MT nucleation activity of the γ-TuRC. **a)** Left, reconstructions of the γ-TuRC with and without Cdk5Rap2-N in grey and yellow, respectively. GCP and γ-tubulin parts are indicated. Right, superposition of the γ-TuRC with and without Cdk5Rap2-N and superposition of the active γ-TuRC (the γ-TuRC with a MT-compatible geometry) in red and the γ-TuRC without Cdk5Rap2-N in grey. Difference in the γ-TuRC reconstructions is indicated by arrow. **b)** MT nucleation assay with the γ-TuRC incubated with and without Cdk5Rap2-N. α/β-tubulin sample as a negative control, the γ-TuRC with α/β-tubulins as a positive control. Scale bar, 10 μm. Right, quantification of MTs from the assay. *P* values are given.

c) Immunoblots of the γ-TuRC incubated with GST-tagged Cdk5Rap2-N using GST and γ-tubulin antibodies. GST sample as a positive control. Molecular weights are indicated.
d) Left, MT nucleation activity assay performed in a *X. laevis* egg extract. Buffer sample as a negative control. Conditions are given. Right, quantification of MT nucleation assay performed in a *X. laevis* egg extract. *P* values are given.
Data in panels (**b-d**) were produced by Dr. Peng Liu.
Figure was modified from Liu *et al*., 2020[219].

Overall, these data provide insights into the molecular architecture of the γ-TuRC, revealing the positions of GCP4,5,6 and identifying a structural scaffold in the lumen of the γ-TuRC, surprisingly including one copy of actin. Biochemical analysis showed a possible role of GCP6 in the assembly of the γ-TuRC and lastly, the γ-TuRC does not mimic MT geometry, indicating that combination of factors is likely required to alter its geometry and make it an effective MT nucleation template.

3.3 Mechanism of γ-TuRC assembly and the role of the γ-TuRC-integrated actin

Results presented in this chapter were published in Nature Communications with me as a co-first author[229].

3.3.1 Cryo-EM analysis of the recombinant human γ-TuRC and identification of MZT1 modules

Cryo-EM structures of the γ-TuRC revealed its very complex architecture with more than 30 assigned proteins assembling in a specific arrangement[219,220,228]. One of the most interesting observations was the location of GCP4,5,6 in the core of the γ-TuRC extended by GCP2-GCP3 units at both sides (Fig. 25a). GCP2 and GCP3 are the vertebrate homologs of fungal Spc97 and Spc98 that in yeasts assemble into the γ-TuSC (Fig. 10a) and such γ-TuSC units can be observed also as a part of the vertebrate γ-TuRC. Modular extension of the γ-TuRC core of GCP4,5,6 by the γ-TuSC units is not symmetric, but only one unit is added on the GCP6-facing side while four γ-TuSC units are added on the GCP4-facing side. All of these observations based on the γ-TuRC structure raised questions about the assembly mechanism of this complex, which is probably tightly controlled to combine all of these components into the uniform γ-TuRC architecture. To address this question, Martin Würtz expressed the recombinant human γ-TuRC with 2xFLAG-GCP5 in insect cells and purified it via a single-step affinity chromatography. It was confirmed before that this purification is yielding the γ-TuRC active in MT nucleation[189,230,231]. Martin Würtz confirmed the presence of all GCPs and γ-tubulin in the eluted sample using SDS-PAGE and an integrity of the purified recombinant human γ-TuRC was verified by negative stain EM performed by Dr. Annett Neuner (Fig. 33a, b). 2D class averaging performed by Martin Würtz, surprisingly revealed the presence of the γ-TuRC assemblies with less than fourteen spokes in addition to the fully assembled γ-TuRC (Fig. 33c). Observation of these smaller intermediates in high particle number in the negative stain EM data provided me with an opportunity to investigate these intermediates at higher resolution using cryo-EM SPA. Therefore, the sample was applied on grids and several thousand images were acquired (Fig. 34a). First, I aimed to confirm the presence of the fully and correctly assembled γ-TuRC. The ratio of the fully assembled γ-TuRC was comparably low. Therefore, I analysed the fully assembled γ-TuRC together with intermediates composed of 12 spokes (either spokes 3-14 or spokes 1-12) increasing the number of particles, which would allow me to reach higher resolution (Fig. 34b). Submitting this set of the particles into 3D auto-refinement yielded a cryo-EM reconstruction at 7.5 Å global resolution (Fig. 34b), which was at sufficient

details to recognise all previously assigned components of the γ-TuRC and to confirm correct subunit architecture of the complex as described for the native γ-TuRCs from different sources[219-221] (Fig. 35a,b). After assigning all GCPs with their associated γ-tubulins and MZT1 modules together with actin in the luminal bridge, the cryo-EM reconstruction was surprisingly not fully covered, leaving the small density segments at the periphery of the GCP3 GRIP2 domains at spokes 2,4,6 and 8 unassigned (Fig. 35a, c). These peripheral density segments remarkably resembled the density segment observed in the *X. laevis* γ-TuRC cryo-EM reconstruction at GCP3$_{(14)}$ (Fig. 25a), which was suggested to represent a module formed by MZT1-GCP3[228]. Thus, I attempted to rigid body fit the MZT1-GCP3 module, as resolved in the luminal bridge of the human γ-TuRC cryo-EM reconstruction (PDB 6X0U)[228], into these peripheral density segments. The MZT1-GCP3 module provided a good fit for all peripheral density segments (Fig. 35c and Fig.36). To exclude that the density segments correspond to structurally similar MZT2 modules, I attempted rigid body fitting of MZT2 modules into the peripheral density segments, but length of α-helices was not consistent with the density segment (Fig. 36b). Taken together, I could confirm correct subunit architecture of the recombinant human γ-TuRC and I additionally identified missing MZT1 modules at the periphery of the GCP3 GRIP2 domains, which could not be localised before (Fig. 35a).

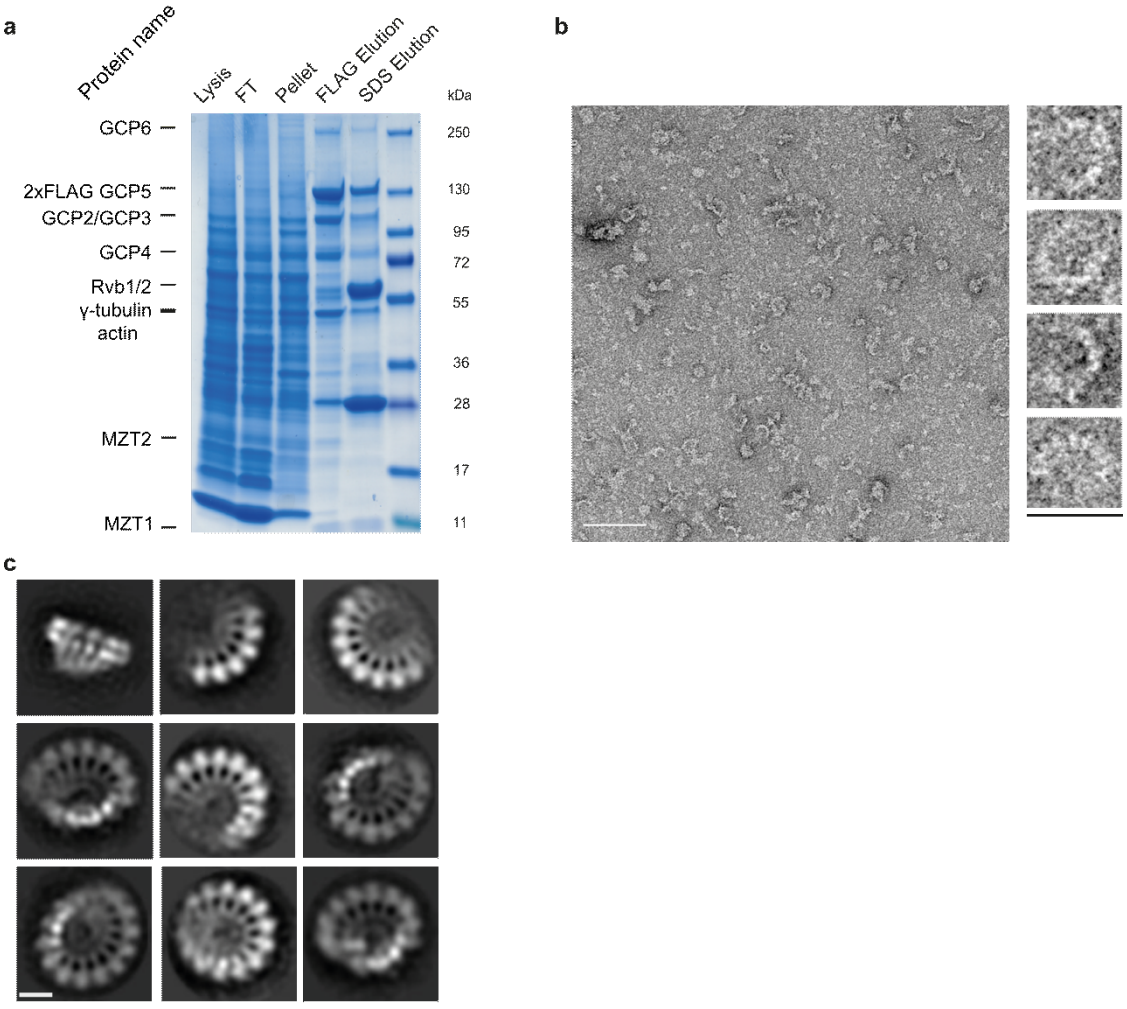

Figure 33: Characterisation of the purified recombinant human γ-TuRC.
a) SDS-PAGE of the purified γ-TuRC. Protein names, applied samples and molecular weights are given (FT-flowthrough).

b) Negative stain EM of the recombinant human γ-TuRC. Zoom on a representative image from acquired data and zoom on four representative particles. Scale bars, 125 nm (image) and 40 nm (particles).
c) Representative class averages from negative stain EM of the recombinant human γ-TuRC. Scale bar, 10 nm.
Data in panels (**a, c**) were produced by Martin Würtz.
Data in panel (**b**) were produced by Dr. Annett Neuner.
Figure was modified from Würtz *et al*., 2022[229].

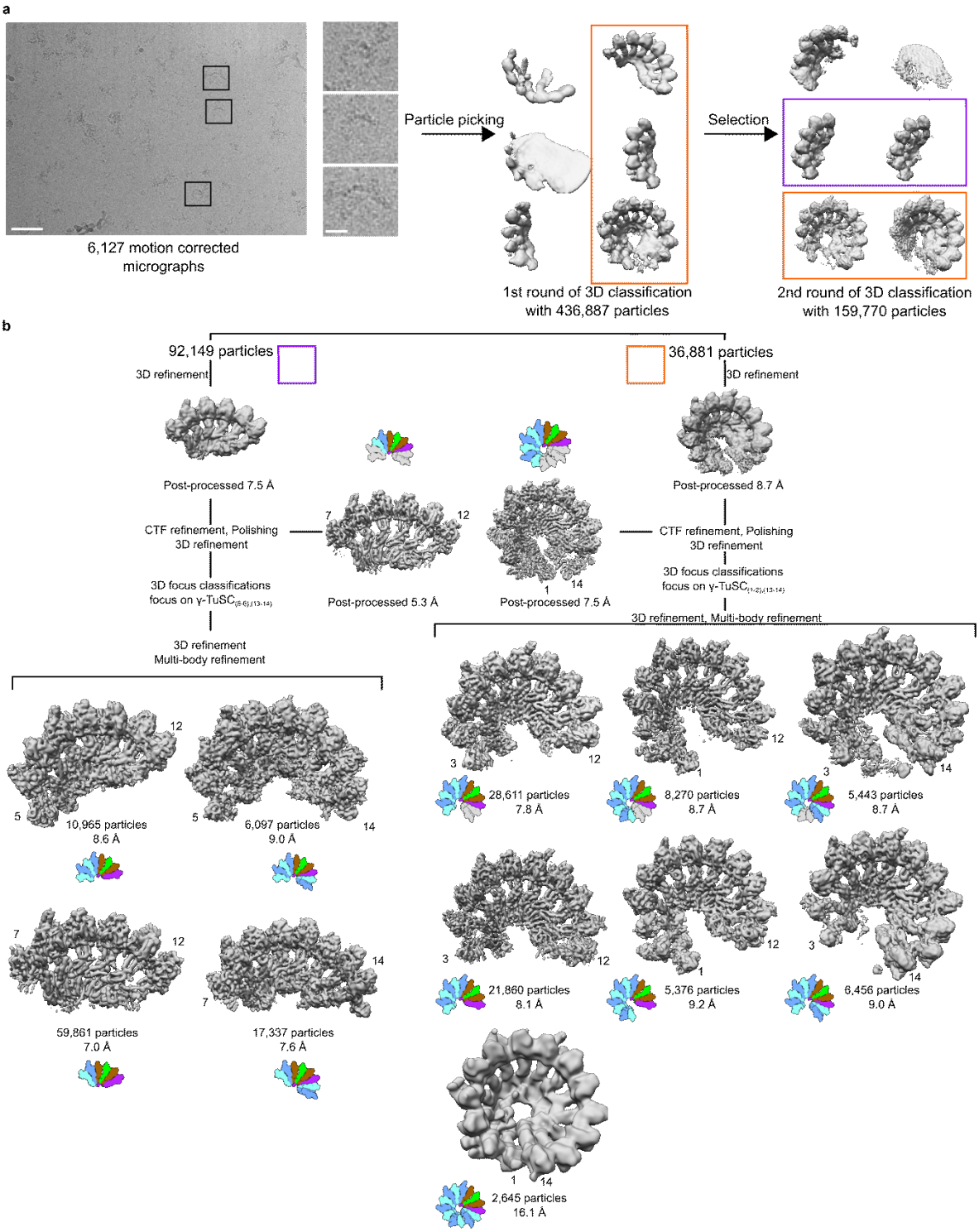

Figure 34: Schematic flowchart of the cryo-EM data processing for the recombinant human γ-TuRC.
a) Zoom on a representative image from acquired data of the recombinant human γ-TuRC. Three representative particles are shown and indicated on the image by black rectangles. Scale bars, 80 nm

(image), 20 nm (particles). Particles from an initial picking were subjected to two rounds of 3D classifications. Selected class averages in the first round are indicated by orange rectangle. Selected class averages from the second round are indicated by orange and purple rectangles according to branches in next processing steps.
b) Two processing branches. Branch for particles of the small γ-TuRC assembly intermediates is indicated by purple rectangle and branch for particles of the large γ-TuRC assembly intermediates is indicated by orange rectangle. All processing steps are indicated (for more details see Methods). The resolution and particle number for each reconstruction are given. Each reconstruction/particle set is depicted in ambient representation and used in next figures of the γ-TuRC assembly intermediates to assign images in each figure to a specific reconstruction/particle set.
Figure was modified from Würtz *et al*., 2022[229].

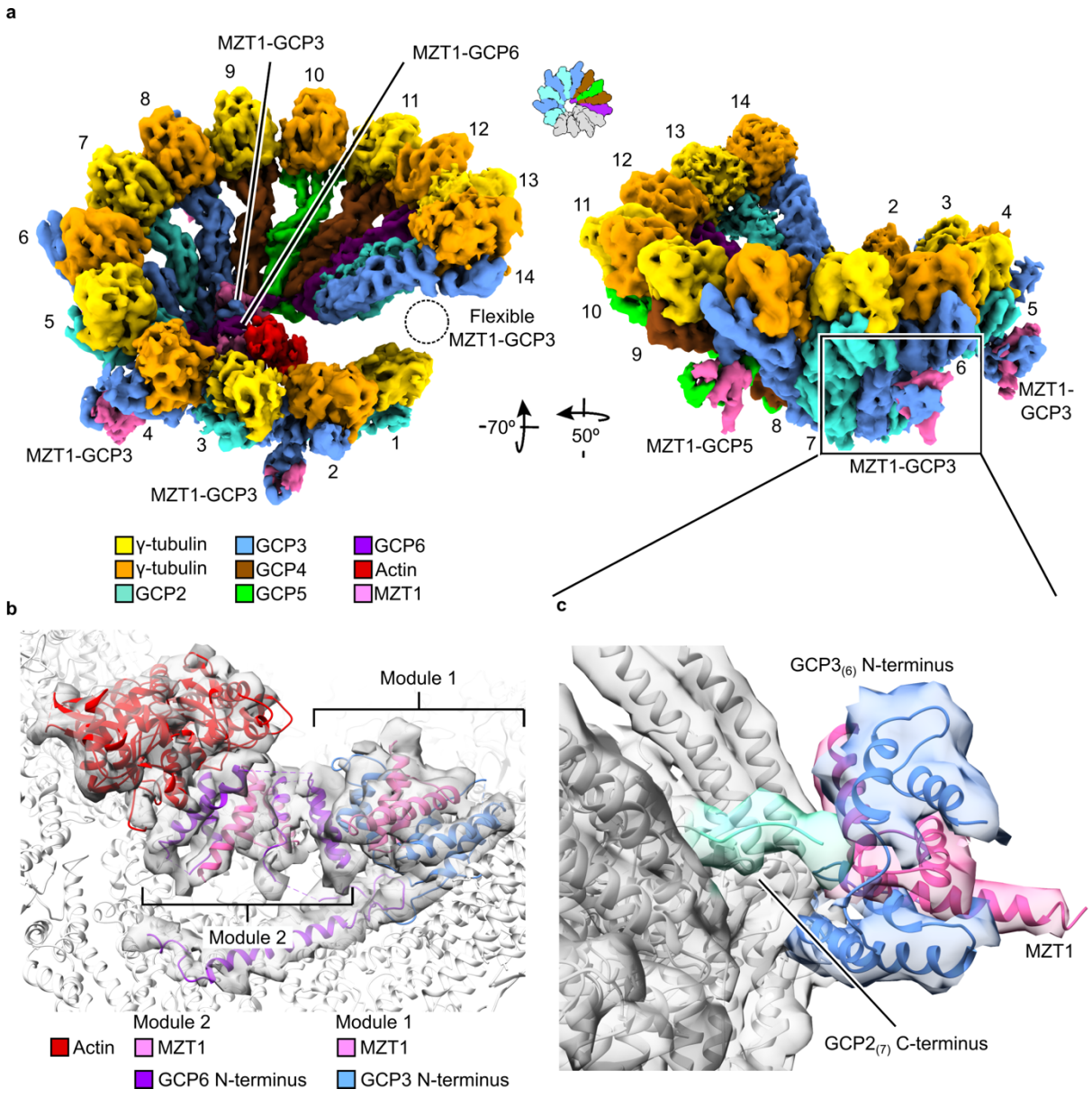

Figure 35: Cryo-EM reconstruction of the recombinant human γ-TuRC.
a) Two views on the segmented cryo-EM reconstruction of the fully assembled γ-TuRC. MZT1 modules are indicated. Unresolved MZT1 module is indicated by dashed circle. Spoke numbering and colour scheme are given. Ambient representation of the particle set used for the reconstruction is given on the top.

b) Zoom on the luminal bridge of the fully assembled γ-TuRC reconstruction. The luminal bridge components are coloured. MZT1 modules of the luminal bridge are indicated. Colour scheme is given. Density segment of the luminal bridge is coloured in transparent grey.
c) Zoom on one the MZT1 module at the periphery of $GCP3_{(6)}$. The GCP2 C-terminus is indicated together with the $GCP3_{(6)}$ N-terminus and MZT1. Colour coding of indicated components and corresponding density segments is same as in panel (**a**). Rest of the atomic model and cryo-EM reconstruction is coloured in grey.
Figure was modified from Würtz *et al*., 2022[229].

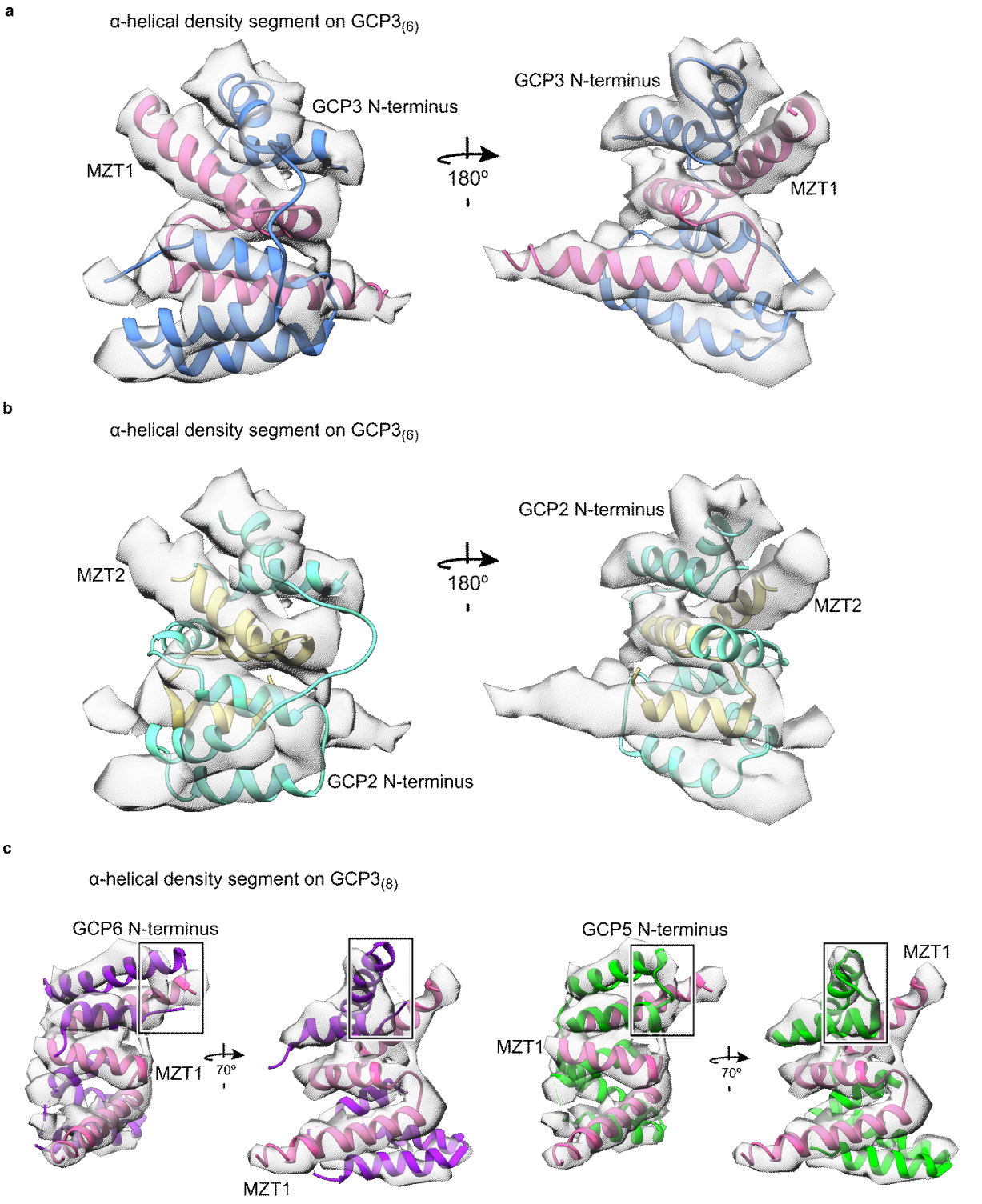

Figure 36: Assignment of MZT1 modules in the helical density segments at the periphery of the recombinant human γ-TuRC.
a) Model of the MZT1-GCP3 module (PDB 6X0U) docked into the α-helical density segment at the periphery of $GCP3_{(6)}$. MZT1 and the GCP3 N-terminus are coloured and indicated. Colour scheme is same as in Figure 35.
b) Model of the MZT2-GCP2 module (PDB 6X0V) docked into the α-helical density segment at the periphery of $GCP3_{(6)}$. MZT2 (yellow) and the GCP2 N-terminus (aquamarine) are indicated.
c) Left, model of the MZT1-GCP6 module (PDB 6M33) docked into the α-helical density segment at the periphery of $GCP3_{(8)}$. Black rectangles are indicating a region of the atomic model extending from the density segment. Right, model of the MZT1-GCP5 module (PDB 6L81) docked into the α-helical density segment at the periphery of $GCP3_{(8)}$. Black rectangles are indicating a region of the atomic model

corresponding to the resolved density segment in contrary to the GCP6 N-terminus. Colour scheme is same as in Figure 35.
Figure was modified from Würtz *et al*., 2022[229].

Next goal was to identify and structurally characterise the γ-TuRC assembly intermediates. To obtain intermediates with different number of spokes, I had to apply several tiers of 3D classification, which yielded different assembly intermediates (Fig. 34b). The most abundant (56%) and at the same time the smallest γ-TuRC intermediate identified by 3D classification contained 6-spokes. The cryo-EM reconstruction of this intermediate reached 5.3 Å global resolution (Fig. 34b), which was sufficient to resolve features as α-helices and unambiguously assign all GCPs included (Fig. 37a). The sequence of identified GCPs in the 6-spoked assembly intermediate was GCP2-3-4-5-4-6 (Fig. 37a, thus corresponding to the γ-TuRC-specific GCPs that form the stable γ-TuRC core (Fig. 35a), associated with one γ-TuSC unit on the GCP4-facing side. These GCPs represent spokes 7-12 of the fully assembled γ-TuRC. Identification of GCP4,5,6 as the components of the smallest observed assembly intermediate is suggesting their role in the assembly mechanism of the γ-TuRC.

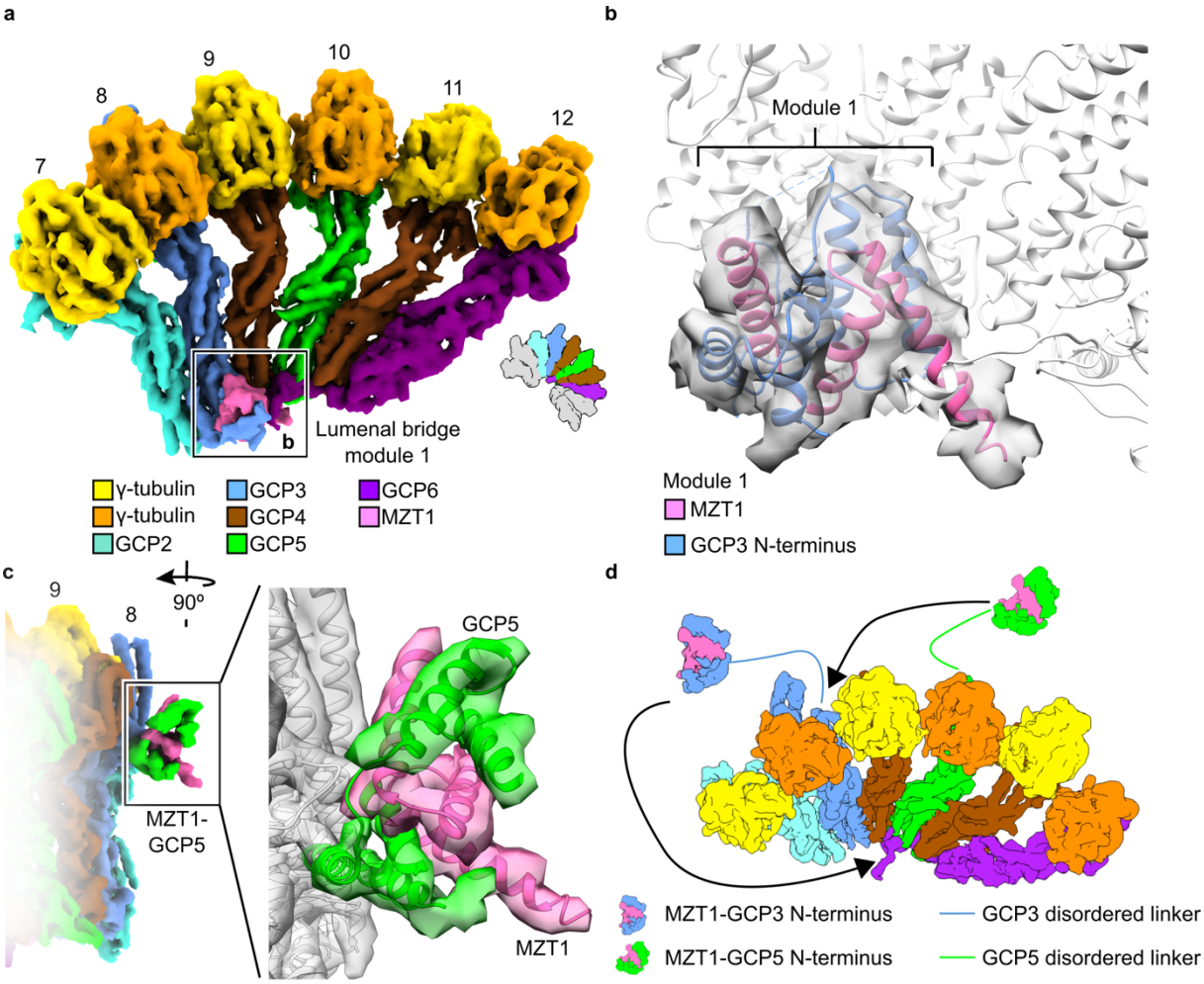

Figure 37: Cryo-EM reconstruction of the 6-spoked assembly intermediate.
a) Segmented density map of the 6-spoked assembly intermediate. The luminal bridge module is indicated. Spoke numbering and colour scheme are given. Ambient representation of the particle set used for the reconstruction is given.

b) Zoom on the luminal bridge module 1. Components of the module 1 are coloured. Rest of the atomic model is coloured in grey. Colour scheme is given and the density segment of the module is coloured in transparent grey.
c) Left, side view of the 6-spoked assembly intermediate with focus on the MZT1-GCP5 module. Spoke numbering is given. Right, zoom on the MZT1-GCP5 module. Components of the MZT1-GCP5 module are coloured with corresponding density segments according to colour scheme in panel (**a**). Rest of the atomic model and density segment are coloured in grey.
d) Schematic representation of a possible MZT1-GCP3 module release by the MZT1-GCP5 module. Components are coloured the same way as in panel (**a**).
Figure was modified from Würtz *et al*., 2022[229].

3.3.2 The 6-spoked assembly intermediate includes the first luminal bridge module and the MZT1-GCP5 module

In the 6-spoked assembly intermediate, the first module of the luminal bridge formed by MZT1 and the GCP3 N-terminus (Fig. 37b) was already resolved. Identification of this module at its canonical position as in the fully assembled γ-TuRC is clear indication that the 6-spoked assembly intermediate is sufficient for stabilisation of this module. The first luminal bridge module could not have been assigned to a specific GCP3 of the γ-TuRC in the previous γ-TuRC cryo-EM reconstruction[228]. Considering that the 6-spoked assembly intermediate contains only $GCP3_{(8)}$ (Fig. 37a), I could unambiguously claim that it is the $GCP3_{(8)}$ N-terminus, which forms the luminal bridge module together with MZT1. In addition to the MZT1 module of the luminal bridge, another MZT1 module was resolved at the periphery of the $GCP3_{(8)}$ GRIP2 domain, similarly as in the cryo-EM reconstruction of the fully assembled γ-TuRC (Fig. 37c). With GCP4 lacking a MZT1 binding site, GCP2 binding to MZT2[189] and the only GCP3 N-terminus in the 6-spoked assembly intermediate already engaged in the first luminal bridge module, the only candidates for formation of this second MZT1 module were GCP5 and GCP6. Both, GCP5 and GCP6 were reported to contain same binding motif for MZT1 similar to GCP3 and the structures of their N-termini in a complex with MZT1 were described using X-ray crystallography[189,232]. To identify which GCP N-terminus forms the MZT1 module at the periphery of $GCP3_{(8)}$, the X-ray structures of GCP5 and GCP6 N-termini in a complex with MZT1[232] (PDB 6L81 and PDB 6M33) were rigid body docked into the density segment (Fig. 36c). Even though the structures of the GCP5 and GCP6 N-termini are similar, differences in length of their α-helices allowed me to exclude the GCP6 N-terminus and thereby assign the GCP5 N-terminus to the MZT1 module at $GCP3_{(8)}$ (Fig. 37c). A potential explanation of a specific binding of MZT1-GCP5 module to the periphery of $GCP3_{(8)}$ is the composite interface between $GCP3_{(8)}$ and $GCP4_{(9)}$ that is unique in the entire complex (Fig. 35a, c). Moreover, competition of the MZT1-GCP5 module for the MZT1 module binding site on $GCP3_{(8)}$ would allow the MZT1-GCP3 module to form the first part of the luminal bridge (Fig. 37d). Taking into account that GCP3,5,6 are the only γ-TuRC components binding to MZT1 via their N-termini and having identified the positions of MZT1 modules formed with the N-termini of GCP5 and GCP6, remaining MZT1-GCP modules identified at the periphery of the GCP3 spoke 2,4,5 and 14 in the fully assembled γ-TuRC could be assigned to the GCP3 N-termini. Overall, I could locate all MZT1 modules in the γ-TuRC (Fig. 35a).

3.3.3 The GCP6 NTE and the first module of the luminal bridge stabilise the 6-spoked assembly intermediate

The 6-spoked assembly intermediate was the most populated subcomplex in the cryo-EM dataset suggesting its high stability. Potential candidates for stabilisation of the 6-spoked assembly intermediate could be components of GCPs thus far unassigned in the γ-TuRC cryo-EM reconstructions, such as the NTEs or the insertions of GCP6 and GCP5 (Fig. 22i).

Analysing the cryo-EM reconstruction, I observed unexplained density segments below the GRIP1 domains of GCP4,5,6 of the 6-spoked assembly intermediate, which suggested that they could be represented either by the GCP6 NTE or the GCP5 NTE or both of them. Since the cryo-EM reconstruction of the 6-spoked assembly intermediate was limited to 5.3 Å resolution, I revisited a higher-resolution cryo-EM reconstruction of the native human γ-TuRC (EMDB 21074, 21069)[220] and re-located the same density features below the GRIP1 domains of GCP4,5,6. Resolution of this cryo-EM reconstruction allowed me to trace these density segments to the GCP5 and GCP6 GRIP1 domains, identifying them as the GCP5 and GCP6 NTEs. When extending these NTEs (Fig. 38a), I could unambiguously fit residue side chains of the GCP5 NTE (210-266) and the GCP6 NTE (282-351), revealing a highly intertwined organisation below the GRIP1 domains of $GCP4_{(9,11)}$, $GCP5_{(10)}$, $GCP6_{(12)}$, which provided an additional interface for the GRIP1 domains as compared to other regions of the γ-TuRC (Fig. 38b, d, e). These interactions explain the stabilisation of the GCP4-5-4-6 module in the 6-spoked assembly intermediate, but not the presence of the $\gamma\text{-TuSC}_{(7\text{-}8)}$ unit because the GCP6 NTE did not contact the GRIP1 domains of the $GCP2_{(7)}$ and $GCP3_{(8)}$. However, the very N-terminus of the newly built segment of the GCP6 NTE bind to the MZT1 N-terminal helix of the first luminal bridge module, containing the $GCP3_{(8)}$ NTE (Fig. 38b, c), explaining the stabilisation of the $\gamma\text{-TuSC}_{(7\text{-}8)}$ unit in the 6-spoked assembly intermediate . All of these observations point to a major role of the GCP6 NTE in the assembly of the 6-spoked assembly intermediate, which is also consistent with defects in γ-TuRC assembly observed after deletion of the GCP6 NTE[233].

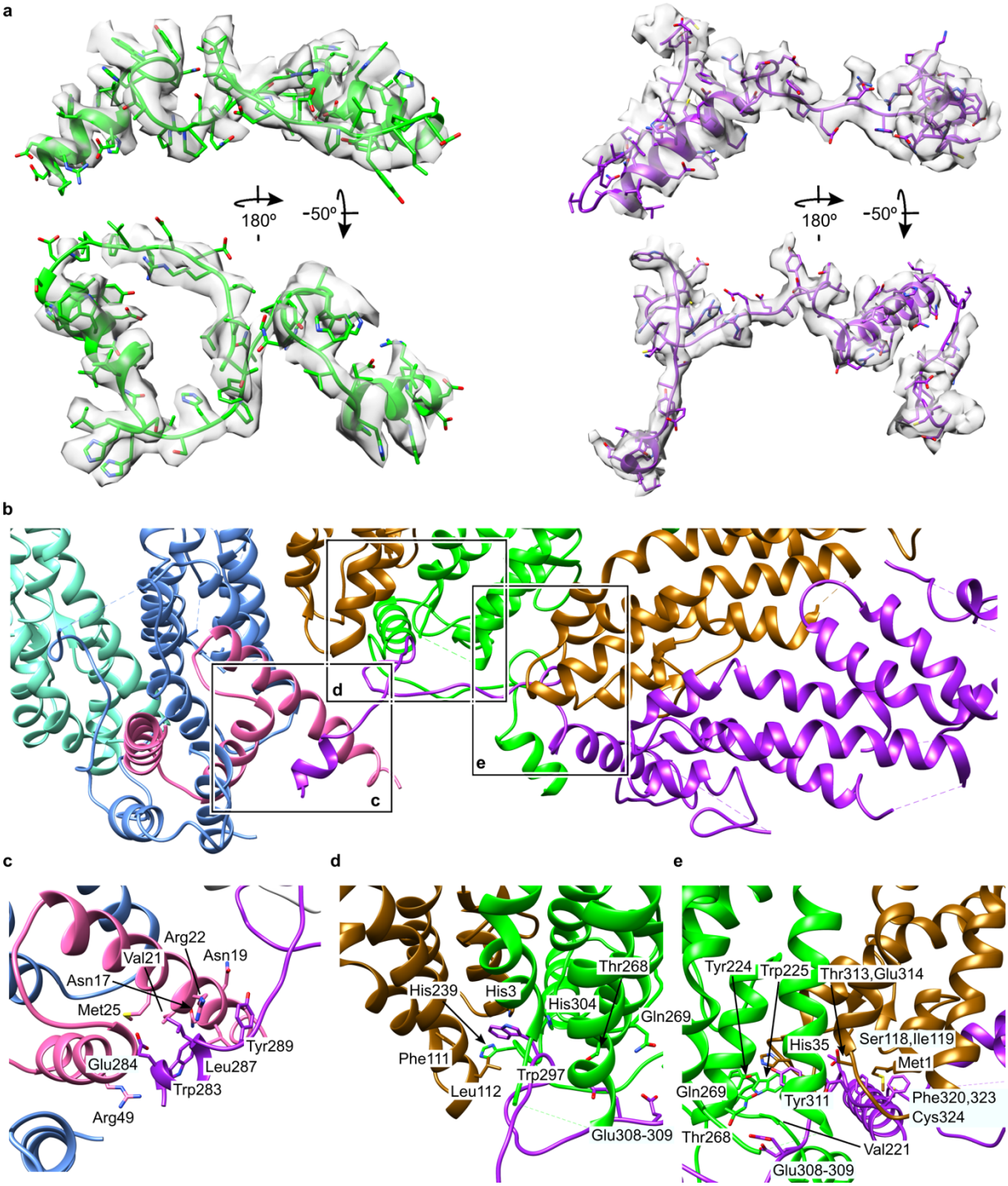

Figure 38: The role of the GCP5 and GCP6 NTEs in the stabilisation of the 6-spoked assembly intermediate.
a) The GCP5 NTE (210-266) and the GCP6 NTE (282-351) built *de novo* according to a published cryo-EM reconstruction of the γ-TuRC (EMD-21074, EMD-21069). Atomic models are shown in ribbon representation with displayed residue side chains and superposed to corresponding density segments.
b) The GCP65 and the GCP6 NTEs intertwined below the GRIP1 domains of GCP4-5-4-6 of the 6-spoked assembly intermediate. The GCP5 and GCP6 NTEs interfaces with other components of the 6-spoked assembly intermediate are indicated by black rectangles. Components are coloured the same way as in Figure 35.
c) Zoom on the GCP6 NTE region interacting with the MZT1 module of the 6-spoked assembly intermediate. Interacting residues are indicated.
d) Zoom on the GCP5 and GCP6 NTEs interacting each other and interacting with the GRIP1 domains of GCP5 and GCP4$_{(9)}$. Interacting residues are indicated.
e) Zoom on the GCP5 and GCP6 NTEs interacting each other and interacting with the GRIP1 domains of GCP5 and GCP4$_{(11)}$. Interacting residues are indicated.

Figure was modified from Würtz *et al*., 2022[229].

As mentioned above, the GCP5 and GCP6 NTEs interact with the GRIP1 domains of GCP4,5,6 of the 6-spoked assembly intermediate, which raised the question of whether a 4-spoked assembly intermediate comprising of only GCP4-5-4-6 can exist as a stable intermediate, or the γ-TuSC$_{(7-8)}$ unit is required to form the first stable γ-TuRC assembly intermediate. Therefore, Martin Würtz expressed all γ-TuRC components except for GCP2-3 to test the stability of the 4-spoked assembly intermediate formed only by GCP4-5-4-6. The sample was purified by Martin Würtz via 2xFLAG-GCP5. SDS-PAGE and immunoblotting confirmed that all components were expressed (Fig. 39a, b). Negative stain EM 2D class averaging performed by Martin Würtz yielded clear 4-spoked assembly intermediates (Fig. 39b, c). Encouraged by these results, Giulia Tonon under my supervision performed cryo-EM SPA and reconstructed the 4-spoked intermediate at 7.8 Å global resolution (Fig. 40a-d), which was sufficient to unambiguously assign GCPs to specific spokes (Fig. 40e) based on the NTEs of GCP5 and GCP6, confirming the expected sequence of GCPs as GCP4-5-4-6 (Fig. 40f). However, the very low number of the particles contributing to the structurally defined 4-spoked assembly intermediate reconstruction despite the extensive size of the dataset, as well as the complete absence of the 4-spoked assembly intermediate when coexpressing all γ-TuRC components, suggested that the 4-spoked assembly intermediate is only a transient state, that is in a fast manner extended by recruitment of the γ-TuSC$_{(7-8)}$ unit.

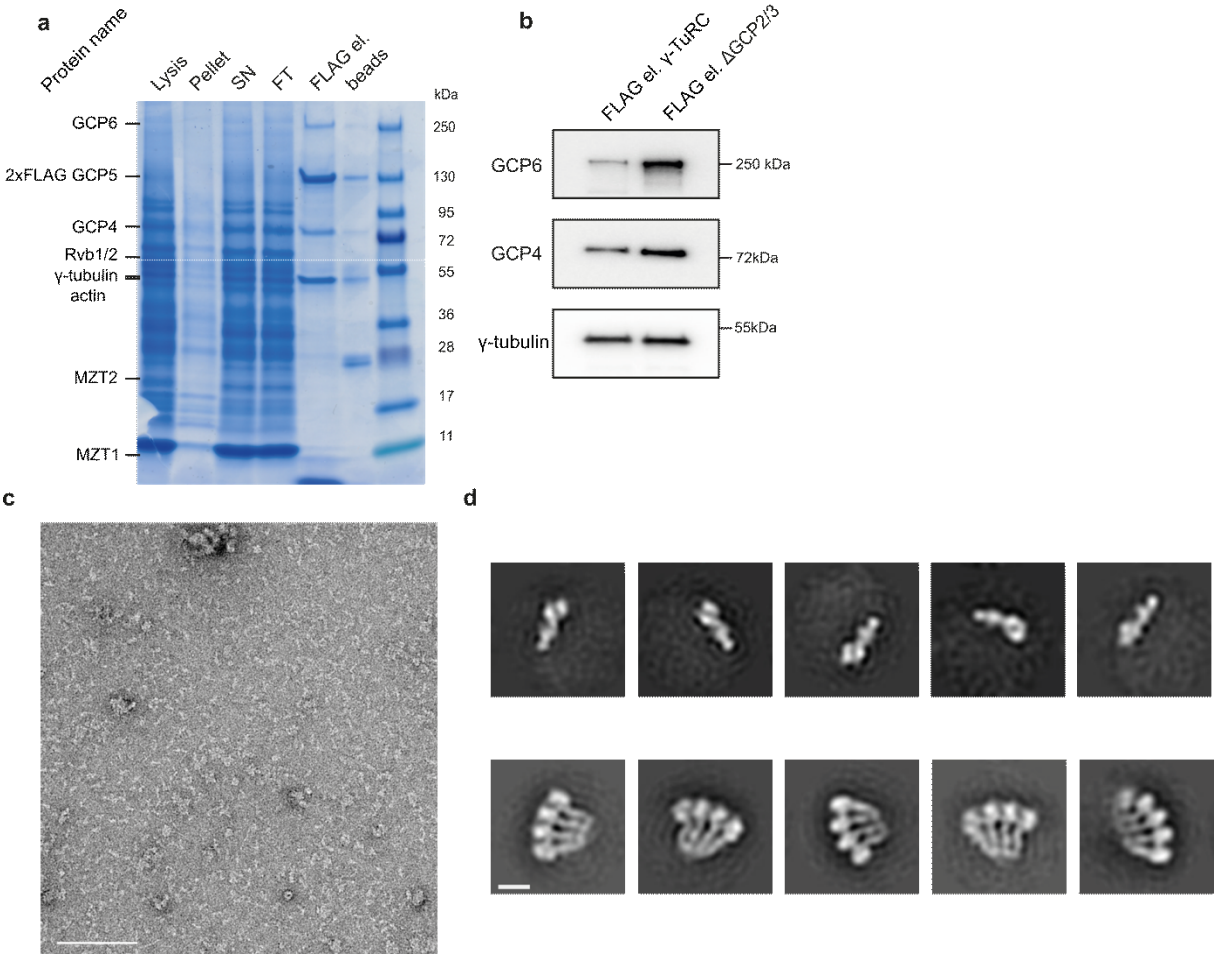

Figure 39: Characterisation of the purified recombinant human γ-TuRC$^{\Delta GCP2/3}$.

a) SDS-PAGE of the purified γ-TuRC$^{\Delta GCP2/3}$. Protein names, applied samples and molecular weights are given (FT-flowthrough).
b) Immunoblot of GCP6, GCP4 and γ-tubulin from the elution of the wild-type recombinant human γ-TuRC and from the recombinant human γ-TuRC$^{\Delta GCP2/3}$. Molecular weights are given.
c) Negative stain EM of the recombinant human γ-TuRC$^{\Delta GCP2/3}$. Zoom on a representative image from acquired data. Scale bar, 125 nm.
d) Representative class averages from negative stain EM of the recombinant human γ-TuRC$^{\Delta GCP2/3}$. Top, class averages of single spokes represented likely by GCP5. Bottom, class averages of the 4-spoked assembly intermediates. Scale bar, 10 nm.
Data in panels (**a, b, d**) were produced by Martin Würtz.
Data in panel (**c**) were produced by Dr. Annett Neuner.
Figure was modified from Würtz *et al*., 2022[229].

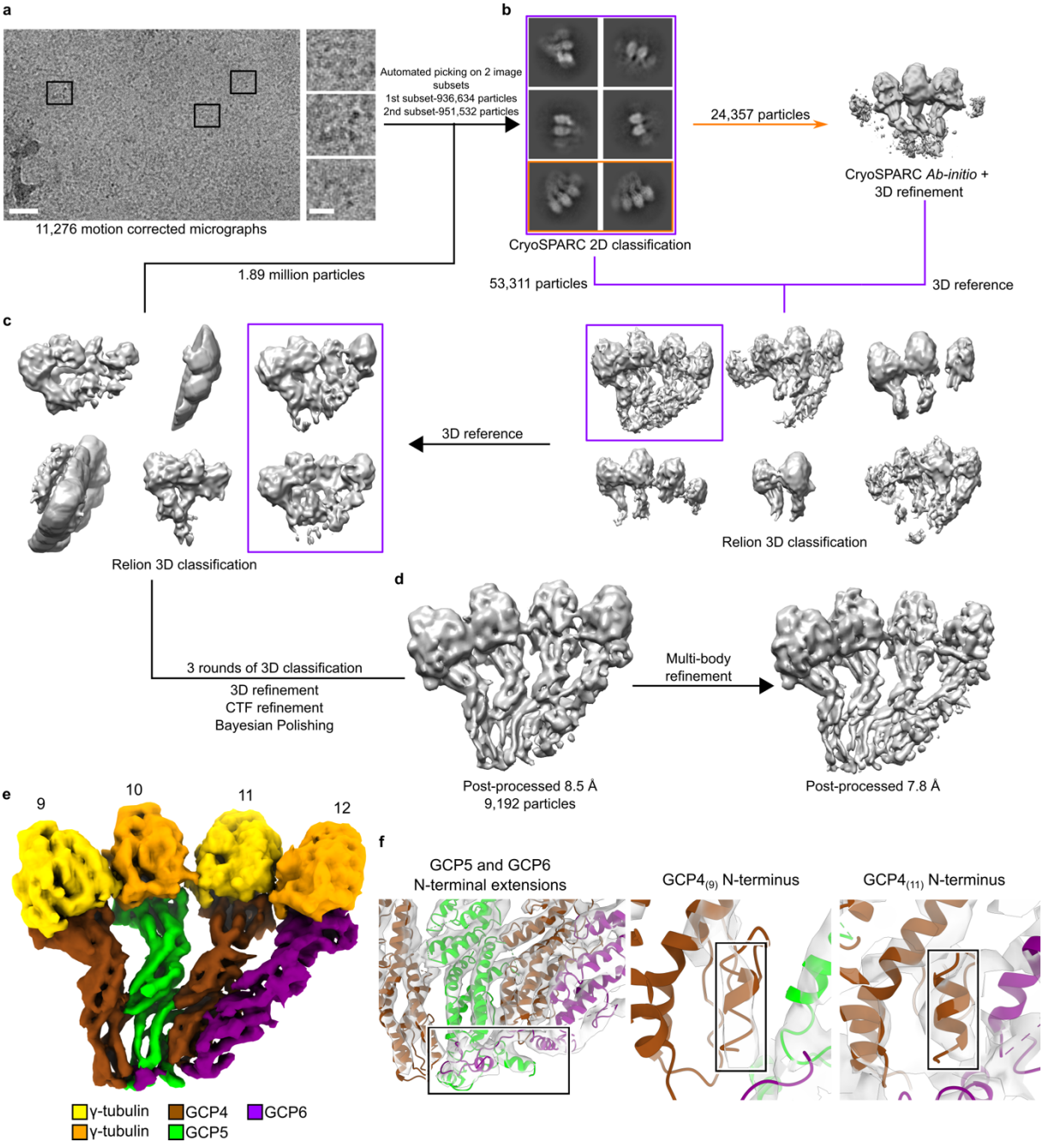

Figure 40: Schematic flowchart of the cryo-EM data processing for the recombinant human γ-TuRC$^{\Delta GCP2/3}$.

a) Zoom on a representative image from acquired data of the recombinant human γ-TuRC$^{\Delta GCP2/3}$. Three representative particles are shown in zoom and indicated on the image by black rectangles. The number of acquired images is given. Scale bars, 30 nm (image) and 10 nm (particles).
b) Selected class averages from cryoSPARC 2D classification after an initial particle picking. Class averages indicated by orange rectangle were subjected to *ab-initio* reconstruction followed by homogeneous refinement. Resulting reconstruction was used as a reference for Relion 3D classification with particles from class averages indicated by purple rectangle. 3D class average indicated by purple rectangle served as a reference for the next processing steps.
c) Particles from the initial picking were split into four subsets and subjected to four consecutive rounds of 3D classification in Relion. Class averages from the first round of classification of the first subset are shown. Selected class averages are indicated by purple rectangle. Final set or particles from 3D classifications were subjected to CTF refinement and Bayesian polishing.
d) Reconstruction after 3D refinement of polished particles. Resolution and input particle number are given. Reconstruction was subjected to multi-body refinement improving the resolution of the 4-spoked assembly intermediate.
e) Segmented cryo-EM reconstruction of the 4-spoked assembly intermediate after multi-body refinement. Colour scheme is given.
f) Zoom on the model features docked in the density segments that unambiguously identify GCPs at specific positions of the cryo-EM reconstruction. Right, the GCP5 and GCP6 NTEs docked in the resolved density segment (black rectangle). Left, the GCP4$_{(9)(11)}$ N-terminal helices docked in the resolved density segments (black rectangles). Colour scheme is same as in panel (**e**).
Data in this figure were produced by Giulia Tonon under my supervision.
Figure was modified from Würtz *et al*., 2022[229].

3.3.4 γ-TuRC assembly is driven by a successive expansion of the 6-spoked assembly intermediate by the γ-TuSC units coupled with their conformational locking

The 6-spoked assembly intermediate represents the first stable subcomplex during γ-TuRC assembly. Extensive 3D classification of the particles in the recombinant human γ-TuRC cryo-EM data revealed additional assembly intermediates that helped me to understand the assembly process of the γ-TuRC and to follow the process from the 6-spoked intermediate to the fully assembled γ-TuRC (Fig. 41a). Notably, all of the reconstructed intermediates could be explained by the γ-TuSC unit addition to the 6-spoked assembly intermediate, indicating that the assembly mechanism is driven by binding of the preformed γ-TuSC units and not by successive spoke-by-spoke expansion. To reach the fully assembled γ-TuRC, the 6-spoked assembly intermediate needs to be expanded by three γ-TuSC units on the GCP2$_{(7)}$-facing side (to form spokes 1-6) and one γ-TuSC unit on the GCP6-facing side (to form spokes 13-14). The assembly on the GCP2$_{(7)}$-facing side starts by recruitment of the γ-TuSC$_{(5-6)}$ unit that binds via the GRIP1 domain interface but its conformational state directly after the expansion is different compared to the one in the fully assembled γ-TuRC (Fig. 41a, b). Specifically, the GRIP2 domains and associated γ-tubulins of the γ-TuSC unit are displaced. The assembly continues by addition of the γ-TuSC$_{(3-4)}$ unit (Fig. 41a, b), which is accompanied by two structural changes. The first change is the repositioning of the γ-TuSC$_{(5-6)}$ unit by moving the GRIP2 domains and associated γ-tubulins 5 Å towards the helical axis of the γ-TuRC (Fig. 41b). The second structural change is the stabilisation of the MZT1-GCP6-actin module that forms the second half of the luminal bridge (Fig. 41a). These two changes, directly coupled to the expansion by the γ-TuSC$_{(3-4)}$ unit, indicate a relation between different assembly events and suggest a precise step-wise mechanism of the process. Similarly as in the case of the γ-TuSC$_{(5-6)}$ unit, conformation of the γ-TuSC$_{(3-4)}$ unit is different from the fully assembled γ-TuRC in regard to the positions of the GRIP2 domains and associated γ-tubulins (Fig. 41b). The last step of the expansion on the GCP2$_{(7)}$-facing side is recruitment of the γ-TuSC$_{(1-2)}$ unit, which triggers a similar conformational change of the γ-TuSC$_{(3-4)}$ unit (Fig. 41b) as seen for the γ-

$TuSC_{(5-6)}$ unit. Different from the first two γ-TuSC units recruited during the assembly on the $GCP2_{(7)}$-facing side, the γ-$TuSC_{(1-2)}$ unit is binding in its γ-TuRC canonical conformation.

Besides expansion on the $GCP2_{(7)}$-facing side, the 6-spoked assembly intermediate also needs to be expanded by the γ-$TuSC_{(13-14)}$ unit on the GCP6-facing side to complete γ-TuRC assembly. Unexpectedly, I observed each of the previously described γ-TuRC assembly intermediates in two states- with and without the γ-$TuSC_{(13-14)}$ unit associated (Fig. 41a). The ratio between states with and without the γ-$TuSC_{(13-14)}$ unit was similar for each intermediate arguing for constant and dynamic association and dissociation of the γ-$TuSC_{(13-14)}$ unit (Fig. 41a) in contrast to a stable recruitment. Stable recruitment would lead to increase of particle fractions representing bigger intermediates with the γ-$TuSC_{(13-14)}$ unit and argue against observed constant ratio for the states with and without the γ-$TuSC_{(13-14)}$. When comparing assembly intermediates containing the γ-$TuSC_{(13-14)}$ unit, I noticed that the position of the γ-$TuSC_{(13-14)}$ unit relative to GCP6 is strongly shifted in the stage after stabilisation of the complete luminal bridge (Fig. 41c), which suggested allosteric interactions during these stages of γ-TuRC assembly. After repositioning, the γ-$TuSC_{(13-14)}$ unit reaches its canonical position in the γ-TuRC, which allows the MZT1 module at $GCP3_{(14)}$ to directly bind to γ-tubulin at $GCP2_{(1)}$, which likely prevents dissociation of the γ-$TuSC_{(13-14)}$ unit (Fig. 41d) and completes the assembly process of the γ-TuRC.

In conclusion, the resolved γ-TuRC intermediates allowed me to delineate the γ-TuRC assembly mechanism starting from the transient 4-spoked assembly intermediate that is rapidly converted to the stable 6-spoked assembly intermediate by incorporation of one γ-TuSC unit. In the next steps, the 6-spoked assembly intermediate is expanded by the addition of three γ-TuSC units on the $GCP2_{(7)}$-facing side while the γ-TuSC unit on the GCP6-facing side is associating and dissociating till it is stabilised in the last steps of the assembly process.

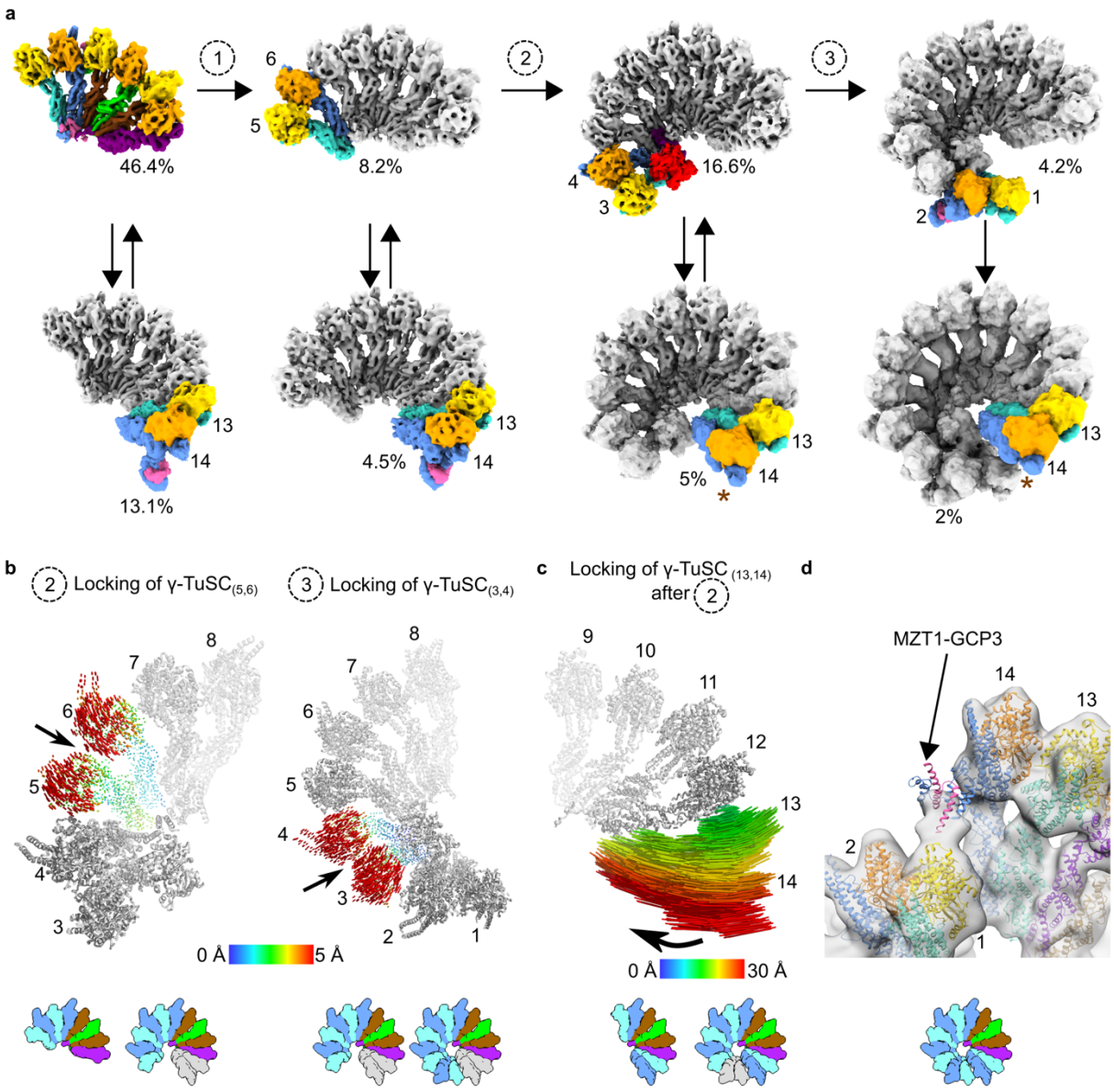

Figure 41: γ-TuRC assembly driven by a successive expansion of the 6-spoked assembly intermediate by the γ-TuSC units.
a) One of the possible γ-TuRC assembly pathways. The γ-TuSC units expanding the γ-TuRC intermediates are coloured the same way as in Figure 35 together with other new components, such as actin. Spoke numbering for the newly bound γ-TuSC units is given per each step. Brown asterisks are indicating the γ-TuSC$_{(13\text{-}14)}$ unit in the locked conformation. The fraction of particles per each reconstruction relative to all particles of the assembly intermediates is given.
b) Left, conformational rearrangement/locking of the γ-TuSC$_{(5\text{-}6)}$ unit upon the expansion of the intermediate by the γ-TuSC$_{(3\text{-}4)}$ unit visualised in vector representation and coloured according to R.M.S.D. Right, conformational rearrangement/locking of the γ-TuSC$_{(3\text{-}4)}$ unit upon the expansion of the intermediate by the γ-TuSC$_{(1\text{-}2)}$ unit. Same representation as on the left side. Colour scheme with R.M.S.D. scale is given. Arrows indicate direction of rearrangements. Spoke numbering is given.
c) Conformational rearrangement/locking of the γ-TuSC$_{(13\text{-}14)}$ unit after the luminal bridge completion visualised as in panel (**b**). Colour scheme with R.M.S.D. scale is given. Arrow indicates direction of the rearrangement.
d) Zoom on the MZT1-GCP3 module at GCP3$_{(14)}$ of the locked γ-TuSC$_{(13\text{-}14)}$ unit. MZT1 is binding to γ-tubulin of GCP2$_{(1)}$. Spoke numbering is given. The MZT1-GCP3 module is indicated by arrow. Ambient representations of particle sets used for the reconstructions are given.
Figure was modified from Würtz *et al*., 2022[229].

3.3.5 Characterisation of the γ-TuSC oligomerisation properties

The main iterative step of γ-TuRC assembly is the expansion of the intermediates by the preformed γ-TuSC units. It has been observed that the human γ-TuSC can oligomerise into a ring-like structure under mild crosslinking conditions[189]. Thus, Martin Würtz decided to characterise oligomerisation properties of the γ-TuSC under a variety of concentrations. Martin Würtz expressed components of the γ-TuSC and purified it via GCP3-2xFLAG and anion exchange chromatography. The purified sample was analysed by SDS-PAGE, negative stain EM and 2D class averaging performed by Dr. Annett Neuner and Martin Würtz (Fig. 42a-c). The sample was diluted in series to investigate the oligomerisation behaviour in a dependence on protein concentration. The ratio of oligomeric to monomeric γ-TuSC units and the size of oligomers increased as a function of concentration (Fig. 43a-c). The γ-TuSC had a capability to self-oligomerise, but only at concentrations higher than 0.5 µM, excluding that concentration-driven γ-TuSC oligomerisation is the central process during γ-TuRC assembly under physiological concentrations. Therefore, it is likely that the γ-TuRC provides some additional stabilisation for the incorporated γ-TuSC units. A candidate to mediate such stabilisation of the γ-TuSC units on the GCP4-facing side is the GCP6 NTE (Fig. 44a), which includes a long N-terminal α-helix (6.4 nm) positioned perpendicularly to the GRIP1 domains of the γ-TuSC$_{(3\text{-}4,5\text{-}6,7\text{-}8)}$ units and extends towards the GRIP1 domain of the γ-TuSC$_{(1\text{-}2)}$ unit (Fig. 44a). Stabilisation of the γ-TuSC$_{(13\text{-}14)}$ unit is likely mediated by an unassigned feature in the γ-TuRC cryo-EM reconstructions directly binding to the GRIP1 domains of the γ-TuSC$_{(13\text{-}14)}$ unit and potential candidates could be the GCP5 or GCP6 insertions (Fig. 44b).

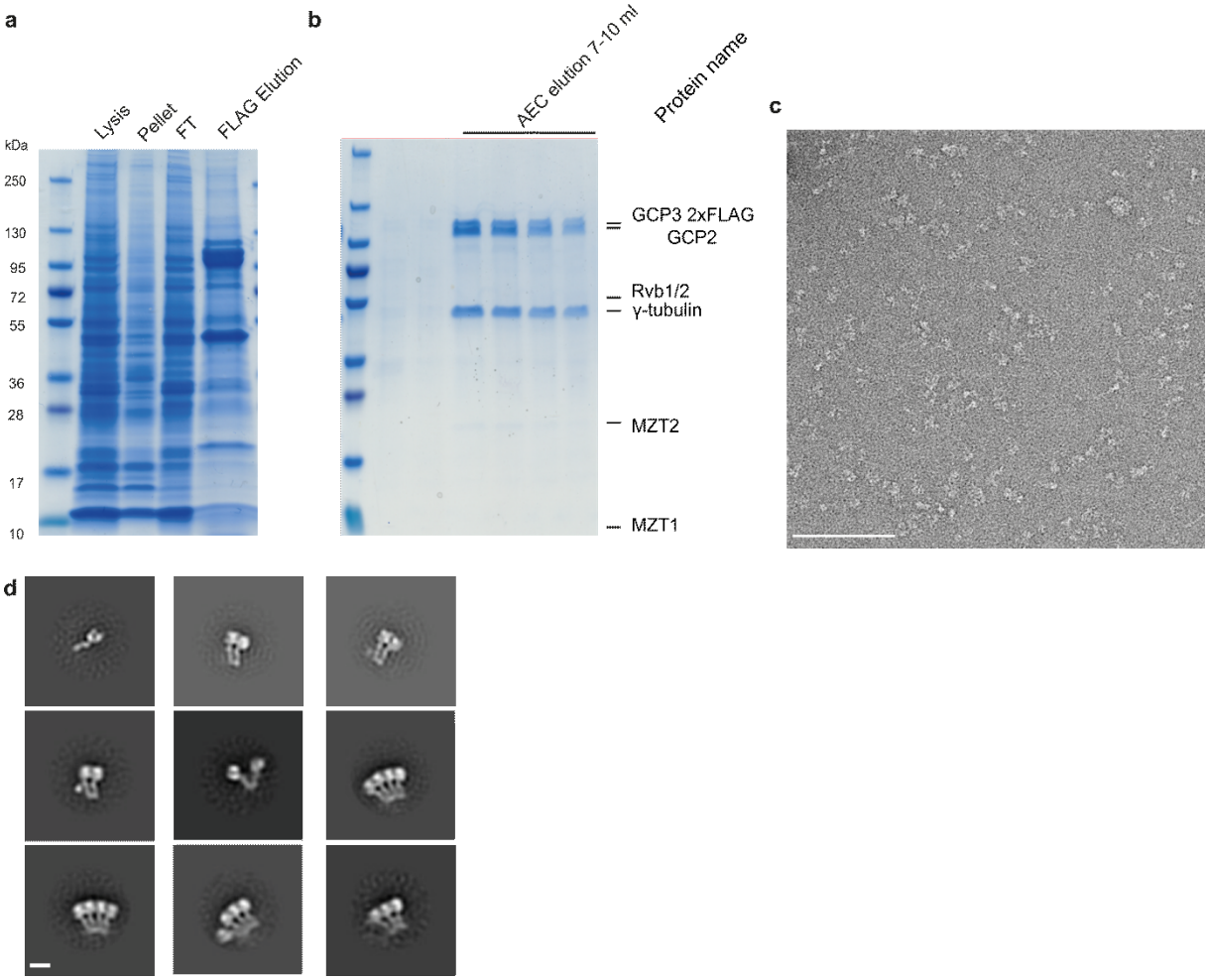

Figure 42: Characterisation of the purified recombinant human γ-TuSC.
a) SDS-PAGE of the purified γ-TuSC. Applied samples and molecular weights are given (FT-flowthrough).
b) SDS-PAGE of the purified γ-TuSC after anion exchange chromatography (AEC). Protein names, applied samples and molecular weights are given.
c) Negative stain EM of the recombinant human γ-TuSC. Zoom on a representative image from acquired data. Scale bar, 125 nm (image).
d) Representative class averages from negative stain EM of the recombinant human γ-TuSC. Scale bar, 10 nm.
Data in panels (**a, b, d**) were produced by Martin Würtz and data in panel (**c**) were produced by Dr. Annett Neuner.
Figure was modified from Würtz *et al*., 2022[229].

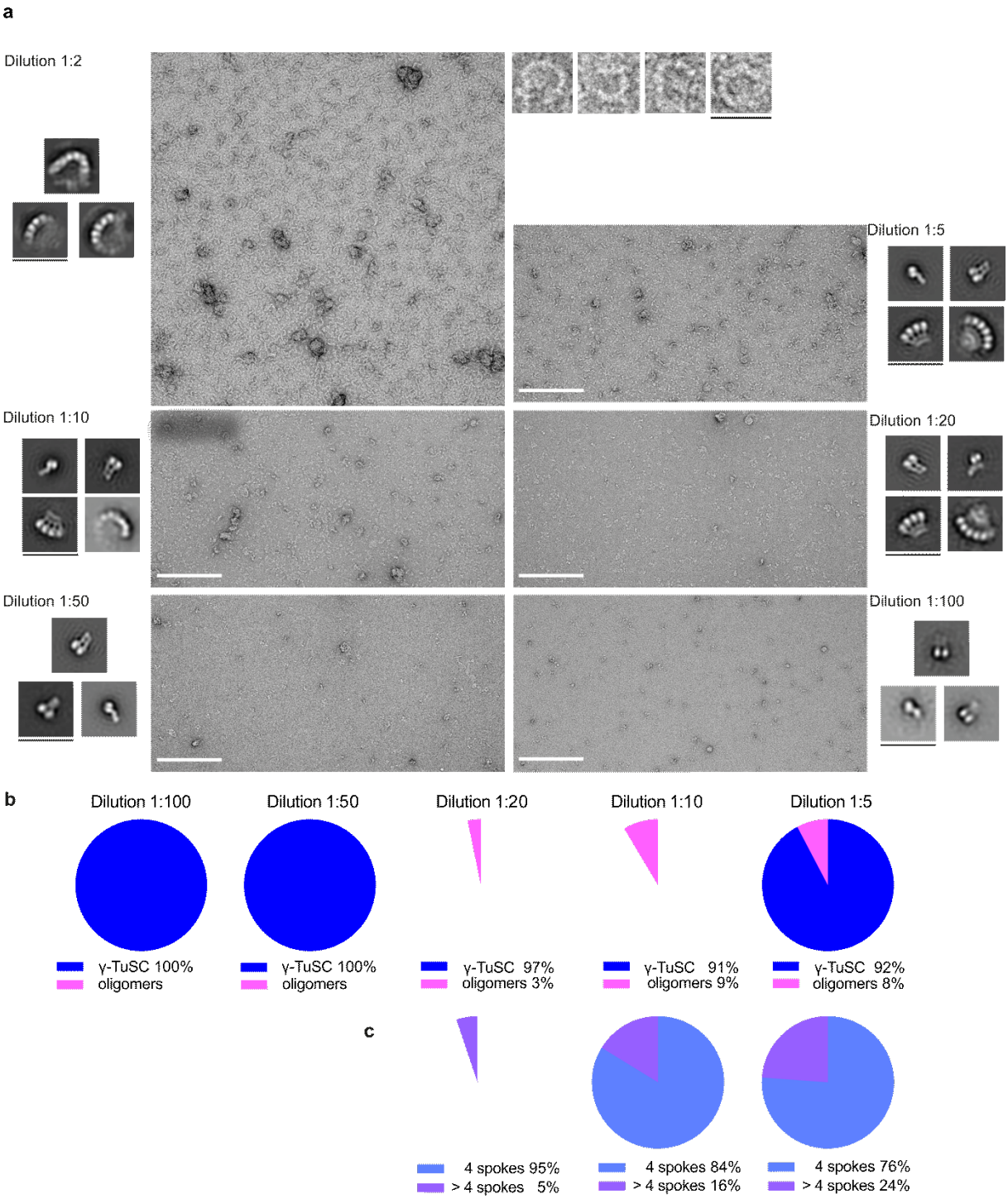

Figure 43: Concentration-dependent oligomerisation of the recombinant human γ-TuSC.
a) Negative stain EM representative images- one per each dilution. Dilution 1:2 with zoom on four representative particles. Representative class averages are shown per each dilution. Scale bars, 250 nm (images), 42 nm (particles and class averages).
b) Ratio of the γ-TuSC monomers (blue) vs γ-TuSC oligomers (pink) in each dilution.
c) Ratio of the γ-TuSC dimers (light blue) vs bigger γ-TuSC oligomers (purple) in each dilution.
Data in panel (**a**) were produced by Martin Würtz and Dr. Annett Neuner and data in panels (**b, c**) were produced by Martin Würtz.
Figure was modified from Würtz *et al*., 2022[229].

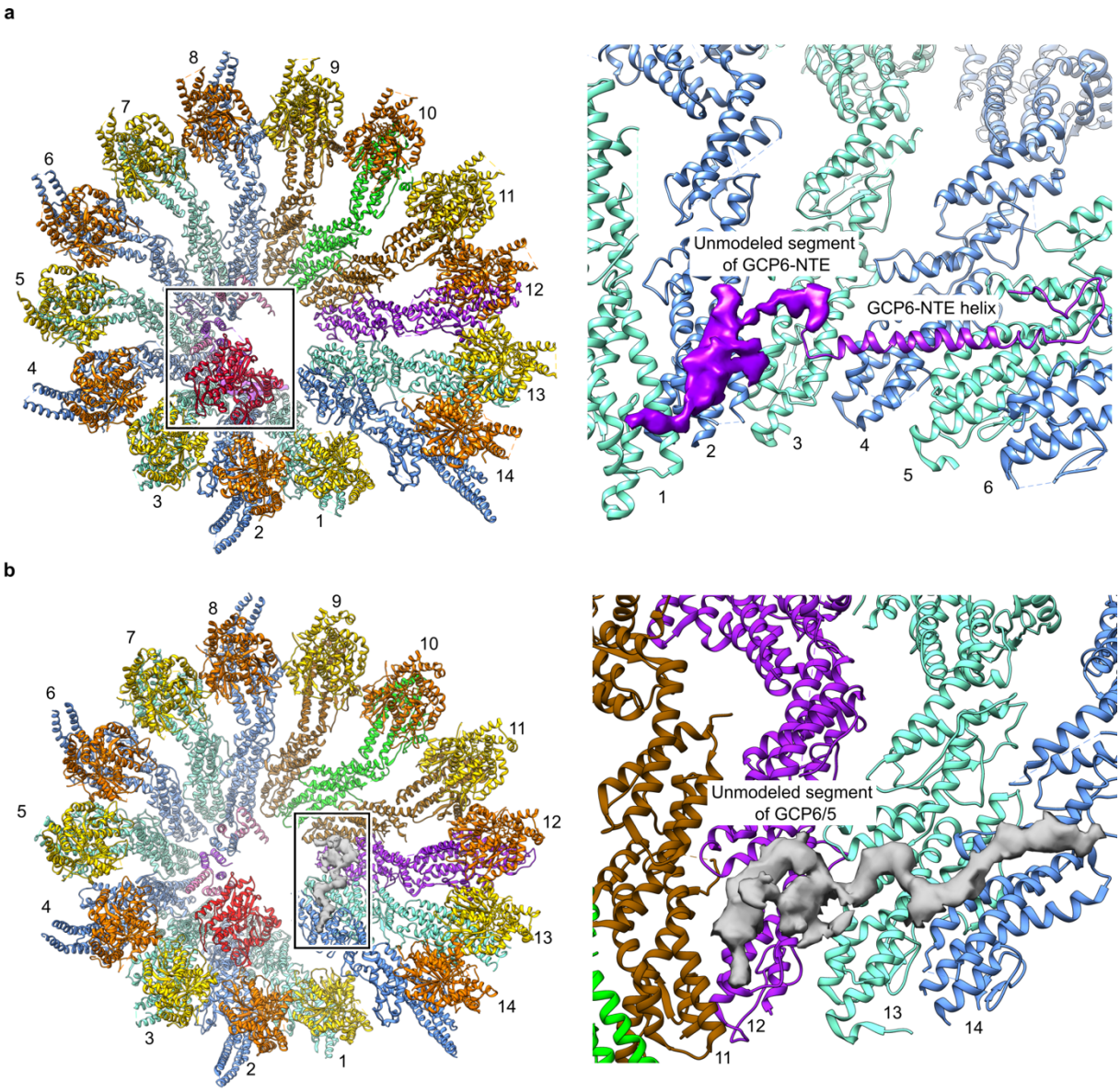

Figure 44: The GCP6 NTE stabilises the γ-TuSC units on the GCP2$_{(7)}$-facing side.
a) Left, model of the γ-TuRC with an indicated region (black rectangle) of the GCP6 NTE. View on the GCP6 NTE interacting with all γ-TuSC units on the GCP2$_{(7)}$-facing side. Spoke numbering is given.
b) Left, model of the γ-TuRC with an indicated region (black rectangle) of an unassigned segment. View on the unassigned segment that is likely represented by the GCP5 or GCP6 insertion and interacts with the γ-TuSC$_{(13-14)}$ unit. Spoke numbering is given.
Figure was modified from Würtz *et al*., 2022[229].

3.3.6 Role of actin in γ-TuRC assembly

The identification of actin as an integral component of the γ-TuRC led to questions about its role, e.g. in structural integrity or in recruitment of the γ-TuSC$_{(1-2)}$ unit, which actin directly interacts with. Introduction of a recombinant system for expression of the γ-TuRC allowed me, Martin Würtz, and Ariani Rahadian (RG Schiebel, ZMBH) to address the role of actin in the γ-TuRC. Because actin is one of the most abundant proteins in the cytosol and essential for cell survival, Martin Würtz and I decided to specifically prevent actin incorporation into the γ-TuRC instead of depleting actin from the expression system. To do so, I revisited a published cryo-EM reconstruction of the γ-TuRC[228] and analysed the interface between actin and its

surrounding components in detail. I could confirm a major interface between actin and the MZT1-GCP6 module, which would likely be responsible for the actin incorporation (Fig. 45a). To test this hypothesis, Ariani Rahadian coexpressed FLAG-MZT1 with the GCP6-NTE (1-126), which was tagged with 8x-His, in *E. coli* and purified the MZT1-GCP6-NTE module. The sample was used for Co-IP experiments, demonstrating the capability of the MZT1-GCP6-NTE module to pull down actin while the GCP6-NTE without MZT1 did not bind to actin. This experiment showed that the MZT1-GCP6-NTE module was sufficient for actin binding, independent from other γ-TuRC components (Fig. 46a). Actin binding to the MZT1-GCP6 module is mediated by the two N-terminal α-helices of GCP6 with several key residues forming the interface (Fig. 45a). Thus, Ariani Rahadian coexpressed FLAG-MZT1 together either with a trimmed version of the GCP6-NTE segment (57-126) or with the GCP6-NTE segment (1-126) containing different combinations of point mutations of the key residues. Co-IP showed no binding of actin to the N-terminally truncated MZT1-GCP6-NTE module, confirming the central role of the two GCP6 N-terminal α-helices in actin binding (Fig. 46a). Additionally, none of the combinations of point mutations pulled down actin, confirming the role of specific GCP6 residues in forming the interface (Fig. 47d). Having validated the role of the GCP6 N-terminus in actin binding, Martin Würtz prepared the mutant recombinant human γ-TuRC by replacing GCP6 by its N-terminally truncated version GCP6$^{(\Delta N56)}$. The recombinant construct was expressed and purified according to the same protocols as the recombinant wild-type γ-TuRC. The presence of the γ-TuRC components and integrity of the complex were confirmed by SDS-PAGE and negative stain EM performed by Dr. Annett Neuner and Martin Würtz (Fig. 47a-c). The γ-TuRC$^{(\Delta N56\text{-}GCP6)}$ was subsequently analysed by cryo-EM, confirming again the presence of assembly intermediates similar to the sample of the recombinant wild-type γ-TuRC, but also showing the fully assembled γ-TuRC$^{(\Delta N56\text{-}GCP6)}$ reconstructed at 7.1 Å global resolution (Fig. 45b). The cryo-EM reconstruction of the γ-TuRC$^{(\Delta N56\text{-}GCP6)}$ was almost identical to the fully assembled wild-type γ-TuRC, except for the absence of actin and the two N-terminal GCP6 α-helices (Fig. 45c and Fig. 46b), while the density segment representing the luminal bridge was still well resolved (Fig. 46c). The presence of MZT1 in the second module further indicated that the two N-terminal GCP6 α-helices are not required for stable MZT1 incorporation (Fig, 46c). Integration of other γ-TuRC components was unaffected, revealing that actin is dispensable for the γ-TuRC structural integrity and γ-TuRC assembly, in particular for recruitment of the γ-TuSC$_{(1\text{-}2)}$ unit (Fig. 46b), which actin interacts with via its D-loop binding to γ-tubulin at GCP3$_{(2)}$ (Fig. 25c). Despite not having a role in the recruitment of the γ-TuSC$_{(1\text{-}2)}$ unit, actin may affect its conformation. Thus, I compared the position and conformation of the γ-TuSC$_{(1\text{-}2)}$ unit in the γ-TuRC$^{(\Delta N56\text{-}GCP6)}$ and in the wild-type γ-TuRC, noticing a displacement of the GRIP2 domains and associated γ-tubulins that resembled the conformational changes observed during the expansion of the 6-spoked assembly intermediate (Fig. 46d). This indicates a possible role of actin in conformational locking of the γ-TuSC$_{(1\text{-}2)}$ unit by pulling its GRIP2 domains and γ-tubulins towards the helical axis of the γ-TuRC, moving them closer to a MT-compatible geometry.

Study of the actin role as an integral component of the γ-TuRC in the arrangement of this complex was followed up by analysis of the actin role in MT nucleation mediated by the γ-TuRC *in vivo*. Dr Enrico Atorino prepared cell lines expressing either the wild-type GCP6 or the N-terminally truncated GCP6 (ΔN-GCP6) or GCP6 with combinations of point mutations of the key residues forming the interface for actin. Depleting the endogenous GCP6 with siRNA, he observed very poor re-nucleation of MTs after their cold-induced depolymerisation for all GCP6 mutant versions compared to the wild-type GCP6, which re-polymerise MTs to a similar extent

as the endogenous GCP6. Furthermore, expression of GCP6 mutant versions in this cell line caused defects in mitosis including mitotic delays of 30-40 minutes, detached spindle poles from centrosomes and defective kinetochore-microtubule attachments probably due to chromosome misalignments.

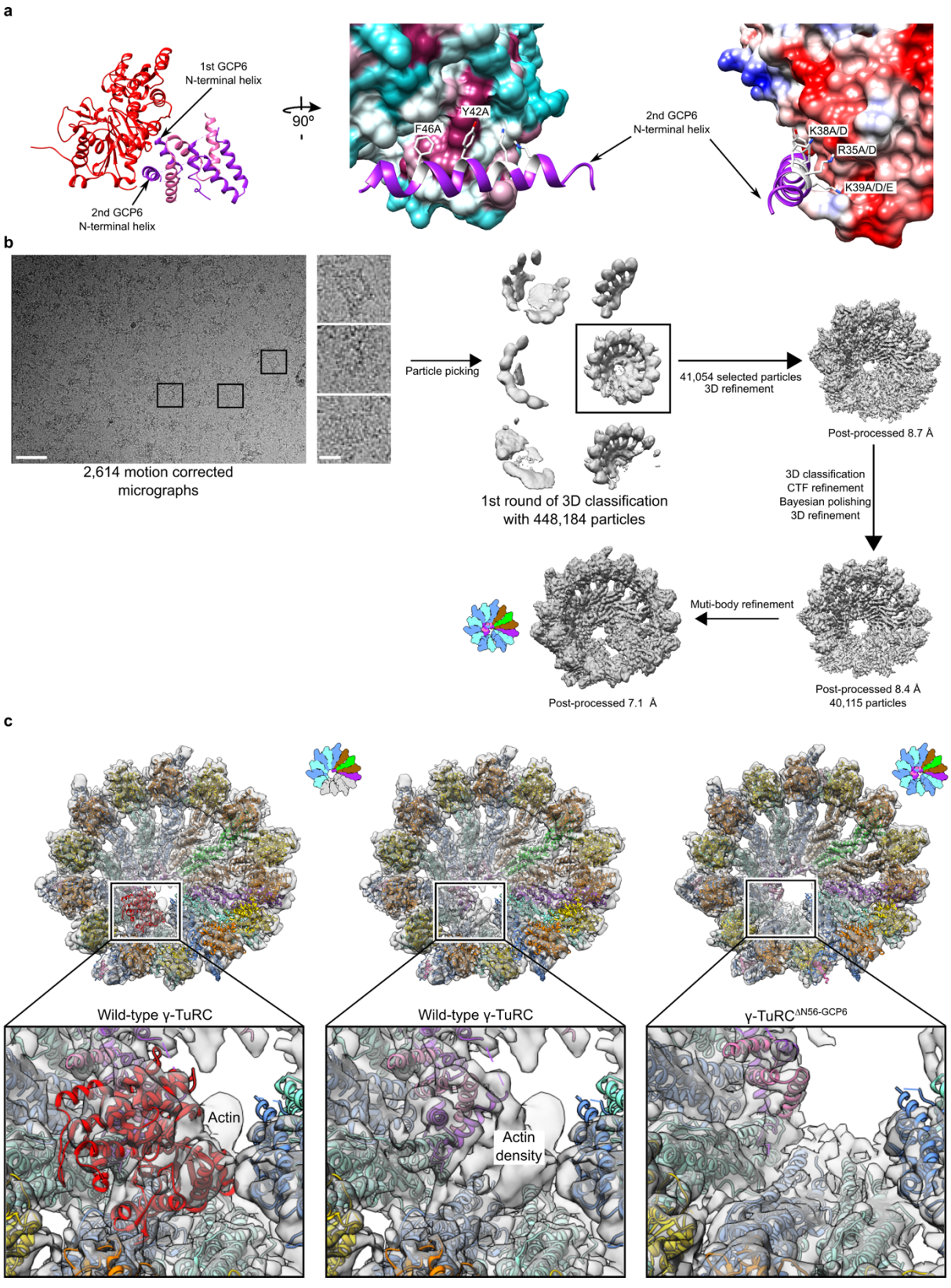

Figure 45: Schematic flowchart of cryo-EM data processing for the recombinant human γ-TuRC$^{\Delta N56\text{-}GCP6}$ and revealing the absence of the actin density segment.
a) Left, characterisation of the actin-MZT1-GCP6 module interface. The first two GCP6 N-terminal α-helices interacting with actin are indicated. Colour scheme same as in Figure 35. Middle, Hydrophobic interface between actin and the second N-terminal helix of GCP6. Actin displayed in surface representation coloured according to a hydrophobicity (cyan-hydrophilic, maroon-hydrophobic). Side chains of residues coming from the GCP6 N-terminal helix interacting with actin are displayed and coloured in white. Hydrophobic residues and their suggested mutations are indicated. Right, Electrostatic interface between actin and the second N-terminal helix of GCP6. Actin displayed in surface representation coloured according to a coulombic potential (blue-positive, white-neutral red-negative). Side chains of residues coming from the GCP6 N-terminal helix interacting with actin are displayed and coloured in white. Positively charged residues and their suggested mutations are indicated.
b) Zoom on a representative image from acquired data of the recombinant human gTuRC$^{\Delta N56\text{-}GCP6}$. Three representative particles are shown and indicated on the image by black rectangles. Scale bars, 80 nm (image), 20 nm (particles). The number of acquired images is given. Picked particles were subjected to two 3D classifications yielding a final set of particles that were refined into the final reconstruction of 7.1 Å resolution. All processing steps are given. Ambient representation of the γ-TuRC$^{\Delta N56\text{-}GCP6}$ particle set is given and used in other figures.
c) Cryo-EM reconstructions of the wild-type γ-TuRC and the γ-TuRC$^{\Delta N56\text{-}GCP6}$ with focus on the actin density segment. The actin density segment is absent in the γ-TuRC$^{\Delta N56\text{-}GCP6}$ reconstruction.
Figure was modified from Würtz *et al*., 2022[229].

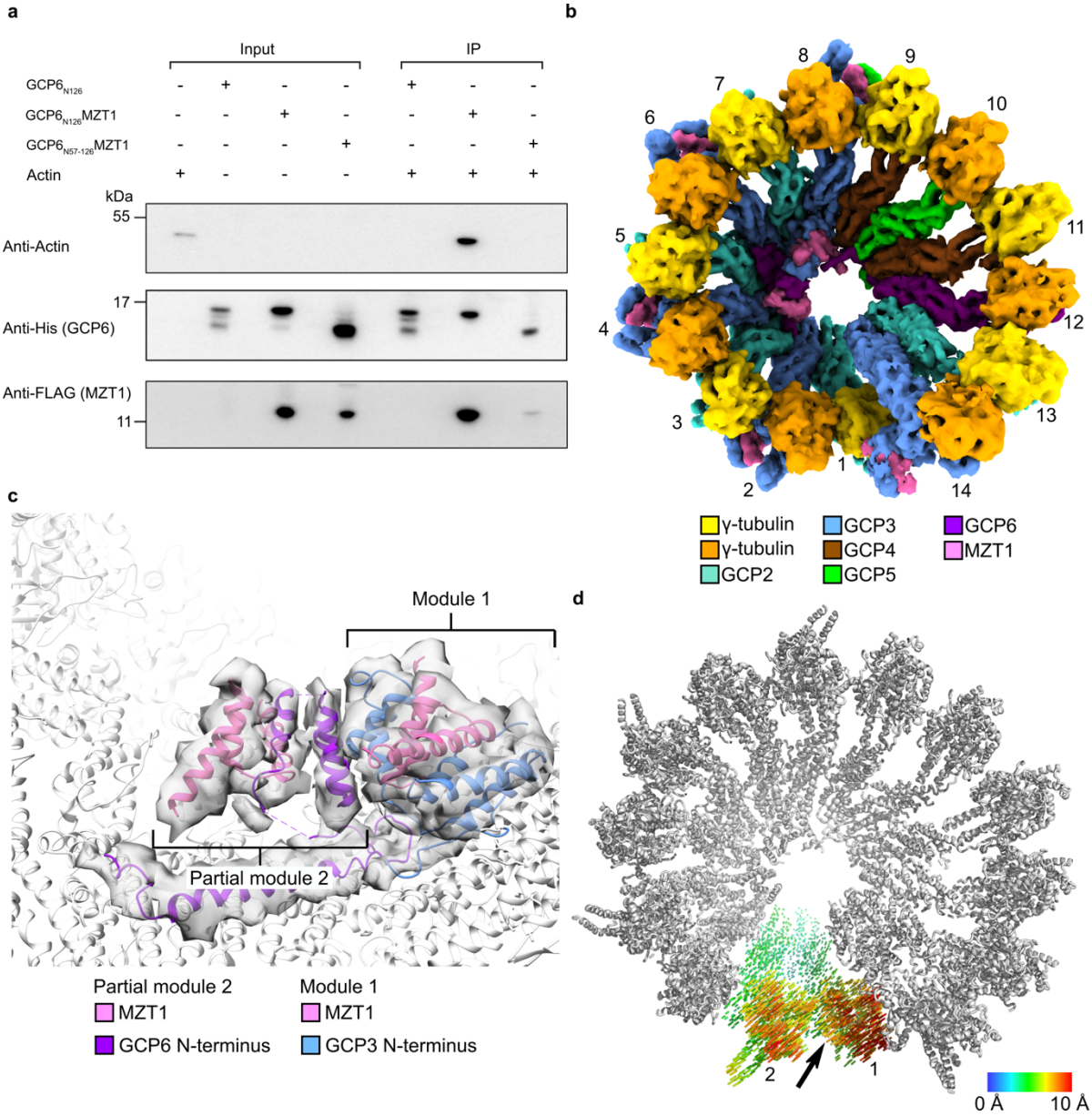

Figure 46: Actin has no impact on γ-TuRC assembly but affects conformation of the γ-TuSC$_{(1-2)}$ unit.
a) Immunoblot of the GCP6 N-terminal constructs with MZT1 and actin. The absence of MZT1 prevents actin binding as well as the absence of the first two N-terminal helices of GCP6 (GCP6$_{N57-126}$).
b) Segmented cryo-EM reconstruction of the GCP6$^{\Delta N56\text{-}GCP6}$ showing an impaired ability to recruit actin into the γ-TuRC. Spoke numbering is given. Colour scheme is given.
c) Zoom on the luminal bridge of the GCP6$^{\Delta N56\text{-}GCP6}$ cryo-EM reconstruction. Components of the luminal bridge are coloured. Rest of the atomic model is coloured in grey. MZT1 modules are indicated and colour scheme is given. Density segment representing the luminal bridge is coloured in transparent grey. Density segments of the deleted GCP6 N-terminal helices and actin are absent as expected.
d) Effect of actin on conformation of the γ-TuSC$_{(1-2)}$ unit visualised in vector representation and coloured according to R.M.S.D. The presence of actin lead to pulling of γ-tubulins from the γ-TuSC$_{(1-2)}$ unit towards the helical axis of the γ-TuRC. Arrow indicates direction of a motion. Colour scheme with R.M.S.D. scale is given.
Data in panel (**a**) were produced by Ariani Rahadian and Anna Böhler.
Figure was modified from Würtz *et al*., 2022[229].

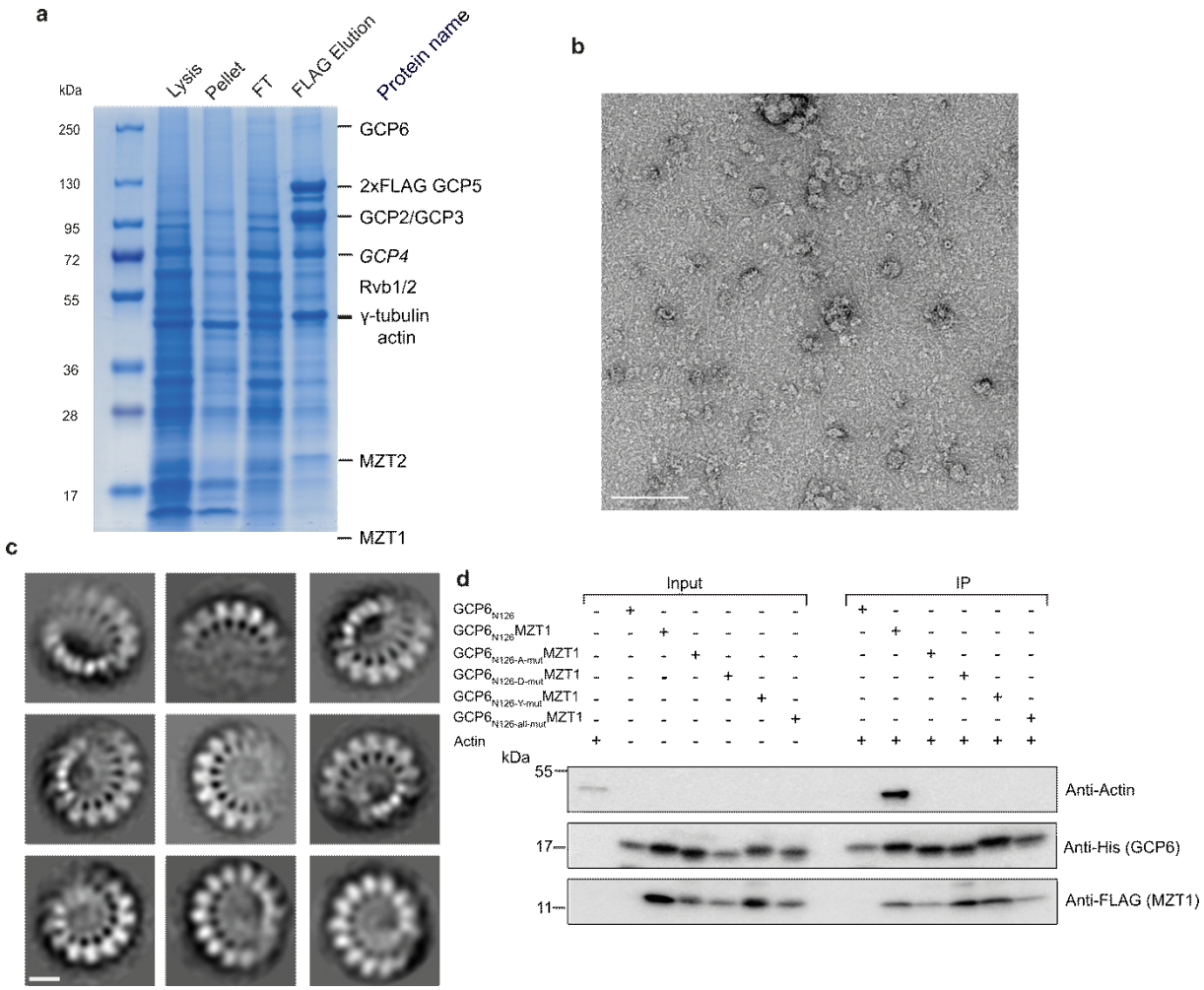

Figure 47: Characterisation of the purified recombinant human γ-TuRC$^{\Delta N56\text{-}GCP6}$.
a) SDS-PAGE of the purified γ-TuRC$^{\Delta N56\text{-}GCP6}$. Protein names, applied samples and molecular weights are given (FT-flowthrough).
b) Negative stain EM of the recombinant human γ-TuRC$^{\Delta N56\text{-}GCP6}$. Zoom on a representative image from acquired data. Scale bar, 125 nm (image).
c) Representative class averages from negative stain EM of the recombinant human γ-TuRC$^{\Delta N56\text{-}GCP6}$. Scale bar, 10 nm.
d) Immunoblot of the GCP6$_{N126}$ construct coexpressed with MZT1. Constructs for GCP6$_{N126}$ with different point mutations suggested according to the analysis of the GCP6-actin interface in Figure 45. Combinations of proteins (GCP6$_{N126}$ with different point mutations), used antibodies and molecular weights are given.
Data in panel (**a, c**) were produced by Martin Würtz.
Data in panel (**b**) were produced by Dr. Annett Neuner.
Data in panel (**d**) were produced by Ariani Rahadian and Anna Böhler.
Figure was modified from Würtz *et al*., 2022[229].

4 Discussion

Studying γ-TuCs using cryo-EM SPA provided new insights into the structure and assembly of fungal and vertebrate MT nucleation templates. Structures of these complexes shed light on their stabilisation principles and conformation in relation to MTs, revealing marked differences between fungal and vertebrate MT nucleation systems. Moreover, I elucidated the roles of specific structural features in establishing the geometry of γ-TuCs and their function. My data were confirmed and complemented by biochemical analyses and together will allow for detailed analysis of these MT nucleation templates in the context of the centrosome or during MT nucleation in the future.

4.1 The *C. albicans* γ-TuSC

4.1.1 Role of the Spc97 NTE

Cryo-EM analysis of the *C. albicans* γ-TuSC revealed a stable heterotetrameric complex (Fig. 10a) of almost identical Y-shape as described before for the *S. cerevisiae* γ-TuSC in cryo-EM reconstruction of a medium resolution [153,223] or for the vertebrate γ-TuSC in the context of the full γ-TuRC[219-221] (Fig. 25a), illustrating stability and conservation of the γ-TuSC quaternary structure. My *C. albicans* γ-TuSC cryo-EM reconstruction allowed to unambiguously fit the GRIP1 and GRIP2 domains of Spc proteins together with their associated γ-tubulins. Surprisingly, assignment of these components did not cover the full cryo-EM reconstruction of the *C. albicans* γ-TuSC but left a small density segment at the periphery of the GRIP1 domains unassigned (Fig. 10a). The reconstruction of the human recombinant γ-TuRC revealed similar segments at the periphery of the γ-TuSC GRIP1 domains that were identified as a part of the GCP2 NTE[189]. Thus, it is likely that the unidentified *C. albicans* density segment is represented by the 100 residues of the Spc97 (GCP2) NTE that were not resolved in the cryo-EM reconstruction (Fig. 10c). Additionally, the density segment projects towards the N-terminal part of the GRIP1 domain in the reconstruction of the *C. albicans* γ-TuSC further supporting this hypothesis. Both fungal and vertebrate GCP2 contain the NTEs preceding the GRIP1 domain, however their length is very different. The NTE of GCP2 was shown to bind MZT2[228], which is not encoded in fungi. Furthermore, AlphaFold[234] predicts the NTE of *S. cerevisiae* Spc97 as an extended loop indicating that the Spc97 NTE does not form a specific fold, contrary to the α-helical character of vertebrate GCP2 NTE segments. This raises questions about the function of the Spc97 NTE and potential binding partners other than MZT2.

4.1.2 Role of the Spc98 NTE

The NTE of Spc98 (the homolog of vertebrate GCP3) in the *C. albicans* γ-TuSC reconstruction was not resolved contrary to the Spc97 (GCP2) NTE (see above). In vertebrates, the GCP3 NTE has been shown to bind MZT1, which is expressed in *C. albicans* but missing in *S. cerevisiae*. Binding of the MZT1 to the Spc98 (GCP3) NTE was shown also for *C. albicans* based on the impotence of the NTE-truncated Spc98 to bind MZT1[159]. The module formed by the vertebrate GCP3 NTE and MZT1 was identified and structurally characterised in the vertebrate γ-TuRC[228,232], forming a globular fold of α-helical bundle contributed by both MZT1 and the GCP3 NTE. Considering that MZT1 is very well conserved across many organisms[159,160,190,235,236] and that AlphaFold[234] predicts an almost identical secondary structure for the *C. albicans* Spc98 NTE as for the vertebrate GCP3 NTE, it is highly probable that similar Spc98-MZT1 modules are being formed in *C. albicans*. However, even in the absence of MZT1 in our expression system for the *C. albicans* γ-TuSC, we could purify a stable complex, indicating that MZT1 is not required for an assembly of the γ-TuSC in *C. albicans*, contrary to the vertebrate system[229,230].

4.1.3 Ligand status of γ-tubulin

It is known that α/β tubulins are GTPases that bind either GTP or GDP. However, nucleotide ligand status of γ-tubulin in γ-TuCs was a mystery for a long time. Investigation of my γ-TuSC reconstruction showed that the *C. albicans* γ-tubulins are in the GDP state when assembled in the γ-TuSC (Fig. 10e, Table 1). This observation was also in agreement with the GDP state determined for γ-tubulins in the vertebrate γ-TuRC cryo-EM reconstructions[189,220], which was surprising considering that purification buffers contained only GTP. Thus, it is unclear whether γ-tubulin binds to Spc (GCP) proteins in a GDP state directly or contains GTP that is hydrolysed upon binding of γ-tubulin to Spc (GCP) proteins. Furthermore, it is not clear whether γ-tubulin in a GDP state binds in the straight conformation or the hydrolysis of GTP changes the conformation of γ-tubulin from curved to straight.

4.1.4 The extended interface between the γ-TuSC spokes

The subunit organisation of γ-TuSCs is similar in *C. albicans* and vertebrates, but the interface between spokes has diverged. Spoke assembly is driven in both systems by the GRIP1 domain interface between Spc97 (GCP2) and Spc98 (GCP3) but the character of the interactions differs in *C. albicans* and vertebrates (Fig. 12a, b). While the vertebrate γ-TuSC interface is characterised by charged residues, the *C. albicans* γ-TuSC contains mostly hydrophobic interactions (Fig. 12a, b). Another difference between the two systems is the GRIP2 domain interface of the *C. albicans* γ-TuSC. Containing insertions in Spc97, Spc98 and γ-tubulin, the *C. albicans* γ-TuSC is forming an extended interface that is stabilised by hydrophobic interactions (Fig. 12c-e). This interface provides additional stabilisation of the quaternary structure as demonstrated by deletion of the insertions that resulted in wider angles between spokes (Fig. 18b, c) and impaired MT nucleation (Fig. 17d and Fig. 18a). A similar interface was resolved recently in the high-resolution cryo-EM reconstruction of the *S. cerevisiae* γ-TuSC[222] but in contrary to the *C. albicans* γ-TuSC, it is formed only by the Spc98 insertion. Looking for a similar extended interface in the vertebrate γ-TuSC, I revealed charged residue patches interacting between adjacent γ-tubulins in the γ-TuRC (Fig. 19a). It still needs to be investigated whether this electrostatic interface has a similar effect on stabilisation of the vertebrate γ-TuSC conformation as the extended interface in the *C. albicans* γ-TuSC.

4.1.5 Sequence alignment of γ-TuSC components provides insights into the evolution of MT templates

Sequence alignment of the γ-TuSC components from organisms at different evolutionary stages revealed several specific differences between the simple fungal γ-TuSC MT nucleation system and the more complex vertebrate MT nucleation system. The *C. albicans* γ-TuSC contains an extended GRIP2 domain interface that was also identified in the *S. cerevisiae* γ-TuSC[222], both of them formed primarily by a Spc98 (GCP3) insertion. This insertion was identified only in fungi of *Saccharomycetes* (Fig. 19b), indicating high organism specificity of this interface. On the other hand, this class of fungi is missing oppositely charged patches on γ-tubulins forming a γ-tubulin interface in other eukaryotes (Fig. 19c). Blast searches further revealed that *Saccharomycetes* species are missing homologs of the γ-TuRC-specific components GCP4,5,6, which were identified in all other searched eukaryotes, including eukaryotes that branched off earlier than *Saccharomycetes* during evolution (Fig. 20). This indicates that the *Saccharomycetes* γ-TuSC system evolved by simplification of an ancestral γ-TuRC system, accompanied by an altered spoke interface. In fungi, the γ-TuSC nucleates MTs not only on the cytosolic side but also on the nuclear side of the SPB. Stabilisation of the γ-TuSC in heterotetrameric form opposed to a 30 nm assembled γ-TuRC may allow for easier

transfer of the complex into the nucleus. Moreover, the fungal MT nucleation system nucleates only a small number of MTs, even during mitosis, compared to the vertebrate system. Thus, assembling the ring-like oligomer of the γ-TuSCs heterotetramers needed for MT nucleation directly at the SPB is likely sufficient, as opposed to the preassembly mechanism of the vertebrate γ-TuRC. Despite the presence of the γ-TuRC-specific GCPs in the most of eukaryotes, some organisms, such as *Drosophila melanogaster*, are viable upon deletion of GCP4,5,6 and nucleate MTs at the centrosome using only the γ-TuSC system[237] as opposed to the vertebrate system where depletion of these proteins leads to spindle defects[179,190]. Such hybrid MT nucleation system may represent step towards a reduction of complexity, as it occurred for Saccharomycetes.

4.1.6 Oligomerisation of the γ-TuSC units

Cryo-EM reconstruction of the *C. albicans* γ-TuSC in a heterotetrameric form showed a diverged arrangement of γ-tubulins from an ideal MT geometry similarly as for the S. cerevisiae γ-TuSC in the open conformation (Fig. 21a and Table 2). Because it was shown that *S. cerevisiae* γ-TuSC can mimic an ideal MT geometry[156], follow-up studies look for a trigger of these rearrangements and recent cryo-EM reconstruction of the *S. cerevisiae* γ-TuSC revealed a role of Spc110 showing that Spc110-induced oligomerisation of the γ-TuSC brings γ-tubulins into an ideal MT geometry[222]. Furthermore, it is highly probable that similar oligomerisation mechanism and rearrangement is mediated via Spc72 on the cytosolic side of the SPB where it takeovers the Spc110 function[139], however this need to be still investigated. Although Spc72 and Spc110 are present at the SPB of the *C. albicans*, oligomerisation behaviour of its γ-TuSCs could still differ from *S. cerevisiae* due to the unique Spc97 insertions (other than the insertions forming the extended interface) that are absent in the *S. cerevisiae* γ-TuSC and not resolved in the *C. albicans* γ-TuSC cryo-EM reconstruction. These insertions may stabilise the oligomerisation by changing the interface between the neighbouring γ-TuSC units. Another interesting aspect of the *C. albicans* γ-TuSC oligomerisation to be elucidated in the future is the role of MZT1 modules and their position in a ring-like complex. Follow-up studies will be necessary to probe the position of MZT1 modules in the *C. albicans* ring-like γ-TuSC oligomer and to explore whether MZT1 modules bind to the lumen of the γ-TuSC oligomer or to the periphery of Spc98 (GCP3) GRIP2 domains as shown in my recent reconstruction of the recombinant human γ-TuRC[220] (Fig. 35a).

4.2 The vertebrate γ-TuRC

4.2.1 Actin is a *bona fide* component of the γ-TuRC and a part of the luminal bridge

Assignment of GCPs into the γ-TuRC reconstruction revealed that the base of this complex is formed by the conserved GRIP1 domains and the conserved GRIP2 domains binding γ-tubulin molecules (Fig. 25b). Besides these regions, the cryo-EM reconstruction resolved a luminal density segment that was not assigned to γ-tubulin or the GRIP domains (Fig. 25a). One density segment in the lumen of the γ-TuRC was surprisingly identified as actin (Fig. 25c and Fig. 29d), which was observed before as a copurified protein of the γ-TuRC but always considered as a contaminant or an unrelated protein[175]. The rest of the luminal bridge density segment (Fig. 25a) was later identified as a multi protein scaffold formed by two structural modules, the MZT1-GCP3 module and the actin-interacting MZT1-GCP6 module[228]. However, these structural data did not provide any information about the role of actin in the γ-TuRC. Only the introduction of a recombinant expression system for the γ-TuRC[189,230,231] provided means to specifically remove actin from the complex. Excluding actin and MZT1 together from the expression system led to perturbed γ-TuRC assembly that resulted in γ-TuRC subcomplexes

with less than 14 spokes[230]. This showed the importance of a structurally intact luminal bridge for γ-TuRC assembly, but the effect could not be attributed specifically to actin, as both actin and MZT1 were excluded from the recombinant system. In our γ-TuRC assembly study, we approached the role of actin differently and dissected its contribution to structural integrity of the γ-TuRC by engineering a GCP6 variant without the actin binding site. Using this approach, I was able to demonstrate that actin does not contribute to the γ-TuRC stability and assembly, observing only small conformational changes on the γ-TuSC$_{(1-2)}$ unit GRIP2 domains with their associated γ-tubulins (Fig. 46b ,d). In combination, these data on mutant variants of the recombinantly expressed γ-TuRC indicate an important role of MZT1 on γ-TuRC assembly and stability by forming the luminal bridge.

Considering the fold of MZT1-GCP modules formed by intertwined α-helices, it is likely that the GCP NTEs are not sufficiently stable without binding of MZT1 and cannot fulfil their function *in vivo*. Consistently, the X-ray structures of the GCP NTEs could only be obtained in a complex with MZT1[232]. While my results excluded a role of actin in γ-TuRC assembly and structural intergrity, *in vivo* experiments with actin-deficient γ-TuRC performed by Dr. Enrico Atorino[229] (RG Schiebel, ZMBH) revealed a role of actin in MT nucleation and spindle formation during mitosis. Defective and detached spindles observed for the actin-deficient γ-TuRC indicates either a direct role of actin in MT nucleation, e.g. by modulating the γ-TuRC geometry (Fig. 46d), or in recruitment of other MT nucleation effectors.

4.2.2 Role of the GCP NTEs and the GCP5 and GCP6 insertions

All GCPs except for GCP4 contain the NTEs and GCP5 and GCP6 have long insertions between the GRIP domains. Two GCP NTEs, one from GCP6 and one from GCP3, were identified as components of MZT1 modules that are part of the luminal bridge[228]. My cryo-EM reconstructions of the γ-TuRC assembly intermediates, specifically the 6-spoked assembly intermediate, allowed me to assign the GCP3$_{(8)}$ NTE to the luminal bridge MZT1 module (Fig. 37a, b). Other MZT1-GCP3 modules were not resolved in the cryo-EM reconstructions of the γ-TuRC (Fig. 25a)[189,220,221] due to flexibility of these modules mediated by a disordered loop of the GCP NTEs between the GRIP1 domain and very N-terminus of the NTEs binding MZT1. The X-ray structures of MZT1 modules also revealed a module of MZT1-GCP5, in which the GCP5 NTE interacts with MZT1 in an almost identical manner as the GCP3 NTE and the GCP6 NTE.

The last type of the NTEs in the γ-TuRC is contributed by GCP2. The cryo-EM reconstruction of the *X. laevis* γ-TuRC did not resolve the position of any GCP2 NTE but a published human γ-TuRC reconstruction identified the position of one GCP2 NTE at spoke 13 and surprisingly in a helical fold with MZT2[228] binding together to the CM1 motif of Cdk5Rap2. The fold of MZT2 modules is similar to MZT1 modules and indicates that all GCP2 NTEs are intertwined with MZT2 and similarly as for the GCP3 NTEs, they are connected to the GRIP1 domains via disordered loop of the NTE, thus unresolved in the cryo-EM reconstructions[219-221]. Stable positioning of one MZT2-GCP2 module at spoke 13 is likely caused by CM1 motif binding that was used for purification of this particular γ-TuRC sample[220] compared to the other cryo-EM reconstructions[189,219,221]. This indicates that stabilisation of the MZT2-GCP2 module is dependent on the other γ-TuRC binding factors and itself may contribute to recruitment of these factors. The recombinant human γ-TuRC reconstruction identified another part of the GCP2 NTE aligned with the GRIP1 interface of each γ-TuSC unit in the γ-TuRC[189] showing another role of the GCP2 NTE, namely in stabilisation of the γ-TuSC units.

Additional GCP regions that were not resolved in the γ-TuRC reconstructions are the GCP5 and GCP6 insertions. The GCP5 insertion with approximately 100 residues is much shorter than the GCP6 insertion containing almost 800 residues (Fig. 22i). Circular dichroism of the N-terminal part of the GCP6 insertion revealed its helical character, which led to the initial hypothesis of the GCP6 insertion being part of the luminal bridge (Fig. 27e). Assignment of MZT1 and the NTEs to the luminal bridge left the GCP6 insertion unassigned. Small density segments lining GCPs in the lumen of the γ-TuRC that were resolved in all cryo-EM reconstructions could potentially represent parts of the GCP5 and GCP6 insertions[189,219-221] (Fig. 46b). The GCP6 insertion contains 9 repeats in human (8 repeats in *X. laevis* GCP6), the structure and function of which remains a mystery. The length of GCP6 insertion create the potential to let it serve as stabilisation or recruitment platform during γ-TuRC assembly, which would be supported by interactions observed towards GCP2 and GCP5 N-terminal segments including their GRIP1 domains. Although its function could not be assigned yet, the GCP6 insertion seems to be important, as genetic studies identified point mutations in patients suffering of microcephaly[238,239].

4.2.3 Identification of binding sites for residual MZT1 modules in the vertebrate γ-TuRC

The luminal bridge is composed of two MZT1 modules leaving five MZT1 modules unresolved and not rigidly bound to the γ-TuRC due to a flexible linker. Resolving the structure of MZT1 modules in the luminal bridge allowed for probing of their presence in other unassigned density segments of at that time available γ-TuRC reconstructions. One such density segment was present in my *X. laevis* γ-TuRC reconstruction at the periphery of $GCP3_{(14)}$ (Fig. 25a). Unexpectedly, the MZT1-GCP3 module of the luminal bridge fitted very well into this density segment, identifying binding site of one of the missing MZT1 modules[228]. Interestingly, the remaining GCP3 spokes in the γ-TuRC reconstructions did not have a stably bound MZT1 module at a similar position, suggesting that stable binding of the MZT1 module at the periphery of the GRIP2 domain of $GCP3_{(14)}$ could be linked to its position at the end of the spiral, in particular its proximity to $GCP2_{(1)}$. The γ-tubulin associated at $GCP2_{(1)}$ slightly contacting the MZT1 module at $GCP3_{(14)}$ could be a key factor for stabilisation of this module. Surprisingly, I could locate further MZT1 modules in the cryo-EM reconstructions of the recombinantly expressed human γ-TuRC and its assembly intermediates where MZT1 modules were present at the periphery of all GCP3 GRIP2 domains (Fig. 35a). Whether these are the only binding sites for MZT1 modules on the γ-TuRC or there are alternative binding sites will have to be established. Resolving MZT1 modules in γ-TuRC assembly intermediates led to assignment of the MZT1-GCP5 module at the periphery of $GCP3_{(8)}$ GRIP2 domain and assignment of the MZT1-GCP3 module in the luminal bridge to a specific GCP3 copy, namely $GCP3_{(8)}$ (Fig. 36a, c and Fig. 37b, c). Whether MZT1 modules are bound on the periphery of the GCP3 GRIP2 domain in the γ-TuSC unit before incorporation of the unit into the γ-TuRC during the assembly or are recruited afterwards remains to be investigated. Considering that most of MZT1 modules were not resolved at the periphery of all GCP3 GRIP2 domains in the reconstructions of the native γ-TuRC[219-221], it is likely that binding or release of MZT1 modules is regulated by PTMs, such as phosphorylation or by other γ-TuRC binding factors that are missing in the recombinant expression system thereby retaining MZT1 modules in their initial position.

4.2.4 Compatibility of the γ-TuRC conformation with the MT lattice

The MT lattice consists of 13 protofilaments while the γ-TuRC left-handed spiral is composed of 14 GCPs with associated γ-tubulins (Fig. 25a). In the 14-spoked fungal γ-TuSC ring-like

oligomer, the first and the last spokes are aligned along the helical axis in order to expose only 13 γ-tubulins for nucleation[156,223], almost perfectly mimicking MT geometry[156]. Interestingly, the geometry of the vertebrate γ-TuRC deviates from MT geometry (Fig. 31b, c), in particular in the second half of the ring harbouring the γ-TuRC-specific GCP4,5,6 and one γ-TuSC unit (Fig. 31e). Moreover, the first and the last spoke of the γ-TuRC are not completely aligned along the MT helical axis, which leaves the γ-tubulin at the first spoke partially exposed. In order to reach a MT-compatible geometry, the γ-TuRC would have to undergo a significant conformational change approximated by closure of the helical spiral, accompanied by alignment of the last and the first spoke (Fig. 31e). One of the helical parameters deviating from MT geometry is the spoke-wise pitch increment, which would lead to loose interfaces between some specific γ-tubulin copies and α/β-tubulin dimers in a typical MT (Fig. 31b). The pitch increment could locally be adjusted by changing angles between the GRIP1 and GRIP2 domains for the spokes with deviations of this parameter (Fig. 31d). It needs to be considered that any change in arrangement of the GRIP1 and GRIP2 domains would also move γ-tubulins closer or further away from the helical axis (Fig. 31c). However, it is still unclear if the γ-TuRC really has to reach MT geometry in order to efficiently nucleate MTs. Cdk5Rap2 is known to increase the γ-TuRC MT nucleation activity significantly, but no change in the geometry of the γ-TuRC upon binding of the Cdk5Rap2 CM1 motif was observed for the human γ-TuRC reconstruction purified via the CM1 motif[220]. This suggests that either the CM1 motif alone is not sufficient to change γ-TuRC geometry and the full length Cdk5Rap2 would be required or that a combination of several effectors, such as NEDD1, CEP192, Cdk5Rap2 and α/β-tubulin dimers binding to the γ-TuRC is necessary to bring the γ-TuRC to a MT-compatible geometry.

4.2.5 γ-TuRC binding partners

While the overall molecular architecture of the γ-TuRC has been described in detail, none of the established γ-TuRC-binding partners could be visualised in the complex with the γ-TuRC thus far. One exception is the CM1 motif of Cdk5Rap2, which was resolved in the cryo-EM reconstruction of the human γ-TuRC[220]. This allowed to identify its binding position on the γ-TuRC at the periphery of $GCP2_{(13)}$, contacting also $GCP6_{(12)}$[220]. Binding of the CM1 motif to $GCP2_{(13)}$ indicates an effect of the unique interface established by the neighbouring GCP6 subunit and the only stably bound MZT2 module[220,228], both likely essential in stabilisation of the CM1 motif and specification of its binding position. The absence of stably bound MZT2 modules at other GCP2 spokes emphasises the importance of GCP6 in defining the binding site. Surprisingly, the CM1 motif binds to the γ-TuRC as a dimer[220], suggesting that two Cdk5Rap2 molecules act on one γ-TuRC in concert, but it is not clear if dimerisation of the CM1 motif on the γ-TuRC is possible for the full length Cdk5Rap2 as well. Interestingly, fungal Spc110 (containing a CM1 motif), is known to act as a dimer on the γ-TuSC but only one copy of the CM1 motif directly binds to the complex but at different spoke position as the CM1 motif of Cdk5Rap2[222].

The other three prominent γ-TuRC binding partners, NEDD1, CEP192 and NME7, do not contain CM1 motifs and their position on the γ-TuRC has not been determined yet. NEDD1 was detected in the purified *X. laevis* γ-TuRC in 1-2 copies per the γ-TuRC by mass spectrometry, but no density segments representing NEDD1 were visible. High stoichiometry of NEDD1 on the γ-TuRC suggests that NEDD1 is not resolved because it is binding to flexible regions of the γ-TuRC, such as the GCP5 and GCP6 insertions or the GCP NTEs that were not resolved in the cryo-EM reconstructions of the native γ-TuRC[219-221]. CEP192 was on the other hand not detected in any purified γ-TuRC sample, but it is not surprising because this protein is reported to bind to the γ-TuRC only in the context of the PCM. Thus, it will be required

to test and establish CEP192 binding to the γ-TuRC via *in vitro* reconstitution, to find out if CEP192 can bind on its own to the γ-TuRC also outside of the PCM and if its binding position overlaps with the CM1 motif on the γ-TuRC. Finally, NME7 was copurified with the *X. laevis* γ-TuRC at high stoichiometry, but it could not be resolved in the reconstruction, as well. NME7 acts on the γ-TuRC by promoting its phosphorylation[181]. It may bind to and induce phosphorylation of the flexible GCP5 and GCP6 insertions, which would explain its absence in the cryo-EM reconstructions[219-221].

4.2.6 γ-TuRC assembly mechanism

The first cryo-EM reconstructions of the γ-TuRC indicated the presence of more than 30 proteins in this complex (Fig. 25a) and subsequent improvement in the resolution of reconstructions clarified the presence of additional components, such as MZT1 and MZT2. Although not all MZT modules are resolved, in particular MZT2 modules, stable fold of MZT proteins and the GCP NTEs indicates that MZT molecules are bound to each NTE of the γ-TuRC GCPs. Together, this increases the number of γ-TuRC proteins that form its base to 41 with most of them present in more than one copy (Fig. 35a). Still, all of the subunits assemble into a uniform γ-TuRC, which indicates tight control of the assembly process. Cryo-EM analysis of the recombinant human γ-TuRC sample allowed me to address its assembly mechanism from a structural perspective. The smallest and at the same time most populated intermediate observed using cryo-EM consisted of 6 spokes, corresponding to GCP2-3-4-5-4-6 that form the core of the fully assembled γ-TuRC at spokes 7-12 (Fig. 37a). Its high abundance and the absence of any smaller assembly intermediates indicate that the 6-spoked assembly intermediate is the smallest stable form. Larger intermediates reflect a modular assembly mechanism driven by the expansion of the 6-spoked intermediate by three preformed γ-TuSC units on the $GCP2_{(7)}$-facing side coupled with their conformational locking (Fig. 41a, b). The γ-$TuSC_{(13-14)}$ unit expanding the 6-spoked assembly intermediate on the GCP6-facing side binds in two different positions-position before and after stabilisation of the MZT1-GCP6-actin module in the luminal bridge (Fig. 41a, c). Stabilisation of the MZT1-GCP6-actin module is observed after recruitment of the γ-$TuSC_{(3-4)}$ unit and either one of these events or both of them may trigger allosteric effect that repositions the γ-$TuSC_{(13-14)}$ unit, e.g. by changing the interaction surface for binding of the γ-$TuSC_{(13-14)}$ unit. Final stabilisation of the γ-$TuSC_{(13-14)}$ unit on the ring is likely achieved by binding to the γ-$TuSC_{(1-2)}$ unit via a contact between γ-tubulin at spoke 1 with MZT1 module of $GCP3_{(14)}$ (Fig. 41d). The expansion of the γ-TuRC on the GCP6-facing side by the second γ-TuSC unit (a potential γ-$TuSC_{(15,16)}$ unit) is sterically impossible under the observed γ-TuRC geometry and would require further opening of the γ-TuRC left-handed spiral. The expansion by the γ-TuSC units is dependent on the presence of RUVBL1 and RUVBL2 ATPases that were shown to be crucial for effective γ-TuRC assembly and binding of γ-TuSC units[189].

Assembly of the γ-TuRC from preformed γ-TuSC units is consistent with results obtained from salt-induced disassembly of the γ-TuRC where γ-TuSC units were stripped away as modules. The existence of preformed γ-TuSC units in human was expected for years based on sucrose gradient sedimentation centrifugations[127,175,233] but never demonstrated on the protein level until recombinant γ-TuRC expression systems were established. When present in very high concentration, the preformed γ-TuSC units can self-oligomerise, but such a behaviour is unlikely under physiological conditions due to the low cytosolic concentration of the γ-TuSC. This suggests that γ-TuSC units are stabilised after the incorporation into the γ-TuRC to prevent their dissociation during the assembly process. Stabilisation of the γ-TuSC unit in the γ-TuRC

is achieved by the GCP6 NTE on the GCP4-facing side and maybe via the GCP5,6 insertions for the γ-TuSC$_{(13,14)}$ unit (Fig. 38a, b). When expressing all γ-TuRC components, the 6-spoked assembly intermediate is the smallest assembled form, but when omitting the γ-TuSC units, GCP4,5,6 assemble into a 4-spoked intermediate (Fig. 40e). This demonstrated that the 6-spoked assembly intermediate is preceded by smaller likely very transient intermediates. The 4-spoked assembly intermediate could be assembled from dimers of GCP4-5 and GCP4-6 or directly spoke-by-spoke from monomeric GCPs. High concentration of copurified ribosomes using 2xFLAG-GCP5 under certain conditions also indicates a potential co-translational step in the assembly process.

Important factors of γ-TuRC assembly are RUVBL1 and RUVBL2 AAA ATPases. Introduction of γ-TuRC recombinant expression systems demonstrated that the γ-TuRC can assemble without coexpression of these two ATPases but efficiency is significantly decreased yielding smaller number of the fully assembled γ-TuRCs[189,231]. The exact role of these ATPases is still elusive although it was shown that they have the ability to bind to the human γ-TuSC units and assemble them into a ring-like oligomers[189]. It is unclear in which step of γ-TuRC assembly these ATPases are participating and what is their function. Both ATPases can either recruit the units of the γ-TuRC and bring them to the assembly intermediates or they bind directly to γ-TuRC assembly intermediates and stabilise them. Another option is that they fulfil both aforementioned functions. It will be interesting to explore whether RUVBL AAA ATPases participate in the assembly of the 4-spoked intermediated formed by GCP4-5-4-6. Another aspect that need to be explored is the RUVBLs ATP hydrolysis during γ-TuRC assembly to find out which functions of these ATPases is affected by it.

5 Perspectives

Insights into the structure of the vertebrate γ-TuRC and the fungal γ-TuSC will allow for a more detailed investigation of MT nucleation mechanisms and how their function is coupled with other cellular factors.

In the future, it would be interesting to characterise the structural role of MZT1 in a ring-like oligomer of the *C. albicans* γ-TuSC and describe the position and role of the Spc97, Spc98 NTEs. Structures of the γ-TuSC with other factors, such as Spc72 and Stu2, would add a new layer of understanding how the fungal γ-TuSC system nucleates MT on the cytosolic face of the SPB and if Spc72 can trigger oligomerisation of the γ-TuSC similarly as its nuclear counterpart Spc110.

Structural characterisation of the γ-TuRC over the last few years led to assignment of almost all γ-TuRC components, revealing its molecular architecture. Assignment of the last missing core components, including four MZT2-GCP2 modules and the GCP5,6 insertions will provide insights into their function. To understand behaviour of the γ-TuRC during MT nucleation, it will be pivotal to unravel its structure in complex with other MT nucleation factors such as TPX2, NEDD1, CEP192, ch-TOG or in complex with the nucleated microtubule.

6 Methods

This section lists only methods directly related to my own work in the project, i.e. cryo-EM, negative stain-EM data processing, model building and model analysis. Methods for the experiments performed only by my collaborators can be found in following publications:
Liu, P., Zupa, E., Neuner, A. *et al.* Insights into the assembly and activation of the microtubule nucleator γ-TuRC. *Nature* **578,** 467–471 (2020). https://doi.org/10.1038/s41586-019-1896-6

Zupa E, Zheng A, Neuner A, *et al*. The cryo-EM structure of a γ -TuSC elucidates architecture and regulation of minimal microtubule nucleation systems. *Nat Commun*. 2020;11(1):5705. Published 2020 Nov 11. doi:10.1038/s41467-020-19456-8

Würtz, M., Zupa, E., Atorino, E.S. *et al.* Modular assembly of the principal microtubule nucleator γ-TuRC. *Nat Commun* **13,** 473 (2022). https://doi.org/10.1038/s41467-022-28079-0

6.1 Study of the *C. albicans* γ-TuSC

6.1.1 Cryo-EM grid preparation and data acquisition of the *C. albicans* γ-TuSC

4.0 µl of the purified *C. albicans* γ-TuSC were applied and incubated for 30 s on Quantifoil holey carbon grids (Cu R2/1; 300 mesh) (Quantifoil Micro Tools GmbH) that were beforehand glow discharged in a Gatan Solarus 950 plasma cleaner (Gatan, Inc.) for 20 s. Afterwards, the grids were blotted for 5-10 s and plunged into liquid ethane using a Vitrobot Mark IV (ThermoFisher Scientific). Grids were stored in liquid nitrogen till acquisition. Acquisition was performed on a Titan Krios transmission electron microscope (ThermoFisher Scientific) operated at 300 kV and equipped with a Gatan K2 direct electron detector (Gatan, Inc.) and a Quanta energy filter (Gatan, Inc.). Data were acquired using a dose fractionation mode (20 frames/frame stack) at 1.07 Å pixel size. Cumulative dose was ~40 $e^-/Å^2$ with a defocus ranging from -2 to -3 µm. Images were acquired in two sessions on two grids using SerialEM[240] acquiring 4 images per hole.

6.1.2 Cryo-EM data processing of the *C. albicans* γ-TuSC

The processing scheme of the *C. albicans* γ-TuSC is presented in Figure 9. Acquired movie stacks were firstly motion corrected using MotionCor2[241] dividing images into 5 x 5 patches for a local motion estimation. Motion corrected images were submitted into Gctf[242] to estimate CTF. All following processing steps were performed in Relion 3.0 Beta[243]. Particle picking was done by application of a grid with spacing of 100 pixels to overcome problems of Relion automated particle picker with a high concentration of particles per image. Particles from initial picking were extracted at a 256 box size but initially binned four times to a box size of 64 pixels corresponding to a pixel size of 4.28 Å. To speed up the processing, particles were divided into four subsets of same size and all subsets were submitted to an initial round of 3D classification with a translational sampling 20 pixels and an increment of 2 pixels, sorting particles into six classes, applying a T-factor of 10 and a shape mask for reference. The reference used for 3D classification was coming from segmentation of the *S. cerevisiae* γ-TuSC oligomer reconstruction in the closed conformation (EMD-2799)[223], low-pass filtered to 15 Å. Classifications produced between one to two class averages reaching a resolution regime sufficient to resolve secondary structure features. Particles from these classes were combined into one set and duplicated particles removed for each of two sessions.

Particles from selected classes in both datasets were extracted at a full spatial resolution corresponding to a box size of 256 and a pixel size of 1.07 Å, and submitted to 3D auto-refinement with solvent-flattened Fourier Shell Correlation. Afterwards, I subject particles from

3D auto-refinement into CTF refinement to estimate beam tilt and per particle defocus. Bayesian polishing[243] was performed after training on 5000 particles for each dataset. Polished particles from both datasets were combined into the final full set and submitted into 3D auto-refinement that resulted in a reconstruction of 4.1 Å global resolution after post-processing. To improve per spoke resolution of the γ-TuSC, the reconstruction was segmented to prepare masks for each spoke that were used in a multi-body refinement approach[224]. The γ-TuSC reconstruction was obtained from individual spokes after multi-body refinement by combination of unfiltered spoke reconstructions into a composite reconstruction using UCSF Chimera[244]. Post-processing of the composite reconstruction yielded 3.6 Å global resolution according to gold standard Fourier Shell Correlation (FSC) criterion with threshold of 0.143. Using Relion local post-processing implementation, I estimated local resolution. For both local resolution and post-processing, I applied b-factor of -300.

6.1.3 Atomic model building of the *C. albicans* γ-TuSC

I used the X-ray structures of human γ-tubulin (PDB 1Z5W)[217] and human GCP4 (PDB 3RIP)[155] as templates to prepare homology models of *C. albicans* γ-tubulin, Spc97 and Spc98 in Phyre2[245]. The homology models of the γ-TuSC components were docked as rigid bodies into the final cryo-EM reconstruction using UCSF Chimera[244], combined into one PDB file and submitted into MDFF with one subsequent cycle of phenix real space refinement using Namdinator[246], applying default parameters for MDFF. The model of the γ-TuSC was afterwards refined and modified according to the cryo-EM reconstruction in Coot[247], including building regions *de novo* (regions that were not build by Phyre2 but resolved in the cryo-EM reconstruction) and deleting regions that were not resolved in the cryo-EM reconstruction. N-terminal segments of 91 and 149 residues are missing in Spc97 and Spc98, respectively, because they were not resolved in the γ-TuSC reconstruction. The models were then subjected separately into real space refinement in Phenix[248] using 0.6 restraint weights. The output models from Phenix were again adjusted in Coot if required and afterwards combined into the model of the γ-TuSC that was submitted to a final round of real space refinement in Phenix using parameters as described above.

6.1.4 γ-tubulin conformation and ligand assignment

Assignment of the γ-tubulin conformation and ligand status was performed in UCSF Chimera[244]. Structural differences between the straight and curved conformations of α/β-tubulins (PDB 4FFB, PDB 5W3F)[67,218] were defined by arrangement of the two α-helices α6 and α7 in β-tubulin. I rigid body docked β-tubulin from both X-ray structures into the density segments representing γ-tubulin in both γ-TuSC spokes. Identification of the γ-tubulin conformation was achieved by 1) measuring R.M.S.D. between the two α-helices (α6, α7) of β-tubulin and the corresponding α-helices of γ-tubulin per each spoke and by 2) measuring cross-correlation between the simulated β-tubulin and γ-tubulin density segments at a resolution of 3.6 Å.

For the γ-tubulin ligand status assignment, the X-ray structure of β-tubulin in the GTP state (PDB 4FFB)[67] was rigid body docked into the γ-tubulin density segments. The density segments covered by the fitted β-tubulin model were removed. The residual density segments in γ-tubulin molecules were overlapping with the nucleotide in the β-tubulin X-ray structure but the GTP γ-phosphate group was not covered, indicating presence of GDP instead of GTP.

6.1.5 Visualisation of interactions within the γ-TuSC

PISA[249] was used to identify exposed and buried residues that participate in intermolecular interactions in the γ-TuSC. Visualisation of residues contributing to intermolecular interactions was done in UCSF Chimera[244] by the 'Render by Attribute-Kd hydrophobicity' function for hydrophobic interfaces and by 'Coulombic surface colouring' function for electrostatic interfaces. Intermolecular interactions were displayed in surface representation for electrostatic interfaces of both involved proteins and hydrophobic interfaces were displayed in surface representation for one interactor and as atomic representation of the involved side chains for the second interactor. Intramolecular hydrophobic interactions for each Spc protein were visualised in atomic representation for the involved residue side chains.

6.1.6 Negative stain EM of the *C. albicans* γ-TuSC

Negative stain EM was performed in collaboration with Dr. Annett Neuner. Purified samples of the wild-type γ-TuSC, the Spc98$^{\Delta D627\text{-}K650}$ mutant γ-TuSC or the Tub4$^{\Delta T38\text{-}K71}$ mutant γ-TuSC were applied in a volume of 5 µl on grids that were beforehand glow-discharged for 30 s. We used 400 copper/palladium mesh grids (PLANO GmbH; Wetzlar-Germany) covered with 10 nm carbon layer prepared according to an in-house protocol by Dr. Annett Neuner. The applied sample was incubated for 30 s, washed three times with distilled water and stained with 3 % uranyl acetate for 2 minutes. Grids were blotted using a Whatman filter paper 50. Data were collected on a Talos L120C TEM (ThermoFisher Scientific) operated at 120 kV and equipped with 4k x 4k Ceta 16M camera (ThermoFisher Scientific). Acquisition for each sample was set in the EPU software package (ThermoFisher Scientific) using 0.2552 nm as an object pixel size for the images. The overall number of images for each dataset was as listed: the wild-type γ-TuSC: 997 images; the Spc98$^{\Delta D627\text{-}K650}$ mutant γ-TuSC: 821; the Tub4$^{\Delta T38\text{-}K71}$ mutant γ-TuSC: 1147 images.

All datasets were processed in Relion 3.0 Beta[243]. The CTF was estimated using Gctf[242]. To prepare a 2D reference for automated particle picking, 1000 particles were manually selected and extracted at a binned pixel size of 0.51 nm in a box size of 128 pixels. Selected particles were submitted into 2D classification with 50 classes and a translational search of 20 pixels with 2 pixel search step and a mask diameter of 400 Å. Class averages that resembled the Y-shape of the γ-TuSC were selected as a reference for automated particle picking. The initial numbers of picked particles for each dataset were listed: 347,445 for the wild-type γ-TuSC, 154,883 for the Spc98$^{\Delta D627\text{-}K650}$ mutant γ-TuSC and 241,205 for the Tub4$^{\Delta T38\text{-}K71}$ mutant γ-TuSC. Particles were extracted with the same parameters as mentioned before and submitted into 2D classification with 200 classes and the same translational search and mask. Class averages representing the γ-TuSC were selected and subjected to a second round of 2D classification with the same parameters as in the first round of 2D classification. For the dataset of the Tub4$^{\Delta T38\text{-}K71}$ mutant γ-TuSC, selected classes were subjected to a third round of 2D classification with 170 classes. Class averages with clearly discernible the Y-shape from each dataset were used for subsequent analysis. The ratio of the straddled γ-TuSC conformation and the wild-type γ-TuSC conformation was calculated from these numbers of the Y-shaped particles: 77,858 for the wild-type γ-TuSC, 11,901 for the Spc98$^{\Delta D627\text{-}K650}$ mutant γ-TuSC and 15,450 for the Tub4$^{\Delta T38\text{-}K71}$ mutant γ-TuSC.

6.1.7 Multiple sequence alignment of GCPs and γ-tubulins

Sequences of Spc97 (GCP2), Spc98 (GCP3) and γ-tubulin were blasted among organisms from different evolutionary development points against *C. albicans* sequences. Alignment of the sequences for Spc97, Spc98 was performed in Promals 3D[250] and for γ-tubulins in MATFF[251] and visualisation was done in Jalview[252] using ClustalX colouring scheme and a

threshold for conservation was 10. Uniprot or NCBI codes for the sequences used for alignments are in Table 4. GCP4,5,6 were identified from UniProt database, published literature and based on PSI-blast E-value against the human versions of these proteins. Identified sequences were used for evolutionary analysis of the γ-TuC complexity in different organisms.

Table 4: Uniprot and NCBI codes of the sequences used for multiple sequence alignments

Organism	GCP2	GCP3	γ-tubulin
Dictyostelium discoideum	CAC47949.1	Q95ZG4	Q55AR3
Coprinopsis cinereal	XP_002910163.1	XP_001837207.2	Q7Z9Z2
Neurospora crassa	XP_962067.1	XP_960965.1	P53377
Giardia Intestinalis	A8BD62	A8BFK8	A8BQF3
Trichomonas vaginalis	A2E313	A2E3S1	A2EAH1
Amphimedon queenslandica	XP_019853680.1	XP_019863806.1	A0A1X7VUX8
Dendronephthya gigantean	XP_028391404.1	XP_028405676.1	XP_028392057.1
Strongylocentrotus_purpuratus	XP_030831245.1	XP_030837580.1	Q9GYY8
Ciona intestinalis	XP_026696722.1	XP_002131421.1	H2XQX6
Clonorchis sinensis	GAA57286.1	GAA53692.1	H2KTT6
Lingula anatine	XP_013411271.1	XP_013415922.1	XP_013407731.1
Crassostrea gigas	XP_011429809.1	XP_011436049.1	K1Q4G7
Tetrahymena thermophila	Q23AE3	Q22ZA9	O00849
Trichinella spiralis	KRY36071.1	KRY40906.1	A0A0V1BZ12
Chlamydomonas reinhardtii	A8J5J8	A8JBY6	Q39582
Arabidopsis thaliana	Q9C5H9	Q9FG37	P38557
Drosophila melanogaster	Q9XYP7	Q9XYP8	P23257
Danio rerio	NP_956416.1	NP_001004513.1	Q7ZVM5
Podarcis muralis	XP_028588014.1	XP_028583946.1	XP_028560954.1
Calypte anna	XP_030309245.1	XP_030325143.1	A0A091HMN8
Homo sapiens	Q9BSJ2	Q96CW5	P23258
Candida albicans	Q59PZ2	A0A1D8PS42	O93807
Saccharomyce cerevisiae	P38863	P53540	P53378
Clavispora lusitaniae	XP_002617032.1	OVF11036.1	C4Y8G4
Ogataea polymorpha	XP_018211750.1	XP_018213099.1	A0A1B7SAP4
Wickerhamomyces ciferrii	XP_011273399.1	XP_011277192.1	K0KDD8

Lachancea fermentati	SCW03932.1	SCW02410.1	A0A1G4M7N1
Ascoidea rubescens	XP_020046155.1	XP_020044979.1	A0A1D2VI38
Schizosaccharomyces pombe	Q9Y705	Q9USQ2	P25295

6.1.8 Analysis of the γ-TuSC geometry

The geometry of the *C. albicans* γ-TuSC and the human γ-TuSC unit in the context of the γ-TuRC (PDB 6V6B)[220] was compared to the *S. cerevisiae* γ-TuSC unit in the context of a ring-like oligomer as resolved in the open (PDB 5FM1)[223] and closed (PDB 5FLZ)[223] conformations. To compare the geometry of the γ-TuSC pairs from different organisms, I rigid body fitted the γ-TuSC *C. albicans* into the *S. cerevisiae* γ-TuSC in the open or closed conformation (EMD-1731)[157] (EMD-2799)[156]. The γ-TuSC was segmented into 6 parts- two copies of γ-tubulins, the Spc97 GRIP1 and GRIP2 domain and the Spc98 GRIP1 and GRIP2 domain before fitting. Similarly, I rigid body fitted the human γ-TuSC after separation into 6 segments- two copies of γ-tubulins, the GCP2 GRIP1 and GRIP2 domain and the GCP3 GRIP1 and GRIP2 domain, into the *S. cerevisiae* γ-TuSC reconstruction in the closed conformation (EMD-2799)[156]. The docked model segments were combined into composite models of the human γ-TuSC and the *C. albicans* γ-TuSC. Afterwards, the original *C. albicans* γ-TuSC model was superposed to the prepared composite *C. albicans* models in the open or closed conformations according to one full spoke comprising of Spc97 and γ-tubulin. The original human γ-TuSC model was superposed to the composite human γ-TuSC model in the closed conformation according to GCP2 with γ-tubulin. Differences in conformation between the models were measured as R.M.S.D. of protein backbones for the individual segments mentioned above. Visualisation of conformational variability was performed in PyMOL (PyMOL v2.1, Schrödinger) using vector representation.

6.2 Study of the γ-TuRC from *X. laevis*

6.2.1 Circular dichroism spectroscopy of xGCP6(546–794)

xGCP6(546–794) was expressed and purified by Anna Böhler for a circular dichroism spectroscopy. Spectroscopy was performed with Anna Böhler and Dr. Szymon Kmiecik (RG Mayer, ZMBH) on a Jasco J715 spectropolarimeter at 25 °C. The length of a cell for recording was 1 mm and spectra were recorded in a wave length range of 190-250 nm with 0.2 nm sampling. One spectrum was built as an average of five scans and intensities were in milidegrees.

6.2.2 Negative stain EM of Cdk5Rap2-N

The sample of the *X. laevis* γ-TuRC incubated with and without Cdk5Rap2-N was prepared by Dr. Peng Liu and negative stain EM data acquisition and particle picking were performed by Dr. Annett Neuner. I imported picked particles into Relion 3.0 Beta[243] and submitted them into 3D classification with 3 classes, using a binned reconstruction of the *X. laevis* γ-TuRC as a reference. 2,205 particles of the γ-TuRC without Cdk5Rap2-N and 1,581 particles of the γ-TuRC with Cdk5Rap2-N were retained and separately subjected to 3D auto-refinement. The resulting reconstructions were compared after superposition according to the first four spokes in UCSF Chimera[244]. Furthermore, the reconstruction obtained for the γ-TuRC with Cdk5Rap2-N was compared to the simulated reconstruction of the γ-TuRC matching MT geometry. For that purpose, I generated a simulated reconstruction of the γ-TuRC at 30 Å resolution. in UCSF Chimera[244], which was subsequently superposed to the reconstruction of the γ-TuRC with Cdk5Rap2-N in the same way as described above.

6.2.3 Cryo-EM grid preparation and data acquisition of the *X. laevis* γ-TuRC

The purified *X. laevis* γ-TuRC was applied by Dr. Annett Neuner and Dr. Peng Liu to homemade graphene oxide-coated holey carbon grids (Cu; R2/1; 200 mesh) in a volume of 4 µl at room temperature and relative humidity of 60-70%. All grids were glow-discharged beforehand in a Gatan Solarus 950 (Gatan, Inc.) for 20 s. The sample was incubated on grids for 30 s and excess of sample was blotted for 5 s or 10 s by a Vitrobot Mark IV (ThermoFisher Scientific), and subsequently, grids were plunged into liquid ethane and stored in liquid nitrogen till acquisition. I acquired several datasets on a Titan Krios transmission electron microscope (ThermoFisher Scientific) operated at 300 kV. Acquisitions were performed on a Gatan K3 camera (Gatan, Inc.) with a Quanta GIF energy filter. The detector was operated in a dose fractionation mode using 70 frames for dataset 1, 60 frames for dataset 2, 46 frames for dataset 3 and 39 frames for dataset 4. The pixel sizes of acquired images were 2.1 Å for datasets 1-3 and 1.35 Å for dataset 4. All data were acquired in SerialEM[240]. Cumulative doses for datasets were as following: 35 e^{-}/Å2 for dataset 1, ~42 e^{-}/Å2 for dataset 2, ~51 e^{-}/Å2 for dataset 3 and ~57 e^{-}/Å2 for dataset 4. Defocus range for all datasets was from -0.5 to -3.5 µm with 2 frame stack per hole applied in case of datasets 1-3 and four frame stacks per hole applied in case of dataset 4.

6.2.4 Cryo-EM data processing for the *X. laevis* γ-TuRC

Image processing was performed almost exclusively in Relion 3.0 Beta[243]. The processing scheme of the *X. laevis* γ-TuRC data is presented in Figure 24. All datasets were processed separately. Movie stacks from each dataset were motion corrected in MotionCor2[241] dividing the image into 5 x 5 patches for local motion correction. CTF was estimated using Gctf software[242]. To generate a reference for automated particle picking, I picked together with Dr. Peng Liu manually 3,000 particles from dataset 1, extracted them in a box size of 128 pixels (4.2 Å pixel size) and ran *ab-initio* reconstruction with default parameters. Artificial 2D projections of the *ab-initio* reconstruction were used as a reference for automated particle picking in all datasets. Picked particles were extracted in a box size of 128 pixels, at a pixel size of 4.2 Å.

Particles from dataset 1-3 were sorted out in two consecutive rounds of 3D classification applying a translational search of 20 pixels with a step of 2 pixels. Selected particles from classes resembling the shape of a left-handed spiral with 14 spokes were re-centered and re-extracted at a box size of 256 pixels corresponding to a pixel size of 2.1 Å. Re-extracted particles were subjected to 3D auto-refinement using a shape mask and applying solvent-flattened Fourier Shell Correlation. Particles were afterwards submitted into CTF refinement, correcting beam tilt and fitting defocus per particle, and later applied to Bayesian polishing[243] trained on 1,000 particles.

Particles picked in dataset 4 were split into 4 subsets and subjected to 3D classification steps with the same setup as for datasets 1-3. Two of four subsets provided classes resembling a left-handed spiral. For subsets that did not provide good classes, I supplied the final set of particles from previous datasets to nucleate 3D classes resembling a left-handed spiral. Particles from previous datasets were afterwards removed to merge only particles from the four subsets of dataset 4. The merged set of particles was subjected to two consecutive rounds of 3D classification selecting a final set of particles that were re-centered and re-extracted at a box size of 256 corresponding to a pixel size of 2.1 Å. Particles were subjected to CTF refinement and Bayesian polishing[243] as described for datasets 1-3.

Polished particles from all four datasets (46,096 particles) were merged together and submitted into 3D auto-refinement. The output reconstruction was used as a basis for segmentation and mask preparation used later in multi-body refinement[224]. Two individual multi-body refinements were submitted. For one multi-body refinement, I prepared a set of 7 masks, each encompassing a dimer of spokes (neighbouring GCPs with associated γ-tubulins). For another multi-body refinement run, I prepared a set of 4 masks. Two of these masks each encompassed the N-terminus of the GRIP2 domains and the full GRIP1 domains of 7 spokes in a row . The other two masks each encompassed the C-terminus of the GRIP2 domains and γ-tubulins of 7 spokes in a row. Unfiltered reconstructed bodies from both multi-body refinements were combined using UCSF Chimera[244] and post-processing estimated resolution of 4.9 Å. To improve resolution per spoke, I prepared another set encompassing 14 masks each representing one spoke and subjected it into another multi-body refinement. Afterwards, I combined bodies from all three multi-body refinements in UCSF Chimera and post-processing estimated resolution of these composite reconstruction at 4.8 Å. I also applied local resolution filtering to the composite reconstruction setting b-factor to -300.

6.2.5 Spoke clustering

To cluster spokes into groups, I used two approaches: a cross-correlation based approach and a R.M.S.D. based approach. In case of the cross-correlation approach, the cryo-EM reconstruction of the *X. laevis* γ-TuRC was segmented spoke-wise, each segment representing one GCP with the associated γ-tubulin, and pairwise cross-correlation was calculated between each spoke density segments in UCSF Chimera[244]. The second approach was based on calculation of R.M.S.D. between atomic models representing the spokes, after domain-wise docking of models for GCP4 (PDB 3RIP)[155] and γ-tubulin (PDB 1Z5W)[217]. To produce as precise fit for each spoke as possible, I docked GCP4 firstly as one rigid body and afterwards, I fine-tuned fit by docking 4 separated bodies of GCP4 to account for a per spoke conformational variability. The bodies were represented by following range of residues: Met1–Lys147, Ile148–Tyr361, Leu362–Lys505 and Ser506–Gln636. The C-terminal helix of GCP4 Ile637–Tyr654 was not docked but manually placed into the reconstruction for one spoke and then kept rigid for the other spoke positions. R.M.S.D. was calculated using UCSF Chimera command 'match'.

6.2.6 Assignment of GCPs to specific spoke cluster

Assignment of GCP identities to specific spokes was based on differences on primary sequence level and on secondary structure level. Docking of GCP4 and γ-tubulin described in previous chapter was used to segment spokes of the γ-TuRC and identify specific density segments for spoke clusters (Fig. 26c). These density segments were compared with information from multiple sequence alignment performed in Promals3D[250] and with secondary structure predictions of all GCPs performed in PSIPRED v3.3[253].

6.2.7 Model building of the *X. laevis* γ-TuRC

Similarly as for the *C. albicans* γ-TuSC, I took advantage of the published X-ray structures of human GCP4 (PDB 3RIP)[155] and human γ-tubulin (PDB 1Z5W)[217] using them as templates to build homology models of the *X. laevis* GCP2,3,4,5,6 and γ-tubulin using Phyre2[245]. The UniProt sequences used for modelling were XP_018080012.1 (GCP2), O73787 (GCP3), Q642S3 (GCP4), XP_018102626.1 (GCP5), Q9DDA7 (GCP6, excluding the insertion domain sequence Leu532–Arg1260) and P23330 (γ-tubulin). The models of GCPs and γ-tubulin were rigid body docked into the γ-TuRC reconstruction, firstly each model as one body. After initial fitting, the last three C-terminal α-helices of all GCP models were manually positioned into the

reconstruction due to the significant deviation. Considering the conformation variability of spokes, each GCP model was after the initial fit split into the following rigid bodies and docked: Leu209–G364, Tyr365–Glu506, Glu507–Ser668, Ser671–Ser714, Ala715–Tyr867 for GCP2; Glu246–Gly389, Arg390–Tyr552, Asn553–Lys691, Gly692–Tyr885 for GCP3; Met1–Lys147, Ile148–Asp349, Ile350–Lys505, Ser506–Tyr654 for GCP4; Thr259–Pro421, Asp422–Leu723, Leu724–Asn847 and Lys848–Ala1014 for GCP5; Gln269–Ala421, Gly422–Leu1015, Lys1016–Ser1464, Asn1465–Tyr1622 for GCP6. Afterwards, all models were refined according to the reconstruction in Coot[247], building components resolved in the reconstruction but missing in the homology models were built and components that were unresolved were removed. The luminal bridge with resolved α-helical features (together 17 α-helices), that were unassigned, was built using poly-alanine α-helical chains. After refinement, the models were combined into one model in UCSF Chimera[244]. The full model including rigid body fitted actin (described in chapter 5.2.8.) was firstly subjected to real space refinement in Phenix[248]. The refinement run yielded a high clashscore that was improved by MDFF using QwikMD[254] and NAMD[255] applying the CHARMM36 force field. MDFF in NAMD was performed by Dr. Till Rudack. MDFF included secondary structure, *cis* peptide and chirality restraints. 40 ps simulation at 300 K was preceded by 800 minimisation steps. The resulting model was afterwards real space refined in Phenix[248] using the submitted model as a reference to restrain secondary structure features. The refined model was submitted to Namdinator[246] tool to run MDFF at 298 K applying 2000 minimisation steps and 20,000 simulation steps in a vacuum with a grid force of 0.3. The output model was corrected for bulky amino acid side chain fit in Coot[247] followed by refinement in Phenix[248]. Application of Namdinator followed by Coot and Phenix refinement was repeated twice till getting final model that was validated in Phenix[248].

6.2.8 Structure-guided approach for identification of actin

Trying to assign components into the luminal bridge density segment, I relied on proteins identified in the sample of the γ-TuRC by LFQ mass spectrometry. Models of proteins included in the mass spectrometry list were downloaded from PDB database or prepared by homology modelling in HHpred[256]. Model fitting into the *X. laevis* γ-TuRC cryo-EM reconstruction was performed in UCSF chimera[244] starting from 10,000 randomly sampled starting positions and orientations using a simulated reconstruction at 6 Å resolution, 50 Å fitting radius around the starting position and global search. The number of fits against cross-correlation coefficients were plotted to evaluate results (Fig. 29). The approach was validated by fitting of GCP4 and γ-tubulin models as positive controls (Fig. 29a) and an ovalbumin model as a negative control (Fig. 29b). NEDD1, NME7 and MZT1 structures were modelled only for segments with high homology to available published structures. Proteins used in the structure-guided approach, which did not result in high number of fits with high cross-correlation coefficient and are not related by previous studies to the γ-TuRC (data that were not plotted) but were abundant in mass spectrometry list, are listed in Table 3.

6.2.9 Measurement of pitch increment and γ-tubulin distance from the helical axis in the γ-TuRC

Measurement of both parameters was based on the helical axis defined for the γ-TuRC and an ideal MT. The γ-TuRC helical axis was defined in the following way. I selected 5 residues per each of 14 spokes (GCP with associated γ-tubulin) of the γ-TuRC (Fig. 31a). Two of the residues were located at γ-tubulin (Thr145, Tyr152). These two residues from each spoke defined two individual centroids. The other three residues were selected on GCPs (first residue: Leu249 of GCP3, Leu216 of GCP2, Met1 of GCP4, Val266 of GCP5, Leu280 of GCP6;

second residue: Pro408 of GCP3, Ser369 of GCP2, Tyr445 of GCP6, Pro166 of GCP4, Glu451 of GCP5; third residue: Leu554 of GCP3, Leu508 of GCP2, Met590 of GCP6, Leu350 of GCP4, Leu711 of GCP5). All five residues were converted to centroids, which served to create the γ-TuRC helical axis in UCSF Chimera[244]. Measurement of the MT helical parameters (PDB 6EVZ)[257] was based on the helical axis that was defined by three centroids each on different layers of tubulins according to residue Gln15. Three centroids created according to γ-tubulin of Gln12, Asn389 of GCP2, Asn444 of GCP3 and Phe102 of GCP2, Phe216 of GCP3 were used to define the helical axis of the *S. cerevisiae* γ-TuSC ring-like oligomer in the closed conformation (PDB 5FLZ)[223]. The helical axes of all three models were used for alignment of models and a coordinate system was defined in the way tha thet helical axes corresponded to the z-axis of a coordinate system. Afterwards, I extracted Cartesian coordinates of all tubulins in three models defined by Gln15, Gln16 and His16 and calculated the helical pitch (Fig. 31b) and radial distances of tubulins (Fig. 31c).

The conformational change required for the isolated γ-TuRC to reach a MT-compatible geometry was visualised in PyMOL (PyMOL v2.1, Schrödinger). I firstly simulated the model of the γ-TuRC in the closed conformation by docking its components domain-wise into the cryo-EM reconstruction of the yeast γ-TuSC oligomer in the closed conformation (EMD-2799)[223]. The γ-TuRC model and the simulated model in the closed conformation were aligned according to spoke 1. The conformational change linking these two models was visualised in PyMOL (PyMOL v2.1, Schrödinger) in vector representation between Cα atoms and coloured according to R.M.S.D. values.

Measurement of relative inclination between the GRIP1 and GRIP2 domains for each spoke was performed based on two axes, one axis per GRIP domain of each GCP. The GRIP1 domain axis was defined using- Ala266 and Gly453 for GCP2, Gly297 and Gly486 for GCP3, Gly49 and Gly280 for GCP4, Gly317 and Gly559 for GCP5 and Gly332 and Gly526 for GCP6. The GRIP2 domain axis was defined using - Leu508 and Phe757 for GCP2, Leu554 and Phe784 for GCP3, Leu350 and Phe592 forGCP4, Leu711 and Phe959 for GCP5 and Met1319 and Phe1553 for GCP6. The inclination between these two axes was measured in UCSF Chimera[244] and quantified for each type of GCP. Angle average for each GCP variant was calculated as mean ± s.e.m by Dr. Peng Liu.

Measurement of distances between neighbouring spokes was based on conserved residues in the GRIP1 domains (Ala266 of GCP2, Gly297 of GCP3, Gly49 of GCP4, Gly317 of GCP5 and Gly332 of GCP6) and the GRIP2 domains (Phe757 of GCP2, Phe784 of GCP3, Phe592 of GCP4, Phe959 of GCP5 and Phe1553 of GCP6) or γ-tubulins (Asn187) and performed in UCSF Chimera[244].

6.3 Study of the recombinant human γ-TuRC

6.3.1 Cryo-EM grid preparation and data acquisition for recombinant human γ-TuRC samples

Purified samples of the recombinant human wild-type γ-TuRC, the γ-TuRC$^{\Delta N56\text{-}GCP6}$ and the recombinant human γ-TuRC$^{\Delta GCP2/3}$ were applied on Quantifoil holey carbon grids (Cu; R2/1; 200 mesh) (Quantifoil Micro Tools GmbH) in a volume of 4 µl at room temperature and relative humidity of 85%. All grids were glow-discharged beforehand in a Gatan Solarus 950 (Gatan, Inc.) for 30 s. Excess of sample was blotted for 0.5 s immediately after sample application and grid was plunged into liquid ethane using a Vitrobot Mark IV (ThermoFisher Scientific) and

stored in liquid nitrogen until acquisition. Data were acquired on a Titan Krios transmission electron microscope (ThermoFisher Scientific) operated at 300 kV. Acquisition was performed using a Gatan K3 camera (Gatan, Inc.) with a Quanta GIF energy filter. The detector was operated in a dose fractionation mode using 50 frames for the wild-type γ-TuRC and the γ-TuRC$^{\Delta N56\text{-}GCP6}$, and 40 frames for the recombinant human γ-TuRC$^{\Delta GCP2/3}$. Nominal pixel size was 2.66 Å for the wild-type γ-TuRC and the γ-TuRC$^{\Delta N56\text{-}GCP6}$; and 1.07 Å for the γ-TuRC$^{\Delta GCP2/3}$. All data were acquired in EPU (ThermoFisher Scientific) applying the 'fast' aberration free image shift acquisition scheme. Cumulative doses and dose rates for datasets were as following: 35 e^-/Å2 and 25 e^-/px/s for the wild-type γ-TuRC, ~42.6 e^-/Å2 and 30 e^-/px/s for the recombinant human γ-TuRC$^{\Delta N56\text{-}GCP6}$, ~62.4 e^-/Å2 and 25 e^-/px/s for the recombinant human γ-TuRC$^{\Delta GCP2/3}$. Defocus range for wild-type γ-TuRC and γ-TuRC$^{\Delta N56\text{-}GCP6}$ was -2 to -2.5 µm with 1 frame stack per hole and for recombinant human γ-TuRC$^{\Delta GCP2/3}$ it was -1 to -3 µm with four frame stacks per hole.

6.3.2 Processing of cryo-EM data for the recombinant wild-type γ-TuRC

Processing of the recombinant human wild-type γ-TuRC was performed in Relion 3.1[243], if not stated otherwise. A simplified processing workflow is visualised in Figure 34. 6,127 frame stacks were motion corrected in MotionCor2[241] and CTF estimation was performed in Gctf[242]. Topaz[258], which was trained on 1,241 manually picked particles from 50 micrographs, was used for automated particle picking. Training parameters included convolutional neural network model resnet8, scaling factor 3 and expectation of 100 particles in average per training micrograph. 436,887 initially picked particles were extracted at a box size of 200 pixels and downscaled to 128 pixels corresponding to a pixel size of 3.9 Å. The particle set was split into four random subsets, each subjected to 3D classification with six classes, applying a T-factor of 20, a spherical mask of 400 Å and a translational offset of 20 pixels with a pixel step of 2. 10 classes resembling the γ-TuRC from all 4 subsets were selected and 159,770 particles from these classes re-centered and re-extracted at a box size of 200 pixels corresponding to a full spatial resolution of 2.66 Å/px. Particles were subjected to another round of 3D classification using previously mentioned parameters with exception of a translational offset that was decreased to 5 pixels with a pixel step of 1. Classification yielded classes resembling "large" assembly states (10–14 spokes; 36,881 particles) and "small" assembly states (6–10 spokes; 92,149 particles). Both particle sets were processed further independently in Relion 3.0 Beta[243] by subjecting them to 3D auto-refinement, CTF refinement and Bayesian polishing[243]. Polished particles were submitted to another 3D auto-refinement, which was used as a base for multi-body refinement[224] with three to five bodies depending on the size of the assembly state. Reconstructed bodies were combined in UCSF Chimera[244] and post-processed in Relion 3.0 Beta[243], reaching 7.5 Å global resolution for the "large" assembly state and 5.3 Å for the "small" assembly state (Fig. 34b). Other γ-TuRC assembly intermediates were derived from these two particle sets by sub-classifications focusing on the peripheral γ-TuSC units. Settings for focused classifications were as following- T-factor of 20, a spherical mask of 400 Å, using from 3 to 6 classes not applying translational and angular sampling.

Particles from "small" assembly states were sorted in two individual 3D classification rounds based on two factors- presence of the γ-TuSC$_{(5,6)}$ unit and the γ-TuSC$_{(13,14)}$ unit. Focused 3D classifications yielded particle combinations with and without the γ-TuSC$_{(5,6)}$ unit and with and without the γ-TuSC$_{(13,14)}$ unit (marked as +/- γ-TuSC$_{(5,6)}$ and +/- γ-TuSC$_{(13,14)}$). All combinations were individually subjected to 3D auto-refinement and multi-body refinement[224] yielding the following reconstructions- spokes 7–12 (7 Å resolution; Fig. 34b), spokes 7–14 (7.6 Å

resolution; Fig. 34b), spokes 5–12 (8.6 Å resolution; Fig. 34b) and spokes 5–14 (9.0 Å resolution; Fig. 34b).

Particles from "large" assembly states were sorted based on two factors- presence of the γ-TuSC$_{(1,2)}$ unit and the γ-TuSC$_{(13,14)}$ unit. 3D classification of this particle set yielded particles with and without the γ-TuSC$_{(1,2)}$ unit and with and without the γ-TuSC$_{(13,14)}$ unit (marked as +/- γ-TuSC$_{(1,2)}$ and +/- γ-TuSC$_{(13,14)}$). I applied 3D auto-refinement and multi-body refinement[224] on these particle combinations to obtain the following reconstructions- spokes 3–12 (8.1 Å resolution; Fig. 34b), spokes 3–14 (9.0 Å resolution; Fig. 34b), spokes 1–12 (9.2 Å resolution; Fig. 34b) and spokes 1–14 (16.1 Å resolution without multi-body refinement; Fig. 34b).

To increase particle numbers for the "large" spoke assembly intermediates, I selected particle sets of +/- γ-TuSC$_{(1,2)}$ independent from their +/-γ-TuSC$_{(13,14)}$ status and *vice versa* and submitted all sets to 3D auto-refinement and multi-body refinement[224]. The particle set of "large" assembly states including the γ-TuSC$_{(1,2)}$ unit reached 8.7 Å resolution (Fig. 34b) and set of "large" assembly states missing the γ-TuSC$_{(1,2)}$ unit reached 7.8 Å resolution (Fig. 34b). The particle set of large assembly "states" including the γ-TuSC$_{(13,14)}$ unit reached 8.7 Å resolution (Fig. 34b).

6.3.3 Processing of cryo-EM data for the recombinant γ-TuRC$^{\Delta N56\text{-}GCP6}$

The processing workflow can be found in Figure 45. Initial data processing of 2,614 frame stacks including motion correction, CTF estimation, automated particle picking and particle extraction was performed the same way as for the recombinant wild-type γ-TuRC. 448,184 picked particles were subjected to 3D classification in two random subsets with the same settings as described for the dataset of the recombinant wild-type γ-TuRC. I selected only classes resembling the 14-spoked γ-TuRC$^{\Delta N56\text{-}GCP6}$, which contained 41,054 particles. Afterwards, selected particles were re-centered and re-extracted at full spatial resolution and subjected to 3D classification with the same parameters as for the recombinant wild-type γ-TuRC. 40,115 particles contained in 5 classes were retained and processed in Relion 3.0 Beta[243] in the same way as the recombinant wild-type γ-TuRC. The final reconstruction reached 7.1 Å global resolution after post-processing.

6.3.4 Processing of cryo-EM data for the recombinant γ-TuRC$^{\Delta GCP2/3}$

The processing workflow can be found in Figure 40. Initial data processing of 11,276 frame stacks including motion correction and CTF estimation was performed the same way as for the recombinant wild-type γ-TuRC. Afterwards, the set of images was split into two subsets for automated picking by Topaz[258] using the same model as for the recombinant wild-type γ-TuRC. Topaz picked overall 936,634 and 951,532 particles from subset 1 and subset 2, respectively. Next, particles were transferred into cryoSPARC[259] and subjected to 2D classification with 200 classes and a circular mask of 250 Å. Two classes resembling the 4-spoked assembly intermediate were selected and 24,357 particles from these classes subjected to *ab-initio* reconstruction. Subsequently, the output of the *ab-initio* reconstruction was used as a reference for homogeneous refinement using the same set of 24,357 previously selected particles. The resulting reconstruction from the homogeneous refinement was composed of 3 resolved spokes with fragmented density segments on the periphery likely corresponding to a fourth spoke. Next, I used the cryoSPARC reconstruction as a reference for Relion 3.1[243] 3D classification with the set of 53,311 particles selected from cryoSPARC 2D classification. The best 3D class was subsequently used as a reference for a series of 3D classification steps

using all ~1.9 million particles picked by Topaz. 3D classifications were submitted with a shape mask and a T-factor of 20. After four rounds of 3D classifications, I obtained 9,192 particles that were processed in Relion 3.0 Beta[243] in the same way for the data on the recombinant wild-type γ-TuRC. Multi-body refinement[224] was performed using 2 bodies- body 1: GCP4-5-4, body 2: GCP6. The final reconstruction reached resolution of 7.8 Å after post-processing.

6.3.5 Model building and refinement

Model building was based on the previously published models of the γ-TuRC: GCP2, GCP3, GCP4, γ-tubulin and actin were taken from PDB 7AS4[189], GCP5 and GCP6 from PDB 6V6S[220]. The NTEs of GCP5 (210-266) and GCP6 (282-351) were built in Coot[247] according to the reconstructions- EMD-21074 and EMD 21069[220]. The luminal bridge, MZT1-GCP3 and MZT1-GCP5 modules were incorporated into the models based on the previously published models- PDB 6X0U[228] for the luminal bridge components and MZT1-GCP3, PDB 6L81[232] for MZT1-GCP5 module and PDB 6M33[232] for MZT1-GCP6 module. All above mentioned components were rigid body docked into the cryo-EM reconstructions in UCSF Chimera[244]. The rigid body fit of GCPs was further improved by domain-wise docking where possible. All components were modified in Coot[247] according to the reconstruction where possible.

Refinement was performed using MDFF in VMD[260] for all γ-TuRC models except the 4-spoked assembly intermediate. Necessary files for refinement were prepared via plugin QwikMD[254] and plugin MDFF[261] that generated configuration file submitted into NAMD software[255]. MDFF run was performed using 2,000 minimisation steps, 20,000 simulation steps in a vacuum with a grid force of 0.3. All models after MDFF were afterwards refined in 2 macrocycles using Phenix real space refinement[248]. The 4-spoked assembly intermediate model was refined in Namdinator[246] applying 2,000 minimisation steps and 20,000 simulation steps in a vacuum with a grid force of 0.3.

Conformational changes were visualised in vector representation using PyMOL (PyMOL v2.1, Schrödinger) as described. Cryo-EM reconstructions were visualised in UCSF Chimera[244] or in UCSF ChimeraX[262].

7 References

1 Takizawa, P. A. & Vale, R. D. The myosin motor, Myo4p, binds Ash1 mRNA via the adapter protein, She3p. *Proc Natl Acad Sci U S A* **97**, 5273-5278, doi:10.1073/pnas.080585897 (2000).

2 Scarborough, E. A. *et al.* Microtubules orchestrate local translation to enable cardiac growth. *Nat Commun* **12**, 1547, doi:10.1038/s41467-021-21685-4 (2021).

3 Pollard, T. D. & Borisy, G. G. Cellular motility driven by assembly and disassembly of actin filaments (vol 112, pg 453, 2002). *Cell* **113**, 549-549, doi:Doi 10.1016/S0092-8674(03)00357-X (2003).

4 Jansen, S. *et al.* Mechanism of Actin Filament Bundling by Fascin. *Journal of Biological Chemistry* **286**, 30087-30096, doi:10.1074/jbc.M111.251439 (2011).

5 Flanagan, L. A. *et al.* Filamin A, the Arp2/3 complex, and the morphology and function of cortical actin filaments in human melanoma cells. *Journal of Cell Biology* **155**, 511-517, doi:DOI 10.1083/jcb.200105148 (2001).

6 Lehtimaki, J. I., Rajakyla, E. K., Tojkander, S. & Lappalainen, P. Generation of stress fibers through myosin-driven reorganization of the actin cortex. *Elife* **10**, doi:ARTN e60710

10.7554/eLife.60710 (2021).

7 Fuchs, E. & Weber, K. Intermediate Filaments - Structure, Dynamics, Function, and Disease. *Annu Rev Biochem* **63**, 345-382, doi:DOI 10.1146/annurev.bi.63.070194.002021 (1994).

8 Lazarides, E. Intermediate Filaments as Mechanical Integrators of Cellular Space. *Nature* **283**, 249-256, doi:DOI 10.1038/283249a0 (1980).

9 Aebi, U., Cohn, J., Buhle, L. & Gerace, L. The Nuclear Lamina Is a Meshwork of Intermediate-Type Filaments. *Nature* **323**, 560-564, doi:DOI 10.1038/323560a0 (1986).

10 Paulin, D. & Li, Z. L. Desmin: a major intermediate filament protein essential for the structural integrity and function of muscle. *Exp Cell Res* **301**, 1-7, doi:10.1016/j.yexcr.2004.08.004 (2004).

11 Gu, L. H. & Coulombe, P. A. Keratin finction in skin epithelia: a broadening palette with surprising shades. *Current Opinion in Cell Biology* **19**, 13-23, doi:10.1016/j.ceb.2006.12.007 (2007).

12 van Bodegraven, E. J. & Etienne-Manneville, S. Intermediate Filaments from Tissue Integrity to Single Molecule Mechanics. *Cells* **10**, doi:10.3390/cells10081905 (2021).

13 Kelly, J. J. *et al.* Snapshots of actin and tubulin folding inside the TRiC chaperonin. *Nat Struct Mol Biol* **29**, 420-429, doi:10.1038/s41594-022-00755-1 (2022).

14 Tian, G. & Cowan, N. J. Tubulin-specific chaperones: components of a molecular machine that assembles the alpha/beta heterodimer. *Methods Cell Biol* **115**, 155-171, doi:10.1016/B978-0-12-407757-7.00011-6 (2013).

15 Erickson, H. P. FtsZ, a prokaryotic homolog of tubulin? *Cell* **80**, 367-370, doi:10.1016/0092-8674(95)90486-7 (1995).

16 Nogales, E., Whittaker, M., Milligan, R. A. & Downing, K. H. High-resolution model of the microtubule. *Cell* **96**, 79-88, doi:10.1016/s0092-8674(00)80961-7 (1999).

17 Tilney, L. G. *et al.* Microtubules: evidence for 13 protofilaments. *J Cell Biol* **59**, 267-275, doi:10.1083/jcb.59.2.267 (1973).

18 Chalfie, M. & Thomson, J. N. Structural and functional diversity in the neuronal microtubules of Caenorhabditis elegans. *J Cell Biol* **93**, 15-23, doi:10.1083/jcb.93.1.15 (1982).

19 Chretien, D. & Wade, R. H. New data on the microtubule surface lattice. *Biol Cell* **71**, 161-174, doi:10.1016/0248-4900(91)90062-r (1991).

20 Pierson, G. B., Burton, P. R. & Himes, R. H. Alterations in number of protofilaments in microtubules assembled in vitro. *J Cell Biol* **76**, 223-228, doi:10.1083/jcb.76.1.223 (1978).

21 Meunier, S. & Vernos, I. Microtubule assembly during mitosis - from distinct origins to distinct functions? *J Cell Sci* **125**, 2805-2814, doi:10.1242/jcs.092429 (2012).

22 Rosenblatt, J. Spindle assembly: asters part their separate ways. *Nat Cell Biol* **7**, 219-222, doi:10.1038/ncb0305-219 (2005).

23 Khodjakov, A., Cole, R. W., Oakley, B. R. & Rieder, C. L. Centrosome-independent mitotic spindle formation in vertebrates. *Curr Biol* **10**, 59-67, doi:10.1016/s0960-9822(99)00276-6 (2000).

24 Splinter, D. *et al.* Bicaudal D2, dynein, and kinesin-1 associate with nuclear pore complexes and regulate centrosome and nuclear positioning during mitotic entry. *PLoS Biol* **8**, e1000350, doi:10.1371/journal.pbio.1000350 (2010).

25 Zhai, Y., Kronebusch, P. J. & Borisy, G. G. Kinetochore microtubule dynamics and the metaphase-anaphase transition. *J Cell Biol* **131**, 721-734, doi:10.1083/jcb.131.3.721 (1995).

26 Wandke, C. *et al.* Human chromokinesins promote chromosome congression and spindle microtubule dynamics during mitosis. *J Cell Biol* **198**, 847-863, doi:10.1083/jcb.201110060 (2012).

27 Vanneste, D., Ferreira, V. & Vernos, I. Chromokinesins: localization-dependent functions and regulation during cell division. *Biochem Soc Trans* **39**, 1154-1160, doi:10.1042/BST0391154 (2011).

28 Cai, S., O'Connell, C. B., Khodjakov, A. & Walczak, C. E. Chromosome congression in the absence of kinetochore fibres. *Nat Cell Biol* **11**, 832-838, doi:10.1038/ncb1890 (2009).

29 Akera, T., Sato, M. & Yamamoto, M. Interpolar microtubules are dispensable in fission yeast meiosis II. *Nat Commun* **3**, 695, doi:10.1038/ncomms1725 (2012).

30 Bakhoum, S. F., Thompson, S. L., Manning, A. L. & Compton, D. A. Genome stability is ensured by temporal control of kinetochore-microtubule dynamics. *Nat Cell Biol* **11**, 27-35, doi:10.1038/ncb1809 (2009).

31 Rieder, C. L. The structure of the cold-stable kinetochore fiber in metaphase PtK1 cells. *Chromosoma* **84**, 145-158, doi:10.1007/BF00293368 (1981).

32 Booth, D. G., Hood, F. E., Prior, I. A. & Royle, S. J. A TACC3/ch-TOG/clathrin complex stabilises kinetochore fibres by inter-microtubule bridging. *EMBO J* **30**, 906-919, doi:10.1038/emboj.2011.15 (2011).

33 Joglekar, A. P., Bloom, K. S. & Salmon, E. D. Mechanisms of force generation by end-on kinetochore-microtubule attachments. *Curr Opin Cell Biol* **22**, 57-67, doi:10.1016/j.ceb.2009.12.010 (2010).

34 Rogers, G. C. *et al.* Two mitotic kinesins cooperate to drive sister chromatid separation during anaphase. *Nature* **427**, 364-370, doi:10.1038/nature02256 (2004).

35 Forth, S. & Kapoor, T. M. The mechanics of microtubule networks in cell division. *J Cell Biol* **216**, 1525-1531, doi:10.1083/jcb.201612064 (2017).

36 Hémonnot, C. *Investigating Cellular Nanoscale with X-rays*, Universitätsverlag Göttingen, (2016).

37 Klena, N. *et al.* Architecture of the centriole cartwheel-containing region revealed by cryo-electron tomography. *EMBO J* **39**, e106246, doi:10.15252/embj.2020106246 (2020).

38 Bettencourt-Dias, M. & Glover, D. M. Centrosome biogenesis and function: centrosomics brings new understanding. *Nat Rev Mol Cell Biol* **8**, 451-463, doi:10.1038/nrm2180 (2007).

39 Mardin, B. R. & Schiebel, E. Breaking the ties that bind: new advances in centrosome biology. *J Cell Biol* **197**, 11-18, doi:10.1083/jcb.201108006 (2012).

40 Li, S., Fernandez, J. J., Marshall, W. F. & Agard, D. A. Electron cryo-tomography provides insight into procentriole architecture and assembly mechanism. *Elife* **8**, doi:10.7554/eLife.43434 (2019).

41 van Breugel, M. *et al.* Structures of SAS-6 suggest its organization in centrioles. *Science* **331**, 1196-1199, doi:10.1126/science.1199325 (2011).

42 Lin, Y. C. *et al.* Human microcephaly protein CEP135 binds to hSAS-6 and CPAP, and is required for centriole assembly. *EMBO J* **32**, 1141-1154, doi:10.1038/emboj.2013.56 (2013).

43 Greenan, G. A., Keszthelyi, B., Vale, R. D. & Agard, D. A. Insights into centriole geometry revealed by cryotomography of doublet and triplet centrioles. *Elife* **7**, doi:10.7554/eLife.36851 (2018).

44 Hirota, T. *et al.* Aurora-A and an interacting activator, the LIM protein Ajuba, are required for mitotic commitment in human cells. *Cell* **114**, 585-598, doi:10.1016/s0092-8674(03)00642-1 (2003).

45 Keryer, G. *et al.* Dissociating the centrosomal matrix protein AKAP450 from centrioles impairs centriole duplication and cell cycle progression. *Mol Biol Cell* **14**, 2436-2446, doi:10.1091/mbc.e02-09-0614 (2003).

46 Gromley, A. *et al.* A novel human protein of the maternal centriole is required for the final stages of cytokinesis and entry into S phase. *J Cell Biol* **161**, 535-545, doi:10.1083/jcb.200301105 (2003).

47 Tsou, M. F. & Stearns, T. Mechanism limiting centrosome duplication to once per cell cycle. *Nature* **442**, 947-951, doi:10.1038/nature04985 (2006).

48 Kilmartin, J. V. Sfi1p has conserved centrin-binding sites and an essential function in budding yeast spindle pole body duplication. *J Cell Biol* **162**, 1211-1221, doi:10.1083/jcb.200307064 (2003).

49 Habedanck, R., Stierhof, Y. D., Wilkinson, C. J. & Nigg, E. A. The Polo kinase Plk4 functions in centriole duplication. *Nat Cell Biol* **7**, 1140-1146, doi:10.1038/ncb1320 (2005).

50 Dutcher, S. K. Long-lost relatives reappear: identification of new members of the tubulin superfamily. *Curr Opin Microbiol* **6**, 634-640, doi:10.1016/j.mib.2003.10.016 (2003).

51 Yang, J. *et al.* Rootletin, a novel coiled-coil protein, is a structural component of the ciliary rootlet. *J Cell Biol* **159**, 431-440, doi:10.1083/jcb.200207153 (2002).

52 Helps, N. R., Luo, X., Barker, H. M. & Cohen, P. T. NIMA-related kinase 2 (Nek2), a cell-cycle-regulated protein kinase localized to centrosomes, is complexed to protein phosphatase 1. *Biochem J* **349**, 509-518, doi:10.1042/0264-6021:3490509 (2000).

53 Meraldi, P. & Nigg, E. A. Centrosome cohesion is regulated by a balance of kinase and phosphatase activities. *J Cell Sci* **114**, 3749-3757, doi:10.1242/jcs.114.20.3749 (2001).

54 Faragher, A. J. & Fry, A. M. Nek2A kinase stimulates centrosome disjunction and is required for formation of bipolar mitotic spindles. *Mol Biol Cell* **14**, 2876-2889, doi:10.1091/mbc.e03-02-0108 (2003).

55 Tanenbaum, M. E. & Medema, R. H. Mechanisms of centrosome separation and bipolar spindle assembly. *Dev Cell* **19**, 797-806, doi:10.1016/j.devcel.2010.11.011 (2010).

56 Alushin, G. M. *et al.* High-resolution microtubule structures reveal the structural transitions in alphabeta-tubulin upon GTP hydrolysis. *Cell* **157**, 1117-1129, doi:10.1016/j.cell.2014.03.053 (2014).

57 Carlier, M. F., Didry, D. & Pantaloni, D. Microtubule elongation and guanosine 5'-triphosphate hydrolysis. Role of guanine nucleotides in microtubule dynamics. *Biochemistry* **26**, 4428-4437, doi:10.1021/bi00388a036 (1987).

58 Akhmanova, A. & Steinmetz, M. O. Control of microtubule organization and dynamics: two ends in the limelight. *Nat Rev Mol Cell Biol* **16**, 711-726, doi:10.1038/nrm4084 (2015).

59 Maurer, S. P. *et al.* EB1 accelerates two conformational transitions important for microtubule maturation and dynamics. *Curr Biol* **24**, 372-384, doi:10.1016/j.cub.2013.12.042 (2014).

60 Mandelkow, E. M., Mandelkow, E. & Milligan, R. A. Microtubule dynamics and microtubule caps: a time-resolved cryo-electron microscopy study. *J Cell Biol* **114**, 977-991, doi:10.1083/jcb.114.5.977 (1991).

61 Buey, R. M., Diaz, J. F. & Andreu, J. M. The nucleotide switch of tubulin and microtubule assembly: a polymerization-driven structural change. *Biochemistry* **45**, 5933-5938, doi:10.1021/bi060334m (2006).

62 Duellberg, C., Cade, N. I., Holmes, D. & Surrey, T. The size of the EB cap determines instantaneous microtubule stability. *Elife* **5**, doi:10.7554/eLife.13470 (2016).

63 Zhang, R., Alushin, G. M., Brown, A. & Nogales, E. Mechanistic Origin of Microtubule Dynamic Instability and Its Modulation by EB Proteins. *Cell* **162**, 849-859, doi:10.1016/j.cell.2015.07.012 (2015).

64 Maurer, S. P., Bieling, P., Cope, J., Hoenger, A. & Surrey, T. GTPgammaS microtubules mimic the growing microtubule end structure recognized by end-binding proteins (EBs). *Proc Natl Acad Sci U S A* **108**, 3988-3993, doi:10.1073/pnas.1014758108 (2011).

65 Mulder, A. M. *et al.* A new model for binding of kinesin 13 to curved microtubule protofilaments. *J Cell Biol* **185**, 51-57, doi:10.1083/jcb.200812052 (2009).

66 Belmont, L. D. & Mitchison, T. J. Identification of a protein that interacts with tubulin dimers and increases the catastrophe rate of microtubules. *Cell* **84**, 623-631, doi:10.1016/s0092-8674(00)81037-5 (1996).

67 Ayaz, P., Ye, X., Huddleston, P., Brautigam, C. A. & Rice, L. M. A TOG:alphabeta-tubulin complex structure reveals conformation-based mechanisms for a microtubule polymerase. *Science* **337**, 857-860, doi:10.1126/science.1221698 (2012).

68 Geyer, E. A. *et al.* A mutation uncouples the tubulin conformational and GTPase cycles, revealing allosteric control of microtubule dynamics. *Elife* **4**, e10113, doi:10.7554/eLife.10113 (2015).

69 Wieczorek, M., Bechstedt, S., Chaaban, S. & Brouhard, G. J. Microtubule-associated proteins control the kinetics of microtubule nucleation. *Nat Cell Biol* **17**, 907-916, doi:10.1038/ncb3188 (2015).

70 Bechstedt, S. & Brouhard, G. J. Doublecortin recognizes the 13-protofilament microtubule cooperatively and tracks microtubule ends. *Dev Cell* **23**, 181-192, doi:10.1016/j.devcel.2012.05.006 (2012).

71 Fourniol, F. J. *et al.* Template-free 13-protofilament microtubule-MAP assembly visualized at 8 A resolution. *J Cell Biol* **191**, 463-470, doi:10.1083/jcb.201007081 (2010).

72 Al-Bassam, J. & Chang, F. Regulation of microtubule dynamics by TOG-domain proteins XMAP215/Dis1 and CLASP. *Trends Cell Biol* **21**, 604-614, doi:10.1016/j.tcb.2011.06.007 (2011).

73 Nehlig, A., Molina, A., Rodrigues-Ferreira, S., Honore, S. & Nahmias, C. Regulation of end-binding protein EB1 in the control of microtubule dynamics. *Cell Mol Life Sci* **74**, 2381-2393, doi:10.1007/s00018-017-2476-2 (2017).

74 Zhang, R., Roostalu, J., Surrey, T. & Nogales, E. Structural insight into TPX2-stimulated microtubule assembly. *Elife* **6**, doi:10.7554/eLife.30959 (2017).

75 Karsenti, E. & Vernos, I. The mitotic spindle: a self-made machine. *Science* **294**, 543-547, doi:10.1126/science.1063488 (2001).

76 Vagnarelli, P. & Earnshaw, W. C. Chromosomal passengers: the four-dimensional regulation of mitotic events. *Chromosoma* **113**, 211-222, doi:10.1007/s00412-004-0307-3 (2004).

77 Scrofani, J., Sardon, T., Meunier, S. & Vernos, I. Microtubule nucleation in mitosis by a RanGTP-dependent protein complex. *Curr Biol* **25**, 131-140, doi:10.1016/j.cub.2014.11.025 (2015).

78 Petry, S., Groen, A. C., Ishihara, K., Mitchison, T. J. & Vale, R. D. Branching microtubule nucleation in Xenopus egg extracts mediated by augmin and TPX2. *Cell* **152**, 768-777, doi:10.1016/j.cell.2012.12.044 (2013).

79 Gruss, O. J. *et al.* Ran induces spindle assembly by reversing the inhibitory effect of importin alpha on TPX2 activity. *Cell* **104**, 83-93, doi:10.1016/s0092-8674(01)00193-3 (2001).

80 King, M. R. & Petry, S. Phase separation of TPX2 enhances and spatially coordinates microtubule nucleation. *Nat Commun* **11**, 270, doi:10.1038/s41467-019-14087-0 (2020).

81 Goshima, G., Mayer, M., Zhang, N., Stuurman, N. & Vale, R. D. Augmin: a protein complex required for centrosome-independent microtubule generation within the spindle. *J Cell Biol* **181**, 421-429, doi:10.1083/jcb.200711053 (2008).

82 Uehara, R. *et al.* The augmin complex plays a critical role in spindle microtubule generation for mitotic progression and cytokinesis in human cells. *Proc Natl Acad Sci U S A* **106**, 6998-7003, doi:10.1073/pnas.0901587106 (2009).

83 Ho, C. M. *et al.* Augmin plays a critical role in organizing the spindle and phragmoplast microtubule arrays in Arabidopsis. *Plant Cell* **23**, 2606-2618, doi:10.1105/tpc.111.086892 (2011).

84 Liu, T. *et al.* Augmin triggers microtubule-dependent microtubule nucleation in interphase plant cells. *Curr Biol* **24**, 2708-2713, doi:10.1016/j.cub.2014.09.053 (2014).

85 Hsia, K. C. *et al.* Reconstitution of the augmin complex provides insights into its architecture and function. *Nat Cell Biol* **16**, 852-863, doi:10.1038/ncb3030 (2014).

86 Chen, J. W. C. *et al.* Cross-linking mass spectrometry identifies new interfaces of Augmin required to localise the gamma-tubulin ring complex to the mitotic spindle. *Biol Open* **6**, 654-663, doi:10.1242/bio.022905 (2017).

87 Thawani, A., Stone, H. A., Shaevitz, J. W. & Petry, S. Spatiotemporal organization of branched microtubule networks. *Elife* **8**, doi:10.7554/eLife.43890 (2019).

88 Chabin-Brion, K. *et al.* The Golgi complex is a microtubule-organizing organelle. *Mol Biol Cell* **12**, 2047-2060, doi:10.1091/mbc.12.7.2047 (2001).

89 Miller, P. M. *et al.* Golgi-derived CLASP-dependent microtubules control Golgi organization and polarized trafficking in motile cells. *Nature Cell Biology* **11**, 1069-U1069, doi:10.1038/ncb1920 (2009).

90 Hurtado, L. *et al.* Disconnecting the Golgi ribbon from the centrosome prevents directional cell migration and ciliogenesis. *J Cell Biol* **193**, 917-933, doi:10.1083/jcb.201011014 (2011).

91 Wu, J. *et al.* Molecular Pathway of Microtubule Organization at the Golgi Apparatus. *Dev Cell* **39**, 44-60, doi:10.1016/j.devcel.2016.08.009 (2016).

92 Wei, J. H., Zhang, Z. C., Wynn, R. M. & Seemann, J. GM130 Regulates Golgi-Derived Spindle Assembly by Activating TPX2 and Capturing Microtubules. *Cell* **162**, 287-299, doi:10.1016/j.cell.2015.06.014 (2015).

93 Rivero, S., Cardenas, J., Bornens, M. & Rios, R. M. Microtubule nucleation at the cis-side of the Golgi apparatus requires AKAP450 and GM130. *EMBO J* **28**, 1016-1028, doi:10.1038/emboj.2009.47 (2009).

94 Wang, Z. *et al.* Conserved motif of CDK5RAP2 mediates its localization to centrosomes and the Golgi complex. *J Biol Chem* **285**, 22658-22665, doi:10.1074/jbc.M110.105965 (2010).

95 Roubin, R. *et al.* Myomegalin is necessary for the formation of centrosomal and Golgi-derived microtubules. *Biol Open* **2**, 238-250, doi:10.1242/bio.20123392 (2013).

96 Efimov, A. *et al.* Asymmetric CLASP-dependent nucleation of noncentrosomal microtubules at the trans-Golgi network. *Dev Cell* **12**, 917-930, doi:10.1016/j.devcel.2007.04.002 (2007).

97 Sanders, A. A. & Kaverina, I. Nucleation and Dynamics of Golgi-derived Microtubules. *Front Neurosci* **9**, 431, doi:10.3389/fnins.2015.00431 (2015).

98 Wang, Z., Zhang, C. & Qi, R. Z. A newly identified myomegalin isoform functions in Golgi microtubule organization and ER-Golgi transport. *J Cell Sci* **127**, 4904-4917, doi:10.1242/jcs.155408 (2014).

99 Bellouze, S. *et al.* Golgi fragmentation in pmn mice is due to a defective ARF1/TBCE cross-talk that coordinates COPI vesicle formation and tubulin polymerization. *Hum Mol Genet* **23**, 5961-5975, doi:10.1093/hmg/ddu320 (2014).

100 Hoppeler-Lebel, A. *et al.* Centrosomal CAP350 protein stabilises microtubules associated with the Golgi complex. *J Cell Sci* **120**, 3299-3308, doi:10.1242/jcs.013102 (2007).

101 Carmena, M., Wheelock, M., Funabiki, H. & Earnshaw, W. C. The chromosomal passenger complex (CPC): from easy rider to the godfather of mitosis. *Nat Rev Mol Cell Biol* **13**, 789-803, doi:10.1038/nrm3474 (2012).

102 Song, J. G. *et al.* Mechanism of how augmin directly targets the gamma-tubulin ring complex to microtubules. *J Cell Biol* **217**, 2417-2428, doi:10.1083/jcb.201711090 (2018).

103 Alfaro-Aco, R., Thawani, A. & Petry, S. Biochemical reconstitution of branching microtubule nucleation. *Elife* **9**, doi:10.7554/eLife.49797 (2020).

104 Wu, J. & Akhmanova, A. Microtubule-Organizing Centers. *Annu Rev Cell Dev Biol* **33**, 51-75, doi:10.1146/annurev-cellbio-100616-060615 (2017).

105 Piccus, R. & Brayson, D. The nuclear envelope: LINCing tissue mechanics to genome regulation in cardiac and skeletal muscle. *Biol Lett* **16**, 20200302, doi:10.1098/rsbl.2020.0302 (2020).

106 Masoud, K., Herzog, E., Chaboute, M. E. & Schmit, A. C. Microtubule nucleation and establishment of the mitotic spindle in vascular plant cells. *Plant J* **75**, 245-257, doi:10.1111/tpj.12179 (2013).

107 Tassin, A. M., Maro, B. & Bornens, M. Fate of microtubule-organizing centers during myogenesis in vitro. *J Cell Biol* **100**, 35-46, doi:10.1083/jcb.100.1.35 (1985).

108 Gimpel, P. *et al.* Nesprin-1alpha-Dependent Microtubule Nucleation from the Nuclear Envelope via Akap450 Is Necessary for Nuclear Positioning in Muscle Cells. *Curr Biol* **27**, 2999-3009 e2999, doi:10.1016/j.cub.2017.08.031 (2017).

109 Crisp, M. *et al.* Coupling of the nucleus and cytoplasm: role of the LINC complex. *J Cell Biol* **172**, 41-53, doi:10.1083/jcb.200509124 (2006).

110 Lee, Y. J. & Liu, B. Microtubule nucleation for the assembly of acentrosomal microtubule arrays in plant cells. *New Phytol* **222**, 1705-1718, doi:10.1111/nph.15705 (2019).

111 Batzenschlager, M., Herzog, E., Houlne, G., Schmit, A. C. & Chaboute, M. E. GIP/MZT1 proteins orchestrate nuclear shaping. *Front Plant Sci* **5**, 29, doi:10.3389/fpls.2014.00029 (2014).

112 Hamada, T. Microtubule organization and microtubule-associated proteins in plant cells. *Int Rev Cell Mol Biol* **312**, 1-52, doi:10.1016/B978-0-12-800178-3.00001-4 (2014).

113 Sanchez, A. D. & Feldman, J. L. Microtubule-organizing centers: from the centrosome to non-centrosomal sites. *Curr Opin Cell Biol* **44**, 93-101, doi:10.1016/j.ceb.2016.09.003 (2017).

114 Shaw, S. L., Kamyar, R. & Ehrhardt, D. W. Sustained microtubule treadmilling in Arabidopsis cortical arrays. *Science* **300**, 1715-1718, doi:10.1126/science.1083529 (2003).

115 Noordstra, I. *et al.* Control of apico-basal epithelial polarity by the microtubule minus-end-binding protein CAMSAP3 and spectraplakin ACF7. *J Cell Sci* **129**, 4278-4288, doi:10.1242/jcs.194878 (2016).

116 Muroyama, A., Seldin, L. & Lechler, T. Divergent regulation of functionally distinct gamma-tubulin complexes during differentiation. *Journal of Cell Biology* **213**, 679-692, doi:10.1083/jcb.201601099 (2016).

117 Lee, C., Scherr, H. M. & Wallingford, J. B. Shroom family proteins regulate gamma-tubulin distribution and microtubule architecture during epithelial cell shape change. *Development* **134**, 1431-1441, doi:10.1242/dev.02828 (2007).

118 Lechler, T. & Fuchs, E. Desmoplakin: An unexpected regulator of microtubule organization in the epidermis. *Journal of Cell Biology* **176**, 147-154, doi:10.1083/jcb.200609109 (2007).

119 Hashimoto, T. Dynamics and regulation of plant interphase microtubules: a comparative view. *Curr Opin Plant Biol* **6**, 568-576, doi:10.1016/j.pbi.2003.09.011 (2003).

120 Oakley, C. E. & Oakley, B. R. Identification of gamma-tubulin, a new member of the tubulin superfamily encoded by mipA gene of Aspergillus nidulans. *Nature* **338**, 662-664, doi:10.1038/338662a0 (1989).

121 Raff, J. W., Kellogg, D. R. & Alberts, B. M. Drosophila gamma-tubulin is part of a complex containing two previously identified centrosomal MAPs. *J Cell Biol* **121**, 823-835, doi:10.1083/jcb.121.4.823 (1993).

122 Zheng, Y., Wong, M. L., Alberts, B. & Mitchison, T. Nucleation of microtubule assembly by a gamma-tubulin-containing ring complex. *Nature* **378**, 578-583, doi:10.1038/378578a0 (1995).

123 Knop, M., Pereira, G., Geissler, S., Grein, K. & Schiebel, E. The spindle pole body component Spc97p interacts with the gamma-tubulin of Saccharomyces cerevisiae and functions in microtubule organization and spindle pole body duplication. *EMBO J* **16**, 1550-1564, doi:10.1093/emboj/16.7.1550 (1997).

124 Geissler, S. *et al.* The spindle pole body component Spc98p interacts with the gamma-tubulin-like Tub4p of Saccharomyces cerevisiae at the sites of microtubule attachment. *EMBO J* **15**, 3899-3911 (1996).

125 Tassin, A. M., Celati, C., Moudjou, M. & Bornens, M. Characterization of the human homologue of the yeast spc98p and its association with gamma-tubulin. *J Cell Biol* **141**, 689-701, doi:10.1083/jcb.141.3.689 (1998).

126 Fava, F. *et al.* Human 76p: A new member of the gamma-tubulin-associated protein family. *J Cell Biol* **147**, 857-868, doi:10.1083/jcb.147.4.857 (1999).

127 Murphy, S. M. *et al.* GCP5 and GCP6: two new members of the human gamma-tubulin complex. *Mol Biol Cell* **12**, 3340-3352, doi:10.1091/mbc.12.11.3340 (2001).

128 Byers, B. & Goetsch, L. Duplication of spindle plaques and integration of the yeast cell cycle. *Cold Spring Harb Symp Quant Biol* **38**, 123-131, doi:10.1101/sqb.1974.038.01.016 (1974).

129 O'Toole, E. T., Winey, M. & McIntosh, J. R. High-voltage electron tomography of spindle pole bodies and early mitotic spindles in the yeast Saccharomyces cerevisiae. *Mol Biol Cell* **10**, 2017-2031, doi:10.1091/mbc.10.6.2017 (1999).

130 Parnaik, V. K. Role of nuclear lamins in nuclear organization, cellular signaling, and inherited diseases. *Int Rev Cell Mol Biol* **266**, 157-206, doi:10.1016/S1937-6448(07)66004-3 (2008).

131 Oshidari, R. *et al.* Nuclear microtubule filaments mediate non-linear directional motion of chromatin and promote DNA repair. *Nat Commun* **9**, 2567, doi:10.1038/s41467-018-05009-7 (2018).

132 Molk, J. N., Salmon, E. D. & Bloom, K. Nuclear congression is driven by cytoplasmic microtubule plus end interactions in S. cerevisiae. *J Cell Biol* **172**, 27-39, doi:10.1083/jcb.200510032 (2006).

133 Knop, M. & Schiebel, E. Spc98p and Spc97p of the yeast gamma-tubulin complex mediate binding to the spindle pole body via their interaction with Spc110p. *EMBO J* **16**, 6985-6995, doi:10.1093/emboj/16.23.6985 (1997).

134 Elliott, S., Knop, M., Schlenstedt, G. & Schiebel, E. Spc29p is a component of the Spc110p subcomplex and is essential for spindle pole body duplication. *Proc Natl Acad Sci U S A* **96**, 6205-6210, doi:10.1073/pnas.96.11.6205 (1999).

135 Adams, I. R. & Kilmartin, J. V. Localization of core spindle pole body (SPB) components during SPB duplication in Saccharomyces cerevisiae. *J Cell Biol* **145**, 809-823, doi:10.1083/jcb.145.4.809 (1999).

136 Schaerer, F., Morgan, G., Winey, M. & Philippsen, P. Cnm67p is a spacer protein of the Saccharomyces cerevisiae spindle pole body outer plaque. *Mol Biol Cell* **12**, 2519-2533, doi:10.1091/mbc.12.8.2519 (2001).

137 Gruneberg, U., Campbell, K., Simpson, C., Grindlay, J. & Schiebel, E. Nud1p links astral microtubule organization and the control of exit from mitosis. *EMBO J* **19**, 6475-6488, doi:10.1093/emboj/19.23.6475 (2000).

138 Knop, M. & Schiebel, E. Receptors determine the cellular localization of a gamma-tubulin complex and thereby the site of microtubule formation. *EMBO J* **17**, 3952-3967, doi:10.1093/emboj/17.14.3952 (1998).

139 Lin, T. C. *et al.* Cell-cycle dependent phosphorylation of yeast pericentrin regulates gamma-TuSC-mediated microtubule nucleation. *Elife* **3**, e02208, doi:10.7554/eLife.02208 (2014).

140 Pereira, G., Grueneberg, U., Knop, M. & Schiebel, E. Interaction of the yeast gamma-tubulin complex-binding protein Spc72p with Kar1p is essential for microtubule function during karyogamy. *EMBO J* **18**, 4180-4195, doi:10.1093/emboj/18.15.4180 (1999).

141 Wigge, P. A. *et al.* Analysis of the Saccharomyces spindle pole by matrix-assisted laser desorption/ionization (MALDI) mass spectrometry. *J Cell Biol* **141**, 967-977, doi:10.1083/jcb.141.4.967 (1998).

142 Chial, H. J., Rout, M. P., Giddings, T. H. & Winey, M. Saccharomyces cerevisiae Ndc1p is a shared component of nuclear pore complexes and spindle pole bodies. *J Cell Biol* **143**, 1789-1800, doi:10.1083/jcb.143.7.1789 (1998).

143 Winey, M., Goetsch, L., Baum, P. & Byers, B. MPS1 and MPS2: novel yeast genes defining distinct steps of spindle pole body duplication. *J Cell Biol* **114**, 745-754, doi:10.1083/jcb.114.4.745 (1991).

144 Schramm, C., Elliott, S., Shevchenko, A. & Schiebel, E. The Bbp1p-Mps2p complex connects the SPB to the nuclear envelope and is essential for SPB duplication. *EMBO J* **19**, 421-433, doi:10.1093/emboj/19.3.421 (2000).

145 Biggins, S. & Rose, M. D. Direct interaction between yeast spindle pole body components: Kar1p is required for Cdc31p localization to the spindle pole body. *J Cell Biol* **125**, 843-852, doi:10.1083/jcb.125.4.843 (1994).

146 Jaspersen, S. L., Giddings, T. H., Jr. & Winey, M. Mps3p is a novel component of the yeast spindle pole body that interacts with the yeast centrin homologue Cdc31p. *J Cell Biol* **159**, 945-956, doi:10.1083/jcb.200208169 (2002).

147 Spang, A., Courtney, I., Fackler, U., Matzner, M. & Schiebel, E. The calcium-binding protein cell division cycle 31 of Saccharomyces cerevisiae is a component of the half bridge of the spindle pole body. *J Cell Biol* **123**, 405-416, doi:10.1083/jcb.123.2.405 (1993).

148 Chen, X. P., Yin, H. & Huffaker, T. C. The yeast spindle pole body component Spc72p interacts with Stu2p and is required for proper microtubule assembly. *J Cell Biol* **141**, 1169-1179, doi:10.1083/jcb.141.5.1169 (1998).

149 Adams, I. R. & Kilmartin, J. V. Spindle pole body duplication: a model for centrosome duplication? *Trends Cell Biol* **10**, 329-335, doi:10.1016/s0962-8924(00)01798-0 (2000).

150 Byers, B. & Goetsch, L. Behavior of spindles and spindle plaques in the cell cycle and conjugation of Saccharomyces cerevisiae. *J Bacteriol* **124**, 511-523, doi:10.1128/jb.124.1.511-523.1975 (1975).

151 Oakley, B. R., Oakley, C. E., Yoon, Y. & Jung, M. K. Gamma-tubulin is a component of the spindle pole body that is essential for microtubule function in Aspergillus nidulans. *Cell* **61**, 1289-1301, doi:10.1016/0092-8674(90)90693-9 (1990).

152 Lin, T. C., Neuner, A. & Schiebel, E. Targeting of gamma-tubulin complexes to microtubule organizing centers: conservation and divergence. *Trends Cell Biol* **25**, 296-307, doi:10.1016/j.tcb.2014.12.002 (2015).

153 Kollman, J. M. *et al.* The structure of the gamma-tubulin small complex: implications of its architecture and flexibility for microtubule nucleation. *Mol Biol Cell* **19**, 207-215, doi:10.1091/mbc.e07-09-0879 (2008).

154 Gunawardane, R. N., Martin, O. C. & Zheng, Y. Characterization of a new gammaTuRC subunit with WD repeats. *Mol Biol Cell* **14**, 1017-1026, doi:10.1091/mbc.e02-01-0034 (2003).

155 Guillet, V. *et al.* Crystal structure of gamma-tubulin complex protein GCP4 provides insight into microtubule nucleation. *Nat Struct Mol Biol* **18**, 915-919, doi:10.1038/nsmb.2083 (2011).

156 Kollman, J. M. *et al.* Ring closure activates yeast gammaTuRC for species-specific microtubule nucleation. *Nat Struct Mol Biol* **22**, 132-137, doi:10.1038/nsmb.2953 (2015).

157 Kollman, J. M., Polka, J. K., Zelter, A., Davis, T. N. & Agard, D. A. Microtubule nucleating gamma-TuSC assembles structures with 13-fold microtubule-like symmetry. *Nature* **466**, 879-882, doi:10.1038/nature09207 (2010).

158 Teixido-Travesa, N. *et al.* The gammaTuRC revisited: a comparative analysis of interphase and mitotic human gammaTuRC redefines the set of core components and identifies the novel subunit GCP8. *Mol Biol Cell* **21**, 3963-3972, doi:10.1091/mbc.E10-05-0408 (2010).

159 Lin, T. C. *et al.* MOZART1 and gamma-tubulin complex receptors are both required to turn gamma-TuSC into an active microtubule nucleation template. *J Cell Biol* **215**, 823-840, doi:10.1083/jcb.201606092 (2016).

160 Hutchins, J. R. *et al.* Systematic analysis of human protein complexes identifies chromosome segregation proteins. *Science* **328**, 593-599, doi:10.1126/science.1181348 (2010).

161 Ayaz, P. *et al.* A tethered delivery mechanism explains the catalytic action of a microtubule polymerase. *Elife* **3**, e03069, doi:10.7554/eLife.03069 (2014).

162 Haase, K. P. *et al.* Stu2 uses a 15-nm parallel coiled coil for kinetochore localization and concomitant regulation of the mitotic spindle. *Mol Biol Cell* **29**, 285-294, doi:10.1091/mbc.E17-01-0057 (2018).

163 Gunzelmann, J. *et al.* The microtubule polymerase Stu2 promotes oligomerization of the gamma-TuSC for cytoplasmic microtubule nucleation. *Elife* **7**, doi:10.7554/eLife.39932 (2018).

164 Nithianantham, S. *et al.* Structural basis of tubulin recruitment and assembly by microtubule polymerases with tumor overexpressed gene (TOG) domain arrays. *Elife* **7**, doi:10.7554/eLife.38922 (2018).

165 Jaspersen, S. L. & Winey, M. The budding yeast spindle pole body: structure, duplication, and function. *Annu Rev Cell Dev Biol* **20**, 1-28, doi:10.1146/annurev.cellbio.20.022003.114106 (2004).

166 Miller, V. J.

167 Sawin, K. E. & Tran, P. T. Cytoplasmic microtubule organization in fission yeast. *Yeast* **23**, 1001-1014, doi:10.1002/yea.1404 (2006).

168 Drummond, D. R. & Cross, R. A. Dynamics of interphase microtubules in Schizosaccharomyces pombe. *Curr Biol* **10**, 766-775, doi:10.1016/s0960-9822(00)00570-4 (2000).

169 Heitz, M. J., Petersen, J., Valovin, S. & Hagan, I. M. MTOC formation during mitotic exit in fission yeast. *J Cell Sci* **114**, 4521-4532, doi:10.1242/jcs.114.24.4521 (2001).

170 Zimmerman, S., Tran, P. T., Daga, R. R., Niwa, O. & Chang, F. Rsp1p, a J domain protein required for disassembly and assembly of microtubule organizing centers during the fission yeast cell cycle. *Dev Cell* **6**, 497-509, doi:10.1016/s1534-5807(04)00096-6 (2004).

171 Venkatram, S., Jennings, J. L., Link, A. & Gould, K. L. Mto2p, a novel fission yeast protein required for cytoplasmic microtubule organization and anchoring of the cytokinetic actin ring. *Mol Biol Cell* **16**, 3052-3063, doi:10.1091/mbc.e04-12-1043 (2005).

172 Lynch, E. M., Groocock, L. M., Borek, W. E. & Sawin, K. E. Activation of the gamma-tubulin complex by the Mto1/2 complex. *Curr Biol* **24**, 896-903, doi:10.1016/j.cub.2014.03.006 (2014).

173 Anders, A., Lourenco, P. C. & Sawin, K. E. Noncore components of the fission yeast gamma-tubulin complex. *Mol Biol Cell* **17**, 5075-5093, doi:10.1091/mbc.e05-11-1009 (2006).

174 Masuda, H. & Toda, T. Synergistic role of fission yeast Alp16GCP6 and Mzt1MOZART1 in gamma-tubulin complex recruitment to mitotic spindle pole bodies and spindle assembly. *Mol Biol Cell* **27**, 1753-1763, doi:10.1091/mbc.E15-08-0577 (2016).

175 Choi, Y. K., Liu, P., Sze, S. K., Dai, C. & Qi, R. Z. CDK5RAP2 stimulates microtubule nucleation by the gamma-tubulin ring complex. *J Cell Biol* **191**, 1089-1095, doi:10.1083/jcb.201007030 (2010).

176 Gunawardane, R. N. *et al.* Characterization and reconstitution of Drosophila gamma-tubulin ring complex subunits. *J Cell Biol* **151**, 1513-1524, doi:10.1083/jcb.151.7.1513 (2000).

177 Moritz, M., Braunfeld, M. B., Guenebaut, V., Heuser, J. & Agard, D. A. Structure of the gamma-tubulin ring complex: a template for microtubule nucleation. *Nat Cell Biol* **2**, 365-370, doi:10.1038/35014058 (2000).

178 Tovey, C. A. & Conduit, P. T. Microtubule nucleation by gamma-tubulin complexes and beyond. *Essays Biochem* **62**, 765-780, doi:10.1042/EBC20180028 (2018).

179 Farache, D. *et al.* Functional Analysis of gamma-Tubulin Complex Proteins Indicates Specific Lateral Association via Their N-terminal Domains. *J Biol Chem* **291**, 23112-23125, doi:10.1074/jbc.M116.744862 (2016).

180 Luders, J., Patel, U. K. & Stearns, T. GCP-WD is a gamma-tubulin targeting factor required for centrosomal and chromatin-mediated microtubule nucleation. *Nat Cell Biol* **8**, 137-147, doi:10.1038/ncb1349 (2006).

181 Liu, P., Choi, Y. K. & Qi, R. Z. NME7 is a functional component of the gamma-tubulin ring complex. *Mol Biol Cell* **25**, 2017-2025, doi:10.1091/mbc.E13-06-0339 (2014).

182 Haren, L. *et al.* NEDD1-dependent recruitment of the gamma-tubulin ring complex to the centrosome is necessary for centriole duplication and spindle assembly. *J Cell Biol* **172**, 505-515, doi:10.1083/jcb.200510028 (2006).

183 Manning, J. A., Shalini, S., Risk, J. M., Day, C. L. & Kumar, S. A direct interaction with NEDD1 regulates gamma-tubulin recruitment to the centrosome. *PLoS One* **5**, e9618, doi:10.1371/journal.pone.0009618 (2010).

184 Zhang, X. *et al.* Sequential phosphorylation of Nedd1 by Cdk1 and Plk1 is required for targeting of the gammaTuRC to the centrosome. *J Cell Sci* **122**, 2240-2251, doi:10.1242/jcs.042747 (2009).

185 Gomez-Ferreria, M. A. *et al.* Novel NEDD1 phosphorylation sites regulate gamma-tubulin binding and mitotic spindle assembly. *J Cell Sci* **125**, 3745-3751, doi:10.1242/jcs.105130 (2012).

186 Lacombe, M. L., Milon, L., Munier, A., Mehus, J. G. & Lambeth, D. O. The human Nm23/nucleoside diphosphate kinases. *J Bioenerg Biomembr* **32**, 247-258, doi:10.1023/a:1005584929050 (2000).

187 Batzenschlager, M. *et al.* Arabidopsis MZT1 homologs GIP1 and GIP2 are essential for centromere architecture. *Proc Natl Acad Sci U S A* **112**, 8656-8660, doi:10.1073/pnas.1506351112 (2015).

188 Cukier, C. D. *et al.* NMR secondary structure and interactions of recombinant human MOZART1 protein, a component of the gamma-tubulin complex. *Protein Sci* **26**, 2240-2248, doi:10.1002/pro.3282 (2017).
189 Zimmermann, F. *et al.* Assembly of the asymmetric human gamma-tubulin ring complex by RUVBL1-RUVBL2 AAA ATPase. *Sci Adv* **6**, doi:10.1126/sciadv.abe0894 (2020).
190 Cota, R. R. *et al.* MZT1 regulates microtubule nucleation by linking gammaTuRC assembly to adapter-mediated targeting and activation. *J Cell Sci* **130**, 406-419, doi:10.1242/jcs.195321 (2017).
191 Fong, K. W., Choi, Y. K., Rattner, J. B. & Qi, R. Z. CDK5RAP2 is a pericentriolar protein that functions in centrosomal attachment of the gamma-tubulin ring complex. *Mol Biol Cell* **19**, 115-125, doi:10.1091/mbc.e07-04-0371 (2008).
192 Lizarraga, S. B. *et al.* Cdk5rap2 regulates centrosome function and chromosome segregation in neuronal progenitors. *Development* **137**, 1907-1917, doi:10.1242/dev.040410 (2010).
193 Thawani, A., Kadzik, R. S. & Petry, S. XMAP215 is a microtubule nucleation factor that functions synergistically with the gamma-tubulin ring complex. *Nat Cell Biol* **20**, 575-585, doi:10.1038/s41556-018-0091-6 (2018).
194 Tournebize, R. *et al.* Control of microtubule dynamics by the antagonistic activities of XMAP215 and XKCM1 in Xenopus egg extracts. *Nat Cell Biol* **2**, 13-19, doi:10.1038/71330 (2000).
195 Brouhard, G. J. *et al.* XMAP215 is a processive microtubule polymerase. *Cell* **132**, 79-88, doi:10.1016/j.cell.2007.11.043 (2008).
196 Byrnes, A. E. & Slep, K. C. TOG-tubulin binding specificity promotes microtubule dynamics and mitotic spindle formation. *J Cell Biol* **216**, 1641-1657, doi:10.1083/jcb.201610090 (2017).
197 Lawo, S., Hasegan, M., Gupta, G. D. & Pelletier, L. Subdiffraction imaging of centrosomes reveals higher-order organizational features of pericentriolar material. *Nat Cell Biol* **14**, 1148-1158, doi:10.1038/ncb2591 (2012).
198 Fry, A. M., Sampson, J., Shak, C. & Shackleton, S. Recent advances in pericentriolar material organization: ordered layers and scaffolding gels. *F1000Res* **6**, 1622, doi:10.12688/f1000research.11652.1 (2017).
199 Fu, J. & Glover, D. M. Structured illumination of the interface between centriole and peri-centriolar material. *Open Biol* **2**, 120104, doi:10.1098/rsob.120104 (2012).
200 Piel, M., Meyer, P., Khodjakov, A., Rieder, C. L. & Bornens, M. The respective contributions of the mother and daughter centrioles to centrosome activity and behavior in vertebrate cells. *J Cell Biol* **149**, 317-330, doi:10.1083/jcb.149.2.317 (2000).
201 Delgehyr, N., Sillibourne, J. & Bornens, M. Microtubule nucleation and anchoring at the centrosome are independent processes linked by ninein function. *J Cell Sci* **118**, 1565-1575, doi:10.1242/jcs.02302 (2005).
202 Joukov, V., Walter, J. C. & De Nicolo, A. The Cep192-organized aurora A-Plk1 cascade is essential for centrosome cycle and bipolar spindle assembly. *Mol Cell* **55**, 578-591, doi:10.1016/j.molcel.2014.06.016 (2014).
203 Woodruff, J. B., Wueseke, O. & Hyman, A. A. Pericentriolar material structure and dynamics. *Philos Trans R Soc Lond B Biol Sci* **369**, doi:10.1098/rstb.2013.0459 (2014).
204 Mennella, V. *et al.* Subdiffraction-resolution fluorescence microscopy reveals a domain of the centrosome critical for pericentriolar material organization. *Nat Cell Biol* **14**, 1159-1168, doi:10.1038/ncb2597 (2012).
205 Haren, L., Stearns, T. & Luders, J. Plk1-dependent recruitment of gamma-tubulin complexes to mitotic centrosomes involves multiple PCM components. *PLoS One* **4**, e5976, doi:10.1371/journal.pone.0005976 (2009).
206 Schlaitz, A. L. *et al.* The C. elegans RSA complex localizes protein phosphatase 2A to centrosomes and regulates mitotic spindle assembly. *Cell* **128**, 115-127, doi:10.1016/j.cell.2006.10.050 (2007).

207 Sumiyoshi, E., Sugimoto, A. & Yamamoto, M. Protein phosphatase 4 is required for centrosome maturation in mitosis and sperm meiosis in C. elegans. *J Cell Sci* **115**, 1403-1410, doi:10.1242/jcs.115.7.1403 (2002).

208 Hanafusa, H. *et al.* PLK1-dependent activation of LRRK1 regulates spindle orientation by phosphorylating CDK5RAP2. *Nat Cell Biol* **17**, 1024-1035, doi:10.1038/ncb3204 (2015).

209 Feng, Z. *et al.* Structural Basis for Mitotic Centrosome Assembly in Flies. *Cell* **169**, 1078-1089 e1013, doi:10.1016/j.cell.2017.05.030 (2017).

210 Conduit, P. T. *et al.* The centrosome-specific phosphorylation of Cnn by Polo/Plk1 drives Cnn scaffold assembly and centrosome maturation. *Dev Cell* **28**, 659-669, doi:10.1016/j.devcel.2014.02.013 (2014).

211 Joukov, V., De Nicolo, A., Rodriguez, A., Walter, J. C. & Livingston, D. M. Centrosomal protein of 192 kDa (Cep192) promotes centrosome-driven spindle assembly by engaging in organelle-specific Aurora A activation. *Proc Natl Acad Sci U S A* **107**, 21022-21027, doi:10.1073/pnas.1014664107 (2010).

212 Bammes, B. E., Jakana, J., Schmid, M. F. & Chiu, W. Radiation damage effects at four specimen temperatures from 4 to 100 K. *J Struct Biol* **169**, 331-341, doi:10.1016/j.jsb.2009.11.001 (2010).

213 Orlova, E. V. & Saibil, H. R. Structural analysis of macromolecular assemblies by electron microscopy. *Chem Rev* **111**, 7710-7748, doi:10.1021/cr100353t (2011).

214 Sigworth, F. J., Doerschuk, P. C., Carazo, J. M. & Scheres, S. H. An introduction to maximum-likelihood methods in cryo-EM. *Methods Enzymol* **482**, 263-294, doi:10.1016/S0076-6879(10)82011-7 (2010).

215 Beckers, M., Mann, D. & Sachse, C. Structural interpretation of cryo-EM image reconstructions. *Prog Biophys Mol Biol* **160**, 26-36, doi:10.1016/j.pbiomolbio.2020.07.004 (2021).

216 Zupa, E. *et al.* The cryo-EM structure of a gamma-TuSC elucidates architecture and regulation of minimal microtubule nucleation systems. *Nat Commun* **11**, 5705, doi:10.1038/s41467-020-19456-8 (2020).

217 Aldaz, H., Rice, L. M., Stearns, T. & Agard, D. A. Insights into microtubule nucleation from the crystal structure of human gamma-tubulin. *Nature* **435**, 523-527, doi:10.1038/nature03586 (2005).

218 Howes, S. C. *et al.* Structural differences between yeast and mammalian microtubules revealed by cryo-EM. *J Cell Biol* **216**, 2669-2677, doi:10.1083/jcb.201612195 (2017).

219 Liu, P. *et al.* Insights into the assembly and activation of the microtubule nucleator gamma-TuRC. *Nature* **578**, 467-471, doi:10.1038/s41586-019-1896-6 (2020).

220 Wieczorek, M. *et al.* Asymmetric Molecular Architecture of the Human gamma-Tubulin Ring Complex. *Cell* **180**, 165-175 e116, doi:10.1016/j.cell.2019.12.007 (2020).

221 Consolati, T. *et al.* Microtubule Nucleation Properties of Single Human gammaTuRCs Explained by Their Cryo-EM Structure. *Dev Cell* **53**, 603-617 e608, doi:10.1016/j.devcel.2020.04.019 (2020).

222 Brilot, A. F. *et al.* CM1-driven assembly and activation of yeast gamma-tubulin small complex underlies microtubule nucleation. *Elife* **10**, doi:10.7554/eLife.65168 (2021).

223 Greenberg, C. H. *et al.* Structure of gamma-tubulin small complex based on a cryo-EM map, chemical cross-links, and a remotely related structure. *J Struct Biol* **194**, 303-310, doi:10.1016/j.jsb.2016.03.006 (2016).

224 Nakane, T., Kimanius, D., Lindahl, E. & Scheres, S. H. Characterisation of molecular motions in cryo-EM single-particle data by multi-body refinement in RELION. *Elife* **7**, doi:10.7554/eLife.36861 (2018).

225 Chou, S. Z. & Pollard, T. D. Mechanism of actin polymerization revealed by cryo-EM structures of actin filaments with three different bound nucleotides. *Proc Natl Acad Sci U S A* **116**, 4265-4274, doi:10.1073/pnas.1807028115 (2019).

226 Kabsch, W., Mannherz, H. G., Suck, D., Pai, E. F. & Holmes, K. C. Atomic structure of the actin:DNase I complex. *Nature* **347**, 37-44, doi:10.1038/347037a0 (1990).

227 Farina, F. *et al.* The centrosome is an actin-organizing centre. *Nat Cell Biol* **18**, 65-75, doi:10.1038/ncb3285 (2016).

228 Wieczorek, M., Huang, T. L., Urnavicius, L., Hsia, K. C. & Kapoor, T. M. MZT Proteins Form Multi-Faceted Structural Modules in the gamma-Tubulin Ring Complex. *Cell Rep* **31**, 107791, doi:10.1016/j.celrep.2020.107791 (2020).

229 Wurtz, M. *et al.* Modular assembly of the principal microtubule nucleator gamma-TuRC. *Nat Commun* **13**, 473, doi:10.1038/s41467-022-28079-0 (2022).

230 Wieczorek, M. *et al.* Biochemical reconstitutions reveal principles of human gamma-TuRC assembly and function. *Journal of Cell Biology* **220**, doi:ARTN e202009146

10.1083/jcb.202009146 (2021).

231 Wurtz, M. *et al.* Reconstitution of the recombinant human gamma-tubulin ring complex. *Open Biol* **11**, 200325, doi:10.1098/rsob.200325 (2021).

232 Huang, T. L., Wang, H. J., Chang, Y. C., Wang, S. W. & Hsia, K. C. Promiscuous Binding of Microprotein Mozart1 to gamma-Tubulin Complex Mediates Specific Subcellular Targeting to Control Microtubule Array Formation. *Cell Rep* **31**, 107836, doi:10.1016/j.celrep.2020.107836 (2020).

233 Haren, L., Farache, D., Emorine, L. & Merdes, A. A stable sub-complex between GCP4, GCP5 and GCP6 promotes the assembly of gamma-tubulin ring complexes. *J Cell Sci* **133**, doi:10.1242/jcs.244368 (2020).

234 Jumper, J. *et al.* Highly accurate protein structure prediction with AlphaFold. *Nature*, doi:10.1038/s41586-021-03819-2 (2021).

235 Janski, N. *et al.* The GCP3-interacting proteins GIP1 and GIP2 are required for gamma-tubulin complex protein localization, spindle integrity, and chromosomal stability. *Plant Cell* **24**, 1171-1187, doi:10.1105/tpc.111.094904 (2012).

236 Dhani, D. K. *et al.* Mzt1/Tam4, a fission yeast MOZART1 homologue, is an essential component of the gamma-tubulin complex and directly interacts with GCP3(Alp6). *Mol Biol Cell* **24**, 3337-3349, doi:10.1091/mbc.E13-05-0253 (2013).

237 Verollet, C. *et al.* Drosophila melanogaster gamma-TuRC is dispensable for targeting gamma-tubulin to the centrosome and microtubule nucleation. *J Cell Biol* **172**, 517-528, doi:10.1083/jcb.200511071 (2006).

238 Hull, S. *et al.* Clinical and Molecular Characterization of Familial Exudative Vitreoretinopathy Associated With Microcephaly. *Am J Ophthalmol* **207**, 87-98, doi:10.1016/j.ajo.2019.05.001 (2019).

239 Shurygina, M. F. *et al.* Genotype Phenotype Correlation and Variability in Microcephaly Associated With Chorioretinopathy or Familial Exudative Vitreoretinopathy. *Invest Ophthalmol Vis Sci* **61**, 2, doi:10.1167/iovs.61.13.2 (2020).

240 Mastronarde, D. N. SerialEM: A Program for Automated Tilt Series Acquisition on Tecnai Microscopes Using Prediction of Specimen Position. *Microscopy and Microanalysis* **9**, 1182-1183, doi:10.1017/S1431927603445911 (2003).

241 Zheng, S. Q. *et al.* MotionCor2: anisotropic correction of beam-induced motion for improved cryo-electron microscopy. *Nat Methods* **14**, 331-332, doi:10.1038/nmeth.4193 (2017).

242 Zhang, K. Gctf: Real-time CTF determination and correction. *J Struct Biol* **193**, 1-12, doi:10.1016/j.jsb.2015.11.003 (2016).

243 Zivanov, J. *et al.* New tools for automated high-resolution cryo-EM structure determination in RELION-3. *Elife* **7**, doi:10.7554/eLife.42166 (2018).

244 Pettersen, E. F. *et al.* UCSF Chimera--a visualization system for exploratory research and analysis. *J Comput Chem* **25**, 1605-1612, doi:10.1002/jcc.20084 (2004).

245 Kelley, L. A., Mezulis, S., Yates, C. M., Wass, M. N. & Sternberg, M. J. The Phyre2 web portal for protein modeling, prediction and analysis. *Nat Protoc* **10**, 845-858, doi:10.1038/nprot.2015.053 (2015).

246 Kidmose, R. T. *et al.* Namdinator - automatic molecular dynamics flexible fitting of structural models into cryo-EM and crystallography experimental maps. *IUCrJ* **6**, 526-531, doi:10.1107/S2052252519007619 (2019).

247 Emsley, P. & Cowtan, K. Coot: model-building tools for molecular graphics. *Acta Crystallogr D Biol Crystallogr* **60**, 2126-2132, doi:10.1107/S0907444904019158 (2004).
248 Afonine, P. V. *et al.* Real-space refinement in PHENIX for cryo-EM and crystallography. *Acta Crystallogr D Struct Biol* **74**, 531-544, doi:10.1107/S2059798318006551 (2018).
249 Krissinel, E. & Henrick, K. Inference of macromolecular assemblies from crystalline state. *J Mol Biol* **372**, 774-797, doi:10.1016/j.jmb.2007.05.022 (2007).
250 Pei, J., Kim, B. H. & Grishin, N. V. PROMALS3D: a tool for multiple protein sequence and structure alignments. *Nucleic Acids Res* **36**, 2295-2300, doi:10.1093/nar/gkn072 (2008).
251 Katoh, K., Rozewicki, J. & Yamada, K. D. MAFFT online service: multiple sequence alignment, interactive sequence choice and visualization. *Brief Bioinform* **20**, 1160-1166, doi:10.1093/bib/bbx108 (2019).
252 Waterhouse, A. M., Procter, J. B., Martin, D. M., Clamp, M. & Barton, G. J. Jalview Version 2--a multiple sequence alignment editor and analysis workbench. *Bioinformatics* **25**, 1189-1191, doi:10.1093/bioinformatics/btp033 (2009).
253 McGuffin, L. J., Bryson, K. & Jones, D. T. The PSIPRED protein structure prediction server. *Bioinformatics* **16**, 404-405, doi:10.1093/bioinformatics/16.4.404 (2000).
254 Ribeiro, J. V. *et al.* QwikMD - Integrative Molecular Dynamics Toolkit for Novices and Experts. *Sci Rep* **6**, 26536, doi:10.1038/srep26536 (2016).
255 Phillips, J. C. *et al.* Scalable molecular dynamics on CPU and GPU architectures with NAMD. *J Chem Phys* **153**, 044130, doi:10.1063/5.0014475 (2020).
256 Zimmermann, L. *et al.* A Completely Reimplemented MPI Bioinformatics Toolkit with a New HHpred Server at its Core. *J Mol Biol* **430**, 2237-2243, doi:10.1016/j.jmb.2017.12.007 (2018).
257 Manka, S. W. & Moores, C. A. The role of tubulin-tubulin lattice contacts in the mechanism of microtubule dynamic instability. *Nat Struct Mol Biol* **25**, 607-615, doi:10.1038/s41594-018-0087-8 (2018).
258 Bepler, T. *et al.* Positive-unlabeled convolutional neural networks for particle picking in cryo-electron micrographs. *Res Comput Mol Biol* **10812**, 245-247 (2018).
259 Punjani, A., Rubinstein, J. L., Fleet, D. J. & Brubaker, M. A. cryoSPARC: algorithms for rapid unsupervised cryo-EM structure determination. *Nat Methods* **14**, 290-296, doi:10.1038/nmeth.4169 (2017).
260 Humphrey, W., Dalke, A. & Schulten, K. VMD: visual molecular dynamics. *J Mol Graph* **14**, 33-38, 27-38, doi:10.1016/0263-7855(96)00018-5 (1996).
261 Trabuco, L. G., Villa, E., Mitra, K., Frank, J. & Schulten, K. Flexible fitting of atomic structures into electron microscopy maps using molecular dynamics. *Structure* **16**, 673-683, doi:10.1016/j.str.2008.03.005 (2008).
262 Goddard, T. D. *et al.* UCSF ChimeraX: Meeting modern challenges in visualization and analysis. *Protein Sci* **27**, 14-25, doi:10.1002/pro.3235 (2018).

8 Publications

Liu, P.*, Zupa, E.*, Neuner, A. *et al.* Insights into the assembly and activation of the microtubule nucleator γ-TuRC. *Nature* **578,** 467–471 (2020). https://doi.org/10.1038/s41586-019-1896-6

Zupa, E.*, Zheng, A.*, Neuner, A. *et al.* The cryo-EM structure of a γ-TuSC elucidates architecture and regulation of minimal microtubule nucleation systems. *Nat Commun* **11,** 5705 (2020). https://doi.org/10.1038/s41467-020-19456-8

Würtz, M.*, Zupa, E.*, Atorino, E.S.* *et al.* Modular assembly of the principal microtubule nucleator γ-TuRC. *Nat Commun* **13,** 473 (2022). https://doi.org/10.1038/s41467-022-28079-0

Zupa E*, Liu P*, Würtz M, Schiebel E, Pfeffer S. The structure of the γ-TuRC: a 25-years-old molecular puzzle. Curr Opin Struct Biol. 2021 Feb;66:15-21. doi: 10.1016/j.sbi.2020.08.008. Epub 2020 Sep 29. PMID: 33002806.

Liu P*, Würtz M*, Zupa E, Pfeffer S, Schiebel E. Microtubule nucleation: The waltz between γ-tubulin ring complex and associated proteins. Curr Opin Cell Biol. 2021 Feb;68:124-131. doi: 10.1016/j.ceb.2020.10.004. Epub 2020 Nov 12. PMID: 33190097.

Martin Würtz*, Anna Böhler*, Annett Neuner, Erik Zupa, Lukas Rohland, Peng Liu, Bram J. A. Vermeulen, Stefan Pfeffer, Sebastian Eustermannand Elmar Schiebel. 2021, Reconstitution of the recombinant human γ-tubulin ring complex, Open Biol.**11:**200325200325 http://doi.org/10.1098/rsob.200325

In preparation:

Erik Zupa*, Martin Würtz*, Annett Neuner *et al.* The augmin complex architecture reveals structural insights into microtubule branching.

* Contributed equally

9 Acknowledgments

During my PhD studies, I obtained and received plenty of experience, advices, assistance and support from many people who in this way contributed to my scientific growth and without whom this work would not be possible.

Most of all, I want to thank my supervisor Dr. Stefan Pfeffer who gave me an opportunity to work in his new and young group full of enthusiastic people, which allowed me to gain huge expertise in cryo-EM and other methods. Additionally, his constant willingness to discuss and explain helped me in my scientific soft skills, such as writing and presentation making, Because of your guidance, Stefan, I learnt to approach and think about projects and research in a critical and a rational way. You provided me with set of skills that I can hugely build on in my future scientific career.

I would like to thank also Prof. Elmar Schiebel who with Dr. Stefan Pfeffer gave me an opportunity to work on a fantastic collaborative PhD project of these two research groups and allowed me to dive into a structural biology void of MT nucleation and fill it with my contributions. Additionally, I want to thank Prof. Elmar Schiebel for all useful suggestions and questions throughout my PhD studies that drove the project.

My next thank goes to Dr. Sebastian Eustermann, my thesis advisory committee member who came up with new point of views on the project and provided me with interesting suggestions for data processing and new approaches how to analyse data.

I want to thank Dr. Petr Chlanda and Prof. Matthias Mayer for accepting offer to be part of my examination committee.

I want to thank Dr. Enrico Atorino, my unofficial PhD advisor for submission of documents. He helped me tremendously with all details for PhD thesis submission that were not clear to me. Thanks to him, all documentation was much easier to prepare and fill.

My deep thanks go to my collaborators from Prof. Schiebel research group. In particular, Dr. Peng Liu, Martin Würtz, Anjun Zheng, Dr. Annett Neuner and Anna Böhler who purified and provided me with all samples for cryo-EM analysis and performed all necessary biological experiments in the project to complement structural biology data. Without them, this work would not have been done. Specific thank to Dr. Annett Neuner who taught me an efficient way of negative stain EM grid preparation and who acquired negative stain EM data for plenty of the purified samples.

Next, I am very thankful to my colleagues from our small Pfeffer group for creating a great working environment. Sebastian Filbeck, thank you for all great ideas for data analysis and giving me insights into cryo-ET world. Your funny, maybe for someone inappropriate jokes always put tears in my eyes and make my day.

Milan Aleksić, thank you for your persistent support throughout my PhD studies and useful relaxing discussions that made me for a minute forget about the work when I need it. You have never doubted me and you do the best impression of my favourite phrase.

Bram Vermeulen, I am so grateful that you became my partner in a crime for collaborative projects with Prof. Schiebel group. Each day, I got opportunity with you to have amazing brainstorming and discussions about scientific papers, experiments, analyses and data in general that helped me to come up with new ideas and drive my research. Additionally, I could talk with you about any world news and sport news.

I also thank our newest group acquisition Sophie Kopetschke who never had an issue to talk with me when I visited her in a office.

Additionally, I would like to thank Giulia Tonon, rotational student in our group that I supervised, for huge enthusiasm that she put into processing of cryo-EM data and for all of her honest feedback of my supervision. I hope that I motivated her as much as she motivated me.

Very important thank goes to Cryo-EM Network at the Heidelberg University (HDcryoNET) that provided me with all instruments for cryo-EM. In this way, I want to thank Dr. Dirk Flemming who analysed some of the negative stain EM data for the project and gave me great advices for operating microscope and grid preparation. Another person from HDCryoNet that I want to thank is Dr. Götz Hofhaus from whom I learnt much about microscopes, detectors and software algorithms for cryo-EM data processing. He was always there when I needed help at a microscope or when I had any problem or issue that I could not solve myself. And I thank both, Dirk and Götz, for caring about cryo-EM microscopes, making them operational. Without you guys, grid screening and data acquisition would not be possible.

Last thank goes to The University Computing Centre (Universitätsrechenzentrum, URZ) that provided me computational resources for an analysis of cryo-EM data. This allowed me to obtain a big part of the results that were published and are shown in this PhD thesis. I would like to thank here specifically Dr. Sabine Richling for a cryo-EM software support. She was always willing to install any new software for data processing when I asked her.